Functional Supports For Heterogeneous Reduction Reactions

Subtitle: Understanding the Relationship between Structure and Performance

Rebecca Stones

Submitted in accordance with the requirements for the degree of Doctor of Philosophy

The University of Leeds

School of Chemistry

September, 2019

The candidate confirms that the work submitted is her own, except where work which has formed part of jointly authored publications has been included. The contribution of the candidate and the other authors to this work has been explicitly indicated below. The candidate confirms that appropriate credit has been given within the thesis where reference has been made to the work of others. Further details of the jointly-authored publications and the contributions of the candidate and the other authors to the work should be included below this statement.

References for jointly authored publications:

1. S. Doherty, J. G. Knight, T. Backhouse, E. Abood, H. Alshaikh, I. J. S. Fairlamb, R. A. Bourne, T. W. Chamberlain and **R. Stones**, *Green Chem.*, 2017, **19**, 1635-1641; Highly efficient aqueous phase chemoselective hydrogenation of α,β-unsaturated aldehydes catalysed by phosphine-decorated polymer immobilized IL-stabilised PdNPs.

The work described in this publication is presented in Chapter 4 of this thesis. Catalyst materials were prepared by Dr Tom Backhouse under the supervision of Dr Simon Doherty at the University of Newcastle. The prepared materials were characterised using transmission electron microscopy by the candidate to gain understanding of the structure activity relationship.

2. S. Doherty, J. G. Knight, T. Backhouse, E. Abood, H. Alshaikh, A. R. Clemmet, J. R. Ellison, R. A. Bourne, T. W. Chamberlain, **R. Stones**, N. J. Warren, I. J. S. Fairlamb and K. R. J. Lovelock, *Adv. Synth. Catal.*, 2018, **360**, 3716-3731; Heteroatom donor-decorated polymer-immobilized ionic liquid stabilized palladium nanoparticles: Efficient catalysts for room-temperature Suzuki-Miyaura cross-coupling in aqueous media.

The work described in this publication is presented in Chapter 4 of this thesis. Catalyst materials were prepared by Dr Tom Backhouse under the supervision of Dr Simon Doherty at the University of Newcastle. The prepared materials were characterised using transmission electron microscopy by the candidate to gain understanding of the structure activity relationship.

3. S. Doherty, J. G. Knight, T. Backhouse, A. Bradford, F. Saunders, R. A. Bourne, T. W. Chamberlain, **R. Stones**, A. Clayton and K. R. J. Lovelock, *Catal. Sci. Technol.*, 2018, **8**, 1454-1467; Highly efficient aqueous phase reduction of nitroarenes catalyzed by phosphine-decorated polymer immobilized ionic liquid stabilized PdNPs.

The work described in this publication is presented in Chapter 4 of this thesis. Catalyst materials were prepared by Dr Tom Backhouse under the supervision of Dr Simon Doherty, X-ray photoelectron spectroscopy measurements of the materials was conducted by Dr A. Bradford at the University of Newcastle. Prepared materials were characterised using transmission electron microscopy by the candidate to gain understanding of the structure activity relationship.

> 4. S. Doherty, J. G. Knight, T. Backhouse, R. J. Summers, E. Abood, W. Simpson, W. Paget, R. A. Bourne, T. W. Chamberlain, **R. Stones**, K. R. J. Lovelock, J. M. Seymour, M. A. Isaacs, C. Hardacre, H. Daly and N. H. Rees, *ACS Catal.*, 2019, **9**, 4777-4791; Highly selective and solvent-dependent reduction of nitrobenzene to *N*-phenylhydroxylamine, azoxybenzene, and aniline catalyzed by phosphino-modified polymer immobilized ionic liquid-stabilized AuNPs.

The work described in this publication is presented in Chapter 4 of this thesis. Catalyst materials were prepared by Dr Tom Backhouse under the supervision of Dr Simon Doherty at the University of Newcastle. The prepared materials were characterised using transmission electron microscopy by the candidate to gain understanding of the structure activity relationship. X-ray photoelectron spectroscopy measurements of the materials was conducted by Dr M. A. Isaacs at the National XPS facility at Harwell.

> 5. A. J. Blacker, G. Maron-Malagon, L. Powell, W. Reynolds, R. Stones and M. R. Chapman, *Org. Process Res. Dev.*, 2018, **22**, 1086-1091; Development of an S_NAr reaction: A practical and scalable strategy to sequester and remove HF.

The work described in this publication was carried out during my time at the University of Leeds. However, it has not been discussed within this thesis.

Acknowledgements

First, and foremost, I would like to thank my supervisor Dr Thomas Chamberlain, not only for the tremendous amount of support he has given me, but for his encouragement and guidance throughout this project. I will be forever grateful for the opportunities you have afforded me that have helped me develop both on a professional and personal level. You have given me the confidence to pursue a career in academia. Thanks, are also needed for your tireless support throughout the last few months of my PhD; I really do appreciate the time and effort it has taken to read my thesis chapters.

I especially need to thank Dr Mike Ward, Dr Nicole Hondow and Dr Zabeada Aslam for providing training and assistance in TEM and STEM-EDX.

There are a number of scientific contributions to this thesis that also need to be acknowledged. Thank you to the Catalysis Hub for granting funding for beam time at Diamond Light Source to obtain XAFs data for my materials. Thank you to Jamie Mannering for running BET analysis of my samples and Jonathan White for running ICP-MS. Thanks, are also due to Jessica Morgan (the perfect MChem) for the work she carried out during her MChem project.

Thanks to the collaborators at the University of Newcastle, Dr Tom Backhouse and Dr Simon Doherty, for providing me with a range of NP-based systems to characterise. The numerous samples definitely helped improve my microscopy skills.

Thank you to all the members of office 2.71 (formerly known of office 2.85). Xiangyi thanks for always being happy to help me clean up oil when an oil bath breaks (keep the lab tidy when I'm gone), Damon, thanks for being so eccentric and keeping life interesting and finally, Jamie thank you for your unwavering support throughout the last two years, whether it be listening to me practice a presentation for the 20th time or constantly having to explain how to plot two graphs in one on origin.

Thanks to Laura, Sam O and Sam G for welcoming me into your respective offices and for always providing a source of entertainment and biscuits. The first year of my PhD would have been very lonely without you. To all members of iPRD, past and present, know that you have contributed in some way to help me through this process so thank you, particularly Will (for upholding our deal), James, Grant, Rachel, Alastair, Chris 1 and Chris 2 (I'll let you decide who's who) and of course Mary.

Massive thanks to Emma, Frances, Kay, Kevin and Ben as life at the University of Leeds would have been every different without you. Our daily lunch time breaks gave me a much-needed pause from the stress that comes with life as a PhD student as well as being source of support and advice. Emma I already miss our hot chocolate breaks and daily chats about all the dance drama. Which leads to me to acknowledge The University of Leeds Dancesport Society for being the perfect distraction, particularly Amber for teaching me to not take life too seriously. You will always be my favourite dance partner.

Finally, and probably most importantly, I need to thank my family especially my amazing mother. Mom thank you for always believing in me even when I didn't believe in myself. I really couldn't have done it without you.

Abstract

The work presented in this thesis describes the preparation and application of novel heterogeneous catalyst systems. Two avenues for the support/stabilisation of catalytically active transition metal nanoparticles (NPs) have been investigated: carbon nanoreactors and polymer immobilised ionic liquids. The effects of simple changes to the fabrication method on the resultant structure of these materials was investigated using a number of characterisation techniques and the efficiency of the support systems was investigated using exploratory chemical reactions to gain insight into the structure activity relationship.

The first systems consist of hollow carbon nanostructures as supports for catalytically active metal NPs. A series of mono- and bimetallic ruthenium and nickel based nanoparticles were encapsulated in graphitic nanofibers (GNFs) using a versatile sublimation deposition approach. The effect of varying the metal loading and fabrication conditions, as well as the Ru:Ni ratio and addition sequence for bimetallic systems, was explored both in terms of structure and catalytic performance of the GNF supported catalysts. By examining the structural changes in the resultant materials this study aims to provide some understanding of how the composition of ruthenium and nickel based bimetallic nanoparticles supported within GNFs can be altered simply through changes in the fabrication method to tailor the activity of the catalyst materials for a given reaction. It was found that lower metal loadings result in a more well-defined structure with a more controlled distribution of MNPs. Additionally, the addition sequence employed during the fabrication of bimetallic systems can drastically alter the resultant structure of the material and therefore their catalytic performance.

Exploratory hydrogenation reactions were employed to probe the catalytic performance, in terms of activity, selectivity and recyclability, of the mono- and bimetallic materials fabricated. It was found that the concerted addition fabrication method for bimetallic RuNiNPs afforded the only active material towards the reduction of nitrobenzene to aniline with the optimum ratio of Ru:Ni being 1:1 ($Ru_{0.5}Ni_{0.5}$NPs@GNFs (concerted addition) had the highest TOF of 24.1 ± 1.7 $mol_{An}mol_{M}^{-1}$/h). The effects of nanoscale confinement in carbon nanoreactors has previously been shown to dramatically affect the activity, selectivity and stability of catalytic chemical transformations. In this study, the confinement effects imposed by the GNF support structure were explored using competitive reduction reactions, where the starting materials

contain the same nitro functional group, but differing sizes, shapes and degrees of aromaticity, to gain further understanding of the interactions between reactant molecules and support structure by looking at which molecule preferentially reacts.

These results demonstrate a general methodology for the controlled fabrication of active and robust, mixed MNP catalysts supported in carbon nanoreactors.

The second systems consist of polymer supports, with differing functionalities, for catalytically relevant Pd and AuNPs. Modification of the polymer support structure in various ways (selective inclusion of various heteroatom donors, inclusion of an ionic liquid (IL) and inclusion of a polyethylene glycol unit (PEG)) were successfully achieved to enable the MNP stabilisation. The effect of varying the multifunctional support structure on the size of MNPs formed was investigated using transmission electron microscopy. Changing the components of the supported structure e.g. selective removal of the IL, had little effect on average MNP size.

Numerous exploratory reactions were employed to probe the catalytic performance, in terms of activity, selectivity and recyclability of the polymer supported materials. These materials were found to achieve high activities/selectivities for a range of reactions (e.g. hydrogenation and Suzuki-Miyaura cross-couplings) under mild reaction conditions with each component of the system plays a vital role in their efficiency; ionic liquid provides stabilisation of MNPs, polymer support prevents leaching of the ionic liquid during catalysis and affords easier recyclability, the heteroatom donor provides further stabilisation of the MNPs, and the polyethylene glycol unit improves the dispersibility of material in aqueous media.

These results demonstrate the ability to tune the activity of a material based on the support system employed.

Table of Contents

Table of Figures

Table of Schemes

Table of Tables

List of Abbreviations

AB	Ammonia Borane
AC	Activated Carbon
AIBN	Azobisisobutyronitrile
BET	Brunauer-Emmett-Teller
BJH	Barrett Joyner Halenda
CNRs	Carbon Nanoreactors
CNSs	Carbon Nanostructures
CNTs	Carbon Nanotubes
CTH	Catalytic Transfer Hydrogenation
CVD	Chemical Vapour Deposition
EDX	Energy Dispersive X-Ray Spectroscopy
EXAFS	Extended X-Ray Absorption Fine Structure
FID	Flame Ionisation Detector
fwhm	Full Width Half Maximum
GC	Gas Chromatography
GNF	Graphitised Nanofiber
HAADF	High-Angle Annular Dark-Field
HAD	Heteroatom Donor
ICP-MS	Inductively Coupled Plasma Mass Spectroscopy
ILs	Ionic Liquids
IPA	2-Propanol
MNPs	Metal Nanoparticles
MWNTS	Multi-Walled Carbon Nanotubes
NA	1-Nitroadamantane
NB	Nitrobenzene
NC	Nitrocyclohexene
NPs	Nanoparticles
NPs/CNTs	CNTs Externally Functionalised with Nanoparticles

NPs@GNFs	GNFs Internally Functionalised with Nanoparticles
PEG	Polyethylene Glycol
PILP	Polymer-Immobilised Ionic Liquid
RGO	Reduced Graphene Oxide
Ru/C	Ruthenium on Activated Carbon
$Ru_{0.75}Ni_{0.25}$NPs	Bimetallic nanoparticles with an Ru:Ni ratio of 3:1
$Ru_{0.5}Ni_{0.5}$NPs	Bimetallic nanoparticles with an Ru:Ni ratio of 1:1
$Ru_{0.25}Ni_{0.75}$NPs	Bimetallic nanoparticles with an Ru:Ni ratio of 1:3
$scCO_2$	Supercritical Carbon Dioxide
SEM	Scanning Electron Microscopy
SSA	Specific Surface Area
STEM	Scanning Transmission Electron Microscopy
SWNTs	Single-Walled Carbon Nanotubes
TEM	Transmission Electron Microscopy
TGA	Thermo-gravimetric Analysis
TOF	Turn Over Frequency
TON	Turn Over Number
TPR	Temperature Programmed Reduction
XANES	X-Ray Absorption Near Edge Structure
XPS	X-Ray Photoelectron Spectroscopy
XRD	X-Ray Diffraction

Chapter 1: Introduction

1.1 Supported MNPs for Heterogeneous Catalysis

Transition metal nanoparticles (MNPs) have been demonstrated to be excellent candidates for catalysis due to their remarkable chemical and physical properties.[1] Their high specific surface area allows for a large proportion of the metals atoms to be accessible to reactant molecules/substrates, resulting in a high catalytic activity.[2] However, they are intrinsically thermodynamically metastable making their application difficult, therefore, the stabilisation of MNPs is important in order to prevent aggregation, sintering and leaching of the metal during catalysis. An effective method to combat these problems is to immobilise the MNPs on porous solid supports such as; silica,[3,4] alumina,[5–7] zeolites,[8,9] and carbon nanomaterials.[10–12] The resultant materials have been utilised as heterogeneous catalysts for a number of reactions including; Fischer-Tropsch synthesis,[3,13–15] oxygen reduction and hydrogen evolution reactions,[11,16,17] Suzuki-Miyaura cross coupling[18,19] and simple hydrogenation reactions.[6,20–22]

Carbon-based materials offer many advantages to their application as catalyst supports including; i) high chemical stability in acidic and basic media, ii) high thermal stability (compared to other supports such as titanium dioxide (TiO_2), alumina (Al_2O_3) and mesoporous silica (SiO_2)),[23] iii) large specific surface area, iv) relative chemical inertness, iv) excellent electron conductivity, v) the possibility to control their porosity and hydrophobic nature by changing their surface chemistry and vi) the opportunity to tune the specific metal-support interactions (which can causes changes in the activity and selectivity of the catalyst).[24,25] Additionally, the functionalisation of most carbon supports with MNPS can be easily achieved.[23,26–29] The synthesis and applications of carbon supported MNPs has been the subject of several reviews.[24,25,30–32]

The high surface areas, low costs, and mass availability of activated carbon and carbon black make them a popular choice when considering carbon as a support material.[25,33] Al-Shaal *et al.*,[34] investigated the hydrogenation/dehydration of levulinic acid (see Scheme 1.1 for possible reaction pathways) catalysed by RuNPs and compared their activity when supported on a number of different supports (i.e. C, SiO_2, Al_2O_3 and TiO_2 (all supported catalysts were 5% by wt. Ru)). Of the catalyst materials screened

they found that the greatest conversion was achieved for Ru-C (100%) compared to significantly lower activities observed for Ru-SiO_2 (2.1%), Ru-Al_2O_3 (8.4%) and Ru-TiO_2 (0%). Additionally, the Ru-C catalyst afforded the highest selectivity towards the desired γ-valerolacetone product (selectivities of 97.5, 81.0 and 75.1% were obtained for Ru-C, Ru-SiO_2 and Al_2O_3, respectively).[34]

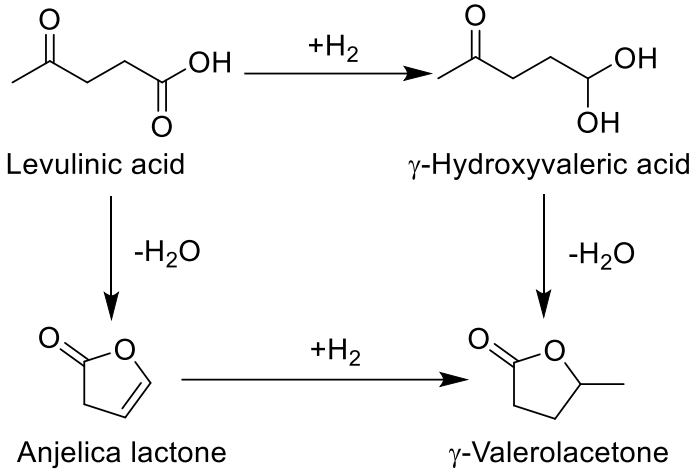

Scheme 1.1: Reaction pathway for the hydrogenation/dehydration of levulinic acid.

Additionally, Zea *et al*.,[35] compared the activity of PdNPs supported on activated carbon or Al_2O_3 for the hydrogenation of acetylene. They reported that although higher overall conversions were obtained for PdNPs-Al_2O_3, the PdNP-C catalyst gave the highest selectivity towards 1-butene (ca. 75% compared to ca. 50% for PdNPs-Al_2O_3).[35]

These studies demonstrate that the support structure can have a profound influence on the activity of supported MNPs. Thermal stability and specific adsorption properties are important factors that influence the final activity and reproducibility of a catalytic system.[36]

Tubular carbon nanostructures, such as carbon nanotubes (CNTs) and graphitised carbon nanofibers (GNFs), have been proposed to be ideal support candidates for the stabilisation of MNPs due to their cylindrical shape. Not only do they help stabilise the MNPs, against coalescence, sintering and poisoning, they provide a unique local environment which can drastically change the pathways of chemical reactions, leading to the formation of new products. [12,19] The properties of CNTs and GNFs compared to activated carbon (AC) are summarised in Table 1.1.

Table 1.1: Properties of CNTs and GNFs compared to AC.[36–38]

Nanocarbon	Porosity / $cm^3\ g^{-1}$	Surface area / $m^2\ g^{-1}$	Thermal resistance / ºC	Internal diameter / nm
SWNTs	Microporous	400-900	~800	1-2
MWNTs	Mesoporous	200-400	~650	10-100
GNFs	Mesoporous	10-200	~600-900	50-70
AC	Microporous	700-1200	~500-600	N/A

1.2 Carbon Nanostructures

Carbon nanostructures (CNSs) such as; CNTs, GNFs, fullerenes and graphitised mesoporous carbon, contain well-defined channels and/or pores of differing shapes and sizes that can be tailored to encapsulate nanoparticle and molecular catalysts. Compared to other nano-containers they have significantly higher thermal stability, have a higher tensile strength than steel and have chemically unreactive internal channels, making them the ideal reaction vessels for performing a vast range of chemical reactions.[19,39] Due to recent advances in production, CNTs have become readily available in large quantities at low cost increasing their potential for application.[40–42] As a result numerous studies have reported the application of CNTs as MNP support structures.[43–53]

Essentially, CNTs can be divided into two categories; single walled nanotubes (SWNTs) and multi walled nanotubes (MWNTs). SWNTs can be thought of as a single graphene sheet (a hexagonal array of sp^2 hybridised carbon atoms) rolled-up into a cylinder (see Figure 1.1), with MWNTs containing concentric tubes of carbon varying in number, from 2 (known as double walled nanotubes (DWNTs)) to several, with increasing numbers of concentric tubes leading to an increase in the average external diameter of the nanotube.[12,36]

The electronic properties of these materials are governed by two principle factors: the diameter of the nanotube and helicity (which is considered theoretically as how a graphene sheet would be rolled-up to make the resultant nanotube). Depending on the arrangement of atoms these CNTs can be metallic (armchair arrangement of atoms) or semi-conducting (zig-zag arrangement of atoms).[36]

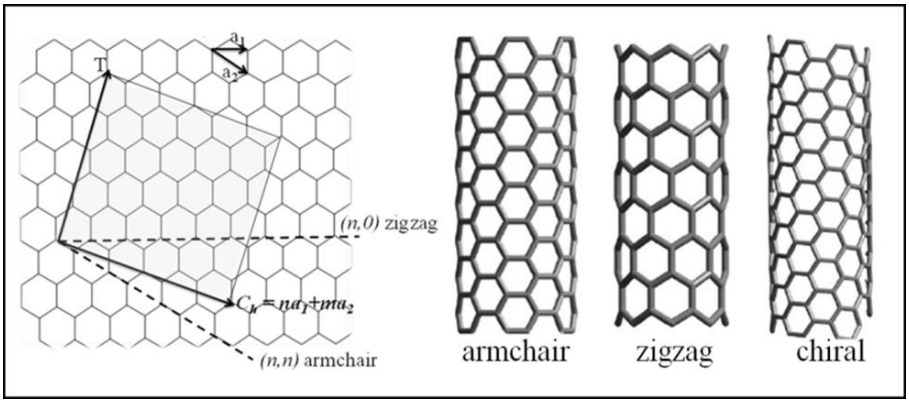

Figure 1.1: Schematic representation of how a 2D graphene sheet can be rolled to afford three SWNTs with differing arrangements of carbon atoms.[54]

There are three common methods for the fabrication of CNTs: i) chemical vapour deposition (CVD),[55–60] ii) arc-discharge[61–65] and iii) laser ablation.[66–70] As CVD allows for control over CNT diameter, high growth rates leading to the formation of high quality structures and more effective control of reaction conditions, it is the most viable option for large scale production.[25] Additionally, CVD can be carried out at reduced temperatures (500-1000 °C) compared to the temperatures required for other methods (>3000 °C).[71–76] CVD is the catalytic deposition of hydrocarbons over a transition metal supported catalyst (see Figure1.2 for typical reaction set up) with the characteristics of the produced CNTs dependent upon experimental conditions such as: temperature, pressure, reaction time, catalyst, catalyst pre-treatment and concentration.[71,77,78]

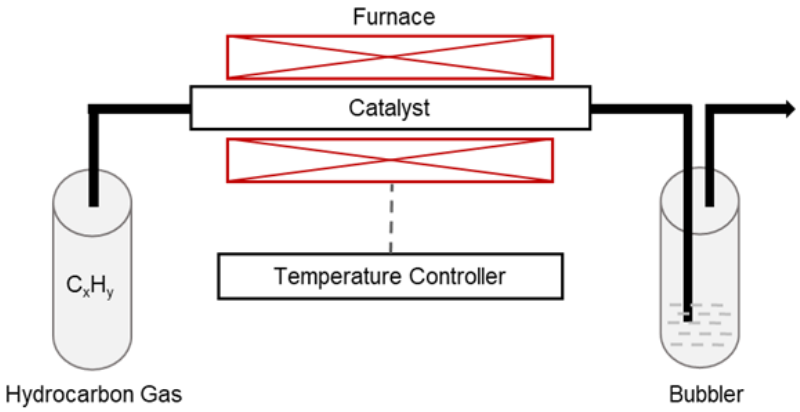

Figure 1.2: Simplified schematic for the CVD process set-up. Adapted from reference 71.

The general reaction procedure for the fabrication of CNTs by CVD is as follows: the pre-prepared support material/catalyst is placed in a tubular reactor/furnace. Once the furnace has reached the desired temperature a mixture of hydrocarbon gas and process gas (typically N_2, H_2 or Ar) is flowed

into the reaction chamber. Decomposition of the carbon precursor takes place and CNTs grow on the catalyst particles in the reactor. These CNTs are later collected from the support surfaces after cooling to room temperature.[71]

Another advantage of this preparation method is the large number of hydrocarbons that be used as the carbon source. These include but is not limited to: methane, ethane, ethanol, ethylene and acetylene.[71,79] Iron, cobalt and nickel catalysts, supported on alumina, silica and magnesium oxide, are most frequently used as catalysts for the growth of CNTs via CVD. However, other transition metals (such as Pd, Pt, Ru, Au, Ag and Cu) and lanthanides (Gd and Eu) as catalysts have been previously reported.[79] Typical reaction times found in the literature are between 30 and 60 minutes.[75] Shajahan *et al.*,[80] reported that for reaction times longer than 30 minutes the quality of CNT is reduced. Conversely, Fazle Kibria and co-workers[80] observed no change in the levels of graphitization in CNT samples obtained between 30 and 180 minutes. The purification of CNTs fabricated through CVD is required to remove the metal catalyst and associated support. However, some catalysts such as MNPs or silica require the use of strong acids which may damage the CNT structure.[72,81–83]

There has been a plethora of methods reported for the decoration of CNTs with MNPs, each offering a certain degree of control over distribution and NP size. These methods include incipient wetness impregnation;[84–95] organometallic grafting;[96] electrochemical deposition;[97] electroless deposition, with and without the use of reducing agents;[98–100] electron beam evaporation;[101] in situ filling during arc-discharge growth of CNTs;[102] and sublimation deposition approaches[12,19-21] (these methods of MNP incorporation are discussed further in Section 1.3.1).

1.2.1 Graphitised Nanofibers (GNFs)

GNFs have a significantly wider internal channel compared to CNTs, with internal diameters typically between 50-70 nm, and are generally much shorter, with a maximum length of ~500 nm. Both of these factors greatly reduce transport resistance, allowing effective transport of molecules through the internal channels and ensuring that the internal cavity is continuously accessible.[39,105] GNFs have been less explored as nano-containers, compared to CNTs, principally as a result of them being less readily accessible as they are only commercially available from a handful of suppliers. However, they possess several unique properties analogous to CNTs, with the added advantage of a larger internal volume, making them a practical and

versatile solid support for heterogeneous catalysis.[39] The outer surface of GNFs is atomically smooth, whereas the surface of the inner cavities contains step-edges approximately 3-4 nm high and spaced evenly apart along the inner channel (Figure1.3b and c).[36,39] These step-edges are a result of stacked graphitic cones (formed by rolled-up sheets of graphene) oriented at an angle of approximately 30 degrees relative to the main GNF growth axis.[37] These graphitic step-edges are the perfect size and shape to immobilise both molecular complexes and MNP based catalytic species where the catalyst is efficiently anchored.[38,106,107]

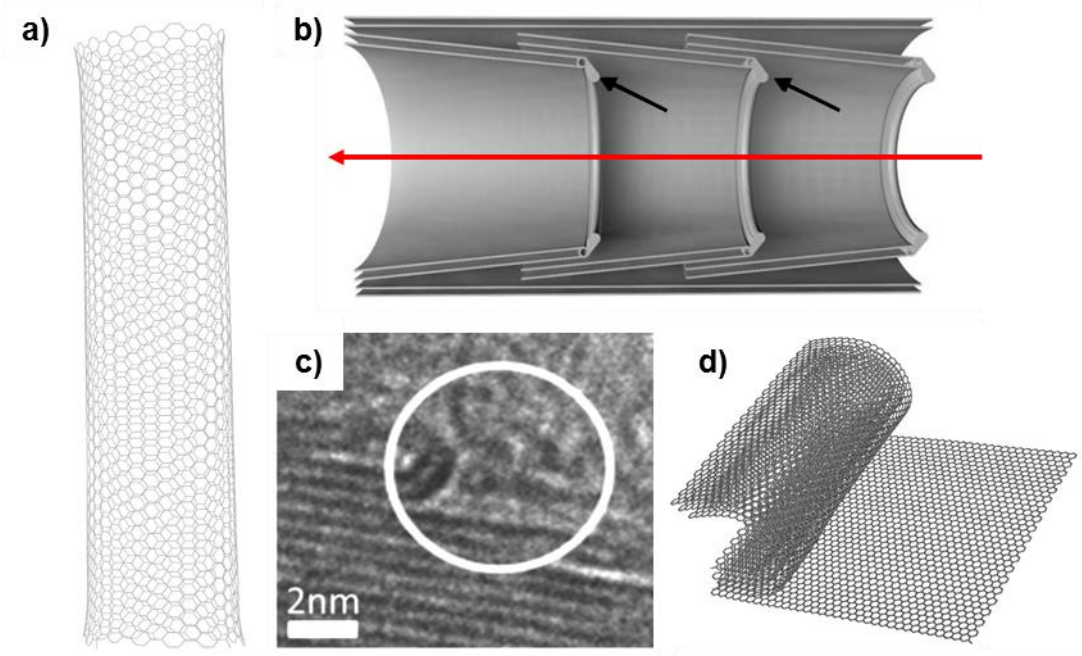

Figure 1.3: a) Atomic structure of a CNT with an atomically smooth interior cavity, CNTs typically have inner diameters of 1-10 nm; b) diagram of a GNF with stacked graphitic step-edges (indicated by the black arrows) along the interior channel (red arrow indicates the main axis of the GNF), GNFs typically have inner diameters of 50-70 nm; and TEM micrograph of the ~3 nm high step-edges on the interior channel of GNFs at which a fullerene molecule is anchored (white circle);[108] and d) representative diagram of the graphitic sheets rolled up to give rise to these step-edges.

This was evidenced by Lebedeva *et al.*,[108,109] who reported the heterogenization of catalytic molecules containing fullerenes. They reported the successful anchoring of the catalyst at the GNF step-edge (Figure 1.4) due to favourable interactions between the catalyst and support structure, in which the fullerene C_{60} molecule was essential.[108,109]

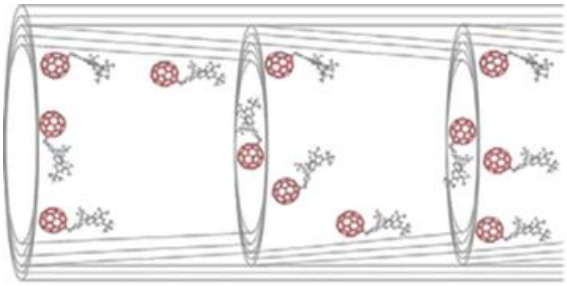

Figure 1.4: Schematic representation of fullerene-containing molecules located preferentially on the step-edges of the GNF interior.[109]

Additionally, Rance *et al.*,[110] reported the successful immobilisation of copper nanoparticles at the step-edges within GNFs leading to a wide distribution of CuNPs within the support structure (see Figure 1.5).[110]

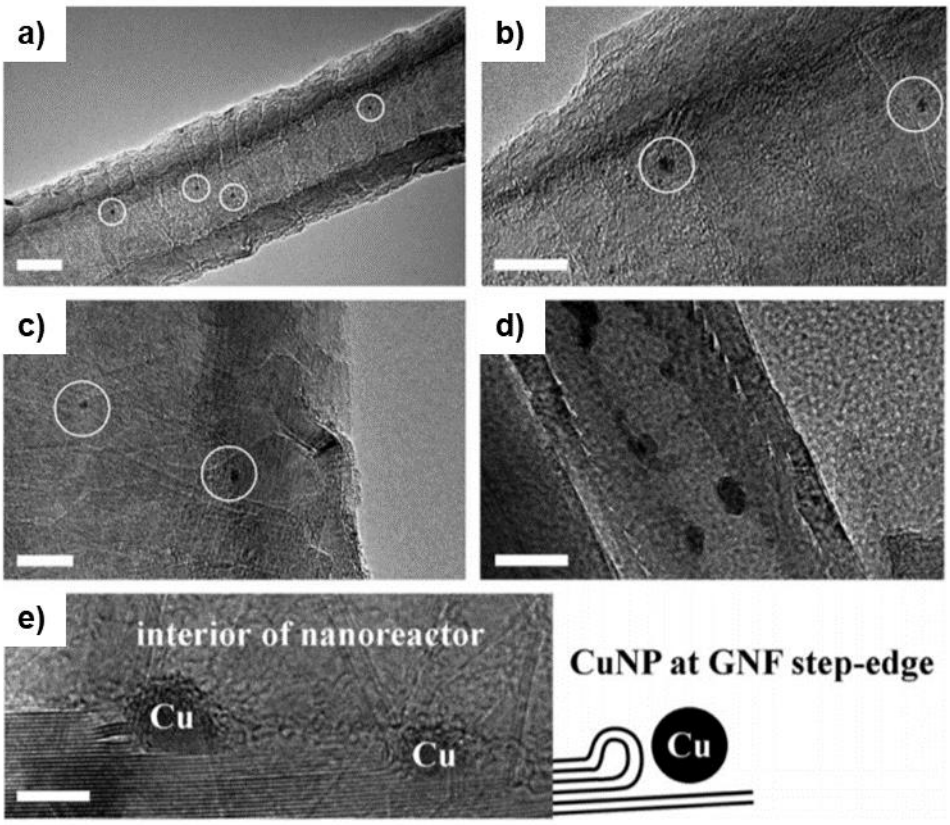

Figure 1.5: High resolution TEM of CuNPs@GNFs immobilised at the step-edges highlighted with white circles. Scale bars are 20 nm (a and d), 10 nm (b and c) and 5 nm (e).[110]

Immobilising catalytic species at the step-edges within GNFs results in beneficial effects in terms of stability activity arising from the confinement imposed by the channel. Immobilising catalytic species within this corrugated interior structure creates localised reaction environments, with can greatly alter the concentrations of reactants as compared to the bulk phase.[37–39]

Comparison between the observed effects of the extreme confinements of DWNTs and MWNTs, and the low confinement of GNFs when used as catalyst supports in the RhNP catalysed hydrosilylation of phenylacetylene and triethylsilane was reported by Solomonsz *et al.*[38] who found that GNFs changed the reaction pathway most significantly (see Figure 1.6).[38]

This demonstrates that whilst GNF impose no restriction on the transport of reactants into/out of their internal channels, they provided the strongest confinement effects. This was attributed to the step-edges of the GNF providing efficient anchoring points for Rh-based catalysts, creating local environments with significantly altered concentrations of reactants compared to the bulk solution.

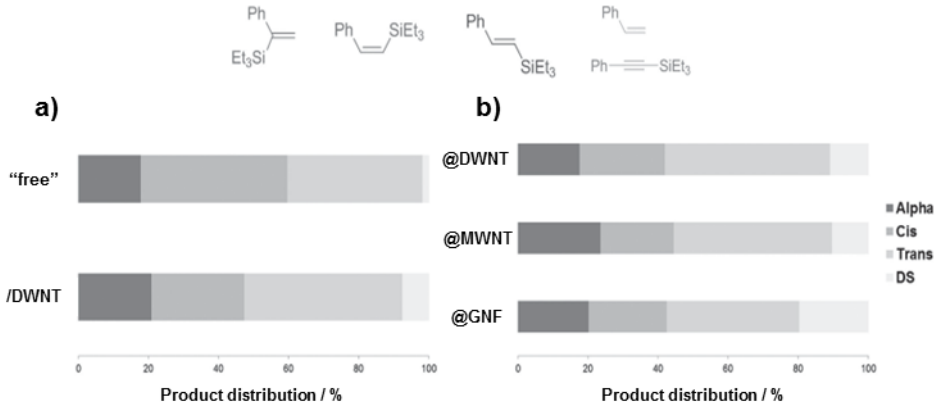

Figure 1.6: Graphical representation of the changes in regioselectivity observed upon supporting RhNPs showing that GNF supported RhNPs exhibited the greatest shift in regioselectivity compared to the unconfined system.[38]

1.3 Carbon Nanoreactors

Encapsulating MNPs inside of carbon nanostructures, to form so-called carbon nanoreactors (CNRs), can drastically alter the properties of the MNPs and strongly depends not only upon the size of the NPs and surface composition, but also the nature of the metal-support interactions.[111] Depending upon these interactions drastic effects on the concentrations, pressures and alignment of reactant molecules, as well as a lower activation energy of a reaction, compared to bulk phase, can be observed.[112] Carrying out reactions inside these CNRs, therefore, provides a way in which the pathways of conventional organic reactions can be altered to yield products different than those obtained from bulk solution.[38] Table 1.2 summarises the effects of CNRs on chemical reactions.

Table 1.2: Effects of carbon nanoreactors on chemical reactions.[19,38,113]

Carbon Support	Interactions between the catalyst and the CNS support	Interactions between the CNR and reactants	Interactions between the CNR and products
CNTs	Stabilisation by van der Waals interactions with the concave interior surface of the CNT.	Attractive interactions lead to higher local concentration of reactants. Alignment of reactants within the CNR facilitate the reaction. Electron transfer or van der Waals interactions lead to a lower activation energy.	Reaction space restrictions lead to one product being preferentially formed over another (*i.e.* linear over branched). Transport resistance due to narrow internal channel.
GNFs	Immobilised at the graphitic step edges of the GNF.	Same as CNTs (see above).	Efficient transport of molecules due to the low diffusion barrier as a result of the wider internal channel.

Nanoscale confinement can influence the activation barrier and overall enthalpy of a desired reaction by changing the stability of the reactants, transition state and products. In addition to thermodynamics, the kinetics of reactions performed in confinement requires more consideration than traditional bulk phase reactions. For reactions performed in confinement multiple steps are involved, specifically the encapsulation of the substrate, subsequent confined reaction and then the extraction of products. Each of these steps introduces an energy barrier and change in enthalpy. For example, the reaction profiles for a simple bimolecular reaction in which A + B → C is performed in both confinement and bulk phases are shown in Figure 1.7a. It is evident that upon confinement the reaction barrier is decreased, compared to bulk, leading to a potential increase in the rate of reaction. However, as mentioned previously, other factors such as diffusion of reagents/products into/out of the nanoreactor need to be considered as the

overall rate of the reaction will be affected by these factors i.e. diffusion limitations could result in an overall lower reaction rate.[113,114]

Confinement can also promote selectivity in an otherwise unselective reaction, if the selective interactions with one transition state over another causes a change between the energy barriers to the formation of multiple products, this is highlighted in Figure 1.3b for the reaction A + B → D + E.[113,114]

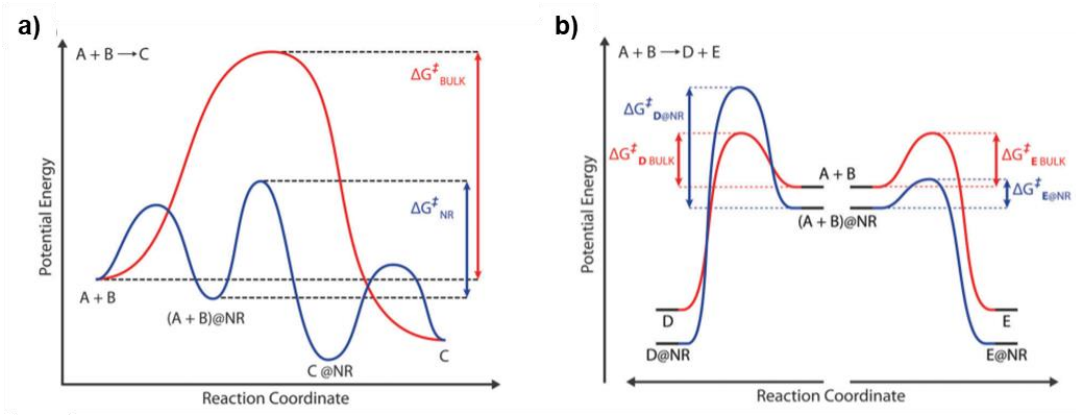

Figure 1.7: Simplified reaction profiles for a reaction carried out in the bulk phase (red line) compared to a reaction performed under nanoscale confinement (blue line) within a nanoreactor (@NR). a) Highlights the changes to the energy profile upon confinement for a bimolecular reaction; and b) highlights the possible selectivity that can arise upon confinement due to selective interactions with one transition state over another for a multiple product reaction.[113,114]

1.3.1 Preparation Methods for MNP in/on Carbon Nanoreactors

Various methods for the decoration of CNRs with MNPs have been previously reported, offering various degrees of control over distribution and particle size.

1.3.1.1. Methods Employed for Depositing MNPS onto the Outer Surface of CNRs

Electrodeposition is a common technique used to decorate the exterior surface of CNTs. The main advantage of this synthetic approach is the ability to control size and distribution of NPs through variations in time, potential and/or solution concentrations.[115] Previous studies reported mainly focus on noble metals such as Pt,[97,116–118] Pd,[97,118,119] and Au.[97] The effectiveness of the electrodeposition of metal nanoparticles onto CNTs has been shown to depend on numerous parameters, such as CNT pre-treatments, the method of manufacturing used for the production of SWNTs, type of SWNTs, the distance of the nanotubes from contact electrode and density of SWNTs in the network.[115] For example, Quinn *et al.*,[97] investigated the electrodeposition of Pt, Pd and Au on SWNT nanoelectrode arrays deposited on non-conductive

supports. Electrical contact to the SWNT network was made through vapour deposited titanium contacts (see Figure 1.8). Control over the MNP size could be controlled by changing the applied potential and concentration of the metal salt in aqueous solution. MNPs of a uniformed sized distribution were obtained at sufficiently negative potentials (nucleation potential, E_n = -0.8 V). The results also indicated that even when the SWNTs were not in contact with the titanium contact electrode; they were plated equally well, showing that the nanotube–nanotube junction was not a source of significant potential loss.[97]

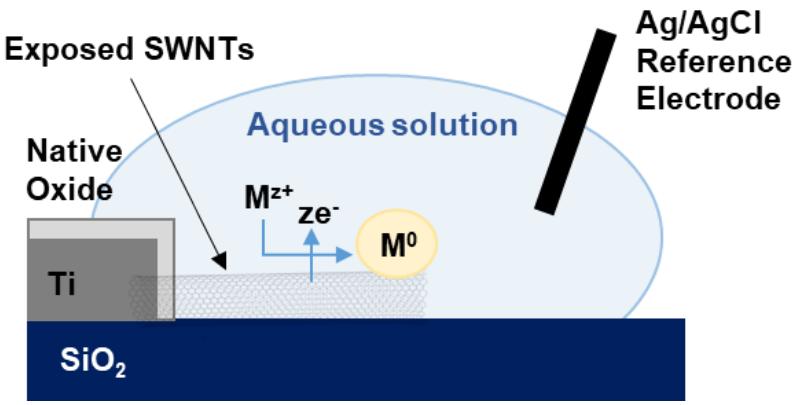

Figure 1.8: Schematic representation of the supported SWNT nanoelectrode. Adapted from reference 97.

Cornello *et al*.,[120] assed the pertinence of several ex situ and in situ approaches for the solution based fabrication of palladium nanoparticle-carbon nanotube composites (summarised in Table 1.3). The ex situ saturation of MWNTs with pre-formed PdNPs stabilised by dodecanethiol,[121] oleylamine[122] and 4-dimethylaminopyridine[123] (under ultrasonic treatment) was conducted to afford the nanostructures MWNT/PdNP-1, MWNT/PdNP-2 and MWNT/PdNP-3, respectively (Table 1.3, lines 1-3).

Table 1. 3: Summary of the approaches used for the preparation of MWNT/PdNP composites and the nature of the stabilising ligand around the PdNPs.[120]

Entry	Catalyst	Approach	Nanoparticle Stabiliser
1	MWNT/PdNP-1	Ex situ	Dodecanethiol
2	MWNT/PdNP-2	Ex situ	Oleylamine
3	MWNT/PdNP-3	Ex situ	4-Dimethylaminopyridine
4	MWNT/PdNP-4	In situ	None
5	MWNT/PdNP-5	In situ	None
6	MWNT/PdNP-6	In situ	Sodium n-dodecylsulfate

Nanostructures MWNT/PdNP-4, MWNT/PdNP-5 and MWNT/PdNP-6 were prepared using adjusted in situ approaches reported in the literature. MWNT/PdNP-4 (Table 1.3, line 4) was prepared in the absence of a stabiliser and reducing agent.[124] MWNT/PdNP-5 (Table 1.3, line 5) was prepared in the absence of a stabiliser.[125] MWNT/PdNP-6 (Table 1.3, line 6) was prepared in the presence of sodium n-dodecylsulfate which acted as both the stabiliser and reducing agent.[126] TEM was employed to assess the structure (e.g. PdNP dispersion and particle size) of all MWNT/PdNP composites. It was found the ex situ preparation approaches afforded greater control over the size of the PdNPs adhered to the outer surface of the MWNTs (with narrower size distributions obtained) with MWNT/PdNP-1 affording the smallest PdNPs (1.1 ± 0.3 nm) greatest distribution of PdNPs on the support structure with a high metal loading, which are all favourable characteristics when considering their use in catalysis.[120]

1.3.1.2 Methods Employed for the Encapsulation of MNPS within CNRs

The effect of the location of the NPs in/on nanoreactors on the resultant activity, has been investigated for a number of catalytic systems. In general, though NPs located on the exterior of the nanoreactors are more accessible to reagents, than those located on the interior of the nanoreactor, they have been found to be less active,[50,110,127] as such there is considerable interest in developing methods to control the encapsulation of MNPs within carbon nanoreactor supports.

One of the most widely used approaches, for the in situ encapsulation of MNPS within CNTs, seems to be incipient wetness impregnation due to its simplicity and versatility.[84–95] This method allows for good control over metal loading but complete control over the location of MNPs within the support structure is difficult to achieve. In principal, the precursor solution would be driven into the inner channels of CNTs through capillary forces. However, the solution wetting the outer surface of the CNTs may still retain a proportion of the precursor solution,[128] leading to the formation of MNPs on the outside of the carbon support structure. Tessonnier and co-workers[129] also reported that incipient wetness impregnation could favourably deposit PdNPs on the interior of MWNTs but still lead to the formation of nanoparticles on the exterior surface of the MWNTs.[129] Bao *et al.*,[130] reported the introduction of RuNPs encapsulated within MWNTs via impregnation using an excess of $RuCl_3$ acetone solution with extensive ultrasonic treatment and slow evaporation, followed by hydrogen reduction at 450 °C. This procedure allowed for an enhancement in the number of RuNPs encapsulated within the internal

channels of the support (more than 80%) compared to an impregnation method were ultrasonic treatment and extended stirring was not applied. Figure 1.9 shows the reduced of RuNPs located on the exterior of MWNTs prepared via the two impregnation methods.[130]

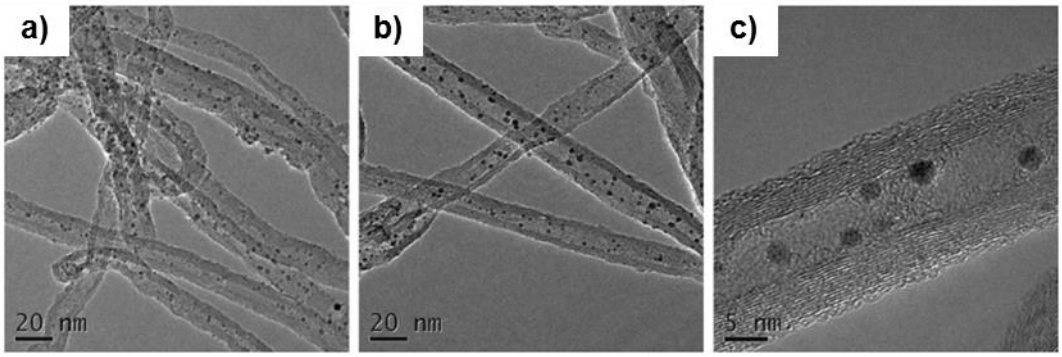

Figure 1.9: TEM micrographs showing the dispersion of RuNPs within MWNTs fabricated using wet impregnation. a) material obtained without being aided by ultrasonic treatment and extended stirring; and b) and c) material obtained by treatment with ultrasonic treatment and extended stirring showing a decrease in the number of RuNPs located on the exterior of the support.[130]

Wang *et al.*,[131] reported the encapsulation of PtNPs within MWNTs. The outer surface of the MWNTs were thermally annealed to ensure their hydrophobicity as incipient wetness impregnation, followed by drying and hydrogen reduction, was used to form PtNPs selectively located on the inner channels of the MWNTs. The hydrophobic nature of the outer surface of the MWNTs minimises the wetting of the outer surface, thus leads to a higher selectivity towards encapsulation of the MNPs (ca. 80% inside).[131] Fu *et al.*,[132] introduced an impregnation-washing method to selectively wash off the metal precursor on the exterior of the MWNTs, so that only precursors inside MWNTs remained, which were converted into nanoparticles after hydrogen reduction. The addition of this washing step afforded an enhanced selectivity toward particles inside the MWNTs.[132]

The main drawback to wet impregnation techniques is often the lack of complete control over the location of the MNPs and so, if selective deposition of MNPs inside CNSs is required, a selective washing step is often required to remove MNPs from the exterior surface of the support structure leading to a significant loss of precursor during synthesis.[133]

Another approach for the introduction of MNPs into the inner cavities of CNRs is sublimation deposition. A gas filling method employing a volatile metal precursor followed by its thermal decomposition under heat treatment or electron beam irradiation has been report by Chamberlain and co-workers.[134]

Carbonyl complexes of transition metals (W, Re and Os) were selectively encapsulated within the interior channels of SWNTs using the procedure highlighted in Figure 1.10. Prior to use the SWNTs were annealed (540 °C for 20 minutes) to remove the termini of the CNTs and any residual water or amorphous carbon from the inner cavities (a 20% weight loss was observed).

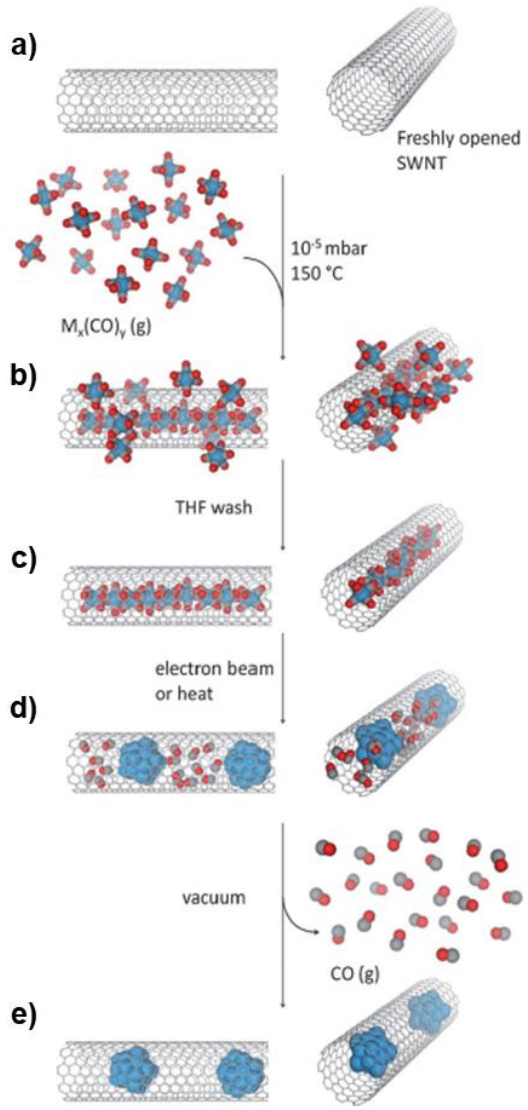

Figure 1.10: Schematic representation for the preparation of uncapped W, Re- or OsNPs encapsulated within SWNTs. a) the carbonyl metal precursors penetrate the SWNT support in the gas phase; b) upon cooling the gaseous metal precursor condenses inside the inner cavities of the SWNTs forming $M_x(CO)_y$@SWNTs; c) a washing step with THF removes any carbonyl molecules on the exterior of the support; d) upon electron beam irradiation or thermal treatment (in a closed vessel under an Ar atmosphere), the metal precursor decomposes into metallic NPs and CO gas; and e) resultant MNPs@SWNTs.[134]

The freshly annealed SWNTs were then sealed in a Pyrex tube, along with the relevant metal carbonyl precursor, under vacuum (10^{-3} mbar) before being heated for 3 days at a temperature 10 °C higher than the sublimation

temperature of the metal carbonyl. As the precursor sublimes into the gaseous phase it is able to penetrate the SWNT walls without relying on capillary forces or the wettability of the SWNTs inner surface. This offers an advantage over wet impregnation methodologies as the filling of the SWNTs is less likely to be hindered by their extremely narrow inner cavities and also allows for the complete filling of the SWNTs.

Upon cooling the gaseous phase metal carbonyl condenses to form the $M_x(CO)_y$@SWNTs composite. Subsequently, any metal precursor deposited on the exterior of the support structure was successfully removed by repeated washing with THF. The $M_x(CO)_y$@SWNTs composite is then either hea treated, at a temperature above the decomposition temp of the metal carbonyl (under Ar), or irradiated with an electron beam leading to the formation of MNPs@SWNTs.[134] This procedure was extended to include the formation of non-precious metal oxide nanoparticles encapsulated within SWNTs by Cui and co-workers.[135]

Although this procedure allowed for in situ filling of MNPs with controlled size distributions, due to the washing step required to remove any material deposited on the outside of the support structure, it is hard to control the metal loadings. Additionally, the washing step relies on the principle that the encapsulated molecules have favourable van der Waals interactions with the concave side of the SWNTs and as such are stabilised to a greater extend and so remain in the inner cavity during washing. However, it is hard to know if all of the metal precursor remains encapsulated within the SWNTs or in fact if a small proportion is also removed.

Arc-discharge synthesis has also been developed for the in situ filling of CNTs.[102] In this method, the tubes are generated along with simultaneous filling of the doped element. The main limitation to this preparation method is the inability to control the size of the nanostructure occupying the inner cavities of the CNTs and often results in the formation of nanowires which are inconvenient for catalysis.[133]

1.3.1.3 Strategies used to Control the Location of MNPs on/in CNSs

Numerous methods for selectively controlling the location of MNPs within CNTs have been previously reported. Ran *et al.*,[50] reported the selective incorporation of RuNPs using an incipient wetness impregnation technique which relied on the pre-treatment of the support to selectively afford the decoration of RuNPs on the interior or exterior of the CNTs. For the fabrication of RuNP-in-CNTs the CNT supports were pre-treated with concentrated HNO_3

for 14 hours at 140 °C to afford open ended CNTs and remove any amorphous carbon or other impurities. $RuCl_3$ in acetone was used as the precursor salt and utilised the capillary forces of CNTs to incorporate the precursor into the inner cavities of CNTs (aided by ultra-sonification) followed by reduction of the salt to afford the corresponding MNPs (12 hours at 110 °C). The same impregnation procedure was employed to fabricate RuNPs-out-CNTs but a different pre-treatment of the CNTs was employed. In this case the CNTs support was pre-treated in nitric acid (5 M) for 5 hours at 110 °C, which allowed for the removal of any amorphous carbon or other impurities, whilst keeping the nanotube caps intact. As the CNTs are capped the $RuCl_3$ acetone solution cannot be drawn into the inner cavity of the support structure and so the RuNPs deposit onto the exterior of the CNTs. Transmission electron microscopy (TEM) was employed to ascertain the success of the preparation methods. From Figure 1.11 it is evident that control over RuNP location has been achieved being adapting the CNT pre-treatment procedure.[50]

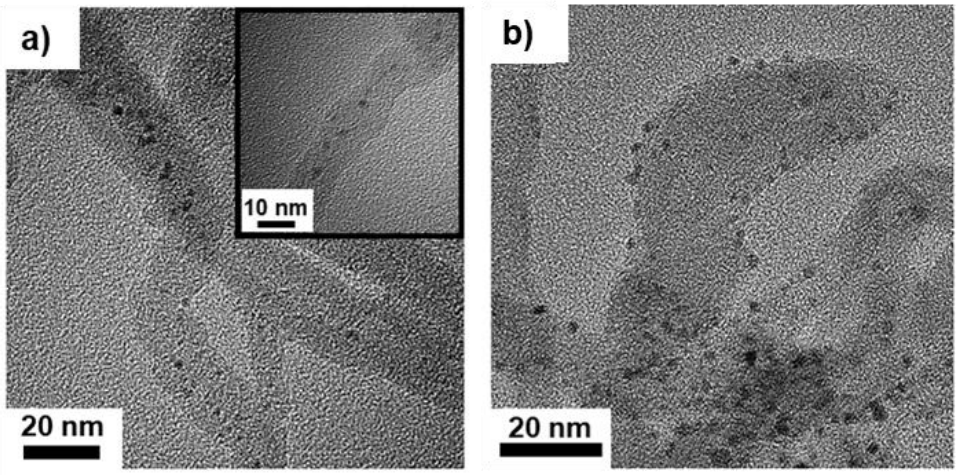

Figure 1.11: TEM micrographs of a) RuNPs-in-CNTs; and b) RuNPs-on-CNTs.[50]

Zhang *et al.*,[136] reported a simple method for the selective deposition of pre-formed AuNP in/on CNTs controlled using CNTs with different internal diameters and/or the surface functionalisation of the interior, exterior or both walls of the CNT support (see Figure 1.12). Previous reports have found that AuNPs could be selectively attached inside CNTs pre-treated with NH_3.[137] Additionally, it has been reported that the pre-oxidation of CNT using a mixture of H_2SO_4 and HNO_3 acids can create adsorption defects in both the inner and outer surfaces of CNTs.[138] Zhang *et al.*,[136] modified the surface of CNTs by their oxidation with H_2SO_4/HNO_3 at 80 or 100 °C. Further pre-treatment of short CNTs with NH_3 at 600 °C was conducted. This led to the different surface functionalities (oxygen and/or nitrogen-containing functional groups) of CNTs depicted in Figure 1.12. TEM revealed that the ends of the CNTs remained

capped after acid treatment at 80 °C (CNTs-o), compared to 40-60% of tubes being opened with acid treatment at 100 °C (CNTs-m) and almost all CNTs were open after further treatment with NH_3 (CNTs-i). This further NH_3 treatment also affected the number of oxygen-containing groups (e.g. carboxylic acids) whilst introducing nitrogen containing groups (e.g. amines). As the CNT caps remained in the CNTs-o sample the AuNP preferentially deposited on the outer surface of the CNTs to form Au/CNTs-o. The comparable inner diameter of CNTs-m (4.2 ± 2.0 nm) with the preformed AuNPs (3.2 ± 1.6 nm) made it difficult for AuNPs to enter the inner channel of the CNTs and so a low portion of AuNPs were encapsulated in the CNTs-m (5-10 %). However, the large size distribution for the inner channels of CNT-m (8.0 ± 2.5 nm) allowed for the encapsulation of AuNPs in CNTs-i to form Au/CNTs-i. Due to the high affinity of Au towards nitrogen and oxygen atoms,[139] the gold NPs also preferentially adhered to the surface functionalised sites.[136]

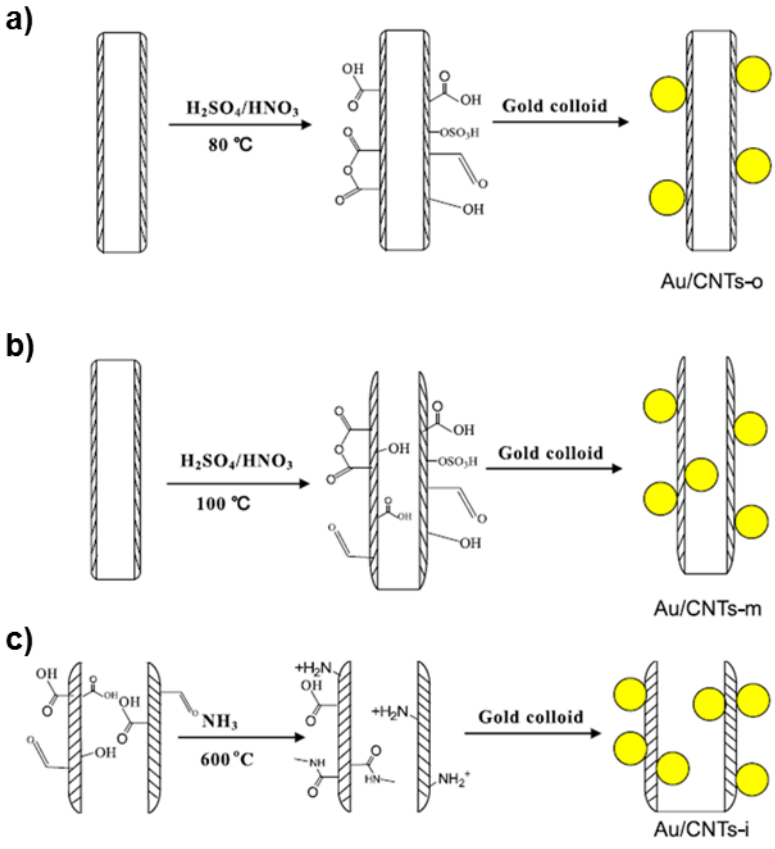

Figure 1.12: Schematic representation of the processes used to selectively immobilise AuNPs on; a) the exterior (Au/CNTs-o)r, b) the interior and exterior (Au/CNTs-m), and c) the exterior (Au/CNTs-i) of CNTs.[140]

Adapting the wet impregnation technique to afford either MNP on the inter or exterior has been investigated by Tessonnier and co-workers.[141] They

reported that is it possible to selectively localise the deposition of MNPs by using a combination of organic and aqueous solvents. The proposed method was based on the CNTs interior channel having a higher affinity for organic solvents. The procedure for the selective encapsulation of NiNPs is depicted in Figure 1.13a. The first step involves impregnating the CNTs with an ethanol solution containing the nickel nitrate precursor. The volume of solution used was lower than the pore volume of the CNTs (4 mL of ethanol per g of CNT was used, when the total pore volume was calculated to be 6 mL per g) to aid favourable filling of the inner channels of CNTs (over filling of the pores of the CNT would lead to formation of MNPs on the exterior of the support). Because of its low surface tension, the ethanolic solution wets the nanotube surface and fills the inner channel of the CNTs. The second step involves that addition of the aqueous phase (pure distilled water) which was expected to remain outside of the CNTs wetting the external surface and displacing any ethanol solution on the outer surface into the interior channel.

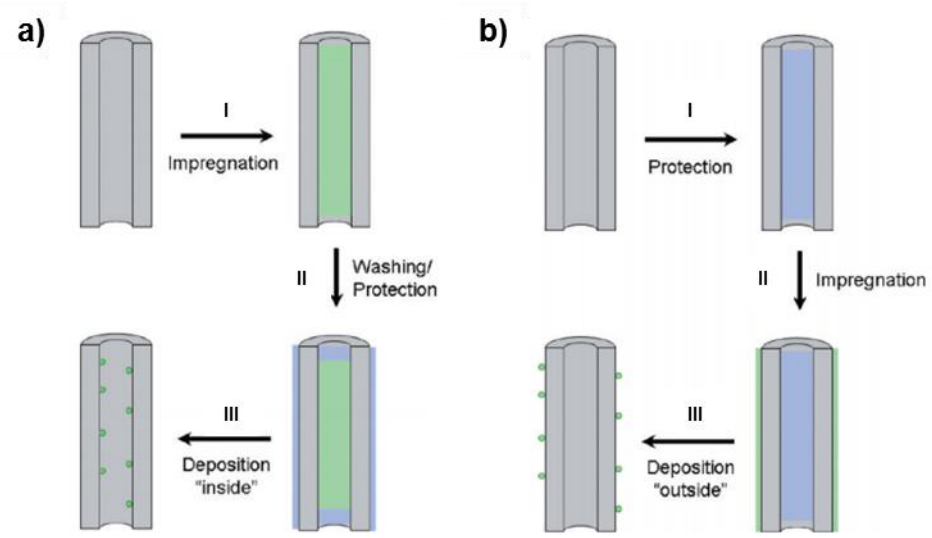

Figure 1.13: Schematic view of a longitudinal cross section of a CNT during the different steps for a) the selective deposition of NiNPs inside CNTs: (I) impregnation with ethanol solution containing the metal precursor, (II) impregnation with water to wash and protect the outer surface of the MWNTs and (III) reduction to afford NiNPs on the interior of MWNTs; and b) the selective deposition of NiNPs outside CNTs: (I) Impregnation of organic solvent to protect the inner channel of MWNTs from metal deposition, (II) impregnation with aqueous solution containing the metal precursor, (III) reduction to afford NiNPs on the exterior of MWNTs. Adapted from reference 141.

The material was then dried overnight at room temperature and then at 50 °C for 10 hours to remove any remaining ethanol. Lastly, the sample was calcined at 350 °C for 2 hours to decompose the metal precursor into NiNPs located on the interior of the support structure.

The selective decoration of NiNPs on the outer surface of the CNTs is highlighted in Figure 1.13b. Comparably, the organic solvent is added first to fill the internal channels of the CNTs followed by an aqueous solution, only this time the aqueous solution contained the nickel nitrate precursor. Because of its higher liquid/solid interface energy, the aqueous solution cannot penetrate the CNTs and as such the channels remains protected and decoration only happens on the outer surface.

TEM was employed to assess the efficiency of the two preparation methods. From Figure 1.14 it is evident that the two step preparation methods are successful in decorating CNTs with NiNPs selectively on the interior or exterior of the support. It is important to note that a TEM tilt series (from -35° to -45° was obtained for the metal outside NiNPs@CNTs sample to confirm that the NiNPs were adhered to the surface of the CNT.[141]

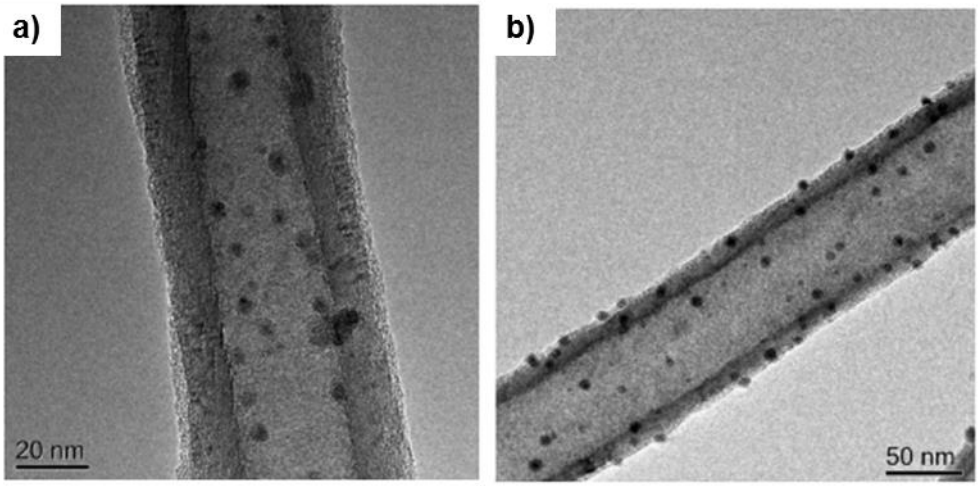

Figure 1.14: Representative TEM micrographs of a) NiNPs inside CNTs prepared by the two step approach highlighted in Figure 1.13a showing the majority of the NiNPs are encapsulated within the support structure, and b) NiNPs outside CNTs prepared by the two step approach highlighted in Figure 1.13b showing that the majority of the NiNPs are located on the exterior. Adapted from reference 141.

The preparation method for the selective confinement of NiNPs in CNTs eliminates the need for a washing step to remove any NiNPs deposited on the exterior surface and therefore control over the metal loading can be achieved. Additionally, it avoids the need for any additional step to add functionality to the support structure which alters the surface chemistry of the CNT walls and could affect it catalytic performance. However, the selective decoration depends upon the surface tension of the organic solvent used and so may be easily transferable to other solvent systems and metal precursors.

1.3.1.2 Selective Removal of MNPs from the Exterior Surface of CNSs

La Torre and co-workers[37] reported a three-step approach for the selective removal of AuNPs adhered to the exterior of GNFs (highlighted in Figure 1.15a). Preformed AuNPs were fabricated using a modified Brust-Schriffin reduction protocol.[142] Insertion of the AuNPs was achieved either through the use of an organic solvent (e.g. pentane) or supercritical CO_2 ($scCO_2$). They found that whilst insertion using conventional organic solvents resulted in the equal deposition of AuNPs on the interior and exterior of the support structure, AuNPs preferentially inserted into the GNFs under supercritical conditions. Additionally, positional control of the AuNPs within GNFs was achieved through preferential host guest interactions at the step-edges of the GNFs, evidenced through the linear arrays of AuNPs seen via scanning transmission electron microscopy (STEM). Although, a higher percentage of AuNPs were encapsulated within the GNFs (using $scCO_2$) a small proportion still remained on the exterior (Figure 1.15b). A three-step process to remove the AuNPs on the exterior whilst retaining the ordered arrays of AuNPs on the interior was proposed and is outlined below.

The first step involves immersing the AuNP-GNF composite into benzene (or cyclohexane) under reduced pressure before being restored to atmospheric pressure rapidly. Under these conditions, the internal channels of the GNFs become filled with liquid benzene due to a combination of capillary action and a favourable pressure gradient. The second step involves lowering the temperature to 0 °C so that the solvent within the channels of the GNFs freezes, therefore protecting the encapsulated AuNPs, whilst the NPs on the exterior of the support remain exposed to the environment. These NPs are effectively removed by employing either aqua regia solution (containing a mixture of thionyl chloride and pyridine) or KI/I^2 to dissolve the gold core of the externally adhered NPs. Followed by the third step of the process which involves the removal of the solvent from the interior channel of the GNFs. High-angle annular dark field STEM (HAADF STEM) was employed to quantify the efficiency of the process by comparing the AuNP-GNF composite before and after washing (see Figure 1.15b and c). From Figure 1.15c it is evident that the protocol was effective for the selective removal of AuNPs adhered to the exterior of GNFs whilst retaining the linear arrays of AuNPs encapsulated within the support.[37]

Although this protocol allows for the preparation of AuNPs@GNFs, where the NPs are located solely on the interior of the support, which is important for practical applications in confined reactions, it involves numerous steps which

could be very time consuming and includes the use of harsh chemicals to dissolve the exterior AuNPs which could result in damage to the support structure. Additionally, the selective washing protocol required to remove MNPs from the exterior surface of the support structure leads to a substantial loss of gold during synthesis.

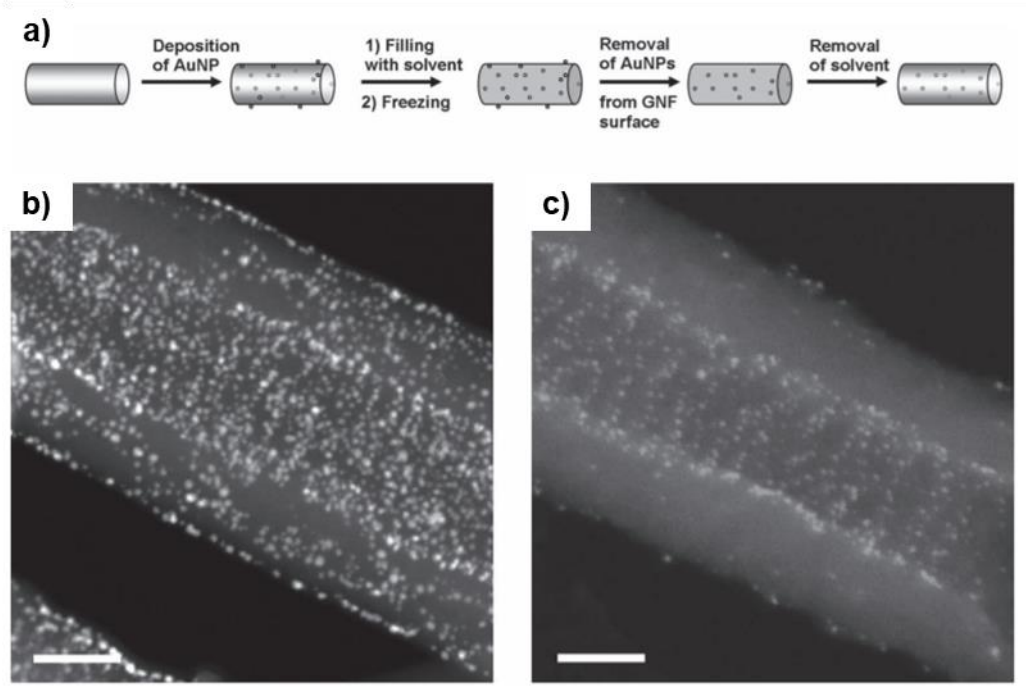

Figure 1.15: a) Schematic representation of the three-step approach used to selectively remove AuNPs from the outer surface of GNFs; HAADF STEM micrograph of AuNP-GNFs before (b) and after (c) the washing procedure. Scale bars: 20 nm.[37]

1.3.1.3 Selective Incorporation of Bimetallic MNPs on/in CNRs

Bimetallic MNPs have been previously reported to lead to an enhancement in catalytic performance with respect to their monometallic counterparts.[143,144] For the selective incorporation of bimetallic MNPs onto/into CNRs the more common approach is to use pre-reformed MNPs rather than making bimetallic MNPs in situ.

Castillejos and co-workers[145] reported a simple and efficient method for the selective confinement of bimetallic PtRuNPs in the inner cavity of CNTs based on controlling the surface chemistry. Firstly the preparation of PtRuNPs was achieved through the hydrogenation of the (1,5-cyclooctadiene)dimethyl platinum(II) and (1,5-cyclooctadiene)(1,3,5-cyclooctatriene) ruthenium metal precursors. 4-(3-Phenylpropyl)pyridine was used as a stabilising ligand for the MNPs as the nitrogen atom in pyridine could coordinate to the MNPs whilst the phenyl ring could interact with the CNT through π-π stacking interactions.

Secondly, the CNTs were surface functionalised in order to introduce different surface species (i.e. carboxylic acid and amide groups with a long alkyl chain) that would induce weak interaction/repulsion between the PtRuNPs and the external surface of the CNTs (see Figure 1.16).

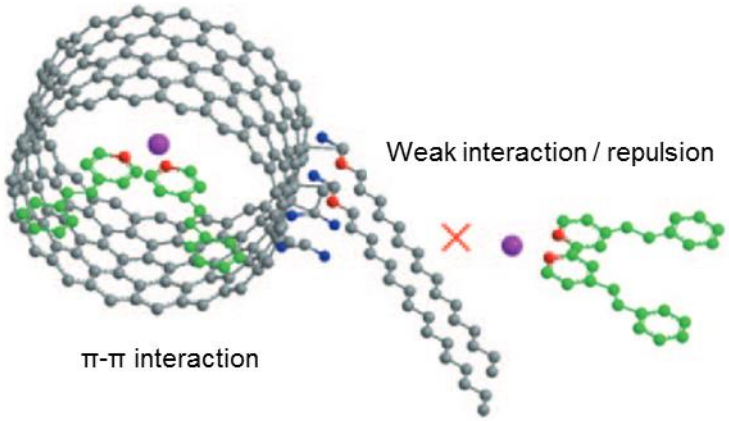

Figure 1.16: Strategy employed to selectively incorporate MNPs within CNTs. Where PtRuNP is the purple circle, N is red, O is blue and C is grey and green.[145]

The preformed PtRuNPs were inserted into the inner cavities using a wet impregnation method. Briefly, the surface functionalised CNTs were immersed into a THF solution of the pre-formed bimetallic PtRuNPs under stirring and ultra-sonification for 2 hours after which the solvent was removed. TEM was employed to evaluate the effectiveness of the selective confinement and confirmed that the PtRuNPs were predominately located on the exterior of the CNT support for metal loadings of 5-23 wt.%.[145]

The selective incorporation of MNPs into/on CNRs was also reported by Solomonsz *et al.*,[39] who looked at the preparation of RhNPs, as well as, bimetallic RhPtNPs carbon nanoreactors (where GNFs were used as the carbon support). The fabrication of the MNPs was performed based on a modified two-phase Brust-Schiffrin reduction,[142] before incorporation into/on the carbon support structure. Control over the location of the MNPs within the support structure was achieved using two different impregnation techniques. To obtain a material were the MNPs were adhered to the exterior of the support a traditional wet impregnation technique was used (i.e. GNFs immersed in hexane solution containing the as-prepared MNPs with ultra-sonification). In order to confine the MNPs within the support structure a mixture of hexane/CO_2 under supercritical conditions was utilised. The use of supercritical CO_2 lowers the diffusion barrier of the as-prepared MNPs into the internal channels of the carbon support.[39]

1.3.2 Structure and Properties of Nanoparticles Deposited on/in CNRs

MNPs encapsulated within the inner cavities of CNTs can exhibit entirely different properties and reactivities compared to MNPs of the same size/composition located on the exterior surface. This is due to the curvature of the CNT walls causing a shift in the π-electron density from the concave inner surface to the convex outer surface, resulting in an electric potential difference.[12]

Castillejos *et al.*,[145] investigated the activity of bimetallic PtRuNPs confined within MWNTs for the selective hydrogenation of cinnamaldehyde to cinnamyl alcohol (see Scheme 1.2 for possible hydrogenation pathways).

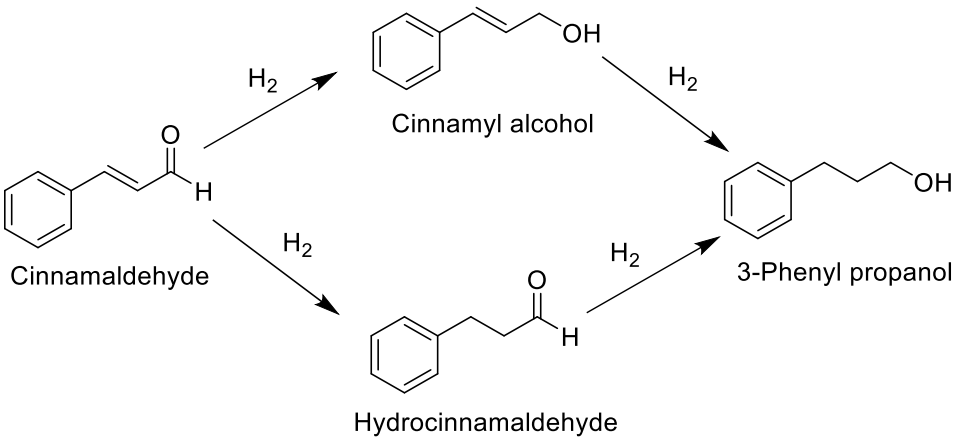

Scheme 1.2: Hydrogenation of cinnamaldehyde illustrating the possible reaction products.

The observed activity for the confined material was compared to MNPs of the same size located on the exterior surface of the MWNTs and discrete MNPs. A significant increase in catalytic performance and selectivity for cinnamyl alcohol was observed for the catalyst confined within the MWNT support structure (see Table 1.4). This was attributed to an enrichment of reactant concentration around the active NPs present in the internal cavity of the MWNTs due to stronger interactions between the reactant molecules and the internal surface of the MWNTs.[145]

Wang et *al*.,[48] reported that CuNPs confined within CNTs substantially increased conversion of methyl acetate to methanol and ethanol, compared to the same catalyst (same metal loading) located on the exterior of the nanotubes (see Figure 1.17). This was attributed to a confinement effect of the CNTs, resulting in the formation of Cu clusters within the internal channels

being more reducible than those located on the exterior, resulting in that same Cu content (metal loading) but different active sites for the two catalysts.[48]

Table 1.4: Summary of catalytic results obtained for the reduction of cinnamaldehyde catalysed by bimetallic PtRuNPs showing that the MNPs located on the interior of the CNTs provide an enhanced activity (where HCAL = hydro-cinnamaldehyde, HCOL = hydrocinnamyl alcohol, and COL = cinnamyl alcohol).[145]

Catalyst	NPs d_{mean} / nm	% NP int.	TOF / h^{-1}	HCAL	HCOL	COL
PtRu/L NPs	2.2	-	30	50	15	35
PtRu/CNT2	2.2/2.2	10	56	33	8	59
PtRu@CNT1	1.6/2.2	30	75	18	12	69
PtRu@CNT3	2/2.5	80	85	0	5	95

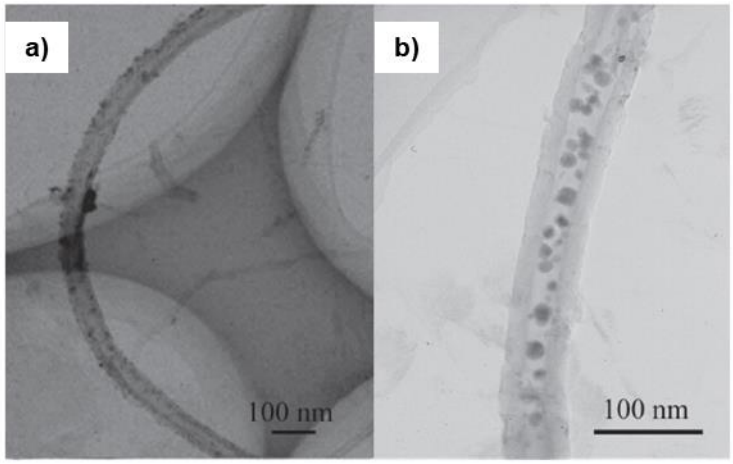

c)

	Coversion (%)	Molecular selectivity (mol%)					
Catalysts	MA	MeOH	EtOH	EA	CO	CH_4	CO_2
10% Cu-outside-CNTs	4.8	49.8	43.7	4.1	2.4	0	0
10% Cu-inside-CNTs	13.9	55.3	31.9	12.8	0	0	0

Figure 1.17: a) TEM micrograph of CuNPs-outside-CNTs; b) TEM micrograph of CuNPs-inside-CNTs; and c) comparison of the performance of CuNPs located on the exterior compared to those located on the interior of the support structure for the hydrogenation of methyl acetate (where MA = methyl acetate and EA = ethyl acetate). Adapted from reference 48.

Additionally, Pan *et al.*[12] reported that the conversion of ethanol was greatly enhanced when RhNPs were confined inside CNTs compared to the same catalyst located on the exterior of the nanotubes.[12]

Very narrow containers such as SWNTs, with an internal diameter of 1-2 nm impose extreme confinement on encapsulated molecules making them ideal for exploration of the fundamental effects of confinement.[39] SWNTs have been previously shown to enable the formation of small, highly stable and dispersed MNPs.[146] The internal channel dimensions of SWNTs are similar to the size of small organic reactant molecules resulting in a significant steric influence on reaction pathways, therefore, exhibiting greater effects on the products of reactions than wider MWNTs.[46] However, the narrow channels of SWNTs lead to mass transfer limitations necessitating the use of high pressures to aid diffusion into and out of the internal channels of the SWNTs.[39,112]

This was evidenced by Chamberlain *et al.*,[46] who reported the encapsulation of ruthenium nanoparticles inside SWNTs and investigated their activity for a series of hydrogenation reactions. The use of $scCO_2$ was found to be essential for successful reactions in SWNTs. Although the extreme confinement lead to the formation of small RuNPs, transport resistance through the SWNT channel lead to a decrease in TOFs obtained in comparison to comparable commercially available porous carbon supports.[46] Additionally, Aygun *et al.*,[104] compared the activity of RuNPs encapsulated within SWNTs to GNF supported controls for the hydrogenation of bulky alkenes (e.g. norbornene). They reported that the use of $scCO_2$ was essential for efficient transport of reactants to the catalytic centres confined within SWNTs. However, similarly to Chamberlain *et al.*[46] they observed lower overall turnover numbers for reactions catalysed by RuNPs@SWNTs which was attributed to a reduction in the accessible volume (30-40%) in SWNTs following the encapsulation of the active MNPs.[104] The extreme confinement imposed by SWNTs resulting in mass transfer limitations negates their use as viable support structures for encapsulating MNPs for use in heterogeneous catalysis.

For example, Pan *et al.*[84] investigated the activity and stability of RhMnNPs (of similar sizes) supported on/in CNTs for the conversion of syngas to ethanol (see Figure 1.18).They found that greater initial yields were achieved for RhMnNPs encapsulated within the CNTs compared to those on the exterior (whose yield continuously decreased from the initial conversion value with time on stream, leading to a conversion 16 times lower than that obtained for MNPs on the interior of the support, after 120 hours). The difference in observed activity for the RhMnNPs depending on their location within/on the support structure was attributed to the different stabilities of the MNPs. It was found that the RhMnNPs on the interior were limited to a size distribution of

5-8 nm even after 112 hours on stream, whereas the RhMnMPs located on the exterior where found to aggregate leading to a higher size distribution of 8-10 nm attributed to the absence of the space restriction imposed by the CNTs (syngas conversion conditions: 320 °C and 50 bar).[84]

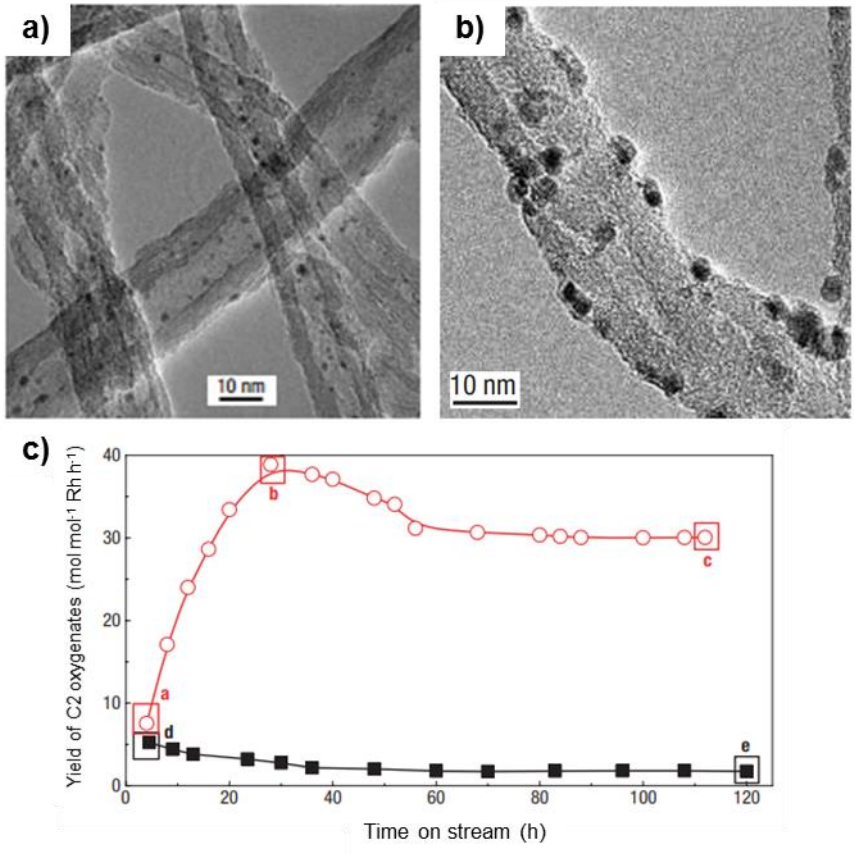

Figure 1.18: a) TEM micrograph of RhMn-in-CNTs; b) RhMn-out-CNTs; and c) yield of C2 oxygenates obtained for RhMnNPs located on the interior/exterior of the CNT support (circle: RhMn-in-CNTs catalyst and squares: RhMn-out-CNTs catalyst) showing that the activity of RhMnNPs depends on their location. Adapted from reference 84.

The enhancement in stability for MNPs located on the interior of carbon nanostructures, compared to the exterior, was also observed by Abbaslou *et al.*,[147] for the iron catalysed Fischer-Tropsch synthesis. After 125 hours on stream they found that the FeNPs encapsulated within the inner cavity of the CNTs remained in the range of 6-111 nm, whereas, those located on the exterior grew up to 24 nm.[147]

La Torre *et al*.,[105] studied the thermally driven growth of AuNP catalysts immobilised both on the inner and outer surfaces of GNFs (Figure 1.19). They reported two different growth mechanisms dependent upon the interactions between the nanoparticle and the interior or exterior surface of the GNF. They reported that the AuNPs anchored at the step edges of the GNF grew to

around 6 nm via Ostwald ripening. The AuNPs on the exterior of the GNF, however, experienced extensive migration and coalescence, and grew to a significantly larger diameter of approximately 13 nm. The increased stability of the AuNPs located on the interior of the GNFs is most likely caused by the strong van der Waals interactions between the step edges and the encapsulated catalyst (due to the larger area of contact between the NPs and GNF), leading to a restriction in migration and therefore lower average particle size. This effect is vital for understanding the mechanisms that govern the properties of the guest molecules and activity of the chemical reactions within carbon nanoreactors.[105]

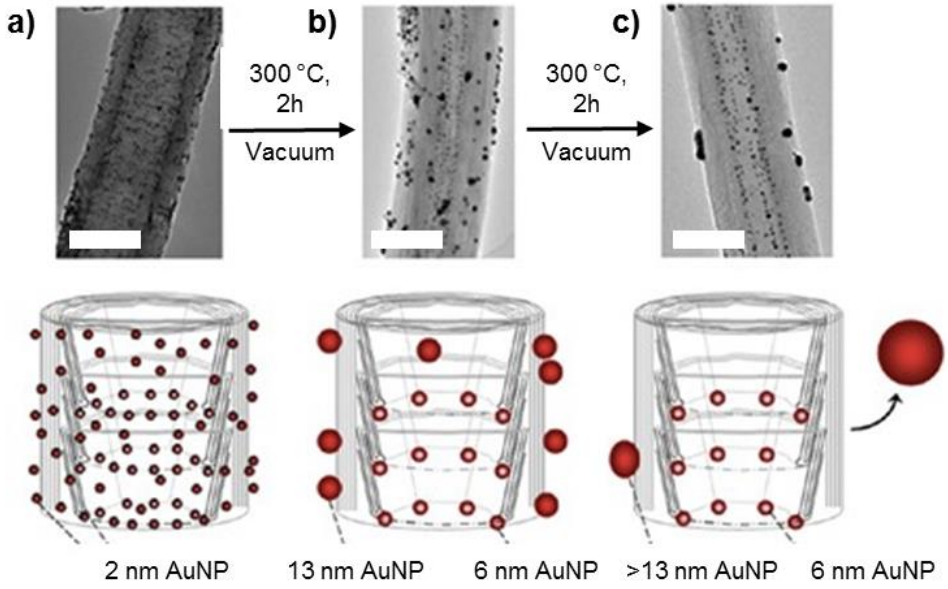

Figure 1.19: TEM images and schematic diagrams illustrating the limited growth of nanoparticles adsorbed at graphitic step-edges (light red), compared to those adsorbed on the flat outer surface of the GNF (dark red). a) AuNPs immediately after deposition, b) AuNPs after heating under vacuum, and c) AuNPs after further heating in air. Scale bars are 40 nm in a)-c).[105]

La Torre *et al*.,[37] also investigated the interactions of AuNPs with the internal surface of GNFs to develop a direct method for controlling the arrangement of preformed AuNPs within GNFs. Dodecanethiolate-stabilised AuNPs with core diameters of 2.3 ± 0.3 nm and 6.0 ± 0.4 nm were prepared, via a modified Brust-Schiffin method, and incorporated into the nanocarbon support structure using a mixture of pentane/CO_2 under supercritical conditions (40 °C and 4000 bar).

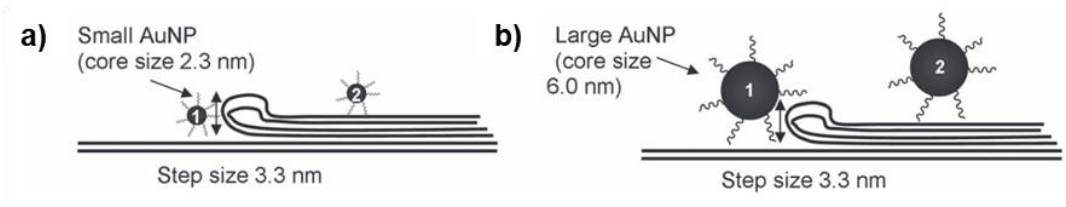

Figure 1.20: Schematic representation of the different sized AuNPs located at the internal step-edge within GNFs showing that a) small AuNPs have a greater area of surface contact than larger AuNPs shown in b).[37]

They found that a highly ordered distribution of NPs along the step-edges of the GNF structure was achieved for small AuNPs, whose size are commensurate with the height of the step-edges, and a more random arrangement for larger AuNPs was observed. This was attributed to a higher contact surface area between the AuNPs and GNFs (for AuNPs of 2.3 ± 0.3 nm, see Figure 1.20) leading to a severe enhancement in the associated van der Waals forces between the stabilised AuNPs and the sp^2 hybridised step-edges.

1.3.3 Interactions between Molecules and Support Structure

Van der Waals interactions between molecules and the inter channels of nanoreactors can also greatly affect the local concentration of the reactants[38] allowing for different reaction kinetics and reaction pathways to be observed and exploited. The diameter of the internal cavity can have a large influence on the position, orientation, and dynamic behaviour of reactant molecules, with the greatest effects observed for SWNTs as these have the smallest internal diameter (close to the size of the reactant molecules). However, the ability of reactants and products to diffuse through the nanoreactor is crucial and therefore, a balance between transport through the support and diameter size is essential.[19]

1.3.3.1 Local Concentration Increase of Reagents Inside Carbon Nanoreactors

GNFs have the ability to create localised nanoscale environments, where the concentrations of certain reactants are different when compared to the bulk solution. The degree of this local concertation effect is dependent upon the affinity of the reactants to the GNF support.[19,148]

The GNF sp^2 hybridised step-edges exhibit π-π stacking interactions with reactant molecules containing aromatic or largely conjugated systems, compared to the rest of the support surface. This can lead to an increase in the local concentration of the starting material in the internal channel of the

nanoreactor which in turn can lead to an increase in reaction rate when two aromatic molecules are needed to come together in order to obtain the desired product.[39,110]

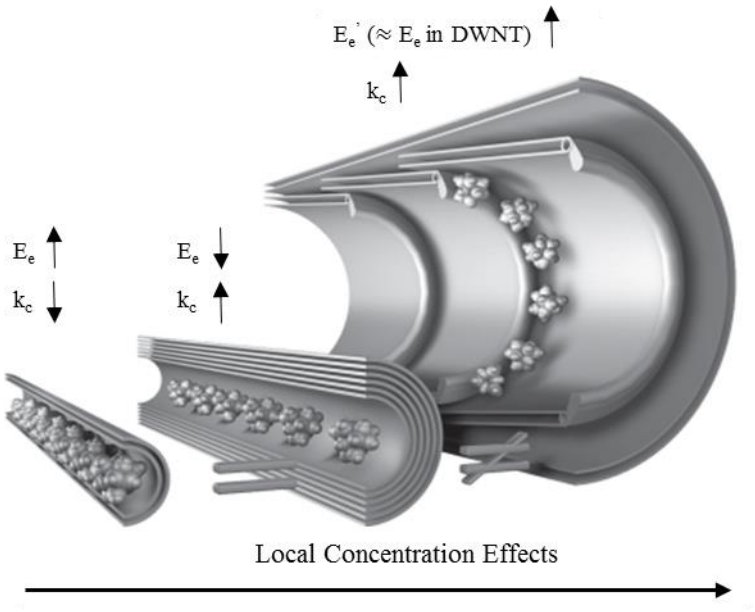

Figure 1.21: Schematic representation of the internal environments of DWNTs, MWNTs and GNFs (from left to right, respectively) and their effect on local concentration, showing a balance between the energy of encapsulation in CNTs (E_e) and step edge encapsulation (E_e') and the mass transfer rate of reactants (k_c), with the greatest effects being seen for GNFs.[38]

An enhanced local concentration effect is observed for GNFs compare to CNTs, due to the step-edges creating a restricted environment, similar to that observed in DWNTs, whilst allowing for efficient transport of molecules through their internal channels due to a larger diameter, (see Figure 1.21).[38]

1.4 Carbon Nanoreactor Supported MNPs for Hydrogenation Reactions

This section looks at the current state of the art, in terms of carbon supported MNPs for hydrogenation reactions (summarised in Table 1.5).

The hydrogenation of benzene catalysed by both Ni[149] and Pd[150] nanoparticles encapsulated in MWNTs has been previously reported. In both cases an increase in catalytic activity was observed as a result of confinement. PdNP encapsulated within MWNT afforded an enhanced turn over frequency (TOF) of 1860 s^{-1} compared to AC (750 s^{-1}) and porous zeolite supports (780 s^{-1}). Additionally, a 4.6-fold increase in activity was obtained for NiNPs encapsulated with the inner cavities of MWNTs compared to those, of similar

sizes and composition, adsorbed onto the exterior of the support. This enhancement was attributed to the Ni species on the interior of the support structure being more readily reduced (evidenced through temperature programmed reduction (TPR) measurements) than those on the exterior. The increase surface contact between the NiNPs on the interior and the support structure presents control over the electron density of the MNPs and therefore helps to increase the catalytic activity.

As interactions between reactant molecules and CNTs are thought to influence the selectivity of a given reaction, several studies have investigated this effect for the selective hydrogenation of cinnamaldehyde, which contains both a carbonyl and alkene moieties which are both subject to reduction. The most desirable product in this reaction is cinnamyl alcohol, which is an important product in food, fragrance and the pharmaceutical industry (see Scheme 1.2 for possible hydrogenation pathways). However, reduction of the C=C bond, to afford hydrocinnamaldehyde, is more facile leading to poor yields of cinnamyl alcohol. As this reaction is sensitive to a range of factors making it has emerged as a common model reaction to study selectivity effects in catalysis.[151]

A comparison between selectivities observed for PtNPs located on/in MWNTs was reported by Ma and co-workers.[152] It was observed that while the PtNPs confined within the MWNTs showed an increase in selectivity towards cinnamyl alcohol (compared to the unconfined catalyst), those adhered to the external surface promoted the complete reduction of cinnamaldehyde to 3-phenyl propanol. However, the MWNTs utilised for the preparation of the two materials had different diameters and morphologies and so a direct comparison cannot be made. Diameters of less than 10 nm were used for the preparation of PtNPs/MWNTs compared to the diameter between 60 and 100 nm used for PtNPs@MWNTs.[152]

The selective hydrogenation of cinnamaldehyde was also invested by Tessonnier and co-workers.[129] They reported that PdNPs (4-6 nm) encapsulated within the internal channel of MWNTs not only exhibited a higher catalytic activity compared to a commercially available unconfined catalyst, PdNPs/AC (complete conversion after 25 hours compared to 27 hours for the unconfined catalyst), but also an enhanced selectivity towards hydrocinnamaldehyde (ca. 80% compared to ca. 50% for the unconfined catalyst). This increased catalyst performance was attributed the differences in morphology of the support materials which in turn lead to modified adsorption properties of the active metal surface.[129] An increase in selectivity

for the hydrogenation of cinnamaldehyde, catalysed by MWNTs supported AuNPs, towards hydrocinnamaldehyde has also been reported by Zhang and co-workers. A 90-fold increase in TOF, for the overall conversion of cinnamaldehyde, was also reported and attributed to the effects of AuNPs confinement within the support, despite only 40% of the AuNPs being estimated to be encapsulate.[136]

Syn gas (a mixture of carbon monoxide and hydrogen) conversion to longer-chain hydrocarbons, particularly useful in transportation fuels, are particularly important hydrogenation reactions, the most well established being the Fischer-Tropsch process.[147,153–156] The process of converting carbon monoxide and hydrogen to hydrocarbons is typically complex involving multiple parallel reaction pathways and as such the activity and selectivity of catalysts are important parameters that need to be established. Due to the numerous factors that can influence the activity and selectivity in these reactions (such as reaction conditions and catalyst properties) it has become an interesting reaction in which to study the nanoscale confinement effect imposed by CNTs. Chen and co-workers[15] reported that Fe nanoparticles encapsulated in the compartment of bean pod-like CNTs (Pod-Fe) can be used as highly stable catalysts for CO hydrogenation to light olefins at high temperature. The catalyst gave a greater selectivity of light olefins (45%) and high stability over a 120 hour reaction (reaction conditions: 320 °C, 0.5 MPa, $CO:H_2 = 1:2$). A catalyst with exposed Fe nanoparticles on the outside of the Pod-Fe (FeO_x/Pod-Fe) showed a selectivity of 42% towards light olefins (C_2-C_4). However, the exposed Fe nanoparticles were easily oxidised, unlike those encapsulated in Pod-Fe which were well protected by the graphene layer and remained in a metallic state, resulting in a lower stability. These results indicate that the graphene shell of Pod-Fe plays an important role in protecting the Fe particles leading to an enhancement of the activity and stability of Fe-based catalysts in high temperature Fischer-Tropsch synthesis.[15]

As mentioned in Section 1.3.2 Pan *et al.*,[84] also studied the reduction of syn gas catalysed by rhodium-manganese alloyed NPs confined within MWNTs and found that a 10-fold increase in catalytic activity was obtained upon confinement. However, more interestingly the confined catalyst also exhibited a 16-fold increase in the selectivity for C2 oxygenates (mainly ethanol). The difference in observed activity for the RhMnNPs depending on their location within/on the support structure was also attributed to the different stabilities of the MNPs.[84]

Table 1.5: Summary of hydrogenation reactions carried within the confinement of CNTs including parameters such as: type of support, internal diameter of support structure (d_{INT}), catalyst species and nanoparticle diameter (d_{NP}).

Substrate	Support	d_{INT} / nm	Catalyst	d_{NP} / nm	Comment on Confinement Effects	Ref
Cinnamaldehyde	MWNTs	10 & 60-100	Pt	2-5	Increased selectivity observed towards cinnamyl alcohol (from 10% to 60%) for NPs located on the interior of CNTs.	152
Cinnamaldehyde	GNFs	40	PtRu	1.5-3	3-Fold increase in activity. Increased selectivity to cinnamyl alcohol (35% to 95%) for NPs on the interior of CNTs.	145,157
Cinnamaldehyde	MWNTs	ca. 50	Pd	ca. 5	Similar conversion obtained compared to Pd/C. Higher selectivity towards hydrocinnamaldehyde observed.	129
Cinnamaldehyde & 1,3-butadiene	MWNTs	2-5 & 5-10	Au	1.5-5	90-Fold increase in TOF for reduction of cinnamaldehyde. Increased selectivity towards hydrocinnamaldehyde.	136
Alkenes & Carbonyls	SWNTs	ca. 1.5	Ru	ca. 1	3-Fold decrease in TOF compared to Ru/C (transport restriction). Enhanced RuNP stability for confined system.	46
Benzene	MWNTs	4-8	Ni	3-7	4.6-Fold increase in activity for NiNPs located on the interior vs the exterior of the MWNT support.	149
Benzene	MWNTs	5-10	Pd	1-8	Higher activity (TOF = 1860 s^{-1}) obtained compared with AC (750 s^{-1}) and zeolite (780 s^{-1}) supports.	150

Cellobiose	MWNTs	3-13	Ru	2-4	Conversion & sugar alcohols yield increases by 15 and 20% respectively. Subtle enhancement with decreasing CNT diameter.	158
Syn gas (CO)	Pod-like CNTs	20-30	Fe	5-20	Significantly improved catalyst stability enabling altered reactivity and alkene selectivity to be observed.	159
Syn gas (CO)	MWNTs	4-8	RhMn	1-2	10-Fold enhancement in activity observed for confined RhMnNPs.	160
CO_2	MWNTs	5-10	Pd	2-4	Greater conversion and selectivity for methanol for confined catalyst than externally adsorbed. 3.7-Fold increase in TOF.	161
Methyl acetate	MWNTs	4-10 & 20-30	Cu	7-10	Enhanced activity. Subtle effect on selectivity with narrower MWNTs having the greatest effect.	48,162
Norbornene and Benzonorbornadiene	SWNTs & GNFs	ca. 1.5 50-70	Ru	ca. 1 ca. 3.5	Enhanced activity for RuNPs confined in GNFs compared to unconfined RuNPs. Changes in selectivity observed.	104
Nitrobenzene	GNFs	50-70	Pt & Pd	2-4	No comment on the effects of confinement.	95
α,β-Unsaturated acids	MWNTs	5-10	Pd	5	Up to 2-fold increase in activity. Enhanced effect of chiral modifier on enantioselectivity.	163

1.5 Summary and Conclusions

The interaction between the support structure and MNPs, as well as the size and shape of the MNPs, has been shown to have a critical effect on the catalytic performance of supported nanoparticle catalysts.[111,127] It is, therefore, important to develop a fundamental understanding of how the conditions used during the fabrication process of these materials affects their structure. Gaining control over the size and the position of encapsulated MNPs is critical if they are to reach their full potential in the diverse range of chemical transformations.

1.6 References

1 A. Roucoux, J. Schulz and H. Patin, *Chem. Rev.*, 2002, **102**, 3757–3778.

2 M. Daniel and D. Astruc, *Chem. Rev.*, 2004, **104**, 293–346.

3 K. Cheng, M. Virginie, V. V. Ordomsky, C. Cordier, P. A. Chernavskii, M. I. Ivantsov, S. Paul, Y. Wang and A. Y. Khodakov, *J. Catal.*, 2015, **328**, 139–150.

4 L. J. Durndell, K. Wilson and A. F. Lee, *RSC Adv.*, 2015, **5**, 80022–80026.

5 F. Dong, Y. Zhu, H. Zheng, Y. Zhu, X. Li and Y. Li, *J. Mol. Catal. A Chem.*, 2015, **398**, 140–148.

6 Z. Gao, M. Dong, G. Wang, P. Sheng, Z. Wu, H. Yang, B. Zhang, G. Wang, J. Wang and Y. Qin, *Angew. Chemie Int. Ed.*, 2015, **54**, 9006–9010.

7 K. Okitsu, A. Yue, S. Tanabe and H. Matsumoto, *Chem. Mater.*, 2000, **12**, 3006–3011.

8 D. K. Mishra, A. A. Dabbawala and J. S. Hwang, *J. Mol. Catal. A Chem.*, 2013, **376**, 63–70.

9 B. Mazonde, S. Cheng, G. Zhang, M. Javed and W. Gao, *Catal. Sci. Technol.*, 2018, **8**, 2802–2808.

10 H. C. N. Arul Dhas and A. Gedanken, *J. Phys. Chem. B*, 1997, **101**, 6834–6838.

11 J. Wang, G. Wang, S. Miao, J. Li and X. Bao, *Faraday Discuss.*, 2014, **176**, 135–151.

12 X. Pan and X. Bao, *Acc. Chem. Res.*, 2011, **44**, 553–562.

13 A. Y. Khodakov, W. Chu and P. Fongarland, *Chem. Rev.*, 2007, **107**, 1692–1744.

14 K. Liu, H. Suo, C. Zhang, J. Xu, Y. Yang, H. Xiang and Y. Li, *Catal. Commun.*, 2010, **12**, 137–141.

15 X. Chen, D. Deng, X. Pan and X. Bao, *Chinese J. Catal.*, 2015, **36**, 1631–1637.

16 J. Li, G. Wang, J. Wang, S. Miao, M. Wei, F. Yang and L. Yu, *Nano Res.*, 2014, **7**, 1519–1527.

17 J. Wang, H. Wu, D. Gao, S. Miao, G. Wang and X. Bao, *Nano Energy*, 2015, **13**, 387–396.

18 B. Cornelio, A. R. Saunders, W. A. Solomonsz, M. Laronze-cochard, A. Fontana, J. Sapi, A. N. Khlobystov and G. A. Rance, *J. Mater. Chem. A*, 2015, **3**, 3918–3927.

19 A. N. Khlobystov, *ACS Nano*, 2011, **5**, 9306–9312.

20 R. V Jagadeesh, T. Stemmler, A. Surkus, H. Junge, K. Junge and M. Beller, *Nat. Protoc.*, 2015, **10**, 548–557.

21 E. Bertolucci, R. Bacsa, A. Benyounes, A. M. Raspolli-Galletti, M. R. Axet and P. Serp, *ChemCatChem*, 2015, **7**, 2971–2978.

22 J. H. Kim, J. H. Park, Y. K. Chung and K. H. Park, *Adv. Synth. Catal.*, 2012, **354**, 2412–2418.

23 E. Lam and J. H. T. Luong, *ACS Catal.*, 2014, **4**, 3393–3410.

24 E. Perez-Mayoral, V. Calvino-Casilda and E. Soriano, *Catal. Sci. Technol.*, 2016, **6**, 1265–1291.

25 L. M. Esteves, H. A. Oliveira and F. B. Passos, *J. Ind. Eng. Chem.*, 2018, **65**, 1–12.

26 J. Huo, R. L. Johnson, P. Duan, H. N. Pham, D. Mendivelso-Perez, E. A. Smith, A. K. Datye, K. Schmidt-Rohr and B. H. Shanks, *Catal. Sci. Technol.*, 2018, **8**, 1151–1160.

27 I. Roche, E. Chainet, M. Chatenet and J. Vondra, *J. Phys. Chem. C*, 2007, **111**, 1434–1443.

28 K. Guo, Y. Zhang, Q. Shi and Z. Yu, *Energy Fuels*, 2017, **31**, 6045–6055.

29 K. Meduri, C. Stauffer, A. Barnum, G. O'Brein Johnson, D. Fan, W. Ji, C. Zhang, P. Tratnyek and J. Jiao, *J. Mater. Res.*, 2018, **33**, 2404–2413.

30 V. Calvino-Casilda, A. J. Lopez-Peinado, C. J. Duran-Valle and R. M. Martin-Aranda, *Catal. Rev. Sci. Eng.*, 2010, **52**, 325–380.

31 P. Munnik, P. E. de Jongh and K. P. de Jong, *Chem. Rev.*, 2015, **115**, 6687–6718.

32 P. Serp and B. Machado, in *Nanostructured Carbon Materials for Catalysis*, 2015.

33 F. Huang, H. Liu and D. Su, *Sci. China Mater*, 2017, **60**, 1149–1167.

34 M. G. Al-shaal, W. R. H. Wright and R. Palkovits, *Green Chem.*, 2012, **14**, 1260–1263.

35 H. Zea, C. Chen, K. Lester, A. Phillips, A. Datye, I. Fonseca and J. Phillips, *Catal. Today*, 2004, **89**, 237–244.

36 P. Serp, M. Corrias and P. Kalck, *Appl. Catal. A Gen.*, 2003, **253**, 337–358.

37 A. La Torre, M. W. Fay, G. A. Rance, M. del C. Gimenez-Lopez, W. A. Solomonsz, P. D. Brown and A. N. Khlobystov, *Small*, 2012, **8**, 1222–1228.

38 W. A. Solomonsz, G. A. Rance and A. N. Khlobystov, *Small*, 2014, **10**, 1866–1872.

39 W. A. Solomonsz, G. A. Rance, M. Suyetin, A. La Torre, E. Bichoutskaia and A. N. Khlobystov, *Chem. Eur. J.*, 2012, **18**, 13180–13187.

40 H. M. Cheng, F. Li, G. Su, H. . Y. Pan, L. L. He, X. Sun and M. S. Dresselhaus, *Appl. Phys. Lett.*, 1998, **72**, 3282–3284.

41 T. W. Ebbesen and P. M. Ajayan, *Nature*, 1992, **358**, 220–222.

42 M. F. L. De Volder, S. H. Tawfick, R. H. Baughman and A. J. Hart, *Science (80-.).*, 2013, **339**, 535–539.

43 D. Deng, L. Yu, X. Chen, G. Wang, L. Jin, X. Pan, J. Deng, G. Sun and X. Bao, *Angew. Chemie - Int. Ed.*, 2013, **52**, 371–375.

44 S. F. Yin, B. Q. Xu, W. X. Zhu, C. F. Ng, X. P. Zhou and C. T. Au, *Catal. Today*, 2004, **93**–**95**, 27–38.

45 E. Esmaeili and A. Rashidi, *J. Nanostructures*, 2014, **4**, 133–144.

46 T. W. Chamberlain, J. H. Earley, D. P. Anderson, A. N. Khlobystov and R. a Bourne, *Chem. Commun.*, 2014, **50**, 5200–5202.

47 G. A. O. Xiu-hui, W. Sheng, G. A. O. Dian-nan, L. I. U. Wei-gang, C. Zhi-ping, W. Ming-zhe and W. Shu-dong, *J. Fuel Chem. Technol.*, 2016, **44**, 928–936.

48 D. Wang, X. Sun, C. Xing, G. Yang, K. Tao, T. Kawabata, K. Matsuda, Y. Tan and N. Tsubaki, *J. Nanosci. Nanotechnol.*, 2013, **13**, 1274–1277.

49 M. Ran, Y. Liu, W. Chu and A. Borgna, *Catal. Letters*, 2013, **143**, 1139–1144.

50 M. Ran, W. Chu, Y. Liu and A. Borgna, *RSC Adv.*, 2015, **5**, 103669–103673.

51 F. Zhang, F. Jiao, X. Pan, K. Gao, J. Xiao, S. Zhang and X. Bao, *ACS Catal.*, 2015, **5**, 1381–1385.

52 H. Zhang, X. Pan, X. Han, X. Liu, X. Wang, W. Shen and X. Bao, *Chem. Sci.*, 2013, **4**, 1075–1078.

53 S. Liu, Z. Yan, Y. Zhang, R. Wang, S. Luo, F. Jing and W. Chu, *ACS Sustain. Chem. Eng.*, 2018, **6**, 14403–14413.

54 V. Choudhary and A. Gupta, in *Polymer/Carbon Nanotube Nanocomposites*, 2011, p. 69.

55 M. Chhowalla, K. B. K. Teo, C. Ducati, N. L. Rupesinghe, G. A. J. Amaratunga, A. C. Ferrari, D. Roy, J. Robertson and W. I. Milne, *J. Appl. Phys.*, 2001, **90**, 5308–5317.

56 G. Che, B. B. Lakshmi, C. R. Martin, E. R. Fisher and R. S. Ruoff, *Chem. Mater.*, 1998, **10**, 260–267.

57 J. Kong, A. M. Cassell and H. Dai, *Chem. Phys. Lett.*, 1998, **292**, 567–574.

58 J. Colomer, C. Stephan, S. Lefrant, G. Van Tendeloo, I. Willems, Z. Konya, A. Fonseca, C. Laurent and J. B. Nagy, *Chem. Phys. Lett.*, 2000, **317**, 83–89.

59 S. Huang, M. Woodson, R. Smalley and J. Liu, *Nano Lett.*, 2004, **4**, 1025–1028.

60 M. Kumar and Y. Ando, *J. Nanosci. Nanotechnol.*, 2010, **10**, 3739–3758.

61 J. L. Hutchison, N. A. Kiselev, E. P. Krinichnaya, A. V Krestinin, R. O. Loutfy, A. P. Morawsky, V. E. Muradyan, E. D. Obraztsova, J. Sloan, S. V Terekhov and D. N. Zakharov, *Carbon N. Y.*, 2001, **39**, 761–770.

62 N. Li, Z. Wang, K. Zhao, Z. Shi, Z. Gu and S. Xu, *Carbon N. Y.*, 2010, **48**, 1580–1585.

63 Z. Shi, Y. Lian, X. Zhou, Z. Gu, Y. Zhang, S. Iijima, L. Zhou, K. T. Yue and S. Zhang, *Carbon N. Y.*, 1999, **37**, 1449–1453.

64 Z. Shi, Y. Lian, F. H. Liao, X. Zhou, Z. Gu, Y. Zhang, S. Iijima, H. Li, K. T. Yue and S.-L. Zhang, *J. Phys. Chem. Solids*, 2000, **61**, 1031–1036.

65 J. Zhao, Y. Su, Z. Yang, L. Wei, Y. Wang and Y. Zhang, *Carbon N. Y.*, 2013, **58**, 92–98.

66 W. K. Maser, E. Munoz, A. M. Benito, M. T. Martinez, G. F. de la Fuente, Y. Maniette, E. Anglaret and J.-L. Sauvajol, *Chem. Phys. Lett.*, 1998, **292**, 587–593.

67 C. D. Scott, S. Arepalli, P. Nikolaev and R. E. Smalley, *Appl. Phys. A*, 2001, **72**, 573–580.

68 Y. Zhang and S. Iijima, *Appl. Phys. Lett.*, 1999, **75**, 3087–3089.

69 M. Yudasaka, F. Kokai, K. Takahashi, R. Yamada, N. Sensui, T. Ichihashi and S. Iijima, *J. Phys. Chem. B*, 1999, **103**, 3576–3581.

70 S. Arepalli, *J. Nanosci. Nanotechnol.*, 2004, **4**, 317–325.

71 K. A. Shah and B. A. Tali, *Mater. Sci. Semicond. Process.*, 2016, **41**, 67–82.

72 P.-X. Hou, C. Liu and H.-M. Cheng, *Carbon N. Y.*, 2013, **46**, 2003–2005.

73 C. Journet, M. Picher and V. Jourdain, *Nanotechnology*, 2012, **23**, 142001 (19pp).

74 C. Liu and H.-M. Cheng, *Mater. Today*, 2013, **16**, 19–28.

75 N. M. Mubarak, E. C. Abdullah, N. S. Jayakumar and J. N. Sahu, *J. Ind. Eng. Chem.*, 2014, **20**, 1186–1197.

76 W.-W. Liu, S.-P. Chai, A. R. Mohamed and U. Hashim, *J. Ind. Eng. Chem.*, 2014, **20**, 1171–1185.

77 P. G. Savva, G. G. Olympiou, C. N. Costa, V. A. Ryzhkov and A. M. Efstathiou, *Catal. Today*, 2005, **102**–**103**, 78–84.

78 R. Purohit, K. Purohit, S. Rana, R. S. Rana and V. Patel, *Procedia Mater. Sci.*, 2014, **6**, 716–728.

79 V. Jourdain and C. Bichara, *Carbon N. Y.*, 2013, **58**, 2–39.

80 M. Shajahan, Y. H. Mo, A. K. M. Fazle Kibria, M. J. Lim and K. S. Nahm, *Carbon N. Y.*, 2004, **42**, 2245–2253.

81 E. Flahaut, A. Peigney, C. Laurent and A. Rousset, *J. Mater. Chem.*, 2000, **10**, 249–252.

82 E. Flahaut, A. Peigney, W. S. Bacsa, R. R. Bacsa and C. Laurent, *J. Mater. Chem.*, 2004, **14**, 646–653.

83 W.-M. Yeoh, K.-Y. Lee, S.-P. Chai, K.-T. Lee and A. R. Mohamed, *New Carbon Mater.*, 2009, **24**, 119–123.

84 X. Pan, Z. Fan, W. Chen, Y. Ding, H. Luo and X. Bao, *Nat. Mater.*, 2007, **6**, 507–511.

85 J. M. Planeix, N. Coustel, B. Coq, V. Brontons, P. S. Kumbhar, R. Dutartre, P. Geneste, P. Bernier and P. M. Ajayan, *J. Am. Chem. Soc.*, 1994, **116**, 7935–7936.

86 R. Gao, C. D. Tan and R. T. K. Baker, *Catal. Today*, 2001, **65**, 19–29.

87 R. Vieira, C. Pham-Huu, N. Keller and M. J. Ledoux, *Chem. Commun.*, 2002, **1**, 954–955.

88 J. N. Wang, Y. Z. Zhao and J. J. Niu, *J. Mater. Chem.*, 2007, **17**, 2251–2256.

89 V. Lordi, N. Yao and J. Wei, *Chem. Mater.*, 2001, **13**, 733–737.

90 J. Kang, S. Zhang, Q. Zhang and Y. Wang, *Angew. Chemie - Int. Ed.*, 2009, **48**, 2565–2568.

91 S. Akbayrak and S. Ozkar, *ACS App. Mater. Interfaces*, 2012, **4**, 6302–6310.

92 W. Li, C. Liang, W. Zhou, J. Qiu, Z. Zhou, G. Sun and Q. Xin, *J. Phys. Chem. B*, 2003, **107**, 6292–6299.

93 R. Chetty, S. Kundu, W. Xia, M. Bron, W. Schuhmann, V. Chirila, W. Brandl, T. Reinecke and M. Muhler, *Electrochim. Acta*, 2009, **54**, 4208–4215.

94 H. Vu, F. Gonçalves, R. Philippe, E. Lamouroux, M. Corrias, Y. Kihn, D. Plee, P. Kalck and P. Serp, *J. Catal.*, 2006, **240**, 18–22.

95 M. Aygün, T. W. Chamberlain, M. C. Gimenez-lopez and A. N. Khlobystov, *Adv. Funct. Mater.*, 2018, **28**, 1–15.

96 R. Giordano, P. Serp, P. Kalck, Y. Kihn, J. Schreiber, C. Marhic and J. Duvail, *Eur. J. Inorg. Chem.*, 2003, 610–617.

97 B. M. Quinn, C. Dekker and S. G. Lemay, *J. Am. Chem. Soc.*, 2005, **127**, 6146–6147.

98 J. Li, M. Moskovits and T. L. Haslett, *Chem. Mater.*, 1998, **10**, 1963–1967.

99 H. C. Choi, M. Shim, S. Bangsaruntip and H. Dai, *J. Am. Chem. Soc.*, 2002, **124**, 9058–9059.

100 L. Qu and L. Dai, *J. Am. Chem. Soc.*, 2005, **127**, 10806–10807.

101 T. W. Chamberlain, T. Zoberbier, J. Biskupek, A. Botos, U. Kaiser and A. N. Khlobystov, *Chem. Sci.*, 2012, **3**, 1919–1924.

102 C. Guerret-Piecourt, Y. Le Bouar, A. Loiseau and H. Pascard, *Relation between metal electronic structure and morphology of metal compounds inside carbon nanotubes*, 1994, vol. 372.

103 T. Zoberbier, T. W. Chamberlain, J. Biskupek, M. Suyetin, A. G. Majouga, E. Besley, U. Kaiser and A. N. Khlobystov, *Small*, 2016, **12**, 1649–1657.

104 M. Aygün, C. T. Stoppiello, M. A. Lebedeva, E. F. Smith, M. C. Gimenez-lopez, N. Khlobystov and T. W. Chamberlain, *J. Mater. Chem. A*, 2017, **5**, 21467–21477.

105 A. La Torre, M. del C. Gimenez-Lopez, M. W. Fay, G. A. Rance, W. A. Solomonsz, T. W. Chamberlain, P. D. Brown and A. N. Khlobystov, *ACS Nano*, 2012, **6**, 2000–2007.

106 M. A. Lebedeva, T. W. Chamberlain, M. S. Der and A. N. Khlobystov, *Chem. Mater.*, 2014, **16**, 6461–6466.

107 B. E. Thomas, C. T. Stoppiello and E. Volkova, *Nanoscale*, 2016, **8**, 11727–11737.

108 M. A. Lebedeva, T. W. Chamberlain, E. S. Davies, D. Mancel, B. E. Thomas, M. Suyetin, E. Bichoutskaia, M. Schrçder and A. N. Khlobystov, *Chem. Eur. J.*, 2013, **19**, 11999–12008.

109 M. A. Lebedeva, T. W. Chamberlain, M. Schroder and A. N. Khlobystov, *Chem. Mater.*, 2014, **26**, 6461–6466.

110 G. A. Rance, W. A. Solomonsz and A. N. Khlobystov, *Chem. Commun.*, 2013, **49**, 1067–1069.

111 B. R. Cuenya, *Thin Solid Films*, 2010, **518**, 3127–3150.

112 W. a Solomonsz, G. a Rance, B. J. Harris and A. N. Khlobystov, *Nanoscale*, 2013, **5**, 12200–12205.

113 S. A. Miners, G. A. Rance and A. N. Khlobystov, *Chem. Soc. Rev.*, 2016, **45**, 4727–4746.

114 J. N. H. Reek, I. F. J. Vankelecom, T. S. Koblenz, J. Wassenaar and J. N. H. Reek, *Chem. Soc. Rev.*, 2008, **37**, 237–432.

115 D. Vairavapandian, P. Vichchulada and M. D. Lay, *Anal. Chem. Acta*, 2008, **626**, 119–129.

116 H.-F. Cui, J.-S. Ye, W.-D. Zhang, J. Wang and F.-S. Sheu, *J. Electroanal. Chem.*, 2005, **577**, 295–302.

117 D.-J. Guo and H.-L. Li, *J. Electroanal. Chem.*, 2004, **573**, 197–202.

118 T. M. Day, P. R. Unwin and J. V Macpherson, *Nano Lett.*, 2007, **7**, 51–57.

119 D.-J. Guo and H.-L. Li, *Electrochem. Commun.*, 2004, **6**, 999–1003.

120 B. Cornelio, G. A. Rance, M. Laronze-Cochard, A. Fontana, J. Sapi and A. N. Khlobystov, *J. Mater. Chem. A*, 2013, **1**, 8737–8744.

121 F. P. Zamborini, S. M. Gross and R. W. Murray, *Langmuir*, 2001, **17**, 481–488.

122 V. Mazumder and S. Sun, *J. Am. Chem. Soc.*, 2009, **131**, 4588–4589.

123 K. A. Flanagan, J. A. Sullivan and H. Mueller-Bunz, *Langmuir*, 2007, **23**, 12508–12520.

124 A. Corma, H. Garcia and A. Leyva, *J. Mol. Catal. A Chem.*, 2005, **230**, 97–105.

125 S. Yang, X. Zhang, H. Mi and X. Ye, *J. Power Sources*, 2008, **175**, 26–32.

126 N. Karousis, G.-E. Tsotsou, F. Evangelista, P. Rudolf, N. Ragoussis and N. Tagmatarchis, *J. Phys. Chem. C*, 2008, **112**, 13463–13469.

127 Z. Chen, Z. Guan, M. Li, Q. Yang and C. Li, *Angew. Chemie - Int. Ed.*, 2011, **50**, 4913–4917.

128 T. W. Ebbesen, *J. Phys. Chem. Solids*, 1996, **57**, 951–955.

129 J. Tessonnier, L. Pesant, G. Ehret, M. J. Ledoux and C. Pham-Huu, *Appl. Catal. A Gen.*, 2005, **288**, 203–210.

130 C. Wang, S. Guo, X. Pan, W. Chen and X. Bao, *J. Mater. Chem.*, 2008, **18**, 5782–5786.

131 X. Wang, N. Li, L. D. Pfefferle and G. L. Haller, *Microporous Mesoporous Mater.*, 2013, **176**, 139–144.

132 Q. Fu, G. Weinberg and D.-S. Su, *New Carbon Mater.*, 2008, **23**, 17–20.

133 P. Serp and E. Castillejos, *ChemCatChem*, 2010, **2**, 41–47.

134 T. W. Chamberlain, T. Zoberbier, J. Biskupek, A. Botos, U. Kaiser and A. N. Khlobystov, *Chem. Sci.*, 2012, **3**, 1919–1924.

135 T. Cui, X. Pan, J. Dong, S. Miao, D. Miao and X. Bao, *Nano Res.*, 2018, **11**, 3132–3144.

136 X. Zhang, Y. C. Guo, Z. C. Zhang, J. Sen Gao and C. M. Xu, *J. Catal.*, 2012, **292**, 213–226.

137 L. Jiang and L. Gao, *Carbon N. Y.*, 2003, **41**, 2923–2929.

138 E. Yoo, L. Gao, T. Komatsu, N. Yagai, K. Arai, T. Yamazaki, K. Matsuishi, T. Matsumoto and J. Nakamura, *J. Phys. Chem. B*, 2004, **108**, 18903–18907.

139 R. Singh, T. Premkumar, J.-Y. Shin and K. E. Geckeler, *Chem. a Eur. J.*, 2010, **16**, 1728–1743.

140 X. Zhang, Y. Cai, Z. C. Zhang, J. Sen Gao and C. M. Xu, *J. Catal.*, 2012, **292**, 213–226.

141 J. Tessonnier, O. Ersen, G. Weinberg, C. Pham-huu, D. S. Su and R. Schlogl, *ACS Nano*, 2009, **3**, 2081–2089.

142 M. Brust, M. Walker, D. Bethell, D. J. Schiffrin and R. Whyman, *J. Chem. Soc., Chem. Commun.*, 1994, 801–802.

143 M. Tang, S. Mao, M. Li, Z. Wei, F. Xu, H. Li and Y. Wang, *ACS Catal.*, 2015, **5**, 3100–3107.

144 J. A. Rodriguez, *Surf. Sci. Rep.*, 1996, **24**, 223–287.

145 E. Castillejos, P. J. Debouttière, L. Roiban, A. Solhy, V. Martinez, Y. Kihn, O. Ersen, K. Philippot, B. Chaudret and P. Serp, *Angew. Chemie - Int. Ed.*, 2009, **48**, 2529–2533.

146 X. Li, T. Hungria, C. Garcia Marcelot, M. R. Axet, P.-F. Fazzini, R. P. Tan, P. Serp and K. Soulantica, *Chem. Commun.*, 2016, 2362–2365.

147 R. M. M. Abbaslou, A. Tavassoli, J. Soltan and A. K. Dalai, *Appl. Catal. A Gen.*, 2009, **367**, 47–52.

148 W. A. Solomonsz, G. A. Rance, B. J. Harris and A. N. Khlobystov, *Nanoscale*, 2013, **5**, 12200–12205.

149 H. Yang, S. Song, R. Rao, X. Wang, Q. Yu and A. Zhang, *J. Mol. Catal. A. Chem.*, 2010, **323**, 33–39.

150 A. M. Zhang, J. L. Dong, Q. H. Xu, H. K. Rhee and X. L. Li, *Catal. Today*, 2004, **93**–**95**, 347–352.

151 P. Gallezot and D. Richard, *Catal. Rev.*, 1998, **40**, 81–126.

152 H. Ma, L. Wang, L. Chen, C. Dong, W. Yu, T. Huang and Y. Qian, *Catal. Commun.*, 2007, **8**, 452–456.

153 M. C. Bahome, L. L. Jewell, D. Hildebrandt, D. Glasser and N. J. Coville, *Appl. Catal. A Gen.*, 2005, **287**, 60–67.

154 W. Chen, Z. Fan, X. Pan and X. Bao, *J. Am. Chem. Soc.*, 2008, **130**, 9414–9419.

155 M. C. Bahome, L. L. Jewell, K. Padayachy, D. Hildebrandt, D. Glasser, A. K. Datye and N. J. Coville, *Appl. Catal. A Gen.*, 2007, **328**, 243–251.

156 A. Tavasoli, M. Trepanier, R. M. Malek Abbaslou, A. K. Dalai and N. Abatzoglou, *Fuel Process. Technol.*, 2009, **90**, 1486–1494.

157 E. Castillejos, M. Jahjah, I. Favier, A. Orejón, C. Pradel, E. Teuma, A. M. Masdeu-Bulto, P. Serp and M. Gomez, *ChemCatChem*, 2012, **4**, 118–122.

158 M. Ran, W. Chu, Y. Liu and A. Borgna, *RSC Adv.*, 2015, **5**, 103669–103673.

159 X. Chen, D. Deng, X. Pan and X. Bao, *Chinese J. Catal.*, 2015, **36**, 1631–1637.

160 X. Pan, Z. Fan, W. E. I. Chen, Y. Ding, H. Luo and X. Bao, *Nat. Mater.*, 2007, **6**, 507–511.

161 J. Wang, S. Lu, J. Li and C. Li, *Chem. Commun.*, 2015, **51**, 17615–17618.

162 D. Wang, G. Yang, Q. Ma, M. Wu, Y. Tan, Y. Yoneyama and N. Tsubaki, *ACS Catal.*, 2012, **2**, 1958–1966.

163 Z. Guan, S. Lu and C. Li, *J. Catal.*, 2014, **311**, 1–5.

Chapter 2: Fabrication and Characterisation of Carbon Nanoreactors

2.1 Introduction

The interaction between the support structure and metal nanoparticles (MNPs), as well as the size and shape of MNPs, has been shown to have a critical effect on the catalytic performance of supported nanoparticle catalysts.[1,2] It is therefore, important to develop a fundamental understanding of how the conditions used during the fabrication process of these materials affects their structure. Gaining control over the size and position of encapsulated MNPs is critical if they are to reach their full potential in a diverse range of chemical transformations.

Encapsulating MNPs within carbon nanostructures (CNSs) enhances the stability of the MNPs and creates a unique confined environment which can alter the pathway of a reaction.[3–5] Numerous methods for the decoration of CNSs with MNPs have been previously reported, offering various degrees of control over particle size and distribution. These methods include incipient wetness impregnation;[6–17] organometallic grafting;[18] in situ filling during arc-discharge growth of carbon nanotubes (CNTs);[19] electrochemical deposition;[20] electroless deposition, with and without the use of reducing agents;[21–23] electron beam evaporation;[24] and sublimation deposition approaches.[12,19-21] Among these techniques, wet impregnation appears to be the most widely used method due to its versatility and simplicity. However, the main drawback to this technique is the lack of control over the location of the MNPs and so, if selective deposition of MNPs inside CNSs is required, a selective washing step is often required to remove MNPs from the exterior surface of the support structure leading to a significant loss of precursor during synthesis.[27]

2.1.1 Fabrication Methods for Metal Nanoparticles within GNFs

The incorporation of various MNPs within graphitised nanofibers (GNFs) have been reported using both solution based and gas filling methods to form MNPs@GNF structures and are summarised in Table 2.1 at the end of this section.

Aygun, M., *et al.*,[17] compared the structure and reactivity of MNPs@GNFs prepared via the two different techniques. The gas filling method employed

used sublimation of a volatile metal precursor followed by its thermal decomposition in an argon atmosphere to afford the relevant MNPs. This was done for both Pt (precursor: $Pt(acac)_2$) and Pd (precursor: $Pd(acac)_2$) MNPs and the resultant materials were referred to as PtNPs@GNFs-1 and PdNPs@GNFs-1, respectively. The second fabrication method was a solution-based approach in which the metal precursor ($Pt(dba)_3$ or $Pd_2(dba)_3$) in $CHCl_3$ was added dropwise to GNFs dispersed in $CHCl_3$, whilst being treated with ultrasonic waves and heated at either 40 or 70 °C for 4 h – 1 day. The resulted suspension was then filtered and washed repeatedly with acetone to give the desired materials referred to as PtNPs@GNFs-2 and PdNPs@GNFs-2. In both cases (Pt and Pd) the gas filling method lead to the MNPs being located solely on the interior of the GNF support structure at the step-edges, whereas, the liquid phase method afforded MNPs mostly on the interior, distributed along the step-edges (with some NPs on the exterior). Although the gas filling method afforded more control over the location of the MNPs on/in the GNF support structure, the solution based method led to the formation of much smaller MNPs for both Pt and Pd (the order in terms of NP size was as follows; PtNPs@GNFs-1>PtNPs@GNFs-2 and PdNPs@GNFs-1>PtNPs@GNFs-2).

Rance, G., *et al.*,[3] reported the preparation of preformed CuNPs which were subsequently adsorbed onto or encapsulated within GNFs. The CuNPs were prepared via a Brust-Schriffrin reduction, before their incorporation on/into the GNFs. The location of the CuNPs in the final material was controlled in the impregnation step (Scheme 2.1).

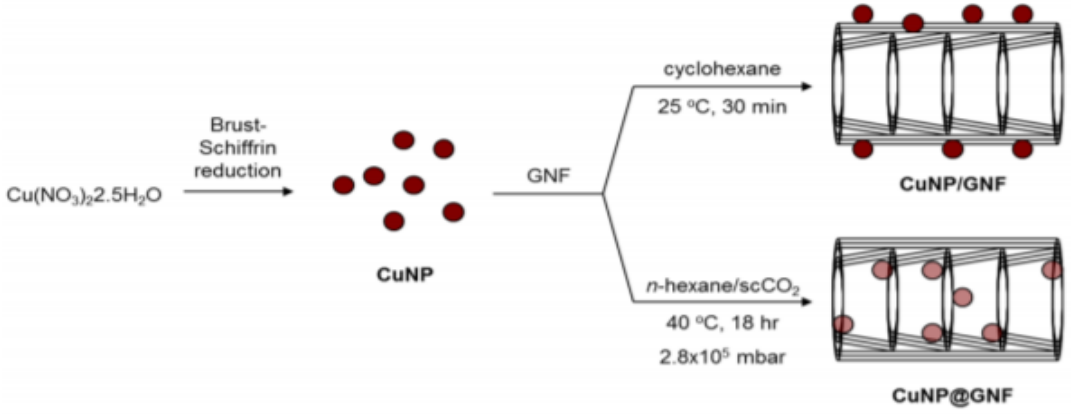

Scheme 2.1: Schematic representation of the methods used for the preparation of CuNPs and their subsequent adsorption or encapsulation in GNFs (controlled through simple changes in the impregnation step).[3]

The use of traditional organic solvent lead to the adsorption of the CuNPs onto the exterior of the GNFs whereas a mixture of hexane/carbon dioxide under

supercritical conditions led to the incorporation of the CuNPs within the GNFs, located primarily at the step-edges.[3]

A similar study was reported by Solomonsz, W. *et al.*,[4] who looked at the preparation of RhNPs, as well as, bimetallic RhPtNPs carbon nanoreactors (where GNFs were used as the carbon support). The fabrication of the MNPs were performed based on a modified two-phase Brust-Schiffrin reduction,[28] before incorporation on/into the carbon support structure. The location of the MNPs on/in the support structure was controlled simply by using two impregnation techniques (Scheme 2.2). The performance of the materials was evaluated using a hydrosilylation reaction, for NPs of the same size located on the interior and exterior of the GNFs. Although this study looked at the activity of a bimetallic NP system it was focused on the confinement effects imposed by the GNF support structure rather than how the fabrication method affected the composition of the RhPtNPs and in turn the catalytic performance of the material.[4] It is clear that gas phase filling methods lead to greater control of the location of the MNPs within the cavity of the support structure.

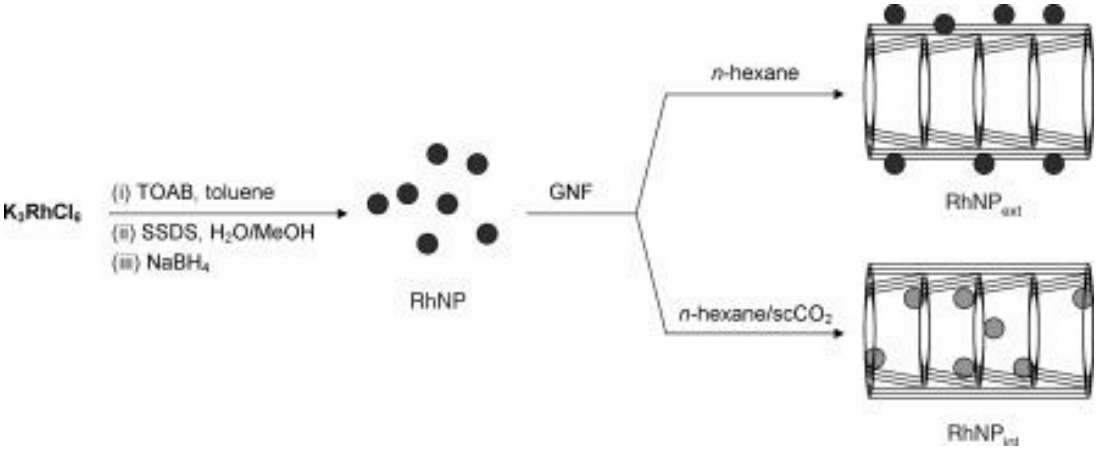

Scheme 2.2: Schematic representation of the methods used for the preparation of RhNPs and their subsequent adsorption or encapsulation in GNFs (controlled through simple changes in the impregnation step). The same approach was employed for the RhPtNPs systems.[4]

Table 2.1: Summary of fabrication methods used for the decoration of GNFs with MNPs and resultant particle sizes.

Metal/Support (wt.%)	Technique	Particle size (nm)	Ref
Pt/S-GNFs[a] (10)	Impregnation of pre-formed PtNPs (reduction of $Pt(acac)_2$) in hexane.	5.3 ± 0.4	29
Pd/GNFs (7.8)	Impregnation from K_2PdCl_4 in deionised water	7.0 ± 2.2	30

Au/GNFs (?)	Pre-formed stabilised AuNPs (modified Brust-Schiffrin reduction) inserted into support structure using supercritical CO_2	2.3 ± 0.4	31
Rh/GNF (1)	Ion-exchange at 100 °C from $RhCl_3$ aqueous solution and $NaBH_4$ reduction	1.1	32
Cu/GNFs (4)	Pre-formed CuNPs (Brust-Schiffrin reduction) either adsorbed on GNFs via impregnation from cyclohexane solution or inserted into GNFs using a mixture of hexane-CO_2 under supercritical conditions	2.87 ± 0.48	3
Rh/GNFs (5.5) RhPt/GNFs (3.3)	Pre-formed MNPs (modified Brust-Schiffrin reduction) either absorbed on GNFs from hexane solution or inserted into GNFs using a mixture of hexane-CO_2 under supercritical conditions	2.95 ± 0.35 4.07 ± 0.86	4
Pt/GNFs (0.5) Pd/GNFs (0.5)	Sublimation deposition of $Pt(acac)_2$ or $Pd(acac)_2$	4.21 ± 1.54 10.79 ± 3.86	17
Pt/GNFs (0.5) Pd/GNFs (0.5)	Impregnation from $Pd_2dba_3.CHCl_3$ or $Ptdba_3$-$CHCl_3$ solution	1.55 ± 0.48 2.26 ± 0.56	17
Co@C_n/GNFs (10) Fe@C_n/GNFs (10)	Impregnation from Co@C_n in hexane Sublimation deposition of $FeCp_2$	29.7 ± 22.8 23.9 ± 14.9	17
Rh/GNF-H[b] (4) Rh/GNF-R[c] (4)	Impregnation from alcoholic solution of $RhCl_3.3H_2O$	19.1 15.1	8
Pt/GNFs (?)	Pre-formed PtNPs inserted into support structure using a mixture of hexane-CO_2 under supercritical conditions	2.75 ± 0.83	33
Ru/GNFs (1)	Sublimation decomposition of $Ru_3(CO)_{12}$	3.58 ± 1.14	26

[a]S-GNFs = Shortened GNFs; [b]GNF-H = Herring-bone type GNFs; [c] GNF-R = Ribbon-like GNFs.

2.1.2 Fabrication Methods for Bimetallic Nanoparticles in Carbon Nanoreactors

The number of literature examples for the fabrication of bimetallic MNPs in GNFs is limited. However, previous studies on bimetallic systems have been

performed for other porous carbon supports. Li, X. *et* al.,[34] studied the confinement effects of CNTs of various diameters (6.5 – 200 nm) on the shape and composition of bimetallic FePt and CoPt nanostructures. The fabrication method employed was the co-reduction of $[Pt(Me)_2(1,5\text{-cyclooctadiene})]$ with $[Co\{N(SiMe_3)_2\}_2(THF)]$ or $[Fe\{N(SiMe_3)_2\}_2]_2$ precursor with H_2 in the presence of 2-benzylbenxonic and 4-(3-phenylpropyl)pyridine. The aromatic stabilising ligands were chosen to promote the incorporation of the MNPs into the CNTs via π-π interactions between the NPs and the internal surface of the CNTs. However, complete control over the location of the MNPs was not achieved with some MNPs still forming on the exterior of the CNTs (removed with washing). It was found that the host channel diameter drastically influenced both the shape and composition of the nano-objects formed. Large diameter CNTs (100–200 nm) lead to the formation of small FePt and CoPt NPs and small diameter CNTs (average 6.5 nm) lead to the formation of wire-like structures which was attributed to the coalescence of NPs.[34]

2.1.3 Summary and Conclusions

In summary numerous methods for the insertion of MNPs into GNFs have been previously reported. These methods allow for various amounts of control over the location of the MNPs within the support structure and control over MNP size. A gas filling approach has been reported to offer the greatest control on MNP location leading to the MNPs being located solely on the interior of the GNF support structure. As nothing systematic has been previously reported to unravel the fabrication conditions/structure relationship in monometallic RuNPs this was investigated using the gas filling approach. This will also act as a reference to help understand how bimetallic RuNiNPs form.

Bimetallic systems are interesting because not only have they been found to enhance the catalytic performance with respect to their monometallic counterparts,[35,36] coupling a noble metal with a cheaper metal reduces the cost of the material overall. Investigation into the composition of bimetallic GNF supported systems has not been extensively undertaken and as such there is a lack of understanding in how the fabrication method can affect the formation of the MNPs.

This Chapter aims to provide understanding of how the composition of ruthenium and nickel based bimetallic nanoparticles encapsulated within GNFs can be altered through simple changes in the fabrication method (i.e. altering the ratio of the Ru and Ni precursors).

2.2 Results and Discussion

2.2.1 Preparation and Characterisation of Monometallic Materials

This section highlights the insertion of RuNPs in GNFs using a previously reported sublimation followed by thermal decomposition method.[26,37,38]

2.2.1.1 Preparation

Following the preparation method/conditions reported by Aygun, M., *et al.*,[26] for the fabrication of RuNPs@GNFs, the effect of varying metal loading on the structure of the nanoreactors was investigated by fabricating a series of RuNPs@GNFs with different amounts of Ru metal (wt.%). This was controlled simply by varying the amount of ruthenium precursor used in the initial sublimation step from 1 to 10% by wt. Ru, whilst keeping the time and temperature of subsequent steps the same for all materials.

Briefly, the ruthenium metal precursor, $Ru_3(CO)_{12}$, was encapsulated in the GNFs using the general procedure outlined in Scheme 2.3.

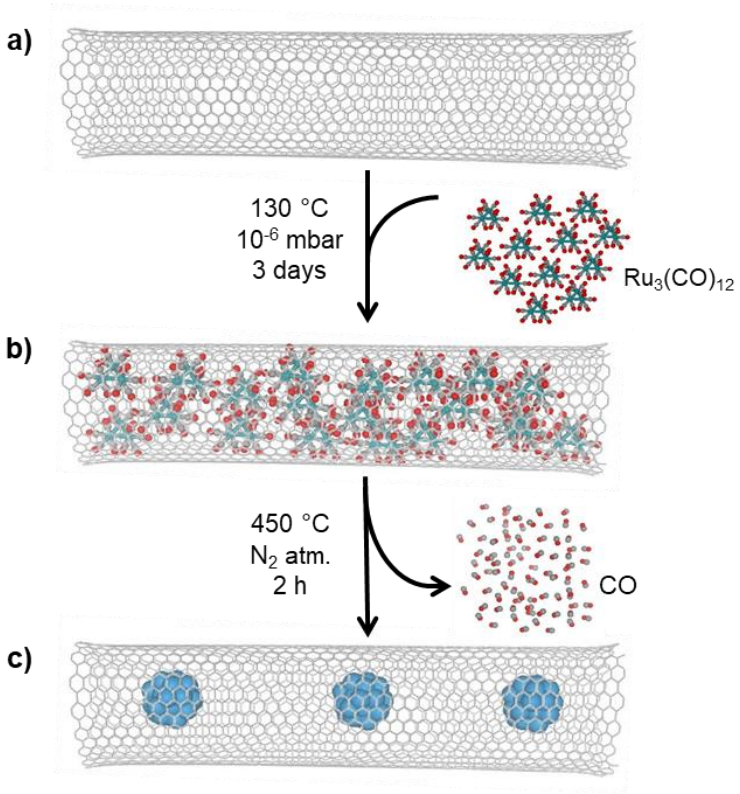

Scheme 2.3: General method reported for the encapsulation of MNPs into CNRs. a) $Ru_3(CO)_{12}$ and freshly annealed CNRs sealed under vacuum in a Pyrex tube and heated at 130 °C for 3 days, to allow for the sublimation of the metal precursor ensuring complete penetration of the nanofibers; b) sample immersed in ice-water bath to give solid phase $Ru_3(CO)_{12}$ precursor inside the internal channel of the CNRs; c) metallic RuNPs deposited within the internal channel of the CNR by thermal decomposition at 450 °C in a nitrogen atmosphere (50 mbar).

Firstly, freshly annealed GNFs and $Ru_3(CO)_{12}$ were sealed under vacuum (10^{-6} mbar) in a pyrex tube and heated at 130 °C for 3 days (a temperature above the sublimation point of $Ru_3(CO)_{12}$ to ensure complete penetration of the nanofibers by the metal precursor). After 3 days, the sample was quickly immersed in an ice bath causing the $Ru_3(CO)_{12}$ to condense from the gas phase to the solid phrase, inside the nanofibers. The sample was then resealed in a pyrex tube under a nitrogen atmosphere (50 mbar) and heated at 450 °C for 2 hours to decompose the carbonyl precursor.

2.2.1.2 Characterisation of RuNPs@GNFs (1, 2, 5 and 10 wt.%)

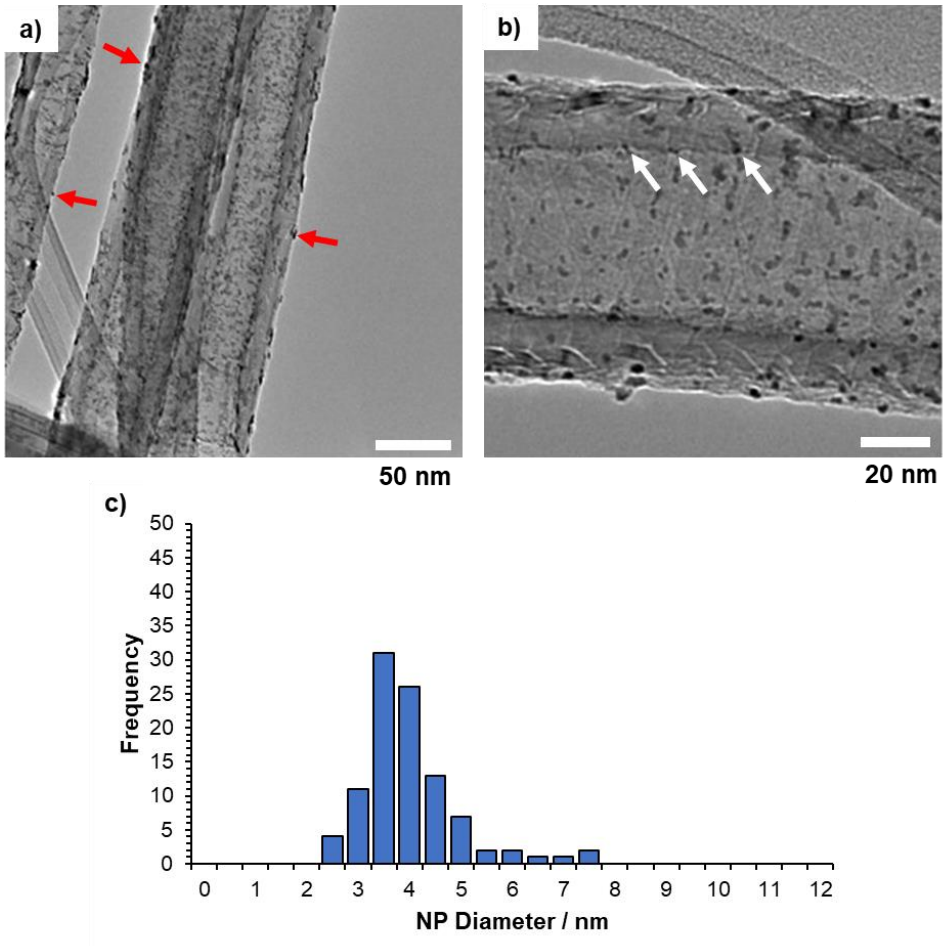

Figure 2.1: a) and b) TEM micrographs of RuNPs@GNFs (5 wt.%) showing the general structure, size, distribution and location of the MNPs. Red and white arrows indicate RuNPs on the exterior of the GNF and at the step edges within the GNF, respectively; and c) particle size distribution showing the average size of the RuNPs to be 4.2 ± 1.2 nm.

Transmission electron microscopy (TEM) was employed to quantify the size, shape and location of the NPs within the nanofibers for each material. TEM confirmed that the nanoparticles were located principally on the interior of the

GNFs, with only a small quantity of NPs located on the exterior (Figure 2.1 for 5 wt.%). Correspondingly, the RuNPs present in RuNPs@GNFs (1, 2, and 10 wt.%) are predominantly located on the interior of the GNFs, again with only a small portion located on the exterior of the support structure (see Figure 2.2).

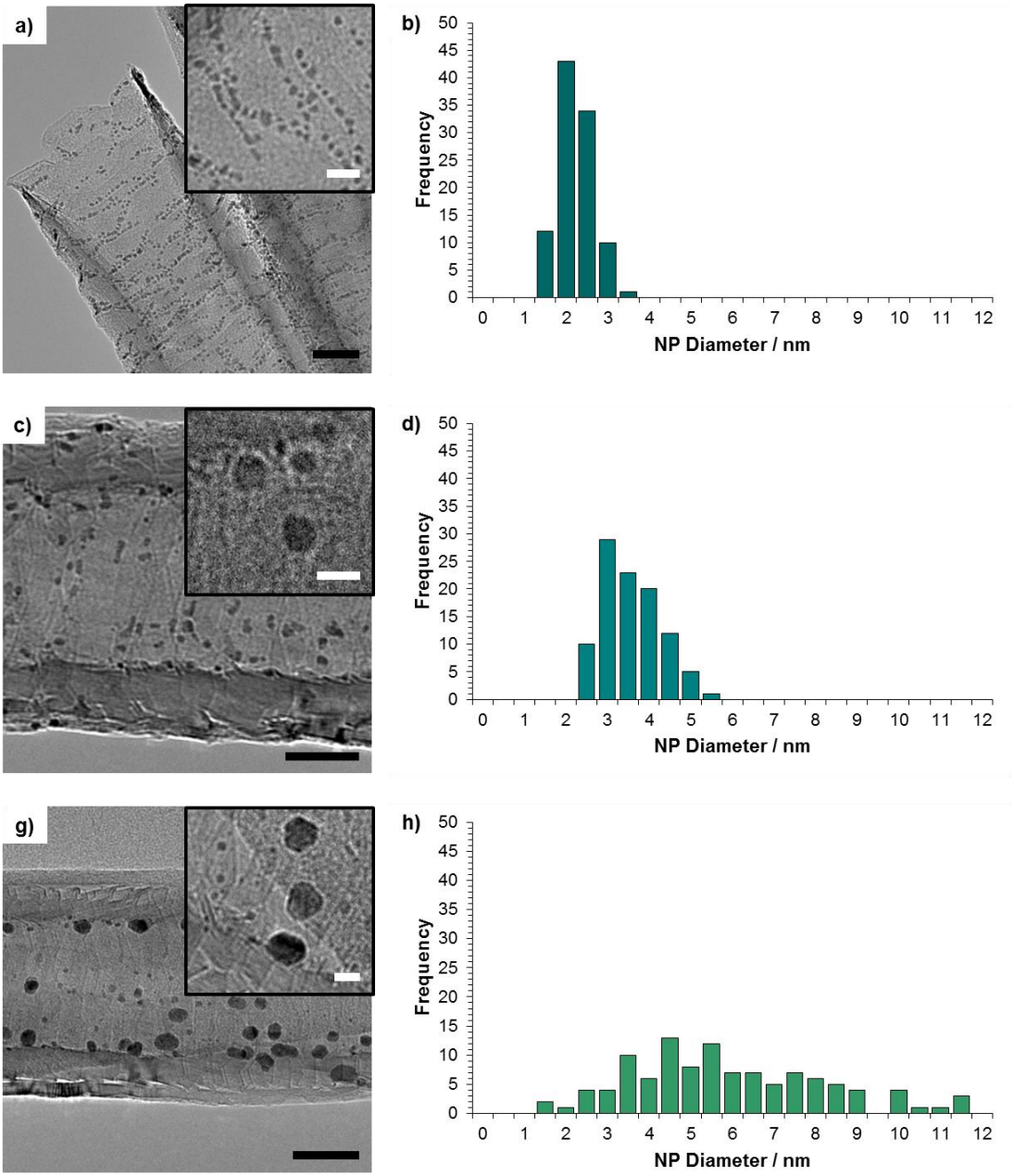

Figure 2.2: a), c) and g) TEM micrographs of RuNPs@GNFs (1, 2 and 10 wt.%) respectively. Showing the general structure, size, distribution and location of the metal nanoparticles. b), d), and h) particle size distribution for RuNPs@GNFs showing the average size of the nanoparticle to be 1.9 ± 0.5, 3.3 ± 0.7 and 6.6 ± 2.3 for 1 wt.%, 2 wt.% and 10 wt.%, respectively. Black and white scale bars are 25 nm and 5 nm, respectively.

Quantitative size analysis was performed for all samples by measuring the diameter of a statistically relevant number of different nanoparticles (>100 samples) from different regions of the TEM sample grid in each case and revealed the average size of the RuNPs to be 1.9 ± 0.5, 3.3 ± 0.7, 4.2 ± 1.2 and 6.6 ± 2.3 nm for RuNPs@GNFs (1 wt.%), RuNPs@GNFs (2 wt.%), RuNPs@GNFs (5 wt.%), and RuNPs@GNFs (10 wt.%), respectively.

Scanning electron microscopy (SEM) was used to gain a more global view of the RuNPs@GNFs (5 wt. %) material and confirmed the location of the RuNPs within the support structure. From Figure 2.3, it can be clearly seen that the majority of the RuNPs are located on the internal channel of the GNFs. It can also be seen that there are some RuNPs are located on the outside of the GNFs as expected from TEM micrographs obtained for this material.

EDX spectroscopy showed characteristic peaks of Ru at 2.6 and 19.2 KeV confirming the composition of the NPs formed in the GNFs (Figure 2.4). Thermogravimetric analysis (TGA) was employed to determine the metal loading of the material. TGA gave an accurate metal loading of 5.6% (Figure 2.5).

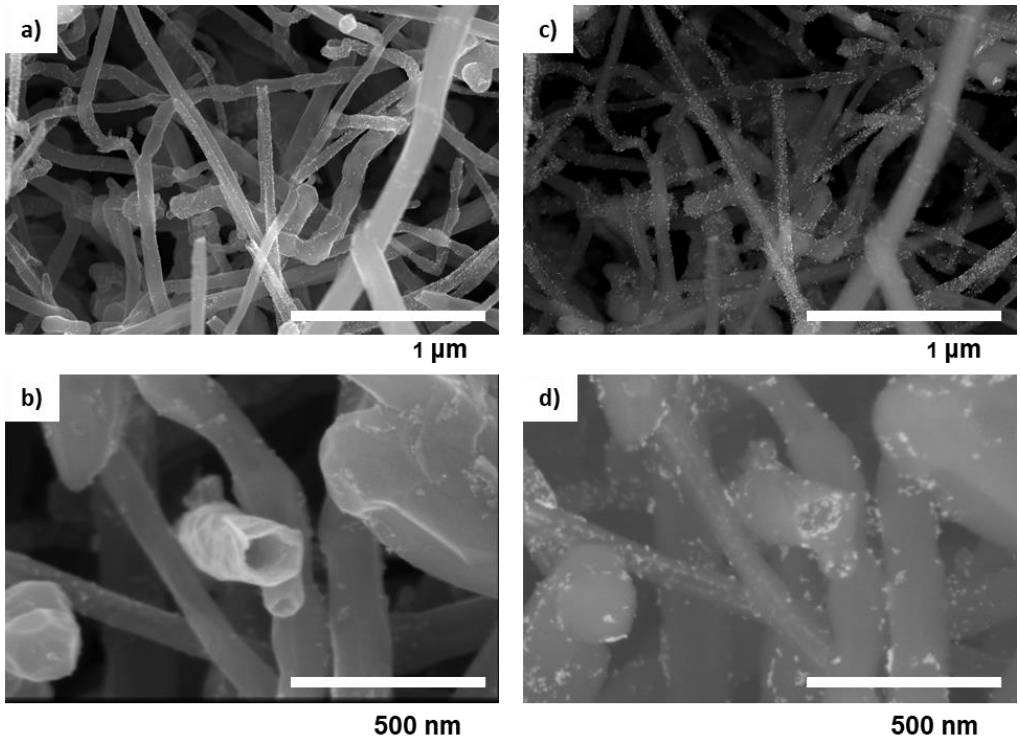

Figure 2.3: SEM images of RuNPs@GNFs (5 wt.% Ru) showing the location of the RuNPs within the sample. a) and b) where taken using a secondary electron TLD detector; whereas images c) and d) were taken using a backscatter detector.

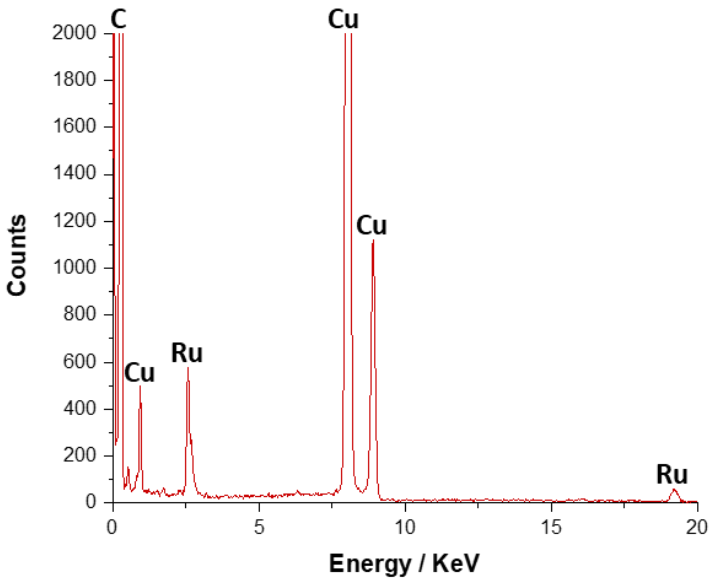

Figure 2.4: EDX spectrum of RuNPs formed by the thermal decomposition of $Ru_3(CO)_{12}$ in GNFs. Characteristic peaks of Ru were identified at 2.6 and 19.2 KeV. Cu peaks are due to the TEM grid used.

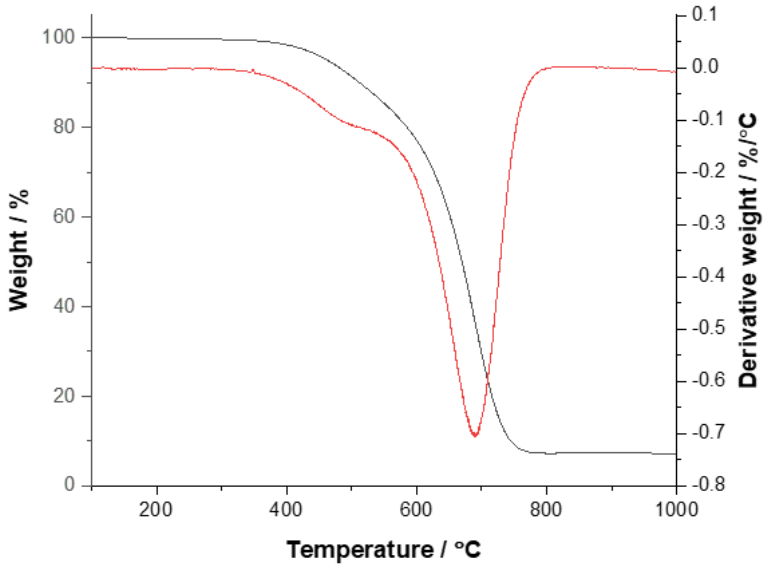

Figure 2.5: TGA plot (black), and corresponding derivative (red), of RuNPs@GNFs (5 wt.%) showing the residual weight remaining after GNF combustion.

2.2.1.3 Characterisation of RuNPs@GNFs (different decomposition temperatures).

The fabrication of RuNPs@GNFs (2 wt.%) was carried out at varying decomposition temperatures (200 – 700 °C) to ascertain whether this parameter had an effect on the formation of the RuNPs (i.e. change in particle

size or location within the support structure). 2% by wt. Ru metal loading was chosen as it would allow for changes in the location of the MNPs to be easily identified as above this metal loading the interior channels of the GNFs become full and as such MNPs will always form on the exterior of the support structure).[17] TEM was employed to quantify the size, shape and location of the NPs within the nanofibers for each material. TEM confirmed that the nanoparticles were located principally on the interior of the GNFs, with only a small quantity of NPs located on the exterior for all materials across the series (Figure 2.6). Quantitative size analysis was performed by measuring the diameter of a statistically relevant number of different nanoparticles (>100 samples) from different regions of the TEM sample grid and revealed the average size of the RuNPs to be 5.8 ± 2.1, 4.2 ± 1.0, 3.3 ± 0.6, 3.7 ± 1.1 and 3.6 ± 0.6 nm for decomposition temperatures of 200, 400, 450, 500 and 700 °C, respectively (summarised in Table 2.2). However, it is noted that the NPs in the sample made at 700 °C are remarkably mono dispersed in terms of size, which could be related to the higher formation temperature leading to faster and more uniform growth. This is not something which has been observed before for GNF supported NP systems and could be explored further in the future if systems in which precise control over NP size are required.

Table 2.2: Summary of decomposition temperature used for the fabrication of RuNPs@GNFs (2 wt.%) and the average diameter of the resultant RuNPs showing no obvious relationship between the average diameter and decomposition temperature.

Temperature / °C	RuNP Diameter / nm
200	5.8 ± 2.1
400	4.2 ± 1.0
450	3.3 ± 0.6
500	3.7 ± 1.1
700	3.6 ± 0.6

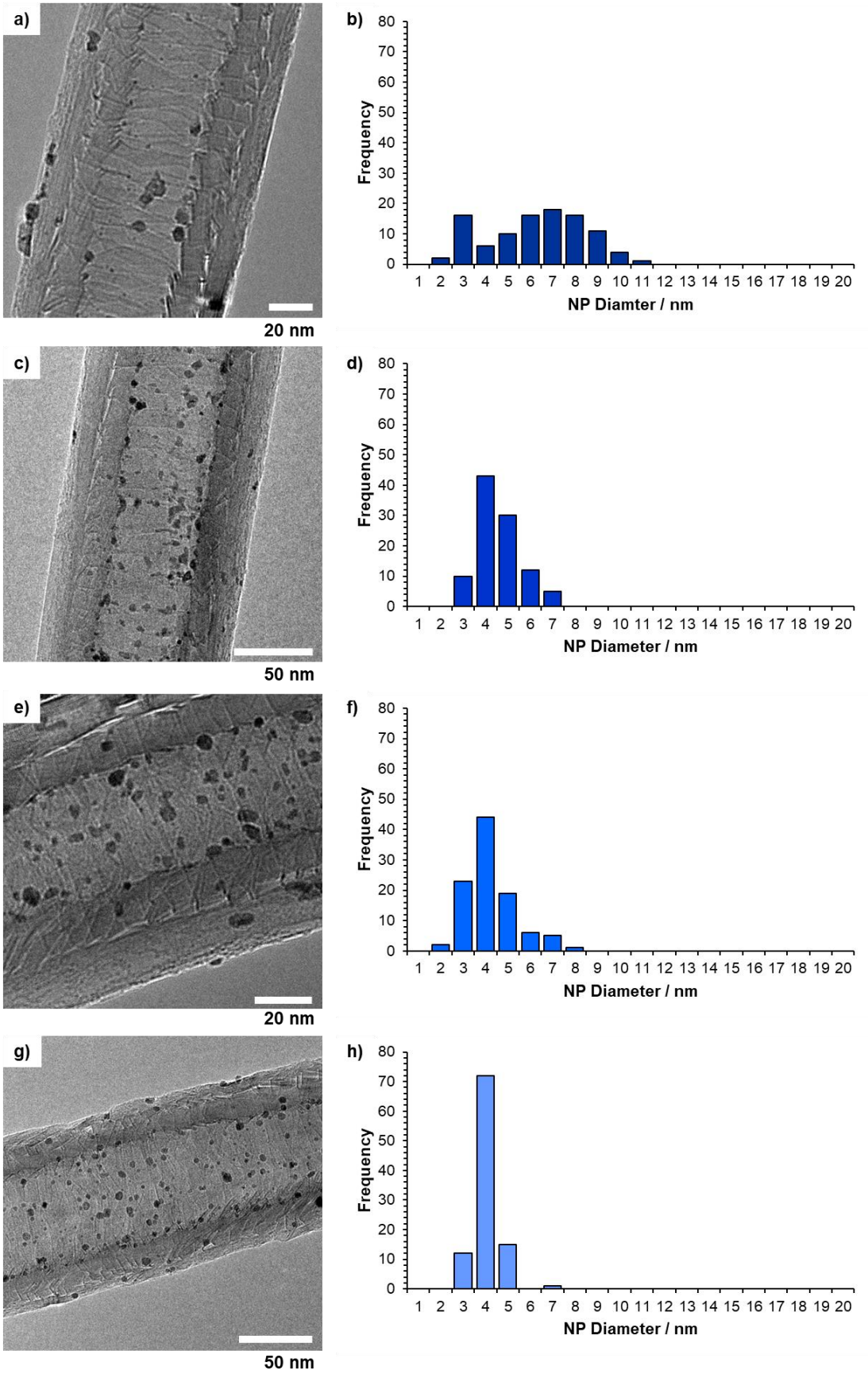

Figure 2.6: TEM micrograph and particle size distribution of RuNPs decomposed at a-b) 200 °C, c-d) 400 °C, e-f) 500 °C and g-h) 700 °C.

2.2.2 Preparation and Characterisation of Bimetallic Materials

Another common route to controlling the catalytic performance of MNP catalysts is through varying the composition of the NPs using mixtures of metals[35,36] As mentioned previously, the composition of bimetallic NPs formed is dependent upon the reaction conditions used during the fabrication process. Currently, little is known regarding how the composition of the MNPs formed on porous carbon supports is related to the fabrication process. This section investigates how systematically varying the fabrication method of bimetallic RuNiNPs@GNFs affects the resultant material (e.g. changing the addition sequence of the metal precursors).

2.2.1.1 Preparation

The fabrication of bimetallic MNPs was carried out using the sublimation followed by thermal decomposition method where $Ru_3(CO)_{12}$ and $NiCp_2$ were used as the metal precursors. Nickelocene was chosen as a suitable metal precursor as the deposition of nickelocene to form nano-objects has been previously reported.[39] For the fabrication of bimetallic NPs supported within GNFs there are two approaches that can be employed (see Scheme 2.4).

The first is a concerted addition approach in which both metal precursors are added at the same time. The second is a sequential addition approach in which one metal precursor is deposited within the support structure and decomposed before the addition of the second metal precursor and subsequent decomposition. In theory each fabrication method could lead to the formation of three different NP systems; 1, mixed metal alloy NPs, 2, core shell NPS and 3, a mixture of the two discrete, monometallic NPs within the same support structure. The fabrication of three bimetallic RuNiNPs@GNFs (5% by wt. total metal) materials with a Ru:Ni weight ratio of 1:1 were carried out using the different addition sequence approaches and are denoted concerted addition, sequential addition (Ru 1^{st}) and sequential addition (Ni 1^{st}) in which Ru and Ni precursors are added first respectively.

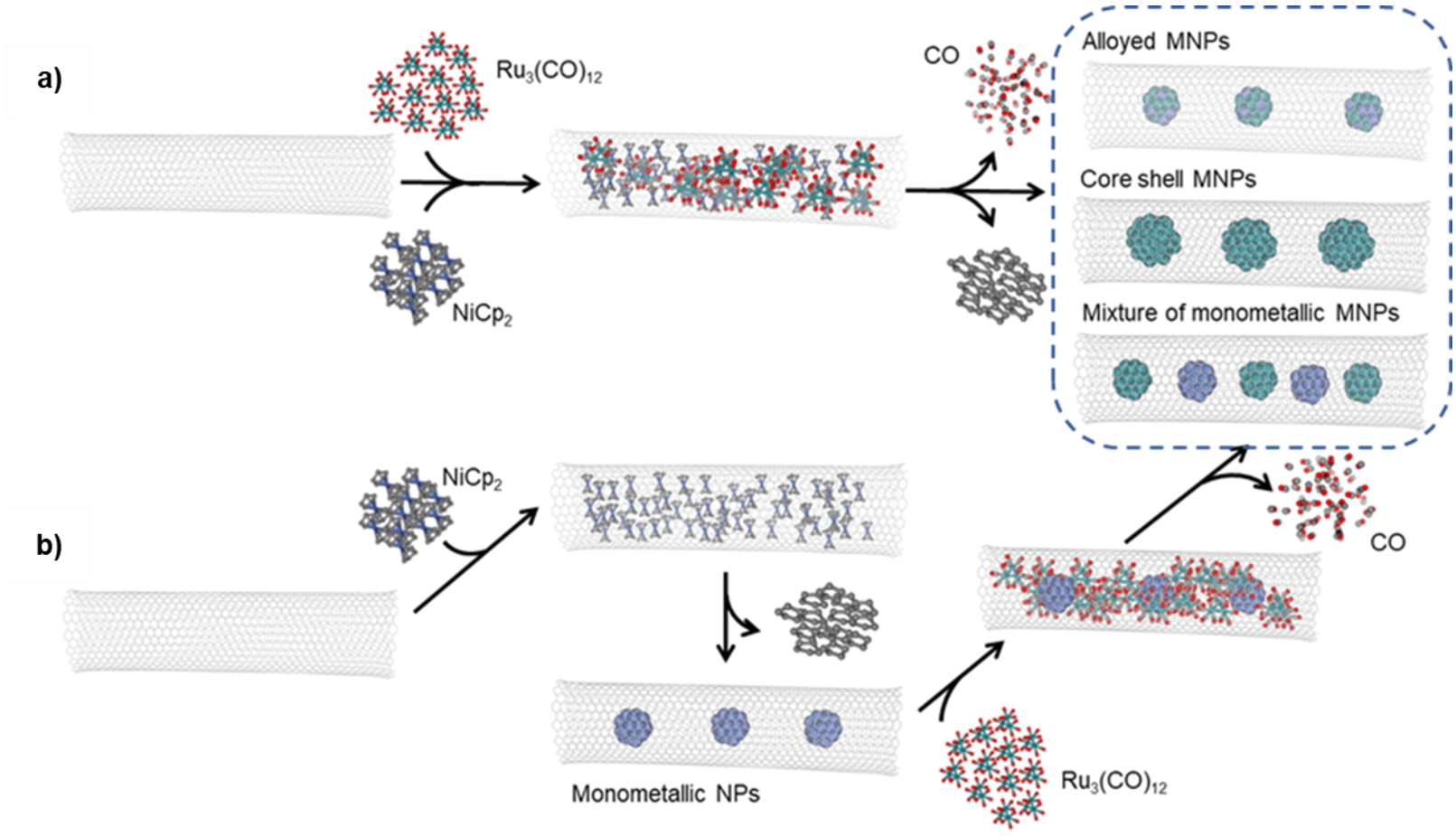

Scheme 2.4: Schematic representation of a) the concerted addition, and b) sequential addition sequences which were employed for the fabrication of bimetallic RuNiNPs@GNFs. The blue box highlights the three different types of nanoparticles which can potentially be formed using this approach.

2.2.1.2 Characterisation of $Ru_{0.5}Ni_{0.5}$NPs@GNFs Fabricated using Different Addition Sequences

2.2.1.2.1 Concerted Addition

High resolution transmission electron microscopy (HRTEM) (Figure 2.7) and scanning transmission electron microscopy (STEM) (Figure 2.8) were employed to quantify the size, shape and location of the NPs within the GNFs. Quantitative size analysis was performed by measuring the diameter of a statistically relevant number of different nanoparticles (>100 samples) from different regions of the TEM sample grid and revealed the average size of the MNPs to be 3.4 ± 1.7 nm.

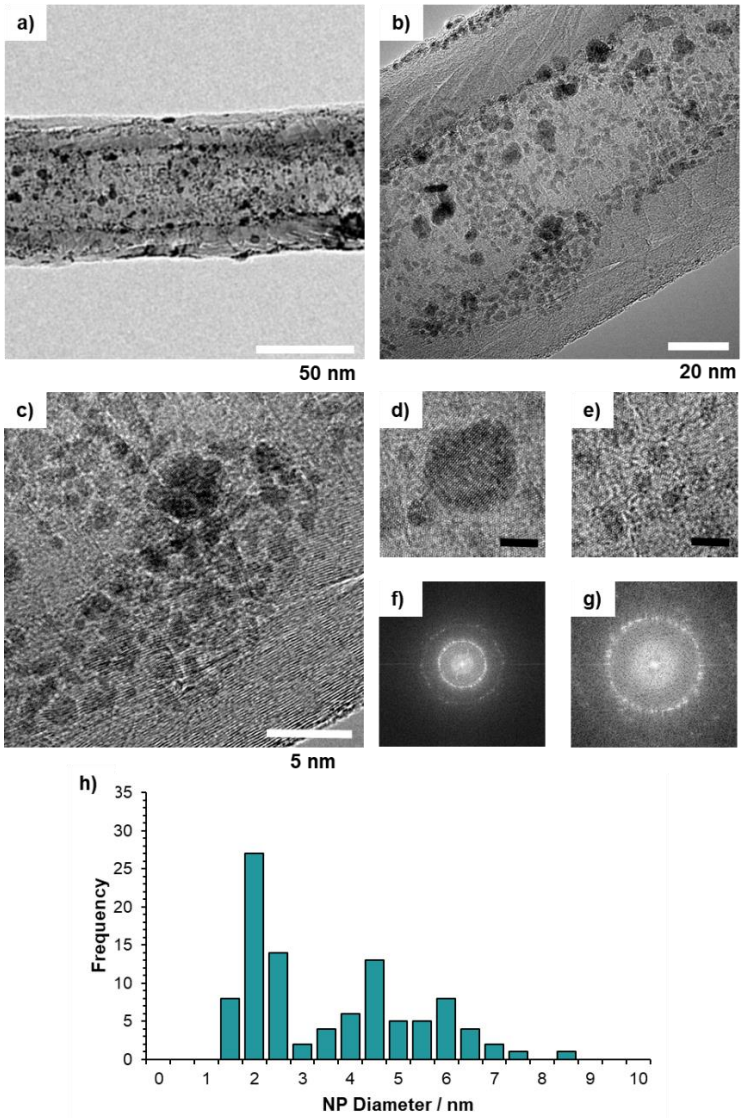

Figure 2.7: a-e) HRTEM micrographs of $Ru_{0.5}Ni_{0.5}$NPs@GNFs fabricated using a concerted addition method; f-g) Fourier transforms of micrographs d and e; and h) particle size distribution showing the average size of the MNPs to be 3.4 ± 1.7 nm. Black scale bar: 2 nm.

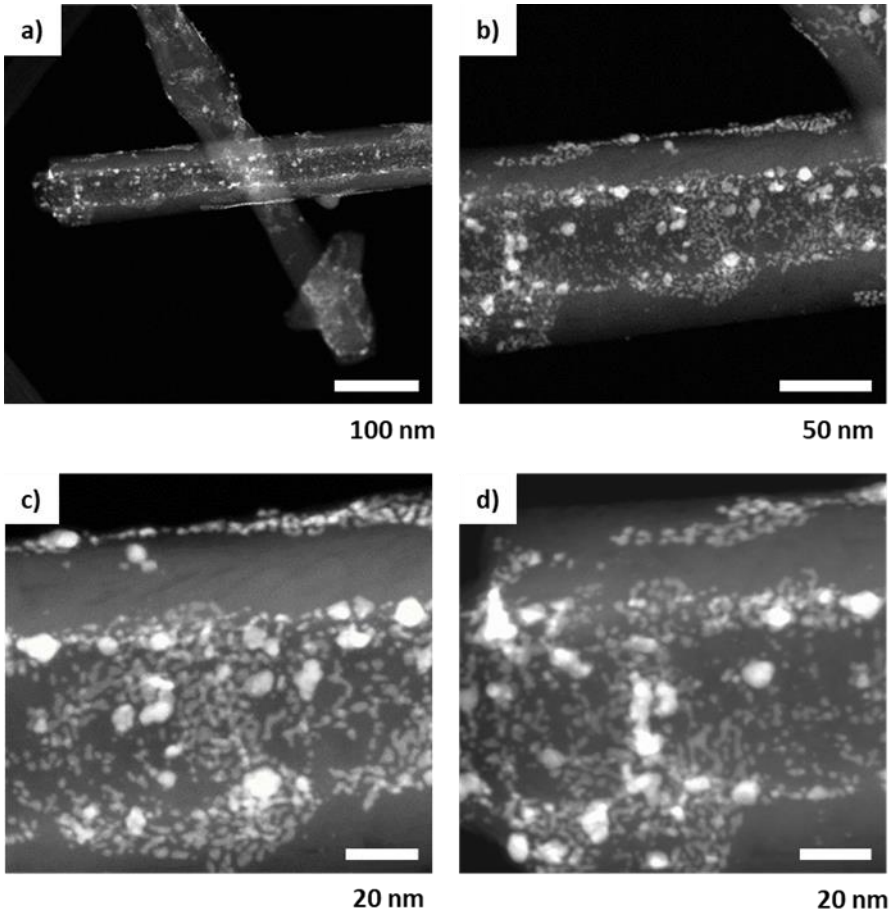

Figure 2.8: a-d) STEM micrographs of $Ru_{0.5}Ni_{0.5}$NPs@GNFs fabricated using a concerted addition approach showing the general structure of the material i.e. location of the NPs within the support structure.

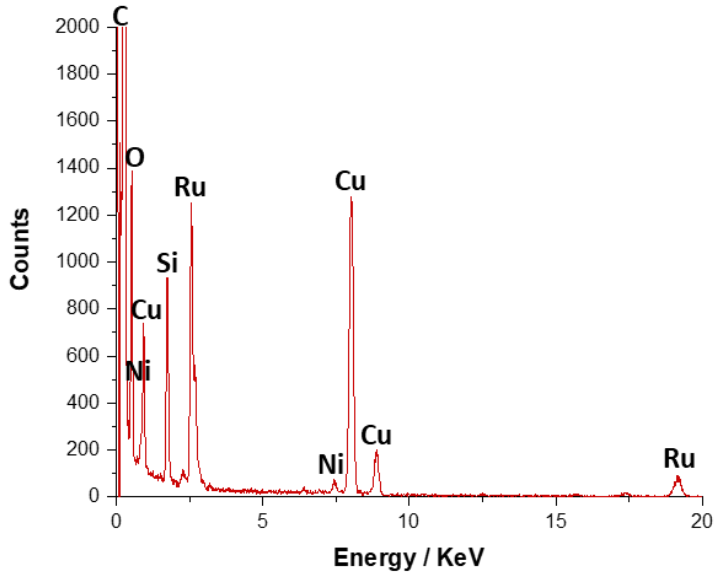

Figure 2.9: EDX spectrum of RuNiNPs formed by the thermal decomposition of $Ru_3(CO)_{12}$ and $NiCp_2$ in GNFs. Characteristic peaks of Ru were identified at 2.6 and 19.2 KeV and characteristic peaks of Ni were identified at 0.9 and 7.5 KeV. Cu peaks are due to the TEM grid used.

EDX spectroscopy was employed to determine the composition of the NPs formed. Characteristic peaks of Ru where identified at 2.6 and 19.2 KeV and characteristic peaks of Ni were identified at 0.9 and 7.5 KeV, confirming their presence in the NPs formed (Figure 2.9).

TGA was employed to determine the metal loading of the material. TGA gave an accurate metal loading of 3.4% (Figure 2.10).

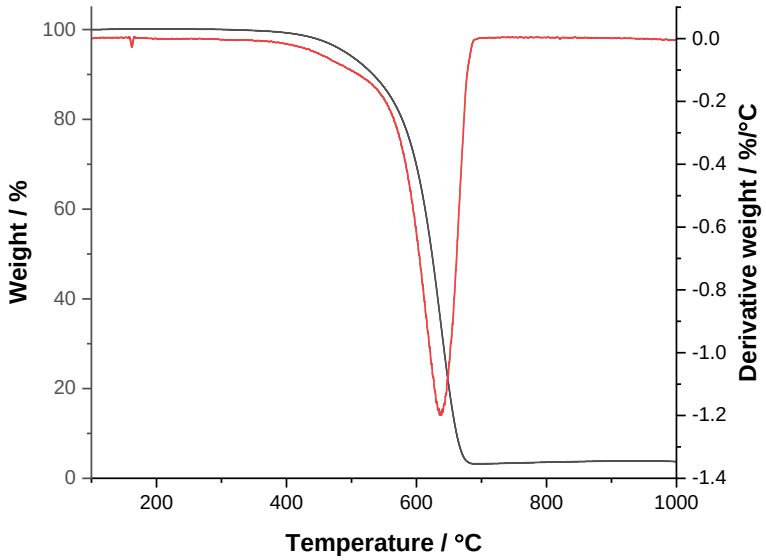

Figure 2.10: TGA plot (black), and corresponding derivative (red), of $Ru_{0.5}Ni_{0.5}$NPs@GNFs (concerted addition) showing the residual weight remaining after GNF combustion.

2.2.1.2.2 Sequential Addition (Ru added 1st)

HRTEM (Figure 2.11) and STEM (Figure 2.12) were employed to quantify the size, shape and location of the NPs within the GNFs. Quantitative size analysis was performed by measuring the diameter of a statistically relevant number of different nanoparticles (>100 samples) from different regions of the TEM sample grid and revealed the average size of the MNPs to be 5.1 ± 1.7 nm.

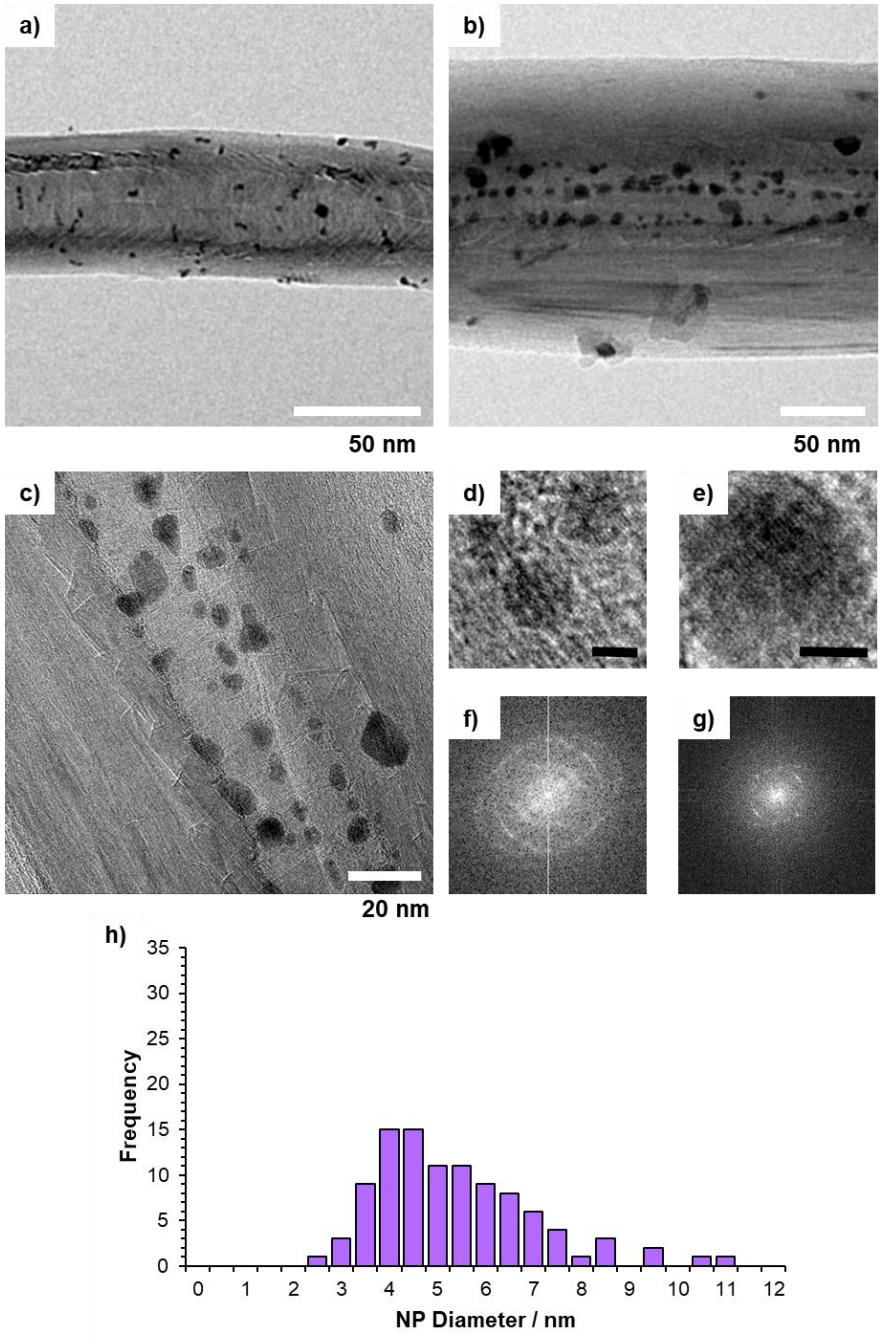

Figure 2.11: a-e) HRTEM micrographs of $Ru_{0.5}Ni_{0.5}$NPs@GNFs fabricated using a sequential addition method in which the ruthenium metal precursor is added and decomposed before the addition of the nickel precursor; f-g) Fourier transforms of micrographs d and e; and h) particle size distribution showing the average size of the MNPs to be 5.1 ± 1.7 nm. Black scale bar: 2 nm.

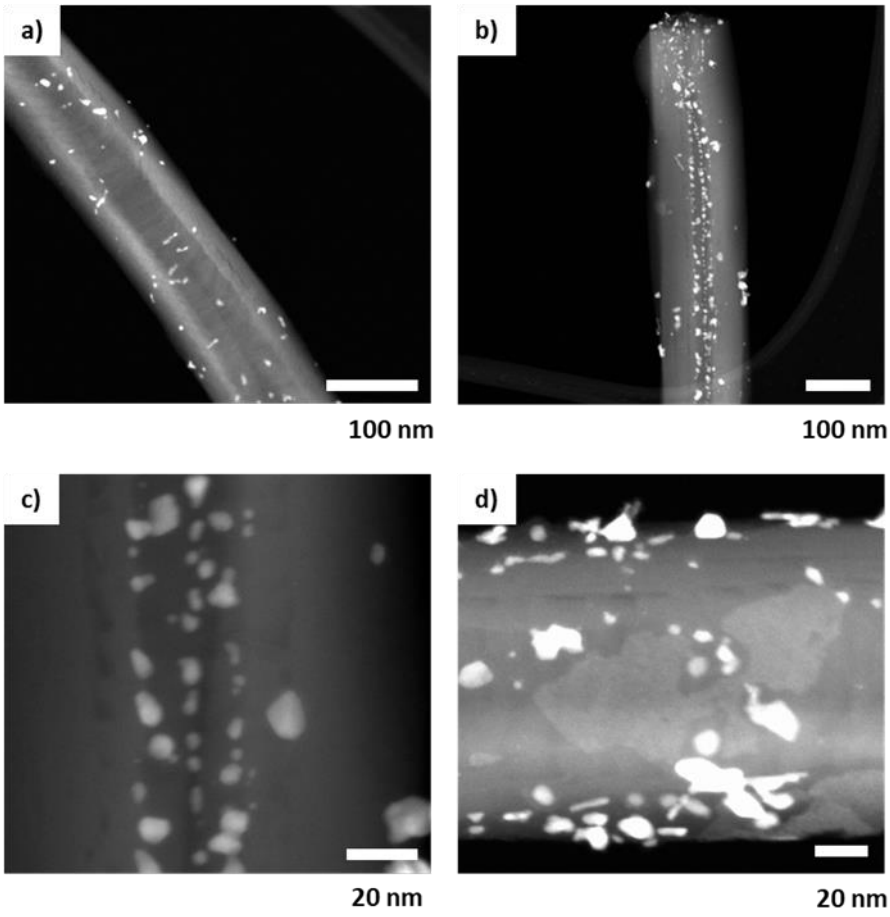

Figure 2.12: a-c) STEM micrographs of $Ru_{0.5}Ni_{0.5}$NPs@GNFs fabricated using a sequential addition method in which the ruthenium metal precursor is added and decomposed before the addition of the nickel precursor showing that the majority of the MNPs are located within the interior channels of the GNFs; and d) STEM micrograph showing a pale grey structure on the outer surface on the GNF support not visible in HRTEM.

EDX spectroscopy was employed to determine the composition of the NPs formed. Characteristic peaks of Ru where identified at 2.6 and 19.2 KeV and characteristic peaks of Ni were identified at 0.9 and 7.5 KeV, confirming their presence in the NPs formed (Figure 2.13).

TGA was employed to determine the metal loading of the material. TGA gave an accurate metal loading of 13.1% (Figure 2.14).

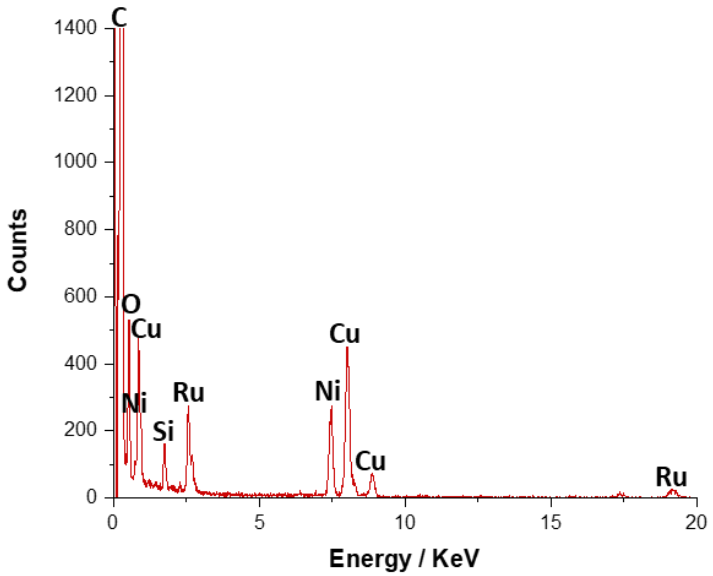

Figure 2.13: EDX spectrum of RuNiNPs formed by the thermal decomposition of $Ru_3(CO)_{12}$ and $NiCp_2$ in GNFs. Characteristic peaks of Ru were identified at 2.6 and 19.2 KeV and characteristic peaks of Ni were identified at 0.9 and 7.5 KeV. Cu peaks are due to the TEM grid used.

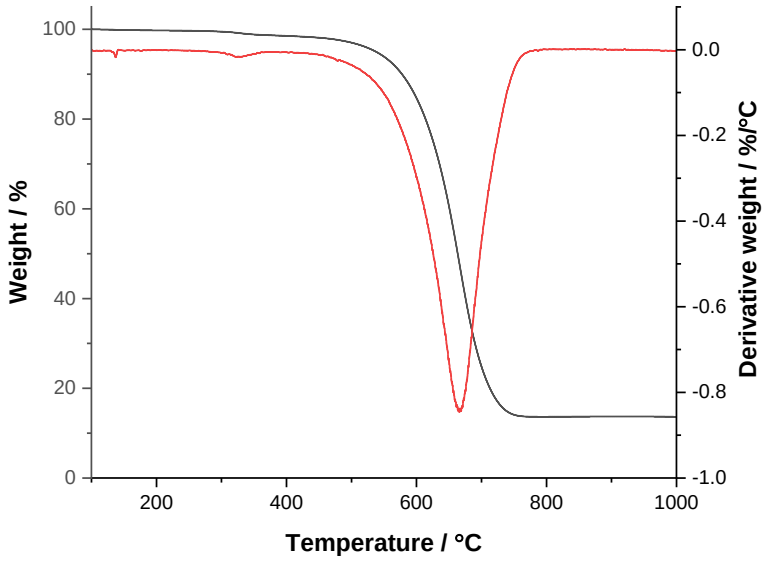

Figure 2.14: TGA plot (black), and corresponding derivative (red), of $Ru_{0.5}Ni_{0.5}$NPs@GNFs (sequential addition, Ru 1st) showing the residual weight remaining after GNF combustion.

2.2.1.2.3 Sequential Addition (Ni added 1st)

HRTEM (Figure 2.15) and STEM (Figure 2.16) were employed to quantify the size, shape and location of the NPs within the GNFs. Quantitative size analysis was performed by measuring the diameter of a statistically relevant number of different nanoparticles (>100 samples) from different regions of the TEM sample grid and revealed the average size of the MNPs to be 2.1 ± 1.5 nm.

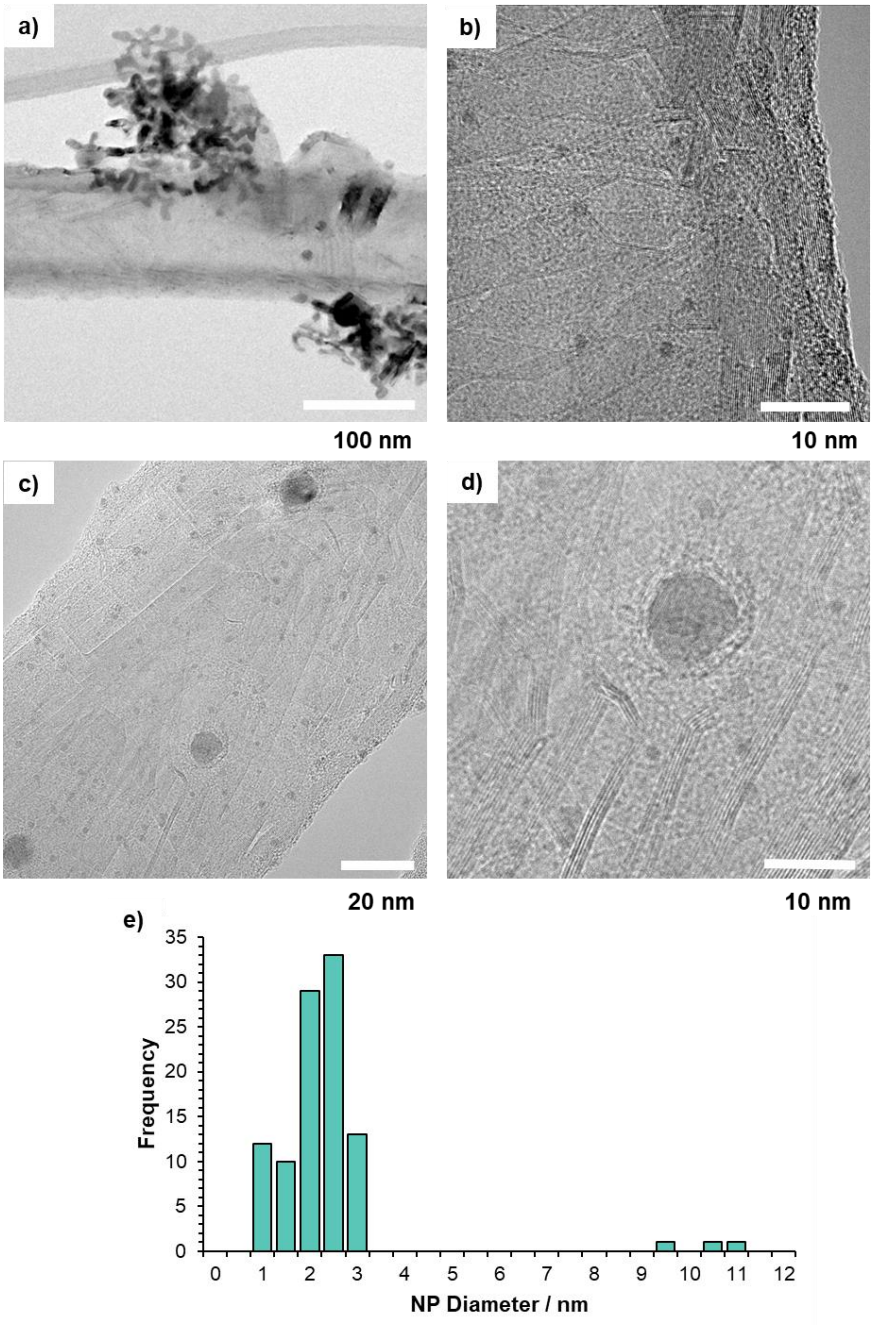

Figure 2.15: a-d) HRTEM micrographs of $Ru_{0.5}Ni_{0.5}$NPs@GNFs fabricated using a sequential addition method in which the nickel metal precursor is added and decomposed before the addition of the ruthenium precursor and e) particle size distribution of the MNPs showing the average size to be 2.1 ± 1.5 nm.

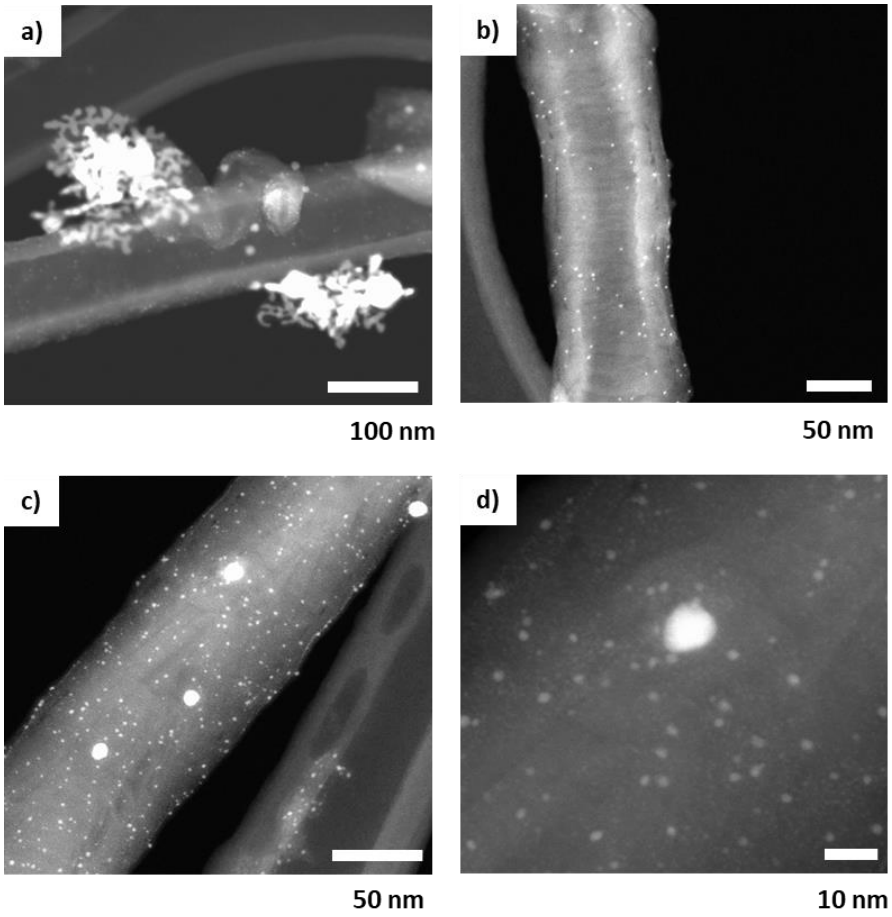

Figure 2.16 STEM micrographs of $Ru_{0.5}Ni_{0.5}$NPs@GNFs fabricated using a sequential addition method in which the nickel metal precursor is added and decomposed before the addition of the ruthenium precursor showing; a) large structures on the exterior of the GNF support; b) small nanoparticles located primarily on the interior of the GNF; and c-d) nanoparticles of two distinct sizes located on the exterior of the GNFs.

EDX spectroscopy was employed to determine the composition of the NPs formed. Characteristic peaks of Ru where identified at 2.6 and 19.2 KeV and characteristic peaks of Ni were identified at 0.9 and 7.5 KeV, confirming their presence in the NPs formed (Figure 2.17).

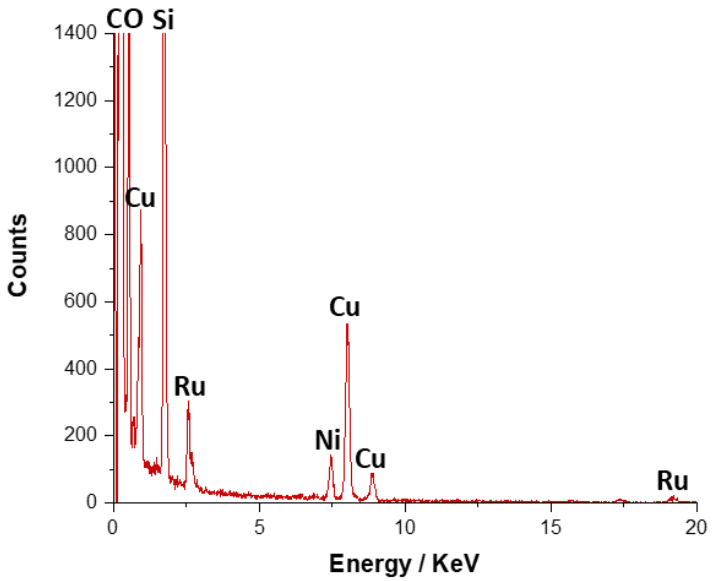

Figure 2.17: EDX spectrum of RuNiNPs formed by the thermal decomposition of $Ru_3(CO)_{12}$ and $NiCp_2$ in GNFs. Characteristic peaks of Ru were identified at 2.6 and 19.2 KeV and characteristic peaks of Ni were identified at 0.9 and 7.5 KeV. Cu peaks are due to the TEM grid used.

TGA was employed to determine the metal loading of the material. TGA gave an accurate metal loading of 8.4% (Figure 2.18).

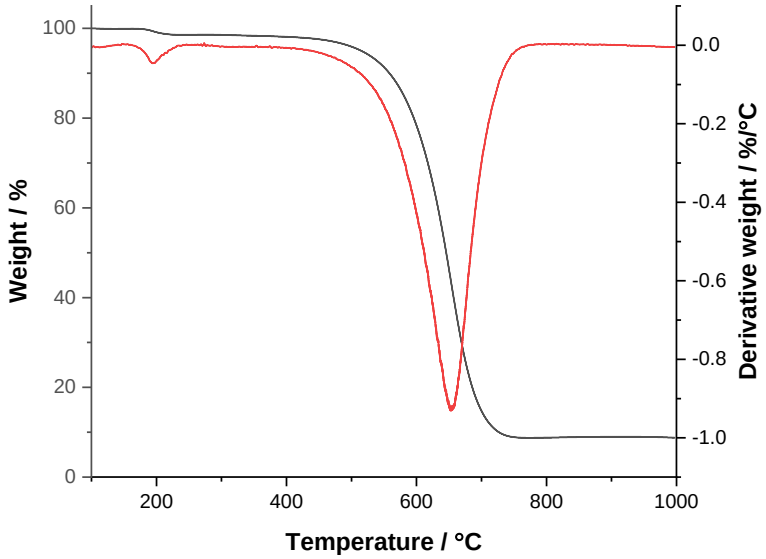

Figure 2.18: TGA plot (black), and corresponding derivative (red), of $Ru_{0.5}Ni_{0.5}$NPs@GNFs (sequential addition, Ni 1st) showing the residual weight remaining after GNF combustion.

2.2.1.3 Characterisation of RuNiNPs@GNFs with Differing Ratios of Ru:Ni

2.2.1.3.1 $Ru_{0.75}Ni_{0.25}$NPs@GNFs [Ru:Ni, 3:1]

TEM was employed to quantify the size, shape and location of the NPs within the GNFs for $Ru_{0.75}Ni_{0.25}$NPs@GNFs (5% by wt. total metal). The MNPs were predominately located at the step edges of the GNFs (Figure 2.19). Quantitative size analysis was performed by measuring the diameter of a statistically relevant number of different nanoparticles (>100 samples) from different regions of the TEM sample grid and revealed the average size of the MNPs to be 6.0 ± 1.1 nm.

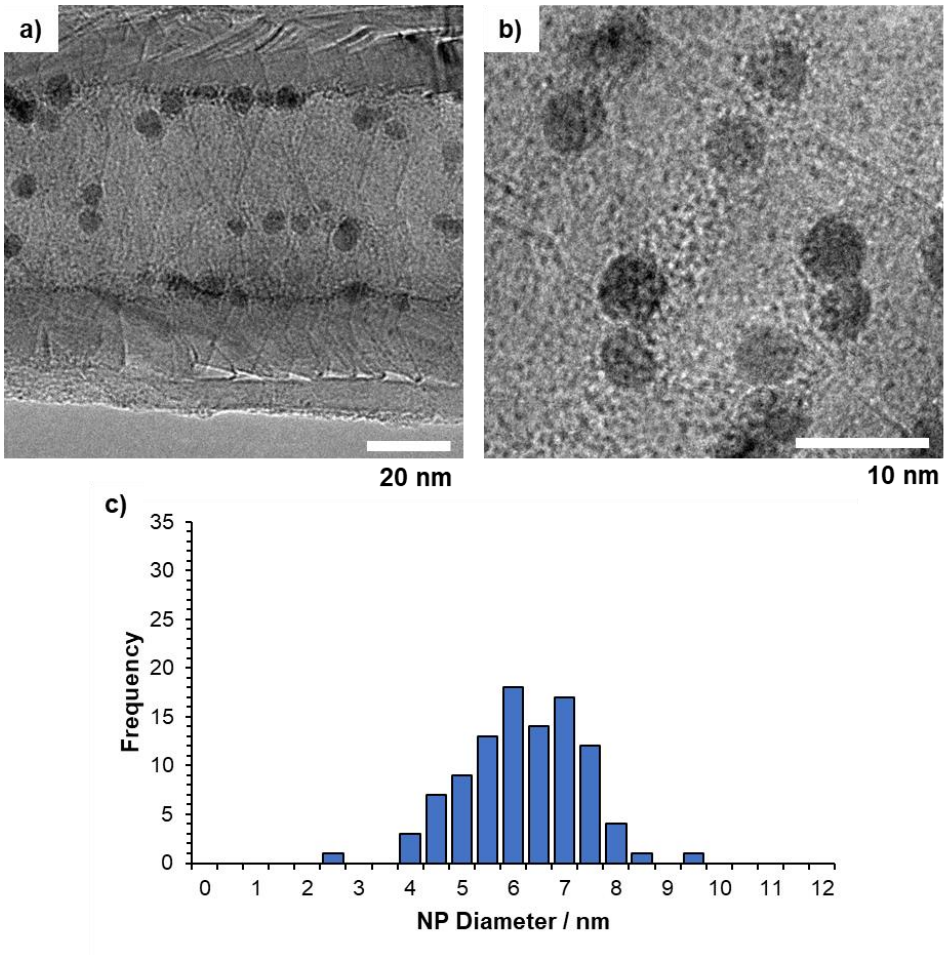

Figure 2.19: a) and b) TEM micrographs of $Ru_{0.75}Ni_{0.25}$NPs@GNFs (5 wt.% total metal) showing the general structure, size, distribution, and location of the MNPs; and c) particle size distribution showing the average size of the MNPs to be 6.0 ± 1.1 nm.

EDX spectroscopy was employed to determine the composition of the NPs formed. Characteristic peaks of Ru where identified at 2.6 and 19.2 KeV and characteristic peaks of Ni were identified at 0.9 and 7.5 KeV, confirming their presence in the NPs formed (Figure 2.20).

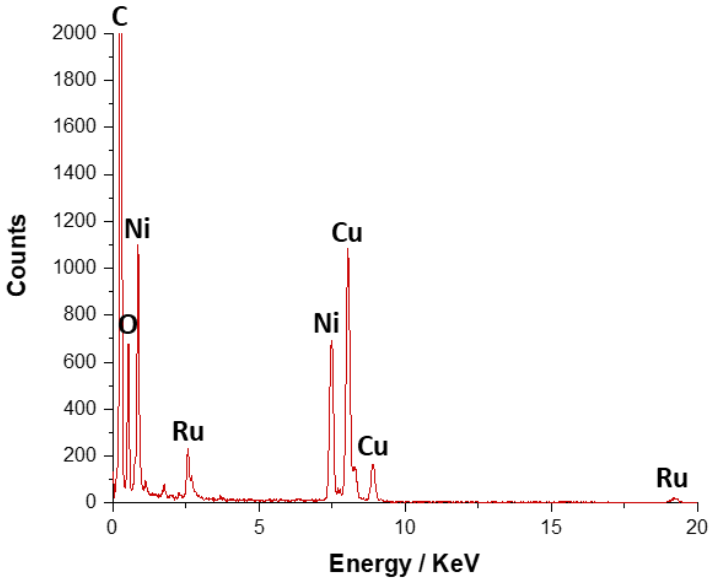

Figure 2.20: EDX spectrum of RuNiNPs formed by the thermal decomposition of $Ru_3(CO)_{12}$ and $NiCp_2$ in GNFs. Characteristic peaks of Ru were identified at 2.6 and 19.2 KeV and characteristic peaks of Ni were identified at 0.9 and 7.5 KeV. Cu peaks are due to the TEM grid used.

TGA was employed to determine the metal loading of the material. TGA gave an accurate metal loading of 3.8% (Figure 2.21).

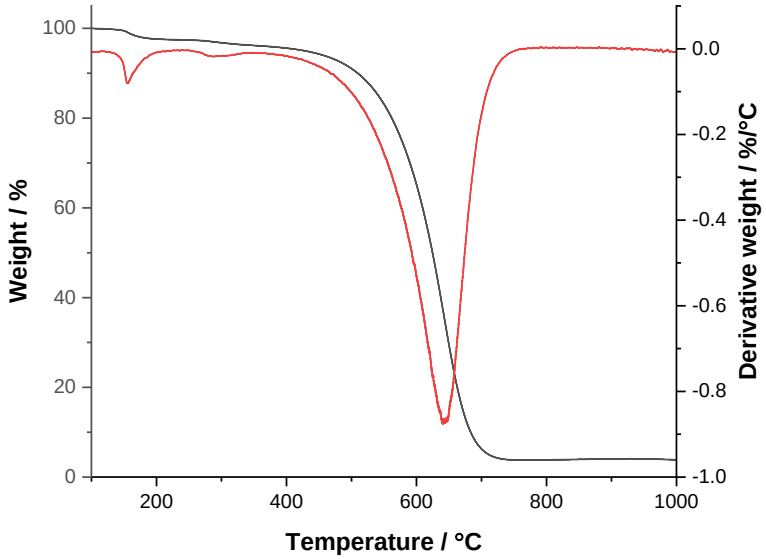

Figure 2.21: TGA plot (black), and corresponding derivative (red), of $Ru_{0.25}Ni_{0.75}$NPs@GNFs (5 wt.% total metal) showing the residual weight remaining after GNF combustion.

The derivative weight plot shows a distinctive peak at ca. 200 °C, this could be due to the decomposition of previously unreacted metal precursor. As this

peak is not present for RuNPs@GNFs it is probably caused by the decomposition of $NiCp_2$.

2.2.1.3.2 $Ru_{0.25}Ni_{0.75}$NPs@GNFs [Ru:Ni, 1:3]

TEM was employed to quantify the size, shape and location of the NPs within the GNFs for $Ru_{0.25}Ni_{0.75}$NPs@GNFs (5% by wt. total metal). The location of the MNPs were predominately located at the step edges of the GNFs (Figure 2.22). Quantitative size analysis was performed by measuring the diameter of a statistically relevant number of different nanoparticles (>100 samples) from different regions of the TEM sample grid and revealed the average size of the MNPs to be 4.0 ± 1.5 nm.

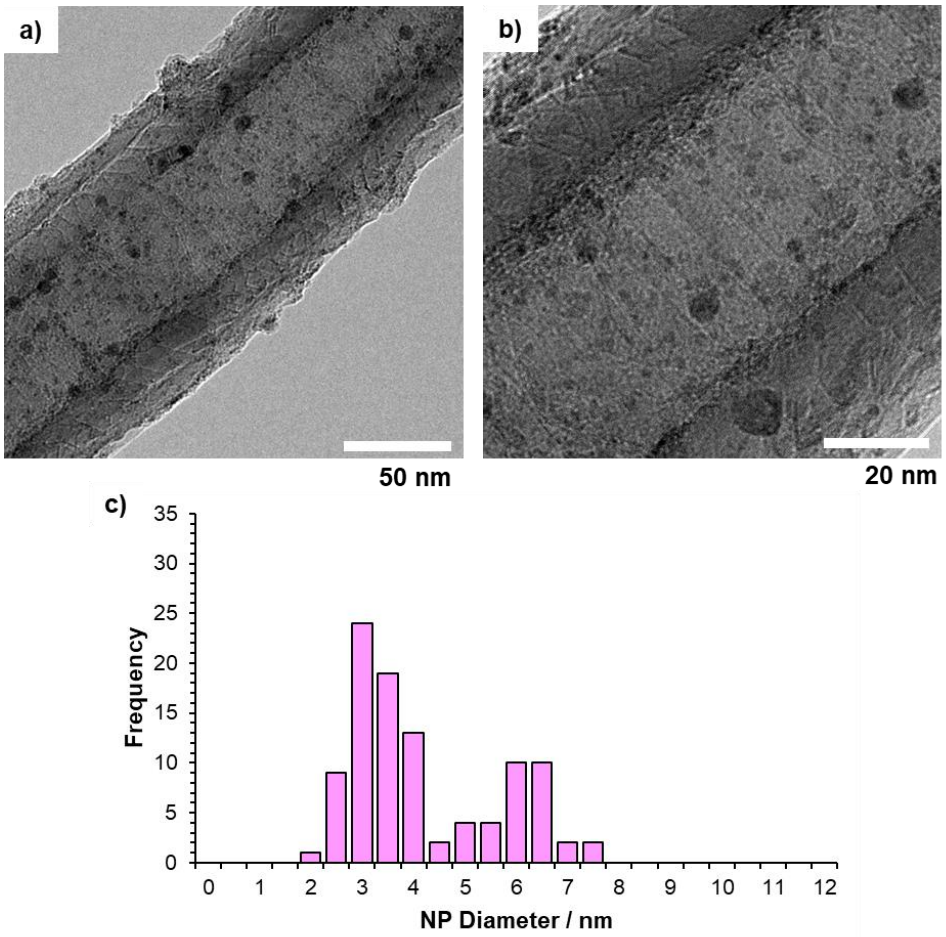

Figure 2.22: a) and b) TEM micrographs of $Ru_{0.25}Ni_{0.75}$NPs@GNFs (5 wt.% total metal) showing the general structure, size, distribution, and location of the MNPs; and c) particle size distribution showing the average size of the MNPs to be 4.0 ± 1.5 nm.

EDX spectroscopy was employed to determine the composition of the NPs formed. Characteristic peaks of Ru where identified at 2.6 and 19.2 KeV and characteristic peaks of Ni were identified at 0.9 and 7.5 KeV, confirming their presence in the NPs formed (Figure 2.23).

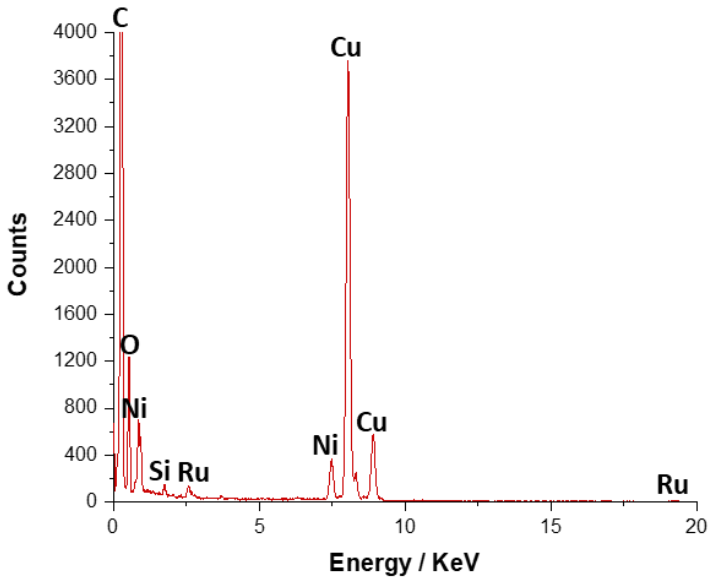

Figure 2.23: EDX spectrum of RuNiNPs formed by the thermal decomposition of $Ru_3(CO)_{12}$ and $NiCp_2$ in GNFs. Characteristic peaks of Ru were identified at 2.6 and 19.2 KeV and characteristic peaks of Ni were identified at 0.9 and 7.5 KeV. Cu peaks are due to the TEM grid used.

TGA was employed to determine the metal loading of the material. TGA gave an accurate metal loading of 5.1% (Figure 2.24).

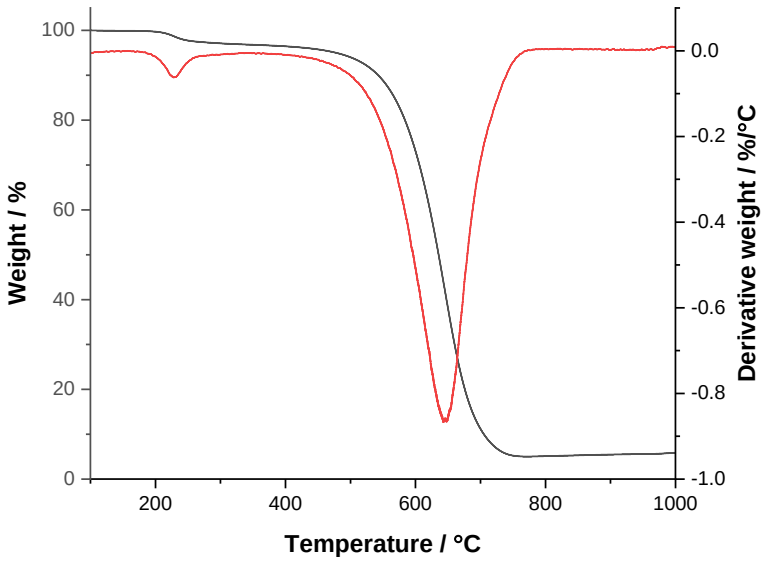

Figure 2.24: TGA plot (black), and corresponding derivative (red), of $Ru_{0.25}Ni_{0.75}$NPs@GNFs (5 wt.% total metal) showing the residual weight remaining after GNF combustion.

The derivative weight plot also shows a distinctive peak at ca. 200 °C. As mentioned previously, this could be due to the decomposition of previously unreacted metal precursor.

2.2.1.3.3 NiNPs@GNFs

TEM was employed to quantify the size, shape and location of the NPs within the nanofibers for NiNPs@GNFs (5 wt.%). The location of the MNPs were predominately located at the step edges of the GNFs with some MNPs on the exterior (Figure 2.25).Quantitative size analysis was performed on the NiNPs located with the support structure by measuring the diameter of a statistically relevant number of different nanoparticles (>100 samples) from different regions of the TEM sample grid and revealed the average size of the MNPs to be 6.1 ± 2.2 nm.

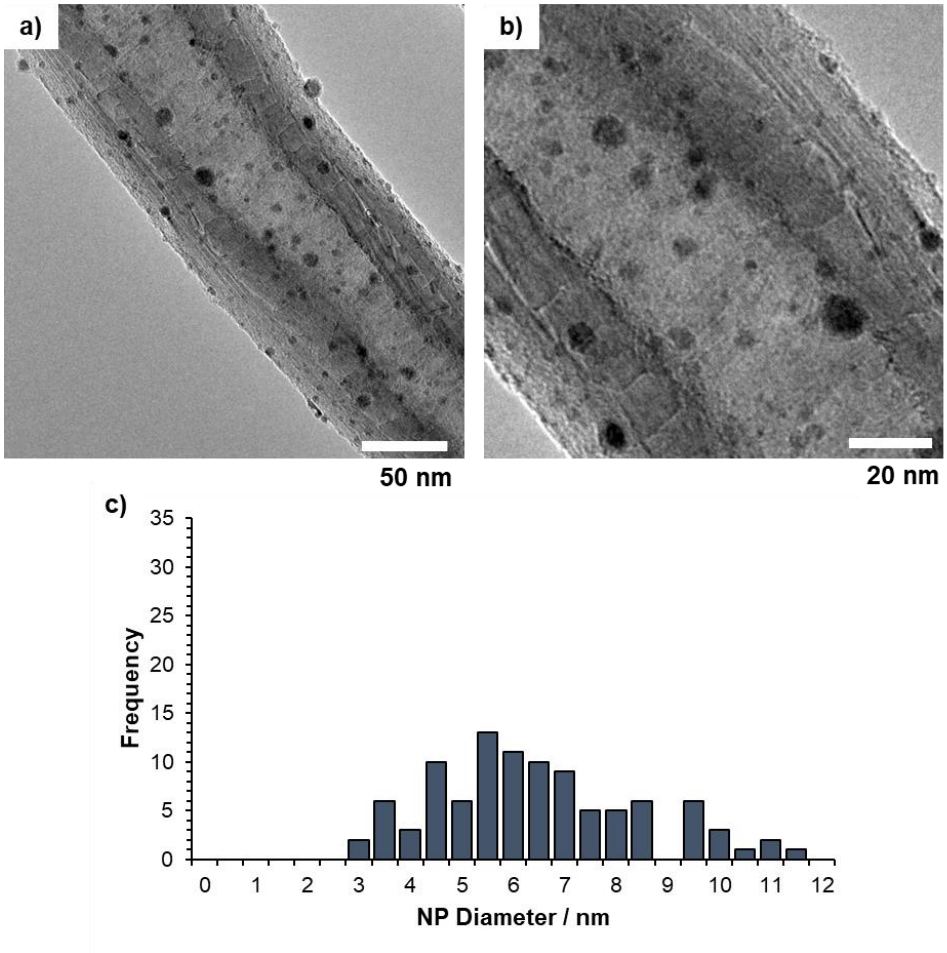

Figure 2.25: a) and b) TEM micrographs of NiNPs@GNFs (5 wt.%) showing the general structure, size, distribution, and location of the MNPs; and c) particle size distribution showing the average size of the MNPs to be 6.1 ± 2.2 nm.

EDX spectroscopy showed characteristic peaks of Ni at 0.9 and 7.5 KeV confirming the composition of the NPs formed in the GNFs (Figure 2.26).

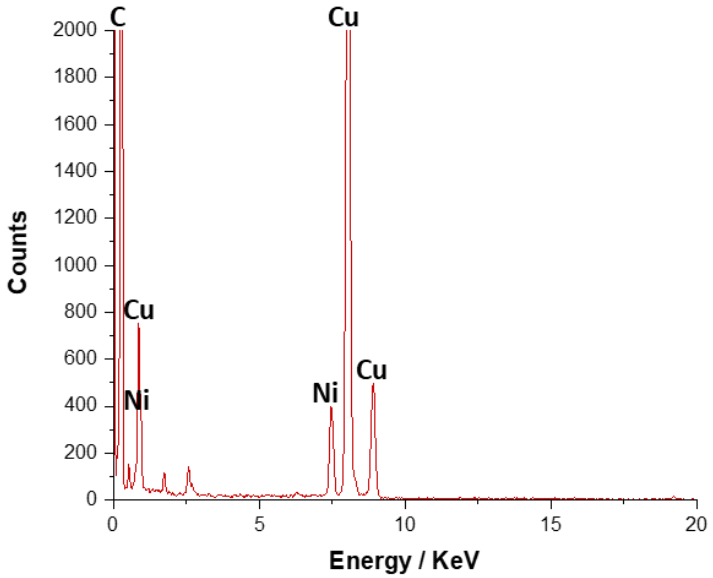

Figure 2.26: EDX spectrum of NiNPs formed by the thermal decomposition of $NiCp_2$ in GNFs. Characteristic peaks of Ni were identified at 0.9 and 7.5 KeV. Cu peaks are due to the TEM grid used.

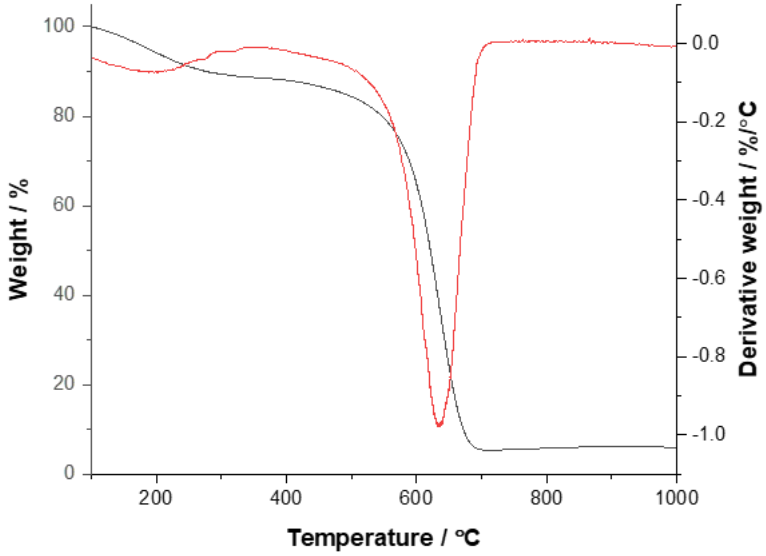

Figure 2.27: TGA plot (black), and corresponding derivative (red), of NiNPs@GNFs (5 wt.%) showing the residual weight remaining after GNF combustion.

TGA was employed to determine the metal loading of the material. TGA gave an accurate metal loading of 4.3% (Figure 2.27).

2.2.3 Discussion

In this section the results of the different fabrication approaches and the effect imposed on the resultant materials are discussed and compared.

2.2.3.1 Effects of Varying Metal Loading

HRTEM revealed that the average diameter of the RuNPs was found to be 1.9 ± 0.5, 3.3 ± 0.7, 4.2 ± 1.2 and 6.6 ± 2.3 nm for RuNPs@GNFs (1 wt.%), RuNPs@GNFs (2 wt.%), RuNPs@GNFs (5 wt.%), and RuNPs@GNFs (10 wt.%), respectively (see Table 2.3).

Table 2.3: Summary of the RuNPs@GNF materials fabricated with differing metal loadings and their corresponding average NP diameters determined from TEM.

Metal loading	Average NP Diameter / nm
1 wt.%	1.9 ± 0.5
2 wt.%	3.3 ± 0.7
5 wt.%	4.2 ± 1.2
10 wt.%	6.6 ± 2.3

Interestingly, there is an increase in nanoparticle size as the % wt. of Ru metal increases (highlighted in Figure 2.28). This implies that the nanoparticles undergo the same initial nucleation step, *i.e.* the same number of seed particles are made in each material, but different growth rates dependent upon the amount of metal available. However, no formal growth mechanism has been reported thus far.

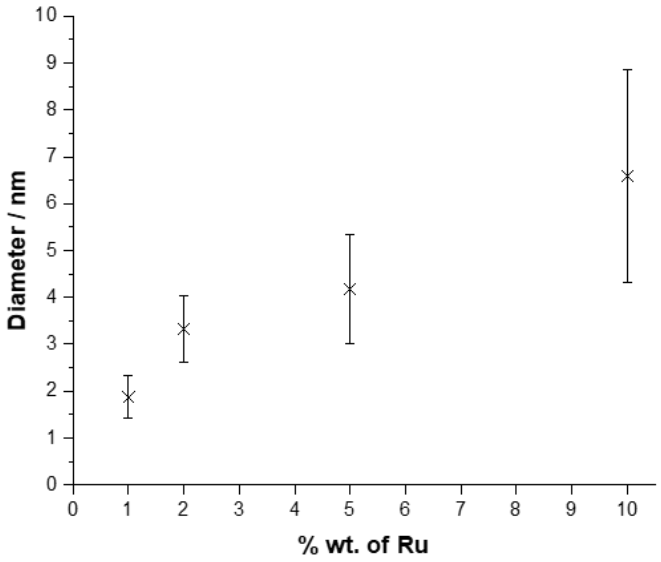

Figure 2.28: Plot of RuNP diameter against the % wt. of Ru metal in each material showing that increasing the amount of metal precursor present increases the size of the RuNPs formed.

The effect of the amount of nucleation centres present on eventual average particle size of a sample has been previously investigated. Wilde and co-workers,[40] reported that for the same initial amount of metal precursor present, for the formation of RhNPs, changes in the formation of the RhNPs i.e. differing sizes, can be observed when the number of nucleation sites changes increased, i.e. more initial nucleation sites led to smaller RhNPs.[40] Therefore, if more nucleation sites were present at higher loadings of Ru the precursor would distribute over this higher number of nucleation sites, and if evenly distributed, large numbers of smaller particles, on average, would be obtained.

In the case of RuNPs@GNFs (1 wt.%) the nanoparticles are aligned along the step edges of the GNFs in well-defined lines and appear to be uniformly distributed throughout the sample (Figure 2.2). In contrast to this, at higher metal loadings, although the majority of the RuNPs are located at the step edges, their arrangement is less uniform. This suggests that using a lower wt.% of metal results in a more well-defined structure with a more controlled distribution of RuNPs, as the Ru precursor preferentially immobilises at the step edges first due to increased interactions between $Ru_3(CO)_{12}$ and the GNF, before spilling over and being distributed elsewhere. Solomonsz *et al.*,[4] reported encapsulated RhNPs residing preferentially at the internal step edges of the GNFs which was attributed to increased van der Waals interactions between the RhNPs and the internal surface of the GNFs.[4]

Powder X-ray diffraction (XRD) was employed to study the crystallinity of the RuNPs present in RuNPs@GNFs (with differing wt.% of Ru). Figure 2.29 shows the XRD pattern obtained for RuNPs@GNFs (5 wt.%) compared to that obtained for a standard GNF sample and a metallic Ru reference pattern.

The diffraction pattern for GNFs has been previously reported and the peaks observed for graphite can be assigned as follows; 2θ = 42° (100), 44° (101), 49° (102), 54° (104), 66° (103), and 77° (110).[41] From Figure 2.29 the peak at 2θ = 38° (for RuNPs@GNFs(5 wt.%)) can be assigned to Ru(100)[42] suggesting that the metallic RuNPs adopt an hexagonally close packed structure. Additionally, the peak at 2θ = 69° can be assigned to Ru(110);[42] however, this peak isn't as prominent. From the Ru reference pattern other peaks at 2θ = 43°, 44°, 58° and 79° are expected for metallic Ru. However, these are not seen in RuNPs@GNFs (5 wt.%) due the GNF peaks overlapping those expected for metallic RuNPs.

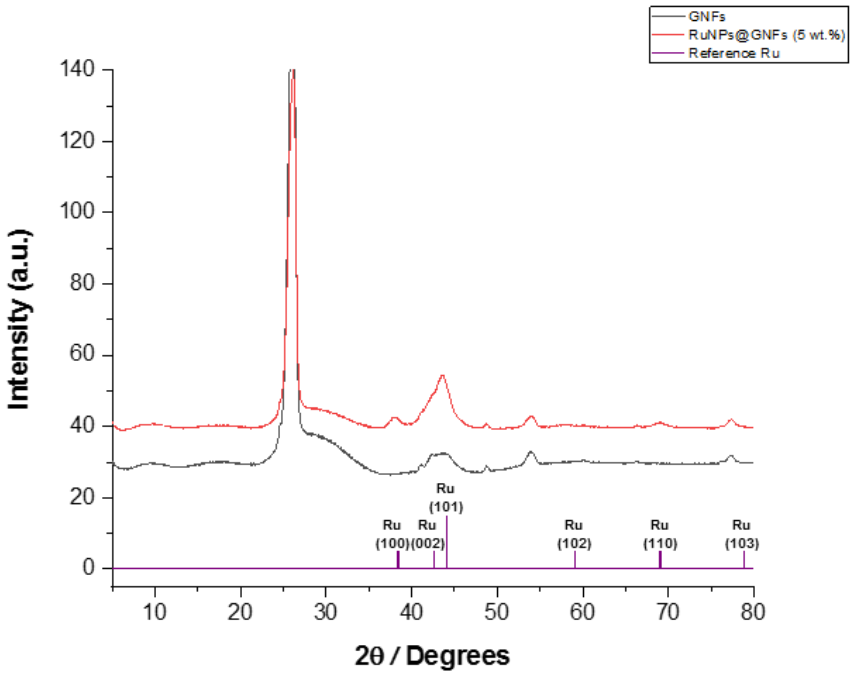

Figure 2.29: Powder XRD pattern for RuNPs@GNFs (5% by wt. Ru) compared to that obtained for GNFs and reference Ru pattern.[42]

The particle size of RuNPs was calculated from the XRD patterns obtained for RuNPs@GNFs (1, 2, 5 and 10 wt.%), see Figure 2.30, using the Scherrer equation and compared to the average MNP diameter obtained from TEM (summarised in Table 2.4). From Table 2.4 it is clear that the average diameter determined by XRD for RuNPs across the series of materials is in good agreement with those obtained from TEM (within the error for each material).

Table 2.4: Comparison of average RuNP particle size determined by TEM and powder XRD across the series of RuNPs@GNFs (1, 2, 5 and 10 wt.%).

Metal loading	NP Diameter from TEM / nm	NP Diameter from XRD[a] / nm
1 wt.%	1.9 ± 0.5	2.0 ± 0.6
2 wt.%	3.3 ± 0.7	4.2 ± 1.4
5 wt.%	4.2 ± 1.2	4.5 ± 0.3
10 wt.%	6.6 ± 2.3	6.6 ± 0.3

[a] Error calculated from the particle sizes given from the Scherrer equation.

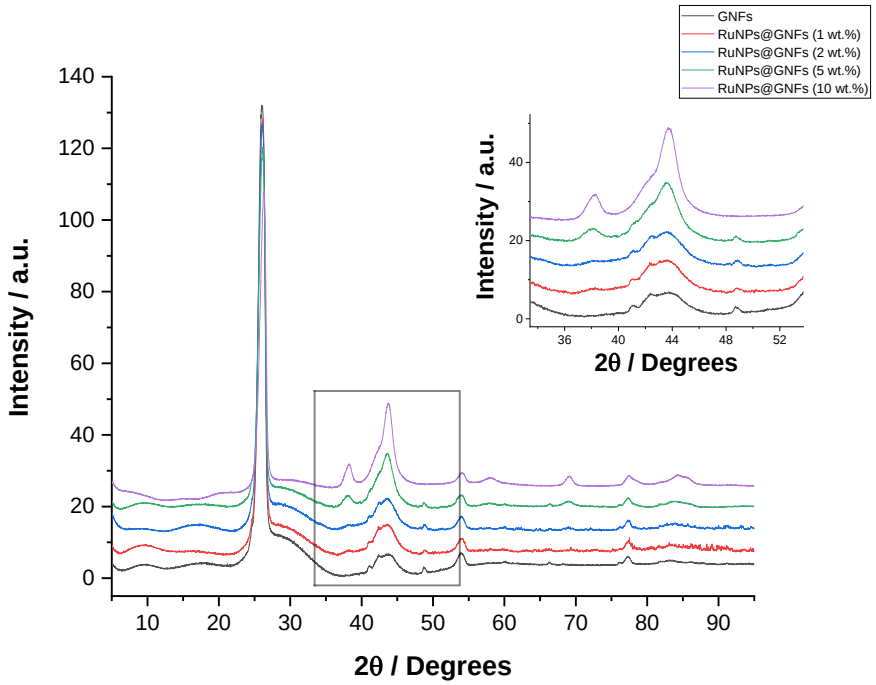

Figure 2.30: Powder XRD patterns for RuNPs@GNFs (1, 2, 5 and 10 wt.%) compared to GNFs (annealed at 450 °C for 3 h). Enlargement shows peak at 2θ = 38° assigned to Ru(100).

2.2.3.2. Effects of Varying the Decomposition Temperature

As the size of RuNPs can greatly affect their activity, further insight into the growth mechanism at different wt.% of Ru is required to determine whether control over size can be achieved using this facile fabrication methodology. To gain understanding of how the fabrication method can affect the structure of resultant materials, the synthesis of RuNPs@GNFs (2 wt.%) was carried out at varying decomposition temperatures to ascertain whether the formation of the NPs was affected. The decomposition temperatures and resultant RuNP diameters are summarised in Table 2.5 and Figure 2.31a. No substantial change in particle size with decomposition temperature is observed suggesting that the size and shape of the GNF step-edges control particle growth via templating. As well as this it also indicates that the material is stable up-to 700 °C, with is an important parameter to consider when looking at these materials for use in heterogeneous catalysis. The templating/stabilising effects of the step-edges within GNFs has been previously proposed by La Torre *et al.*,[31] who studied the growth of AuNP located on the interior/exterior of the GNF support structure. They reported that, under heat treatment conditions (300 °C, 4 hours), the AuNPs on the interior of the GNFs were stabilised through interactions with the step-edges

and the size of the AuNPs was restricted to approximately 6 nm.[31] The sizes obtained for RuNPs@GNFs in this study also appear to be restricted to approximately 6 nm, with a slight decrease in particle size with increasing decomposition temperature. Although the templating/stabilising effects of the step-edges within GNFs has been previously reported this study extends the temperature range investigated (from 300 to 700 °C) and confirms it can be translated to other MNPs.

Table 2.5: Summary of decomposition temperature used for the fabrication of RuNPs@GNFs (2 wt.%) and the average diameter of the resultant RuNPs showing no obvious relationship between the average diameter and decomposition temperature.

Temperature / °C	RuNP Diameter / nm
200	5.8 ± 2.1
400	4.2 ± 1.0
450	3.3 ± 0.6
500	3.7 ± 1.1
700	3.6 ± 0.6

Although the average RuNP diameter remains mostly unchanged across decomposition temperatures, there is a considerable difference in the standard deviation, with lower temperatures leading to a greater variation in RuNP diameter (see Figure 6 (in section 2.2.1.3)). This could be due to a decrease in decomposition rate (at lower decomposition temperatures) leading to a smaller number of seed particles but the same amount of Ru metal present affording the formation of larger NPs.

As no obvious relationship was observed between the average diameter of the RuNPs formed and the decomposition temperature, the location of the RuNPs within each sample was investigated to determine if this was affected by decomposition temperature. To do this statistical analysis was performed to determine the percentage of RuNPs located within the inner channel of the GNFs compared to the exterior wall. From Figure 2.31b, it is evident that there is no significant increase in the average filling density (i.e. the percentage of MNPs located on the interior of the GNF support structure) with increasing decomposition temperature but a finer variation between individual GNFs is observed, c.f. significantly higher error for the sample prepared at 200 °C.

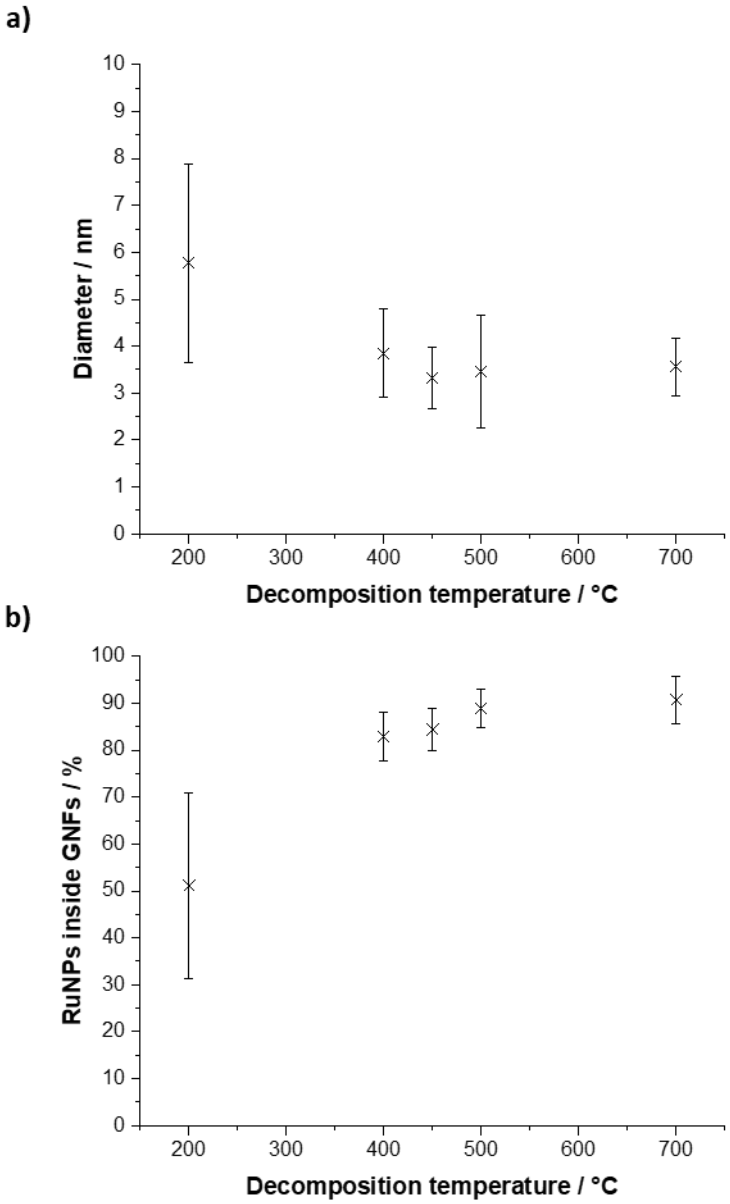

Figure 2.31: a) Plot of decomposition temperature against average RuNP diameter showing no significant change in RuNP diameter with increasing decomposition temperature; and b) plot of decomposition temperature against % of RuNPs inside the GNFs for RuNPs@GNFs (2 wt.%) showing no significant increase in the average filling density with increasing decomposition temperature after the lower value seen at 200 °C.

2.2.3.3 Changing the Addition Sequence for Bimetallic Systems

As mentioned previously, two different approaches can be employed for the fabrication of bimetallic NPs supported within GNFs (see section 2.2.1.1). The fabrication of three bimetallic RuNiNPs@GNFs (5 wt.% total metal) with a Ru:Ni ratio of 1:1 were carried out using the different fabrication methods. HRTEM reveals that simply changing the addition sequence of the metal precursors greatly affects the structure of the resultant materials (Figure 2.32).

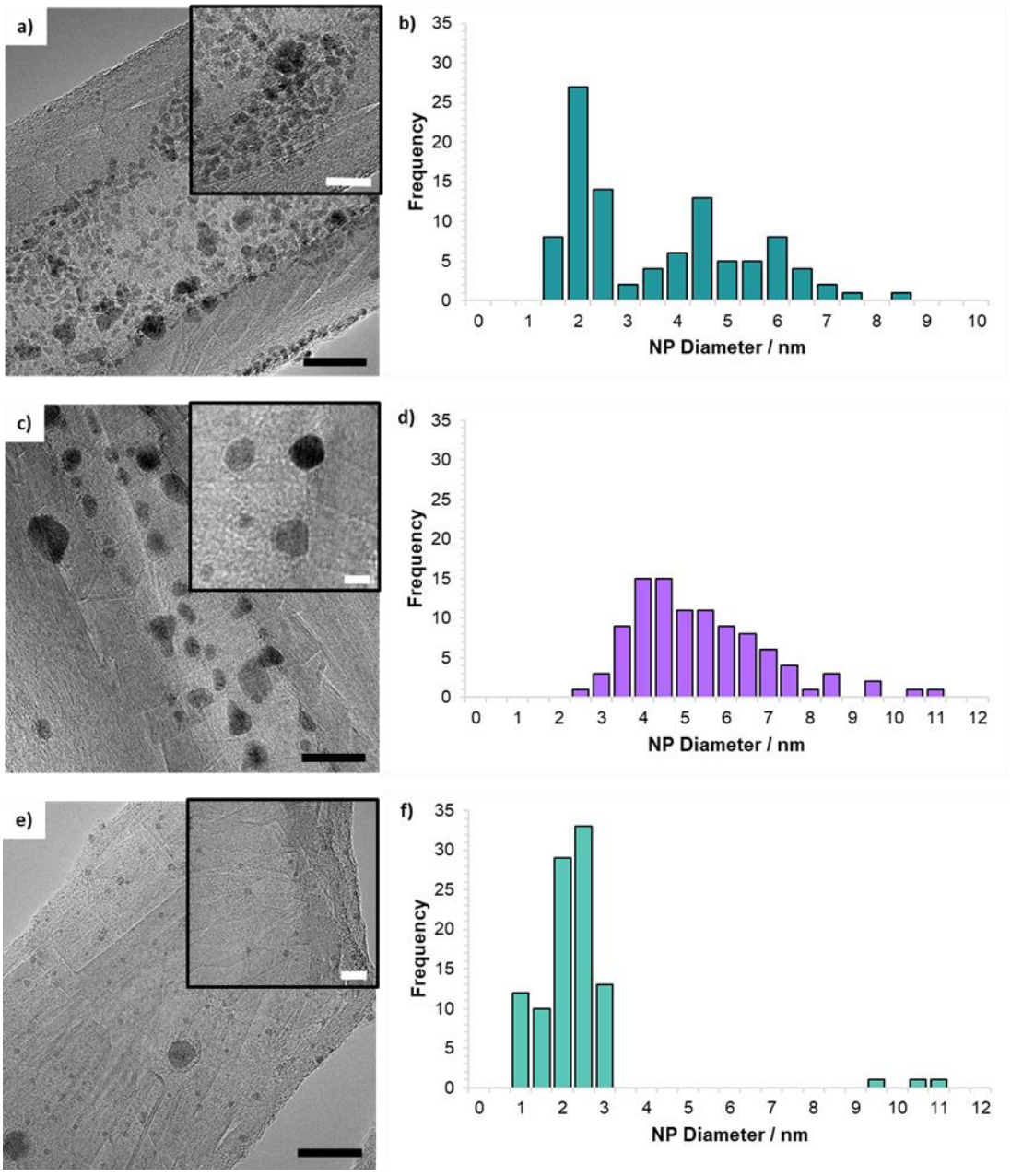

Figure 2.32: Representative HRTEM images of the materials made via a) concerted addition; c) sequential addition (Ru 1st); and e) sequential addition (Ni 1st). b), d), and f) The particle size distributions for each material determined by measuring 100 particles. Mean particle diameters were found to be 3.4 ± 1.7 nm, 5.1 ± 1.7 nm and 2.1 ± 1.5 nm. Black and white scale bars are 20 nm and 5 nm, respectively

The average diameter of the MNPs for the concerted addition, sequential addition (Ru 1st) and sequential addition (Ni 1st) were found to be 3.4 ± 1.7, 5.1 ± 1.7, and 2.1 ± 1.5 nm, respectively. The size distribution for the three materials can be found in Figure 2.32.

Interestingly, the size distribution for the concerted addition material appears to have a binomial distribution potentially indicative of two distinct, differently sized types of NPs (see Figure 2.33). This can be seen in the insert of

Figure 2.32a where there appears to be one larger MNP surrounded my many more, much smaller MNPs. If the binomial distribution is separated into two separate histograms (by measuring the average diameter of the two distinctly different sized MNPs separately) then the average diameter of the smaller and larger MNPs is found to be 1.9 ± 0.3 nm and 5.2 ± 1.3 nm, respectively.

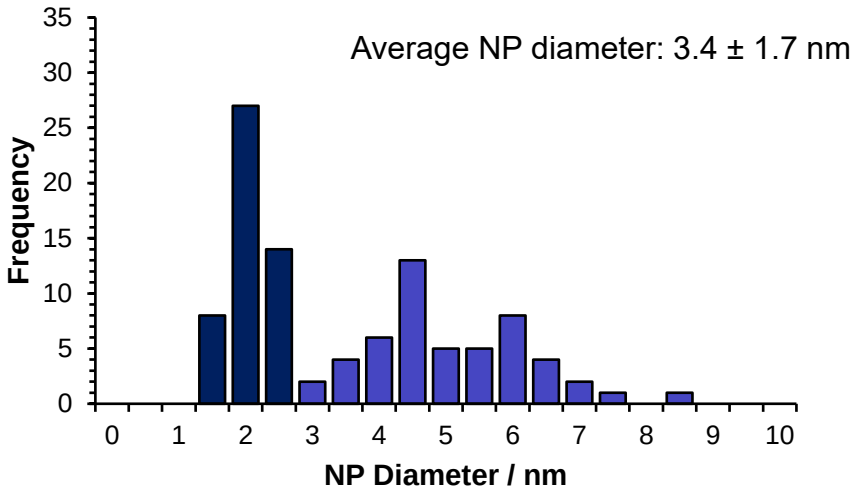

Figure 2.33: NP size distribution for $Ru_{0.5}Ni_{0.5}$NPs@GNFs showing a binomial distribution indicating two different sized NPs present in the sample.

These are comparable to the average sizes obtained for sequential addition (Ru 1st), 5.2 ± 1.3 ≈ 5.1 ± 1.7 nm, and sequential addition (Ni 1st), 1.9 ± 0.3 ≈ 2.1 ± 1.5 nm. This could be due to the different compositions of the MNPs formed in each material. The MNPs of comparable size (~5 nm) present in both the concerted addition material and the sequential addition (Ru 1st) were determined to be mixed metal RuNiNPs or monometallic NiNPs. The MNPs of comparable size (~2 nm) present in both the concerted addition material and the sequential addition (Ni 1st) were found to be monometallic RuNPs in both cases (see below for STEM-EDX of each material).

As mentioned previously, the fabrication methods employed in this study could lead to the formation of three different NP systems i.e. mixed metal alloy NPs, core shell NPs or a mixture of two separate monometallic NPs within the same support structure. STEM-EDX analysis was performed on several GNFs from each sample in order to determine whether the addition sequence influenced the composition of the resultant MNPs. In the case of $Ru_{0.5}Ni_{0.5}$NPs@GNFs (concerted addition) it was found that the MNPs were a mixture of bimetallic MNPs, which can be described as random alloys, and monometallic Ru or NiNPs (see Figure 2.34).

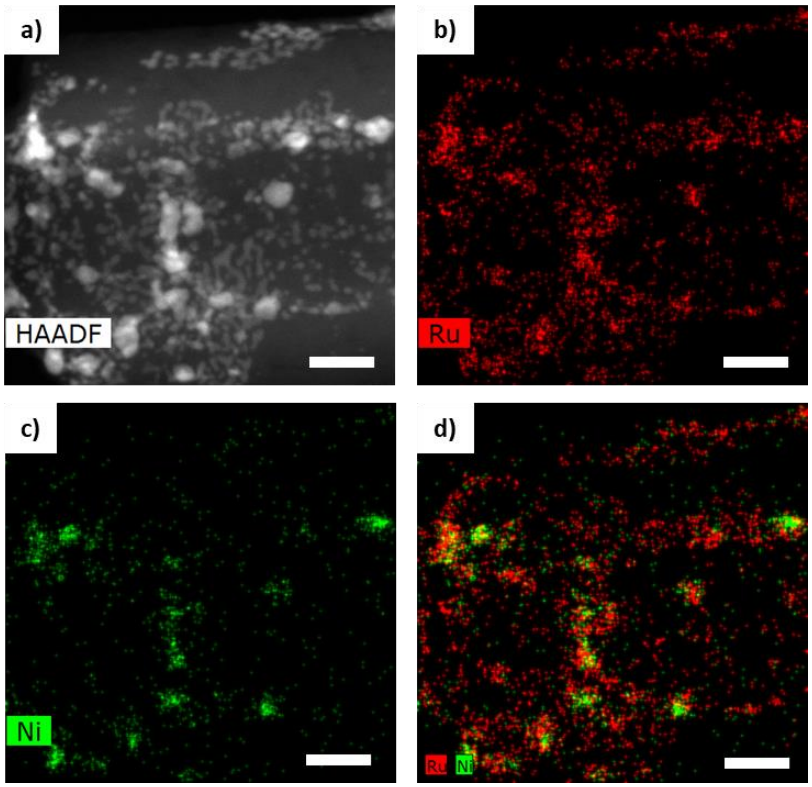

Figure 2.34: a) HAADF STEM micrograph of the concerted addition material; and b-d) STEM-EDX map showing the composition of the MNPs present. Scale bar: 20 nm.

HRTEM corroborates the formation of these two types of MNPs (mixed metal alloys and monometallic Ni or Ru NPs). Figure 2.35 shows MNPs with different crystal domains within the same NP as well as MNP containing a single crystal domain.

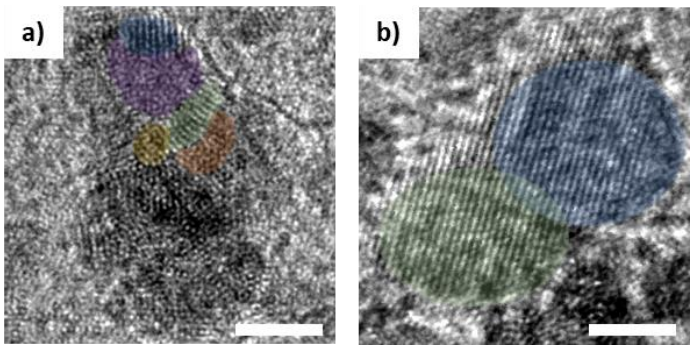

Figure 2.35: TEM images showing MNPs formed using the concerted addition fabrication method. a) A metal alloyed NP were the coloured areas show the different crystal domains within the NP; and b) two monometallic NPs were the coloured area shows the single crystal domains of each NP. Scale bar: 3 nm.

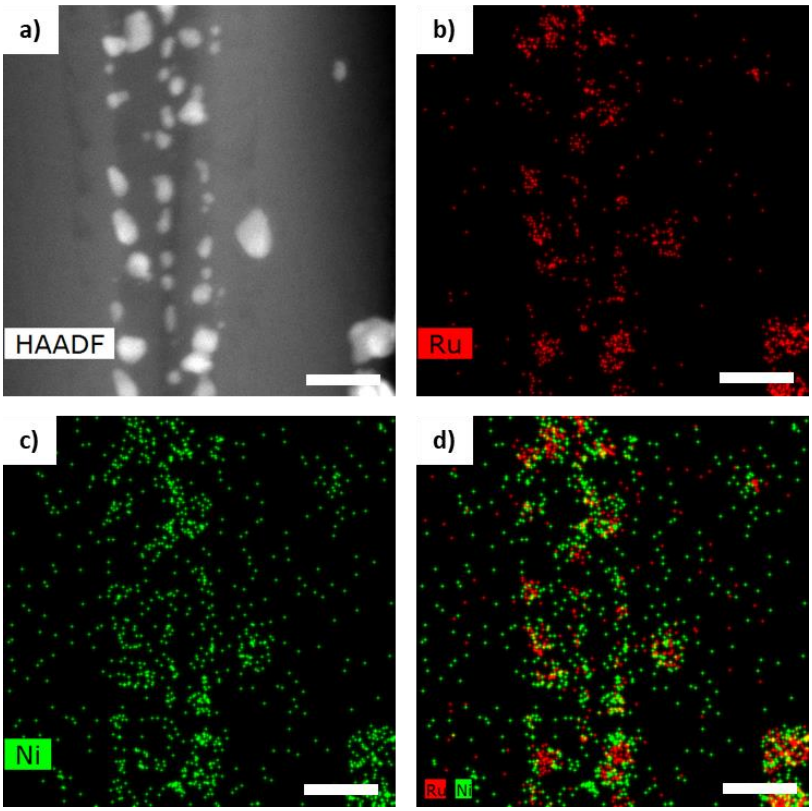

Figure 2.36: a) HAADF STEM micrograph of the sequential addition (Ru 1st) material; and b-d) STEM-EDX map showing the composition of the MNPs present. Scale bars: 20 nm.

STEM-EDX analysis for $Ru_{0.5}Ni_{0.5}$NPs@GNFs (sequential addition Ru 1st) show similarities to $Ru_{0.5}Ni_{0.5}$NPs@GNFs (concerted addition). It was also found that a mixture of bimetallic and monometallic NiNPs were present (Figure 2.36).

Interestingly, for the sequential addition (Ru 1st) material a light-grey structure was found on the outer surface of the GNF support, this was not visible via HRTEM, which EDX mapping indicates is a nickel sheet structure (see Figure 2.37). Ni sheets have been reported previously to be formed via atomic layer deposition of a number of nickel precursors, including; nickelocene,[39,43,44] (tetramethylethylene-diamine)nickel(acetylacetonate),[45] nickel acetylacetonate,[46] bis(1-(tert-butylimino)-2,3-dimethylbutan-2-olate)nickel[47] and bis(N,N′-diisopropylacetamidinato)nickel,[48] see review for full details.[49] Most methods require thermal decomposition of a nickel complex in the presence of a reactant gas, e.g. ammonia or mixtures of water and H_2. Specifically related to the materials I observe, atomic layer deposition of nickel films on carbon nanostructures of graphite was reported by Lee *et al.*[50] using NH_3 to form Ni nanowires on the terraces of the graphite surface and subsequent treatment to transform these wires into a continuous film.[51] In my methodology it is hypothesised that the low pressure in the sealed ampoule

and the small gas molecules formed from $NiCp_2$ decomposition, methane, H_2 etc. mimic this environment, playing the role of this reactant gas and the step-edges of the GNF and features of the surface anchor the nickel NPs and the template the Ni film.[49,51]

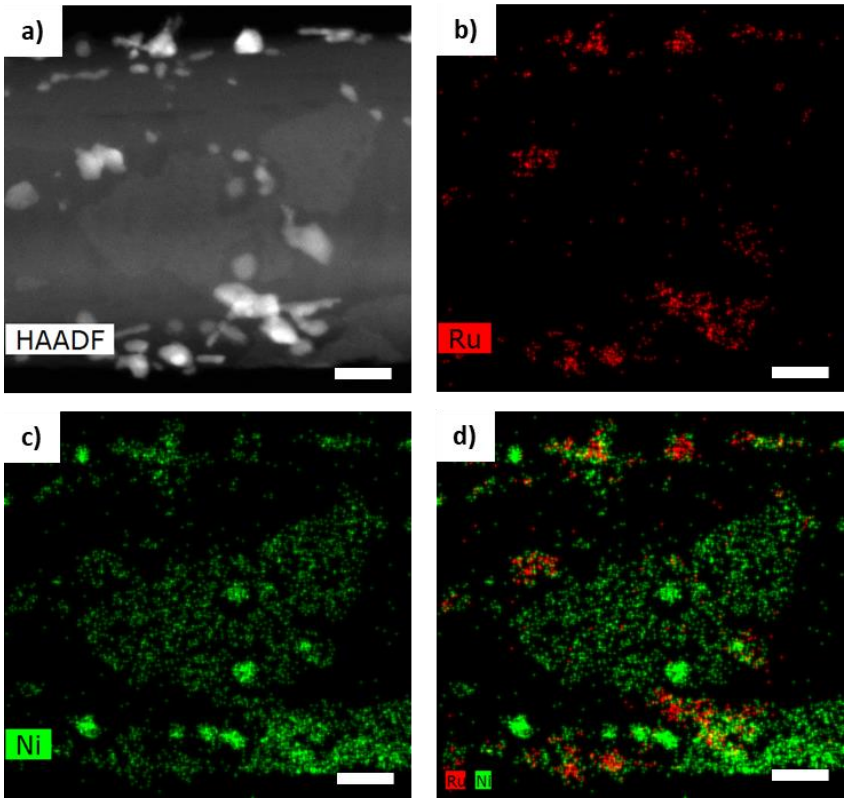

Figure 2.37: a) HAADF STEM micrograph of the sequential addition (Ru 1st) material showing a light grey structure on the exterior of the carbon support not visible in HRTEM; and b-d) STEM-EDX map showing the composition of the light grey structure and MNPs present. Scale bars: 20 nm.

The effect of changing the addition sequence, for the fabrication of RuNiNPs@GNFs, on resultant structure is most evident for the sequential addition (Ni 1st) material which gave rise the flower-like structures on the outer surface of the GNFs. STEM-EDX was employed to determine the composition of the flower-like structures which were found to be either a nickel carbide composite or a nickel structure surrounded by amorphous carbon (see Figure 2.38).

Ni and NiO nanoflowers are of interest for a variety of applications, including catalysis,[52] electroanalytical applications,[53] batteries[54] and supercapacitors,[55] due to their high surface areas and electrical conductivity. As a result, significant work has been done to control the structure of these nanomaterials, principally for nickel 2+ salts and using a wide variety of conditions including; Rühe *et al.*[56] formed nickel nanoflowers via electrodeposition of Ni^{2+} ions from solution on to polymer surfaces. Du *et al*.[50] used a nickel ethylene glycol

precursor made via an *in situ* two-step process involving reaction of $NiCl_2$ and sodium tartrate under hydrothermal conditions at 473 K to form nickel tartrate followed by decomposition of this intermediate to form nickel ethylene glycol nanoflowers, which were then sintered at relatively high temperature of 673 K to form NiO nanoflowers with a uniform size distribution (50-100 nm). Ibupoto *et al*.[57] synthesized NiO nanoflowers after growing $Ni(OH)_2$ on a gold substrate in alkaline media for 4-6 hours at 98 °C and annealing for 2–3 hours at 450 °C. Yang *et al*.[58] synthesized $Ni(OH)_2$ nanoflowers by heating at 45 °C for 2 hours an ammoniacal solution of nickel hexammine. The product was washed and dried for one day.

High surface area, flower like nanoparticles are particularly interesting for analytical applications, with electrochemical devices based on nickel metal, oxide and hydroxide published previously.[57,58] However, the complex synthesis required followed by a subsequent step to adhere them to or modify electrode surfaces with the nanoflowers has so far not allowed fast generation of simple and low cost electrochemical devices. An interesting device is reported by Niu *et al*.[59] who used electrodeposition of nickel (0.2 M Ni(II), 1 M H_2SO_4) applying a high current to the electrode (0.1 A for 30 s). In these conditions, nickel is electrodeposited on the electrode surface while large amounts of hydrogen bubbles are generated, and a three-dimensional porous nickel structure is created on the electrode surface. However, issues with scale up reduce the industrial applicability of this approach as it is limited to mm^2-cm^2 scale electrodes due to lack of control over the deposition process.[59]

The potential advantages of my approach are the fact that it forms the nanoflowers directly onto the carbon surface (ideal if the system is to be used as an electrode), is low cost due to the minimal use of chemicals and work up, scalable due to the simplicity and able to be transferred to other carbon nanostructures solely by incorporating them into the initial stage of the synthesis, replacing the GNFs However, to harness this methodology it is important to understand how these nanoflowers are formed so it was investigated further. The formation of these structures could form either after the first decomposition step, after the second sublimation step or after the second decomposition step. As these structures were not present in NiNPs@GNFs (5 wt.%) it was thought that these structures were formed in one of the subsequent steps after the first decomposition. The fabrication process was repeated taking samples of the material after each fabrication step, to be analysed by TEM, to determine at what point the flower-like structures formed.

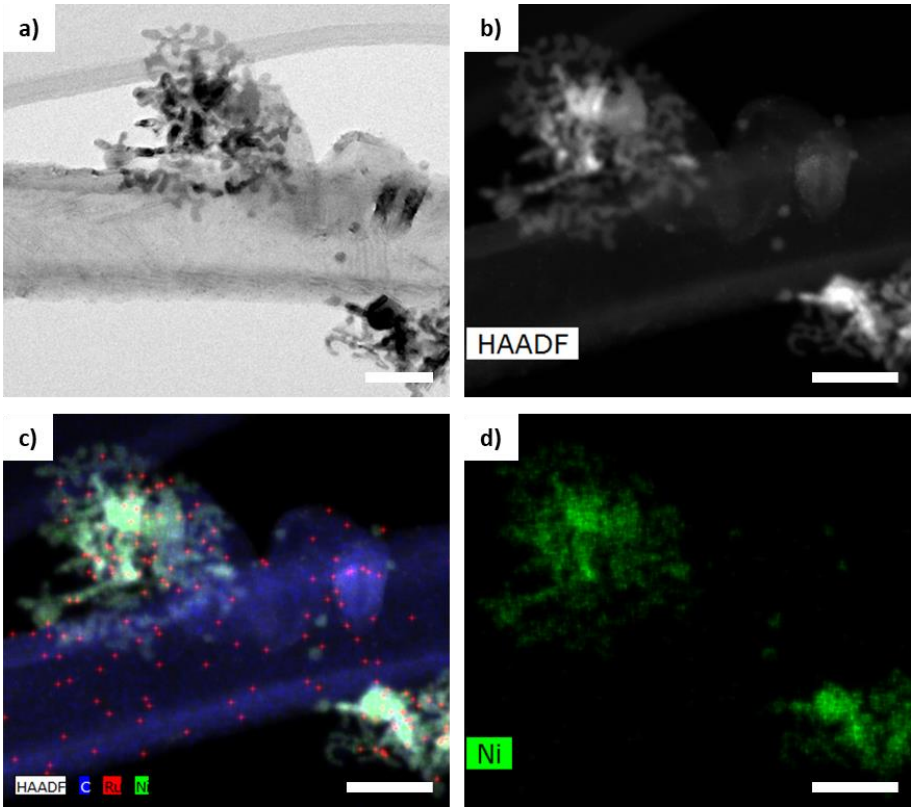

Figure 2.38: a) TEM and b) HADDF STEM micrograph of the sequential addition (Ni 1st) material showing a flower-like structure on the exterior surface of the GNF support; and c) and d) STEM-EDX map showing the composition of the flower-like structure to be either nickel carbide or nickel surrounded by amorphous carbon. Scale bars: 50 nm.

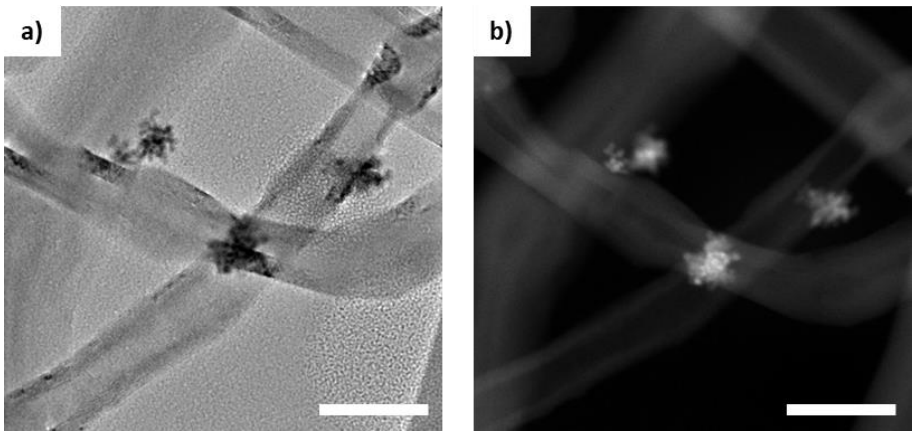

Figure 2.39: a) TEM micrograph and b) STEM micrograph of the sequential addition (Ni 1st) material after the first decomposition step showing that the flower-like structures on the exterior of the GNFs had begun to form.

From TEM and STEM it is clear that the flower like structures begin to form after the first decomposition step (Figure 2.39), clusters of small MNPs on the exterior of the GNF support, which was unexpected due to them not being present in the NiNPs@GNFs (5 wt.%) material. These clusters of MNPs undergo coalescence during the second decomposition step leading to the formation of larger MNPs (Figure 2.40).

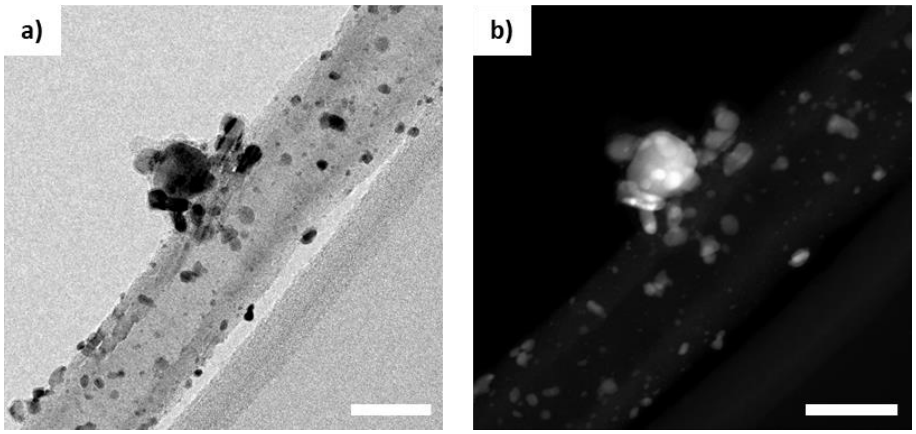

Figure 2.40: a) TEM micrograph and b) STEM micrograph of the sequential addition (Ni 1st) material after the second decomposition step showing that the NPs coalesce and form larger NPs.

MNPs located on the interior and exterior of the GNFs for the sequential addition (Ni 1st) material were also evidenced by TEM. STEM-EDX analysis was performed and the composition of these NPs was found to be solely discrete monometallic Ru or Ni NPs (Figure 2.41). HRTEM corroborates the formation of these monometallic MNPs. Figure 2.42 shows a MNP containing a single crystal domain.

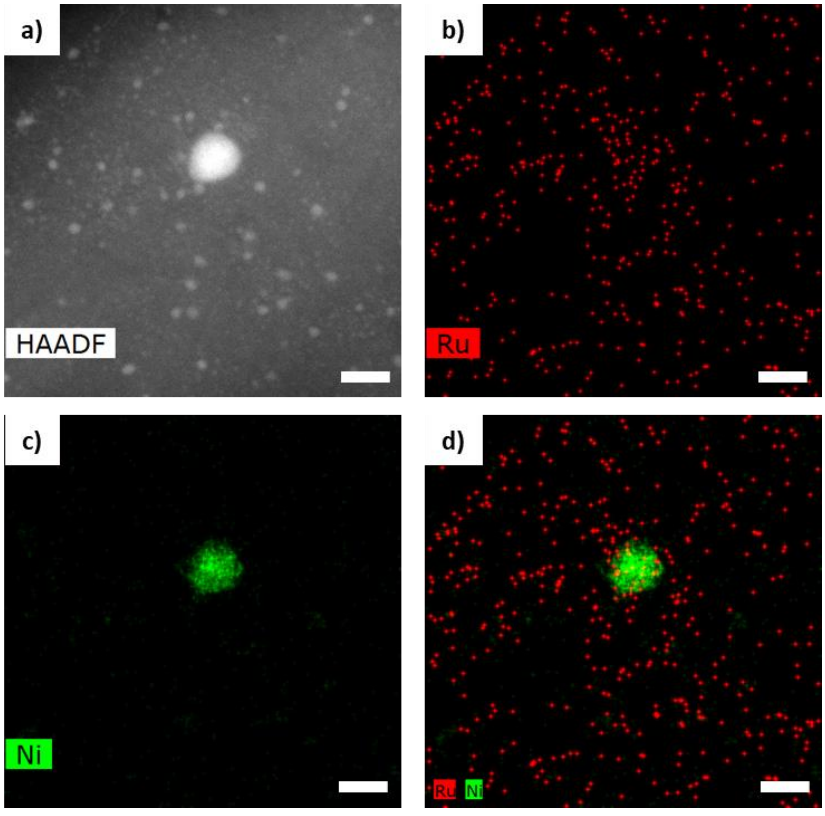

Figure 2.41: a) HAADF STEM micrograph of the sequential addition (Ni 1st) material; and b-d) STEM-EDX map showing the composition of the MNPs present. Scale bars: 10 nm.

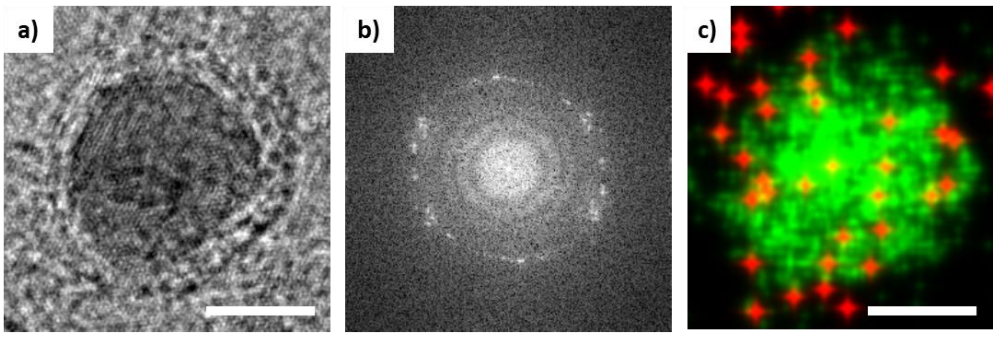

Figure 2.42: a) HRTEM of MNP in sequential addition (Ni 1st) material; b) Fourier transform of a); and c) STEM-EDX map of MNP showing the composition to be monometallic Ni.

One common feature across the three materials is the larger NPs with diameters between 4-12 nm. These MNPs were classified into three categories; mixed metal NPs, monometallic RuNPs and monometallic NiNPs. The categorisation of the MNPs was predominately done using EDX mapping of the individual NPs in each material (see Figure 2.43). A MNP was determined bimetallic it contained 30% or more of the 2nd metal (evidenced through the EDX map). For all MNPs their classification of bimetallic or monometallic was further analysed through examination of the crystal domains present in the MNPs (evidence from TEM). The percentages of each category for the type of MNPs are summarised in Table 2.6. A mixture of mono-metallic NPs and mixed metal NPs were formed for the concerted addition and sequential addition (Ru 1st) fabrication methods with an approximate ratio of 1:1. In contrast only mono-metallic (Ni) NPs where formed using the sequential addition (Ni 1st) fabrication method.

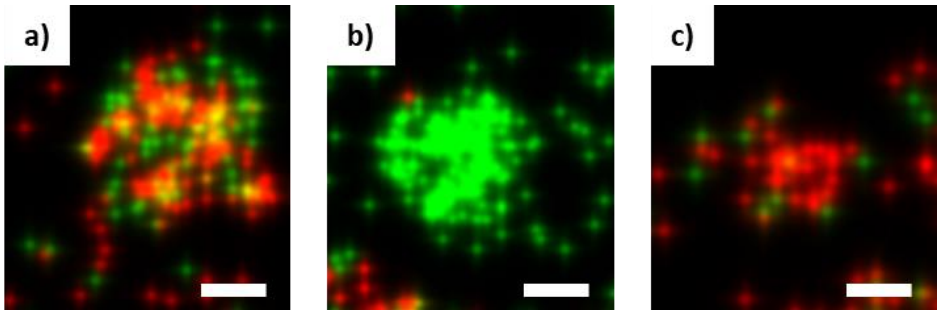

Figure 2.43: Examples of EDX mapping of; a) a mixed metal NP; b) mono-metallic NiNP; and c) mono-metallic RuNP. Where red indicates the presence of Ru and green indicates the presence of Ni. Scale bars: 2 nm.

Another common feature between the concerted addition and sequential addition (Ni 1st) fabrication methods is the formation of small NPs with diameters between 1 - 3 nm. In both cases STEM-EDX mapping showed these NPs to be mono-metallic Ru (see Figure 2.34 and Figure 2.41).

Table 2.6: Percentages of MNPs (diameters between 4 - 12 nm) with different compositions present in $Ru_{0.5}Ni_{0.5}$NPs@GNFs (different addition sequences).[a]

Material	Mixed metal NPs	Mono-metallic NiNPs	Mono-metallic RuNPs
Sequential addition (Ru 1st)	50%	50%	0%
Concerted addition	42%	50%	8%
Sequential addition (Ni 1st)	0%	100%	0%

[a]Percentages calculated from determining the composition of 12 MNPs in each material.

Extended X-ray absorption fine structure (EXAFS) spectroscopy and X-ray absorption near-edge structure (XANES) spectroscopy are commonly used techniques to examine the local environment of atoms in mono- and bimetallic NPs (e.g. morphology and electronic states).[60–62] Due to its sensitivity to the charge states of metals, adsorbates, and support materials, XANES is a powerful tool with which to study the electronic structure of catalytic materials.[61] Near edge features were analysed by XANES for $Ru_{0.5}Ni_{0.5}$NPs@GNFs (concerted addition), $Ru_{0.5}Ni_{0.5}$NPs@GNFs (Ru 1st), $Ru_{0.5}Ni_{0.5}$NPs@GNFs (Ni 1st) along with control measurements for RuNPs@GNFs and NiNPs@GNFs (all material 5% by wt. total metal). Figure 2.44 shows the spectra obtained for the Ru K-edge and the edge energies are summarised in Table 2.7. Across the series of materials, the white line intensity remains essentially unchanged for the bimetallic materials compared to the monometallic RuNPs@GNFs. The edge position (measured at the half-height of the edge jump) is dependent on the electronic charge of the Ru atoms and remains unchanged across the series of materials. A slight decrease in edge energy is observed for $Ru_{0.5}Ni_{0.5}$NPs@GNFs (Ru 1st) compared to the monometallic RuNPs@GNFs. This differs from the increase observed for $Ru_{0.5}Ni_{0.5}$NPs@GNFs (added together). Changes in edge energy could be attributed to the change in electronic state of Ru due to the electron donating ability of Ni. The small differences in spectral shape may be attributed to alloying with Ni.

Figure 2.45 shows the spectra obtained for the Ni K-edge with edge energies summarised in Table 2.8. Across the series of materials, the white line intensity decreases compared to monometallic NiNPs@GNFs, with the

biggest decrease observed for $Ru_{0.5}Ni_{0.5}$NPs@GNFs (Ni 1st). No significant change in edge energy is observed across the series of materials.

Table 2.7: Summary of Ru edge energies observed for $Ru_{0.5}Ni_{0.5}$NPs@GNFs, fabricated using the three addition sequences, compared to RuNPs@GNFs (all 5 wt.% total metal) showing a slight decrease in edge energy for concerted addition (Ru 1st) and an increase in edge energy for the concreted addition material.

Material	Edge energy / eV
RuNPs@GNFs	22127.1 ± 2.4
$Ru_{0.5}Ni_{0.5}$NPs@GNFs (Ru 1st)	22121.2 ± 1.0
$Ru_{0.5}Ni_{0.5}$NPs@GNFs	22134.3 ± 1.5
$Ru_{0.5}Ni_{0.5}$NPs@GNFs (Ni 1st)	22131.0 ± 1.0

Zhu *et al.*,[63] reported the use of XANES to gain insight into the relationship between surface structure and catalytic properties of Ni/NiO/C and Ru–Ni/C. XANES spectra at the Ni K-edge for various samples (Ni/Ni(OH)$_2$/C, Ru–Ni/C, Ru-Ni/NiO/C, NiO, Ni(OH)$_2$ and Ni-foil) were recorded. It was found that the white line intensity decreased in the following order: Ni/Ni(OH)$_2$/C > Ru-Ni/NiO/C >Ru–Ni/C which was attributed to a larger proportion of nickel atoms present in the metallic state on the Ru-Ni/C catalyst (compared to the other material).[63] For the RuNiNPs@GNFs materials made by the different addition sequences there is a change in the white line intensity (for the Ni K-edge spectra) observed for the bimetallic materials compared to the monometallic NiNPs@GNFs. This suggests that that there is a smaller proportion of nickel atoms present in the metallic state for the bimetallic materials compared to the monometallic material.

Mori, *et al.*,[64] investigated the changes in electronic states for Ru/TiO$_2$ and RuNi/TiO$_2$ using XANES spectroscopy. They reported that the edge position was dependent on the electronic charge of the Ru atoms. As a slight shift (ca. 1 eV) to lower energy in the Ru K-edge energy was observed for RuNi/TiO$_2$ compared to Ru/TiO$_2$ they concluded that there was a change in the electronic state of Ru in RuNi/TiO$_2$ due to the electron donating ability of Ni. The electronic charge can transfer from Ni atoms to Ru atoms because of their differences in electron negativities (Ni, 1.91; Ru, 2.20).[64] As a slight decrease in edge energy was observed for $Ru_{0.5}Ni_{0.5}$NPs@GNFs (Ru 1st) compared to the monometallic RuNPs@GNFs this could be attributed to a

change in the electronic state of Ru in due to the electron donating ability of Ni. However, different support structures are used between this study and that reported by Mori and co-workers, which could lead to an effect on the electronic properties of the supported MNPs.

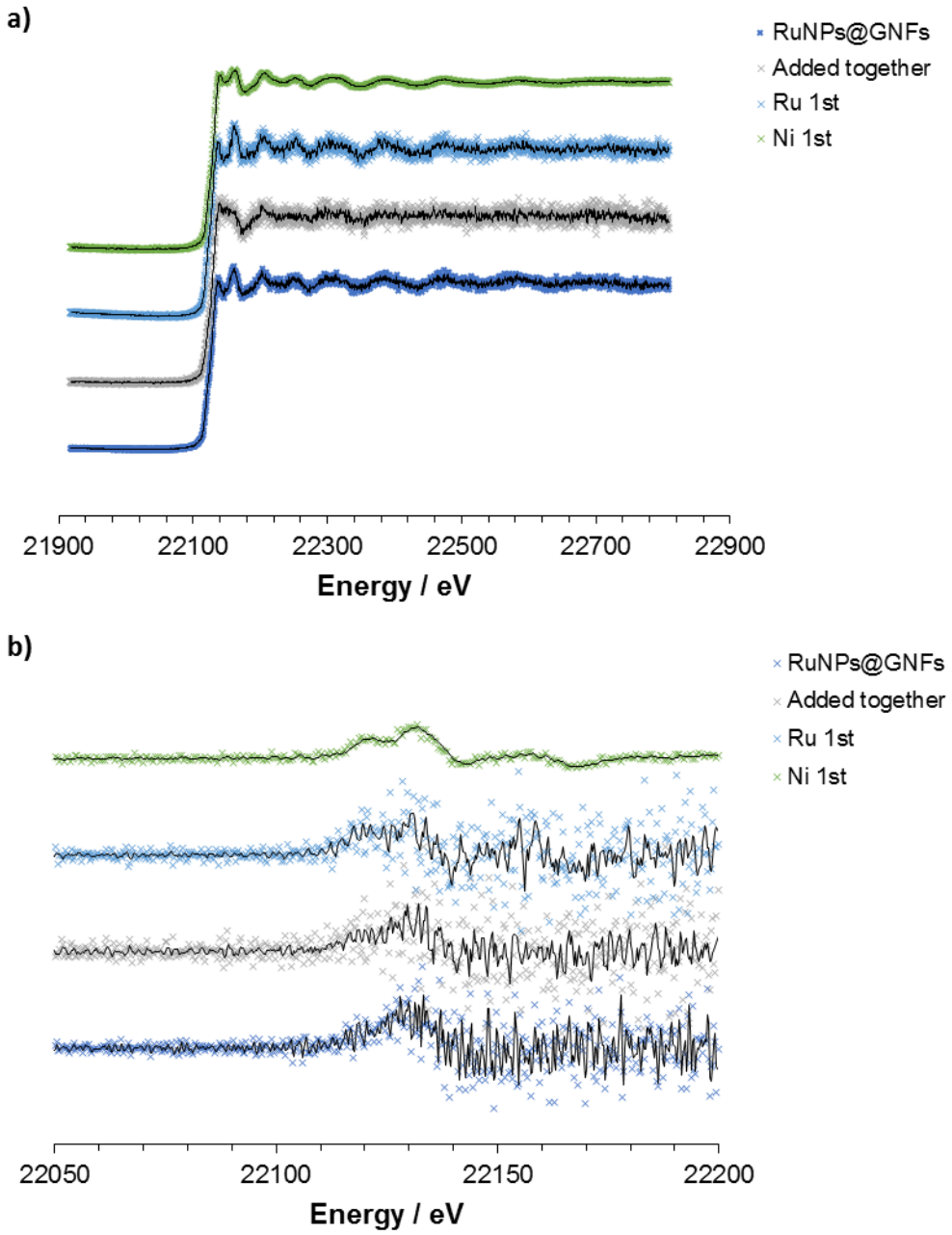

Figure 2.44: a) Normalised XANES spectra for the Ru K-edge of $Ru_{0.5}Ni_{0.5}$NPs@GNFs, fabricated using the three addition sequences, compared to RuNPs@GNFs (all 5 wt.% total metal); and b) first order derivative of a) showing the position of the Ru-edge energy.

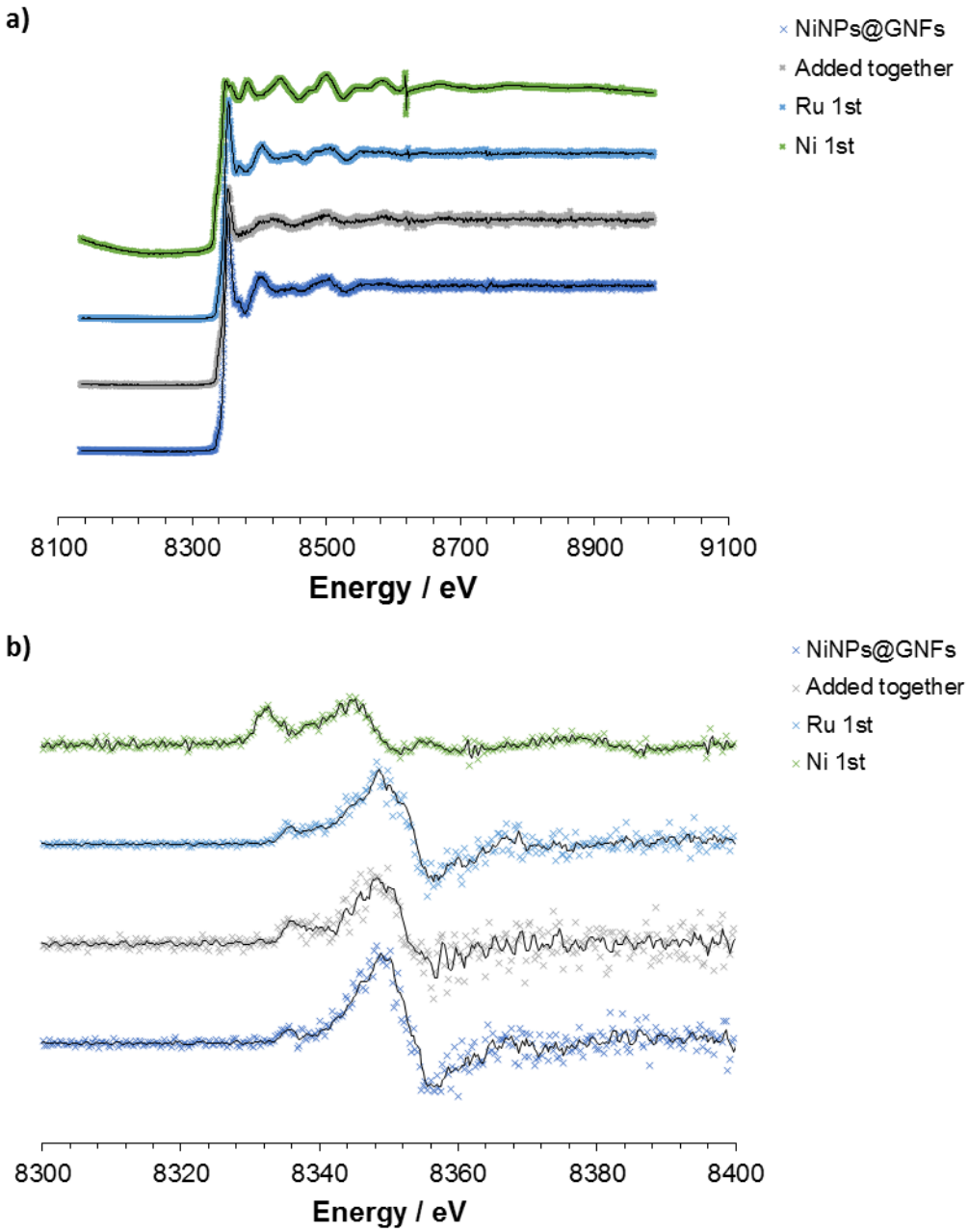

Figure 2.45: a) Normalised XANES spectra for the Ni K-edge of $Ru_{0.5}Ni_{0.5}$NPs@GNFs, fabricated using the three addition sequences, compared to RuNPs@GNFs (all 5 wt.% total metal); and b) first order derivative of a) showing the position of the Ni-edge energy.

Table 2.8: Summary of Ni-edge energies observed for $Ru_{0.5}Ni_{0.5}$NPs@GNFs, fabricated using the three addition sequences, compared to RuNPs@GNFs (all 5 wt.% total metal) showing no significant change in edge energy.

Material	Edge energy / eV
NiNPs@GNFs	8350.1 ± 0.7
$Ru_{0.5}Ni_{0.5}$NPs@GNFs (Ru 1st)	8351.5 ± 2.0
$Ru_{0.5}Ni_{0.5}$NPs@GNFs	8348.6 ± 1.8
$Ru_{0.5}Ni_{0.5}$NPs@GNFs (Ni 1st)	8343.7 ± 0.7

2.2.3.4 Changing the ratio of Ru:Ni for Bimetallic Systems

The effect of varying the ratio of Ru:Ni has also been investigated. The fabrication of three bimetallic RuNiNPs@GNFs, with differing ratios of Ru:Ni but the same total metal loading (5 wt.%), was performed using a concerted addition approach. These materials have the following Ru:Ni ratios; 3:1, 1:1, 1:3, and are denoted $Ru_{0.75}Ni_{0.25}$NPs@GNFs, $Ru_{0.5}Ni_{0.5}$NPs@GNFs, $Ru_{0.25}Ni_{0.75}$NPs@GNFs, respectively. A monometallic NiNPs@GNFs (5 wt.%) has also been fabricated to enable direct comparison with the bimetallic materials. All materials were analysed by HRTEM and the elemental composition of the RuNiNPs@GNFs and NiNPs@GNFs materials were confirmed by EDX (see Section 2.2.1.3).

Table 2.9: Summary of mono- and bimetallic materials fabricated (all 5% by wt. total metal) and the average diameters of the NPs formed showing no substantial change in MNP diameter across the series (within error).

Material	NP Diameter / nm
RuNPs@GNFs	4.2 ± 1.2
$Ru_{0.75}Ni_{0.25}$NPs@GNFs	6.0 ± 1.1
$Ru_{0.5}Ni_{0.5}$NPs@GNFs	3.4 ± 1.7
$Ru_{0.25}Ni_{0.75}$NPs@GNFs	4.0 ± 1.5
NiNPs@GNFs	6.1 ± 2.2

The average NP diameters afforded for these materials are summarised in Table 2.9. Interestingly, compared to the 5% by wt. RuNPs@GNFs material

(c.f. d_{NP} = 4.2 ± 1.2 nm) the $Ru_{0.5}Ni_{0.5}$NPs@GNFs had a similar average diameter (within error) of 3.4 ± 1.7 nm in contrast to the slightly larger NiNPs observed in the NiNPs@GNFs system (c.f. d_{NP} = 6.1 ± 2.2 nm).

Accurate metal loadings for each material were determined by thermogravimetric analysis (TGA) and are summarised in Table 2.10. A GNF control sample was run to ensure complete combustion of the carbon support was achieved (Figure 2.46) so that any residual weight remaining in the TGAs run of the MNPs@GNFs materials could be attributed to the metal loading. The metal loading across the series varies from 3-6%.

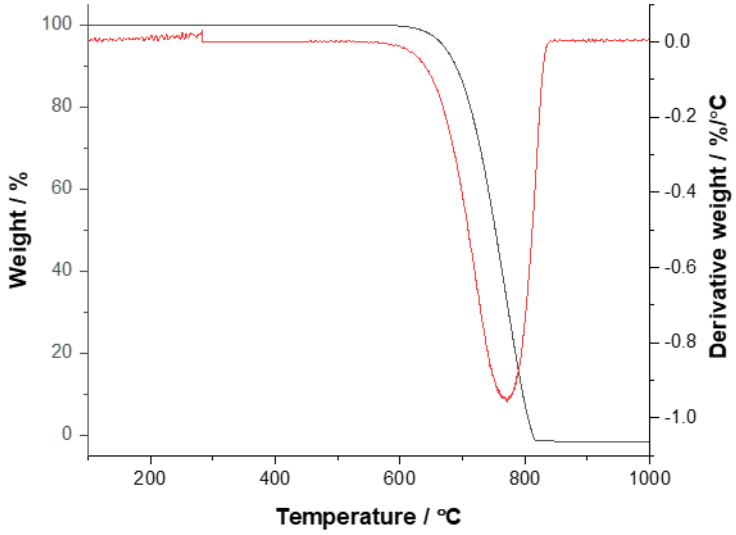

Figure 2.46: TGA of GNFs showing their complete combustion.

Table 2.10: Summary of the metal loadings obtained from TGA showing that the total metal present across the series of materials varies from 3-6%.

Material	Metal Loading / %
RuNPs@GNFs	5.6 ± 0.9
$Ru_{0.75}Ni_{0.25}$NPs@GNFs	3.8 ± 0.9
$Ru_{0.5}Ni_{0.5}$NPs@GNFs	3.4 ± 0.9
$Ru_{0.25}Ni_{0.75}$NPs@GNFs	5.1 ± 0.9
NiNPs@GNFs	4.3 ± 0.9

Although TGA can be used to determine the metal loading it does not distinguish between the amount of Ru and Ni present within the material. As such inductively coupled plasma mass spectrometry (ICP-MS) was employed.

To test the validity of the results obtained by ICP-MS the Ru content of commercially available Ru/C (5 wt.%) was investigated. Samples were prepared based on a previously reported digestion method for Ru metal.[26]

Three repeat measurements gave Ru concentrations of 0.10, 0.01 and 0.16 mg of Ru per litre which correspond to Ru metal loadings of the same value (0.10%, 0.01% and 0.16%). Clearly this isn't correct, not only are the values inconsistent, they are much lower than what they should be (i.e. 5 mg/L). This discrepancy is most probably due to problems during the digestion of the Ru metal. Due to the inconsistent results obtained for commercially available Ru/C (5 wt.%) ICP-MS analysis was not performed on the GNF-based materials.

Near edge features were analysed by XANES for $Ru_{0.75}Ni_{0.25}$NPs@GNFs and $Ru_{0.25}Ni_{0.75}$NPs@GNFs and compared to the spectra obtained for $Ru_{0.5}Ni_{0.5}$NPs@GNFs (concerted addition), RuNPs@GNFs and NiNPs@GNFs (all materials 5% by wt.% total metal. Figure 2.47 shows the spectra obtained for the Ru K-edge and the edge energies are summarised in Table 2.11. There is an increase in white line intensity observed for $Ru_{0.75}Ni_{0.25}$NPs@GNFs compared to monometallic RuNPs@GNFs. The white line intensity for all other materials across the series remains essentially unchanged. No significant change in edge energy is observed across the series of materials.

Figure 2.48 shows the spectra obtained for the Ni K-edge with edge energies summarised in Table 2.12. The white line intensity decreases for all bimetallic materials compared to monometallic NiNPs@GNFs, with the biggest decrease observed for $Ru_{0.75}Ni_{0.25}$NPs@GNFs. No significant change in edge energy is observed across the series of materials.

Zhang *et al.*,[65] previously reported the use of X-ray absorption spectroscopy to inspect the electronic states and morphology of bimetallic RuNiNPs with differing Ru:Ni ratios (85:15, 70:30 and 50:50) at the atomic scale. Both the Ru K-edge and Ni K-edge of the different RuNiNP samples were similar to those obtained for the Ru powder and Ni, indicating that both Ru and Ni were in the metallic state. However, small changes in their absorption energies were observed as the edge shifts towards higher energy at the Ru K-edge as Ni content increases and to lower energy at the Ni K-edge as Ru content

increases suggesting a charge transfer from Ru to Ni in the bimetallic RuNiNPs.[65] No changes in the absorption energies are observed for any of the bimetallic RuNiNPs@GNFs at both the Ru and Ni K-edge. However, the RuNPs report by Zhang *et al*.[65] were not supported and as such does not rule out the possibility of a charge transfer happening between Ru and Ni in the prepared RuNiNPs@GNFs materials as the carbon support could be influencing the electronic structure of the RuNiNPs.

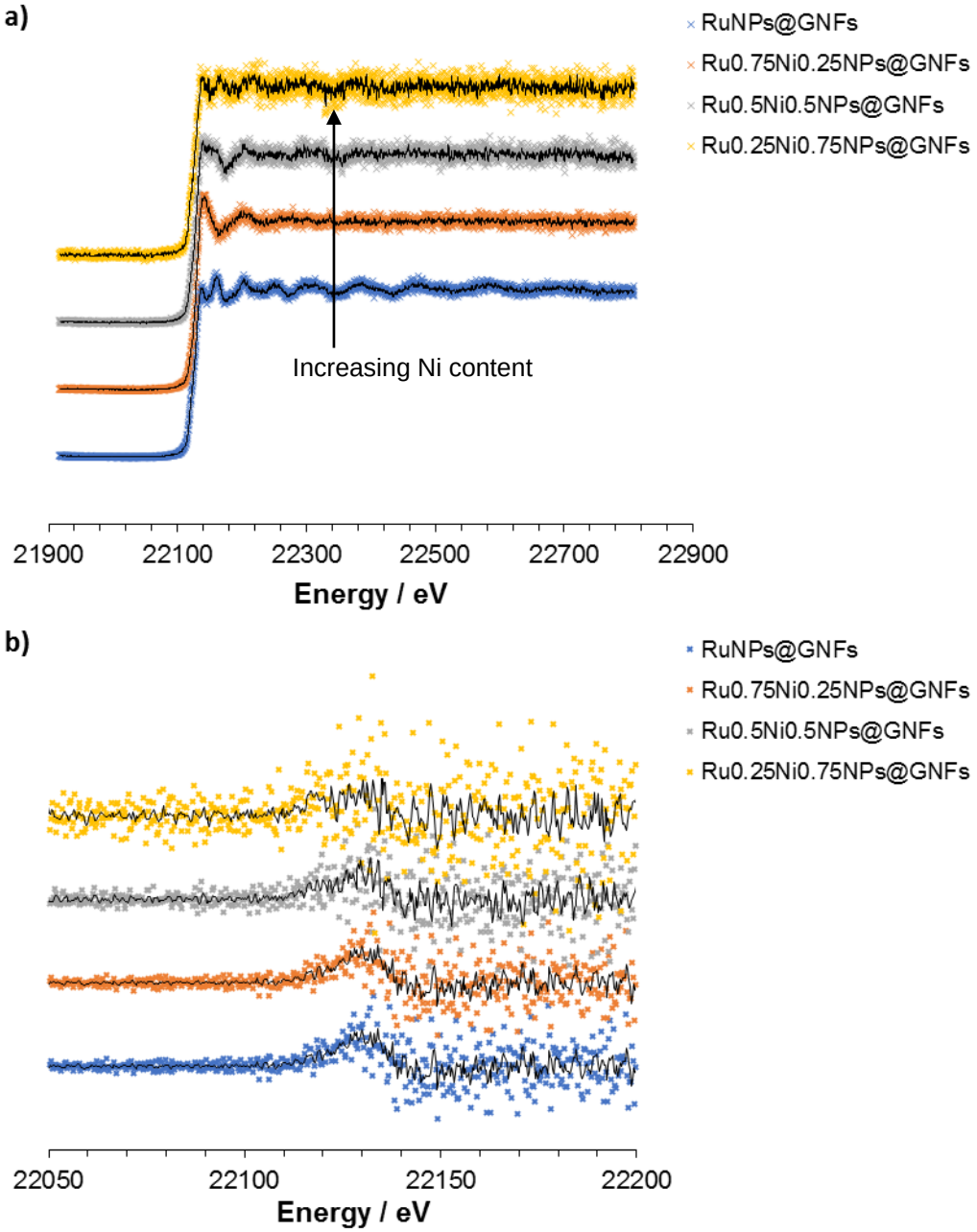

Figure 2.47: a) Normalised XANES spectra for the Ru K-edge of Ru0.5Ni0.5NPs@GNFs, fabricated using the three addition sequences, compared to RuNPs@GNFs (all 5 wt.% total metal); and b) first order derivative of a) showing the position of the Ru-edge energy.

Table 2.11: Summary of Ru-edge energies observed for RuNiNPs@GNFs with differing ratio of Ru:Ni, compared to RuNPs@GNFs (all 5 wt.% total metal) showing no substantial difference in energy across the series (within error).

Material	Edge energy / eV
RuNPs@GNFs	22127.1 ± 2.4
$Ru_{0.75}Ni_{0.25}$NPs@GNFs	22130.0 ± 3.0
$Ru_{0.5}Ni_{0.5}$NPs@GNFs	22134.3 ± 1.5
$Ru_{0.25}Ni_{0.75}$NPs@GNFs	22134.6 ± 1.1

Table 2.12: Summary of Ni-edge energies observed for RuNiNPs@GNFs with differing ratio of Ru:Ni, compared to NiNPs@GNFs (all 5 wt.% total metal) showing no significant change in edge energy.

Material	Edge energy / eV
NiNPs@GNFs	8350.1 ± 0.7
$Ru_{0.75}Ni_{0.25}$NPs@GNFs	8348.7 ± 2.1
$Ru_{0.5}Ni_{0.5}$NPs@GNFs	8348.6 ± 1.8
$Ru_{0.25}Ni_{0.75}$NPs@GNFs	8351.6 ± 1.8

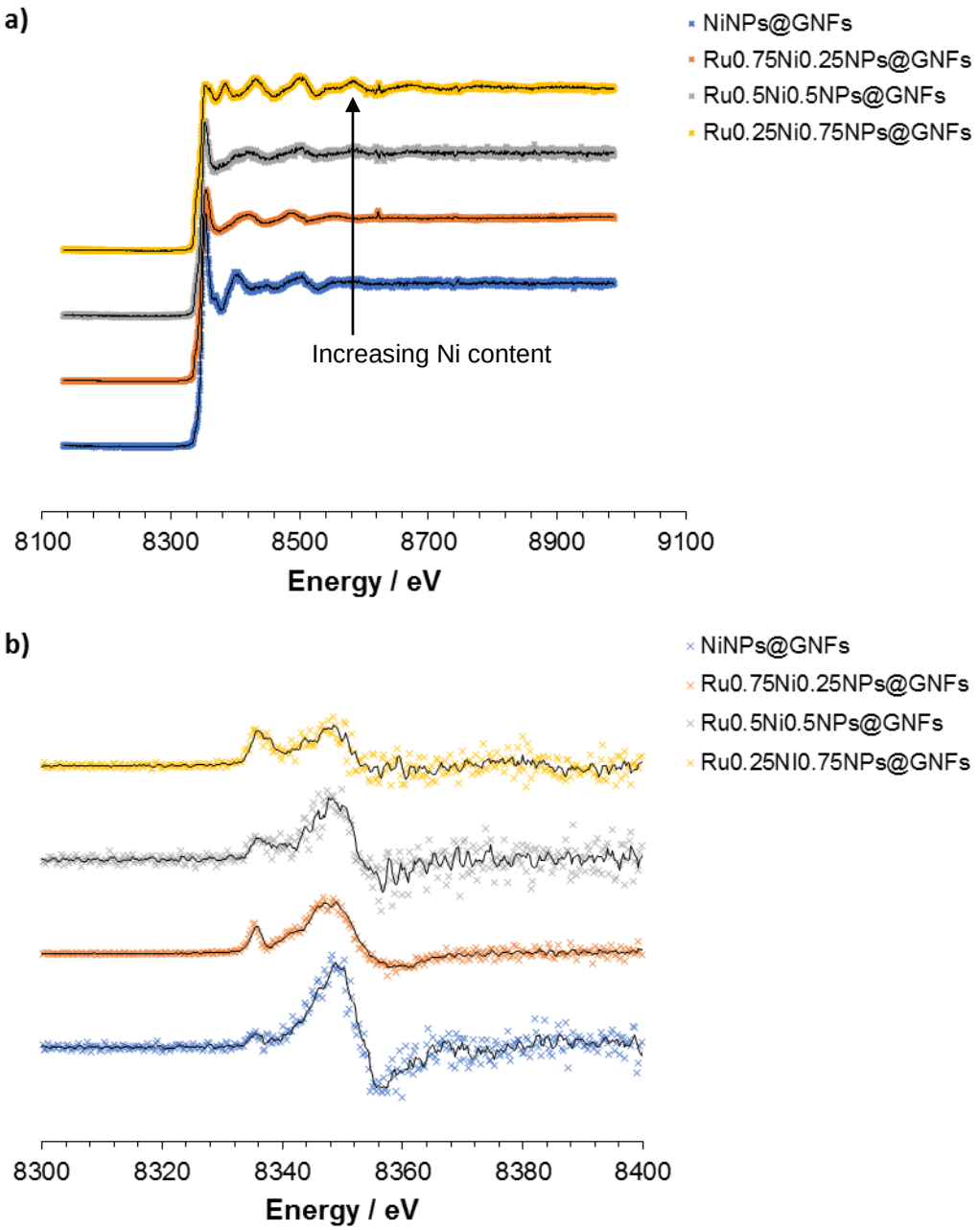

Figure 2.48: a) Normalised XANES spectra for the Ni K-edge of $Ru_{0.5}Ni_{0.5}$NPs@GNFs, fabricated using the three addition sequences, compared to RuNPs@GNFs (all 5 wt.% total metal); and b) first order derivative of a) showing the position of the Ni-edge energy.

Brunauer-Emmett-Teller (BET) measurements based on isothermal N_2 gas adsorption at -196 °C (77 K) were performed for RuNPs@GNFs and NiNPs@GNFs along with a control measurement of GNFs, to quantify the surface area of the materials (Figure 2.49). Barrett Joyner Halenda (BJH) theory was also employed to determine the pore volume and pore size distribution for each material and is summarised in Table 2.13. All three materials exhibit a type IV nitrogen adsorption isotherm,[66] with an increase in

volume adsorbed at higher P/P_o and a hysteresis loop indicative of meso- and macroporosity.

The specific surface area (SSA) obtained for GNFs (14.80 m^2 g^{-1}) is comparable to that previously reported (12.08 m^2 g^{-1}).[26] An increase in SSA of NiNPs@GNFs (29.13 m^2 g^{-1}) compared to empty GNFs (14.80 m^2 g^{-1}) was observed and can be attributed to the presence of NiNPs. Unexpectedly, the SSA of RuNPs@GNFs (14.85 m2 g^{-1}) is the same as that observed for GNFs suggesting that the incorporation of RuNPs into the support structure has no effect on the SSA. This contrasts the increase observed by Aygun, M. *et al.*[26] who reported an increase in SSA for RuNPs@GNFs (28.53 m^2 g^{-1}) compared to GNFs (12.08 m^2 g^{-1}).[26] This is could be caused by a blocking of the internal cavities of the GNFs not allowing N_2 to access the full internal volume of the material.

Table 2.13: Summary of the physiochemical properties (specific surface area (SSA), mesopore volume (BJH) and pore size distribution) of RuNPs@GNFs (5 wt.%), NiNPs@GNFs (5 wt.%) and GNF materials.[a]

Material	**SSA (m^2 g^{-1})**	**BJH Vol (cm^3 g^{-1})**	**Average mesoporous size (nm)**
RuNPs@GNFs (5 wt.%)	14.85	0.04	30-40
NiNPs@GNFs (5 wt.%)	29.13	0.03	50-60
GNFs[b]	14.80	0.04	40-50 (not smooth)

[a]All samples were degassed at 120 °C for 3 hours under a stream of N_2 prior to use.

[b]GNFs were annealed at 450 °C for 3 hours prior to being degassed.

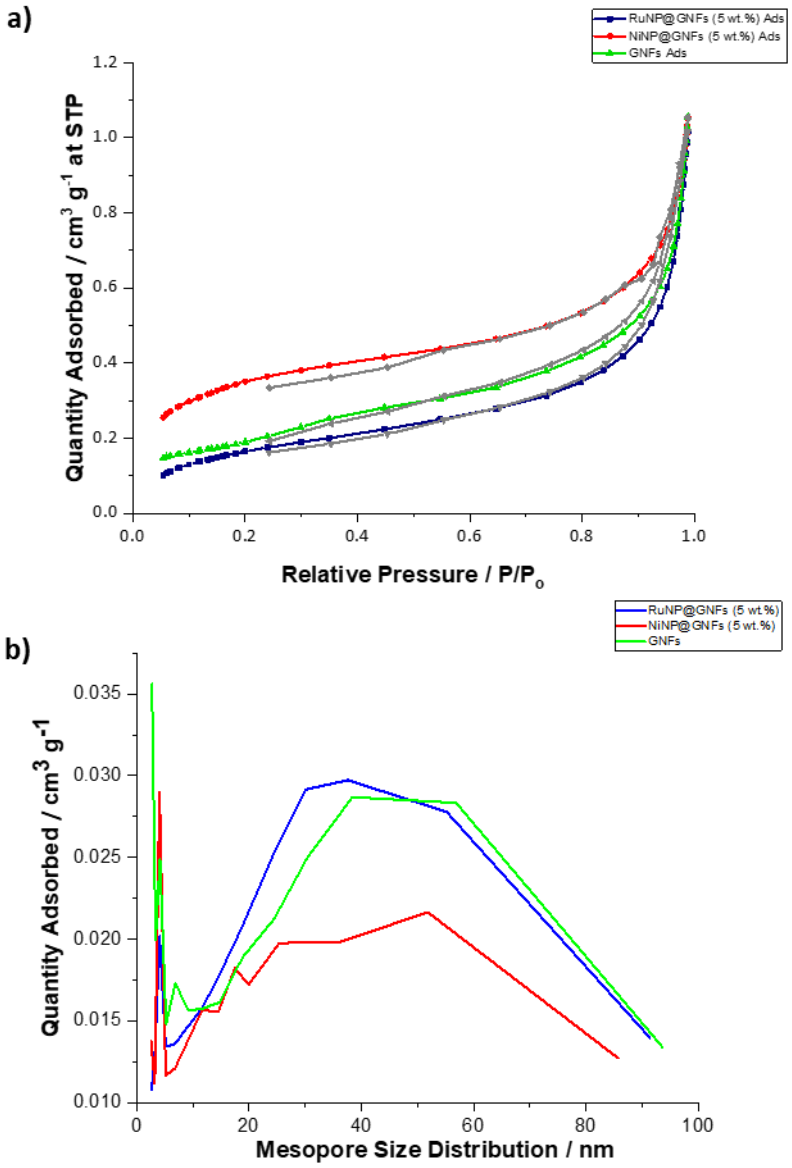

Figure 2.49: a) N_2 adsorption isotherms; and b) pore size distribution; of RuNPs@GNFs (5 wt.%), NiNPs@GNFs (5 wt.%) and GNFs.

2.3 Conclusions

The fabrication of mono- and bimetallic nanoparticles encapsulated in GNFs has been successfully carried out via sublimation of a volatile metal precursor/s, in the presence of the support structure, followed by thermal decomposition. Monometallic Ru based materials were fabricated with varying metal loadings (1-10 wt.%). TEM and powder XRD showed that the average diameter of the RuNPs increased with increasing wt.% of Ru metal present. Effect of decomposition temperature has been investigated for RuNPs@GNFs (2 wt.%), between 200-700 °C, results indicate that the step-edges of the GNFs template the size of the RuNPs formed and that the

material is stable up to 700 °C which is exciting as it provides the opportunity for catalytic reactions to be carried out at high temperatures with no loss in catalytic activity due to migration or coalescence of the MNPs, ultimately increasing the rate of reaction.

The fabrication of three bimetallic RuNiNPs@GNFs (5% by wt. total metal) with a Ru:Ni ratio of 1:1 was carried out using the same fabrication method but with different addition sequences for the metal precursors. HRTEM and STEM-EDX revealed that simply changing the addition sequence of the metal precursors greatly affected the resultant structure of the material. The sequential addition approaches lead to the formation of some interesting Ni nanostructures. These structures have the potential for use as novel electrode materials in electrochemical devices due to their high surface areas.

The effect of varying the ratio of Ru:Ni has also been investigated through the fabrication of three bimetallic RuNiNPs@GNFs, with differing ratios of Ru:Ni but the same total metal (5 wt.%), using a concerted addition approach. No significate change in the average diameter of MNPs present in these materials was observed which indicates that the incorporation of nickel into the RuNPs@GNFs material has very little effect on particle size, and as such, any changes witnessed in the catalytic activity of the materials will be due to other factors (such as MNP composition) rather than average particle diameter.

2.4 Experimental

2.4.1 General Considerations

The GNFs (PR-19-XT-PS) were purchased from Pyrograf Products and used without further purification. All other reagents were of analytical grade quality and used as supplied from Sigma-Aldrich and Fischer Scientific, unless otherwise stated.

2.4.2 Catalyst Preparation

2.4.2.1 RuNPs@GNFs (1, 2, 5 and 10 wt.%)

GNFs were annealed at 450 °C for 3 hours in air prior to use. The metal carbonyl precursor, $Ru_3(CO)_{12}$, was combined with freshly annealed GNFs in a Pyrex tube and sealed under vacuum (10^{-6} mbar) using a high vacuum filling rig (see Figure 2.50) before being heated in an oil bath at 130 °C for 3 days.

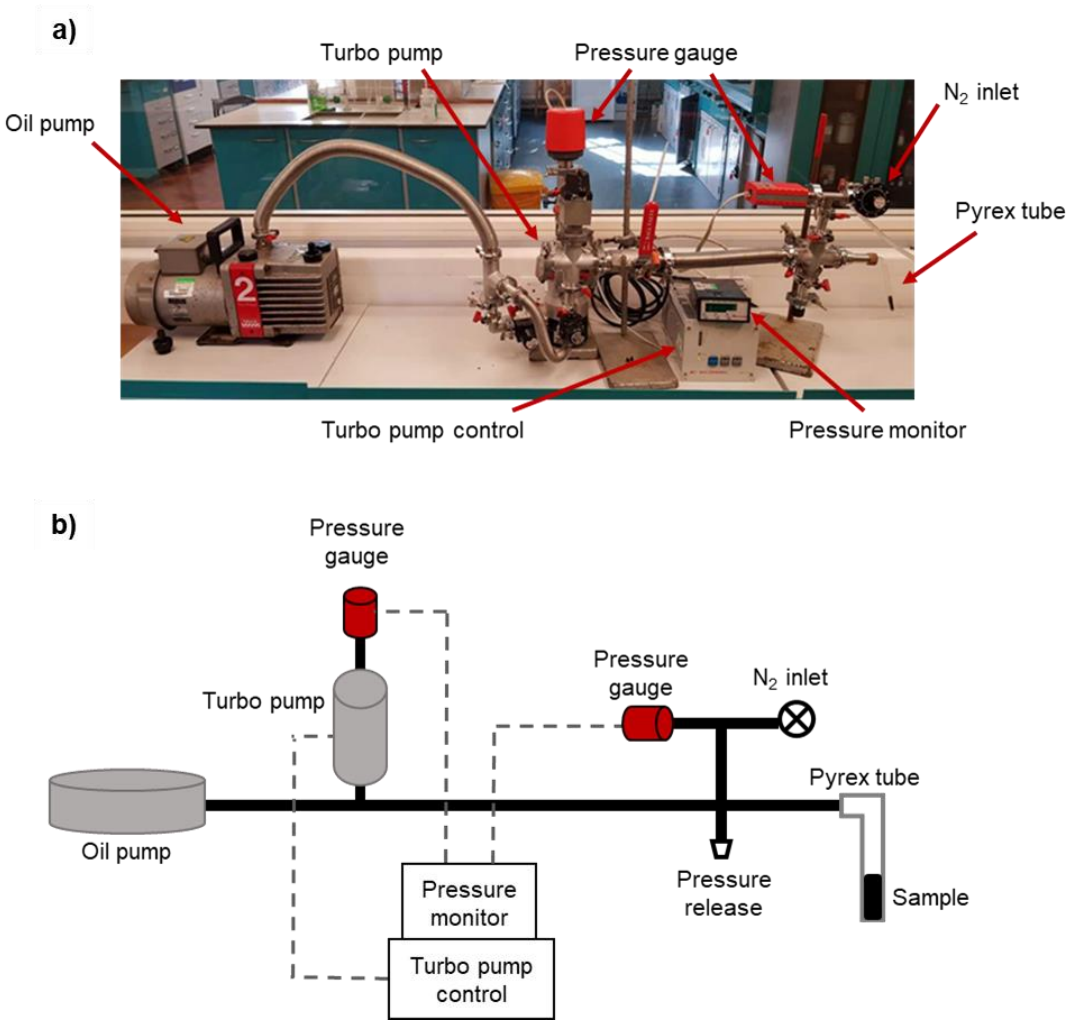

Figure 2.50: a) Photograph of the high vacuum filling rig used to seal samples under vacuum or a nitrogen atmosphere; and b) schematic diagram of the system showing the different pumping stages and the sample stage of the high vacuum filling rig.

After 3 days, the sample inside the Pyrex tube was cooled by immersing it in an ice-water bath. The sample was then transferred into another Pyrex tube and sealed under a nitrogen atmosphere (50 mbar). This was then heated at 450 °C for 2 hours in order to decompose the metal precursor into the desired pure metal nanoparticles. The quantities used for the RuNP materials are summarised in Table 2.14.

Table 2.14: Mass of metal precursor and carbon support used in the fabrication of the RuNPs@GNFs.

Metal Loading (wt.%)	Mass of $Ru_3(CO)_{12}$ / mg	Mass of GNFs / mg
1	0.5	20
2	0.8	20
5	2.2	20
10	2.2	10

2.4.2.2 RuNiNPs@GNFs (5 wt.%)

The quantities used for the fabrication of RuNiNPs@GNFs with differing ratios of Ru:Ni are summarised in Table 2.15.

Table 2.15: Mass of metal precursor and carbon support used in the fabrication of RuNiNPs@GNFs (5% by wt. total metal) with differing ratios of Ru:Ni.

Ru:Ni Weight Ratio	Mass of $Ru_3(CO)_{12}$ / mg	Mass of $NiCp_2$ / mg	Mass of GNFs[a] / mg
3:1	1.6	0.8	20
1:1	1.1	1.6	20
1:3	0.5	2.4	20

2.4.2.3 NiNPs@GNFs (5 wt.%)

The experimental procedure followed in outlined in Section 2.4.2.1. However, nickelocene (5% by wt. Ni), loaded in the glovebox to avoid decomposition, was used as the metal precursor.

2.4.3 Characterisation of Materials

Transmission electron microscopy was performed on a FEI Tecnai field emission gun with an accelerating voltage of 200 kV. Samples for TEM were prepared by dispersing the material in 2-propanol using an ultrasonic bath and deposited onto a lacey carbon film coated copper grid. Energy dispersive X-ray spectroscopy was carried out using an Oxford Instruments INCA 350 EDX system/80 mm X-Max SDD detector fitted to the Tecnai. Scanning transmission electron microscopy was performed on a FEI Titan3 Themis 300: X-FEG with an accelerating voltage of 300 KeV, fitted with a FEI Super-X-4-detector EDX system for elemental mapping. Thermogravimetric

analysis was performed on a TA instruments SDT-Q600. The experiments were carried out from room temperature to 1000 °C with a heating rate of 5 °C min^{-1}. Powder X-ray diffraction patterns were collected on a Bruker D2 Phaser equipped with a Cu Kα x-ray source (λ = 0.154 nm) operating at 30 kV and 10 mA. Diffraction patterns were collected between 2Θ values of 5 and 95° (step size of 0.2). X-ray absorption fine structure (XAFS) performed at the Diamond light source (beam size: 200 µm x 250 µm, energy: 2.05 – 35 KeV).

ICP-MS was used to determine the Ru content of the solutions using a Thermo Scientific iCAPQc ICP-MS at wavelengths of 240.272 and 349.894 nm. Ru/C (3 x 10 mg) was heated at 900 °C in a muffle furnace to remove of all the carbon material and only leave the Ru metal content. The residual material was then dissolved in nitric acid (2.5 mL, 69% HNO_3) and heated at 50 °C overnight (approx. 12 hours) with stirring. Calibration Ru solutions (0.1, 0.2, 0.5, 1, 2, 5 and 7.5 mg L^{-1}) were prepared using a Ru Standard (purchased from Alfa Aesar (Ru 1000 µg/mL)) and 10% HNO_3 and gave a linear plot with an R coefficient of 0.9999. Blanked showed 0 mg L^{-1} of Ru. Nitrogen adsorption and desorption isotherms were measured at -196 °C (77 K) using a Micromeritic TriStar 3000 apparatus and analysed using TriStar 3000 (V6.04) software. The isotherms were recorded at a relative pressure (P/P0) between 0.05 and 1 with 29 points of measurement in the adsorption stage and 17 points in the desorption stage. The GNF samples were degassed on a Micrometric FlowPrep 060 at 120 °C for 3 hours under a stream of N_2.

2.5 References

1 B. R. Cuenya, *Thin Solid Films*, 2010, **518**, 3127–3150.

2 Z. Chen, Z. Guan, M. Li, Q. Yang and C. Li, *Angew. Chemie - Int. Ed.*, 2011, **50**, 4913–4917.

3 G. A. Rance, W. A. Solomonsz and A. N. Khlobystov, *Chem. Commun.*, 2013, **49**, 1067–1069.

4 W. A. Solomonsz, G. A. Rance, M. Suyetin, A. La Torre, E. Bichoutskaia and A. N. Khlobystov, *Chem. Eur. J.*, 2012, **18**, 13180–13187.

5 W. A. Solomonsz, G. A. Rance, B. J. Harris and A. N. Khlobystov, *Nanoscale*, 2013, **5**, 12200–12205.

6 X. Pan, Z. Fan, W. Chen, Y. Ding, H. Luo and X. Bao, *Nat. Mater.*, 2007, **6**, 507–511.

7 J. M. Planeix, N. Coustel, B. Coq, V. Brontons, P. S. Kumbhar, R. Dutartre, P. Geneste, P. Bernier and P. M. Ajayan, *J. Am. Chem. Soc.*, 1994, **116**, 7935–7936.

8 R. Gao, C. D. Tan and R. T. K. Baker, *Catal. Today*, 2001, **65**, 19–29.

9 R. Vieira, C. Pham-Huu, N. Keller and M. J. Ledoux, *Chem. Commun.*, 2002, **1**, 954–955.

10 J. N. Wang, Y. Z. Zhao and J. J. Niu, *J. Mater. Chem.*, 2007, **17**, 2251–2256.

11 V. Lordi, N. Yao and J. Wei, *Chem. Mater.*, 2001, **13**, 733–737.

12 J. Kang, S. Zhang, Q. Zhang and Y. Wang, *Angew. Chemie - Int. Ed.*, 2009, **48**, 2565–2568.

13 S. Akbayrak and S. Ozkar, *ACS App. Mater. Interfaces*, 2012, **4**, 6302–6310.

14 W. Li, C. Liang, W. Zhou, J. Qiu, Z. Zhou, G. Sun and Q. Xin, *J. Phys. Chem. B*, 2003, **107**, 6292–6299.

15 R. Chetty, S. Kundu, W. Xia, M. Bron, W. Schuhmann, V. Chirila, W. Brandl, T. Reinecke and M. Muhler, *Electrochim. Acta*, 2009, **54**, 4208–4215.

16 H. Vu, F. Gonçalves, R. Philippe, E. Lamouroux, M. Corrias, Y. Kihn, D. Plee, P. Kalck and P. Serp, *J. Catal.*, 2006, **240**, 18–22.

17 M. Aygün, T. W. Chamberlain, M. C. Gimenez-lopez and A. N. Khlobystov, *Adv. Funct. Mater.*, 2018, **28**, 1–15.

18 R. Giordano, P. Serp, P. Kalck, Y. Kihn, J. Schreiber, C. Marhic and J. Duvail, *Eur. J. Inorg. Chem.*, 2003, 610–617.

19 C. Guerret-Piecourt, Y. Le Bouar, A. Loiseau and H. Pascard, *Relation between metal electronic structure and morphology of metal compounds inside carbon nanotubes*, 1994, vol. 372.

20 B. M. Quinn, C. Dekker and S. G. Lemay, *J. Am. Chem. Soc.*, 2005, **127**, 6146–6147.

21 J. Li, M. Moskovits and T. L. Haslett, *Chem. Mater.*, 1998, **10**, 1963–1967.

22 H. C. Choi, M. Shim, S. Bangsaruntip and H. Dai, *J. Am. Chem. Soc.*, 2002, **124**, 9058–9059.

23 L. Qu and L. Dai, *J. Am. Chem. Soc.*, 2005, **127**, 10806–10807.

24 T. W. Chamberlain, T. Zoberbier, J. Biskupek, A. Botos, U. Kaiser and A. N. Khlobystov, *Chem. Sci.*, 2012, **3**, 1919–1924.

25 T. Zoberbier, T. W. Chamberlain, J. Biskupek, M. Suyetin, A. G. Majouga, E. Besley, U. Kaiser and A. N. Khlobystov, *Small*, 2016, **12**, 1649–1657.

26 M. Aygün, C. T. Stoppiello, M. A. Lebedeva, E. F. Smith, M. C. Gimenez-lopez, N. Khlobystov and T. W. Chamberlain, *J. Mater. Chem. A*, 2017, **5**, 21467–21477.

27 P. Serp and E. Castillejos, *ChemCatChem*, 2010, **2**, 41–47.

28 M. Brust, M. Walker, D. Bethell, D. J. Schiffrin and R. Whyman, *J. Chem. Soc., Chem. Commun.*, 1994, 801–802.

29 M. C. Gimenez-lopez, A. Kurtoglu, D. A. Walsh and A. N. Khlobystov,

Adv. Mater., 2016, **28**, 9103–9108.

30 B. Cornelio, A. R. Saunders, W. A. Solomonsz, M. Laronze-cochard, A. Fontana, J. Sapi, A. N. Khlobystov and G. A. Rance, *J. Mater. Chem. A*, 2015, **3**, 3918–3927.

31 A. La Torre, M. del C. Gimenez-Lopez, M. W. Fay, G. A. Rance, W. A. Solomonsz, T. W. Chamberlain, P. D. Brown and A. N. Khlobystov, *ACS Nano*, 2012, **6**, 2000–2007.

32 T. G. Ros, D. E. Keller, A. J. Van Dillen, J. W. Geus and D. C. Koningsberger, *J. Catal.*, 2002, **211**, 85–102.

33 W. a Solomonsz, G. a Rance, B. J. Harris and A. N. Khlobystov, *Nanoscale*, 2013, **5**, 12200–12205.

34 X. Li, T. Hungria, C. Garcia Marcelot, M. R. Axet, P.-F. Fazzini, R. P. Tan, P. Serp and K. Soulantica, *Chem. Commun.*, 2016, 2362–2365.

35 M. Tang, S. Mao, M. Li, Z. Wei, F. Xu, H. Li and Y. Wang, *ACS Catal.*, 2015, **5**, 3100–3107.

36 J. A. Rodriguez, *Surf. Sci. Rep.*, 1996, **24**, 223–287.

37 T. W. Chamberlain, T. Zoberbier, J. Biskupek, A. Botos, U. Kaiser and A. N. Khlobystov, *Chem. Sci.*, 2012, **3**, 1919–1924.

38 T. W. Chamberlain, J. Biskupek, S. T. Skowron, A. V Markevich, S. Kurasch, O. Reimer, K. E. Walker, G. A. Rance, X. Feng, K. Mu, A. Turchanin, M. A. Lebedeva, A. G. Majouga, V. G. Nenajdenko, U. Kaiser, E. Besley and A. N. Khlobystov, *ACS Nano*, 2017, **11**, 2509–2520.

39 J. Chae, H.-S. Park and S. Kang, *Electrochem. Solid-State Lett.*, 2002, **5**, C64–C67.

40 C. A. Wilde, Y. Ryabenkova, I. M. Firth, L. Pratt, J. Railton, M. Bravo-sanchez, N. Sano, P. J. Cumpson, P. D. Coates, X. Liu and M. Conte, *Appl. Catal. A, Gen.*, 2019, **570**, 271–282.

41 I. O. Bashkin, V. E. Antonov, A. V Bazhenov, I. K. Bdikin, D. N. Borisenko, E. P. Krinichnaya, A. P. Moravsky, A. I. Harkunov, Y. M. Shul'ga, Y. A. Ossipyan and E. G. Ponyatovsky, *J. Exp. Theor. Phys.*, 2004, **79**, 226–230.

42 H. E. Swanson, R. K. Fuyat and G. M. Ugrinic, *Natl. Bur. Stand. (U.S.),Circular 539*, 1995, **4**, 1–74.

43 Y.-P. Wang, Z.-J. Ding, Q.-X. Liu, W.-J. Liu, S.-J. Ding and D. W. Zhang, *J. Mater. Chem. C*, 2016, **4**, 11059–11066.

44 G. Yuan, H. Shimizu, T. Momose and Y. Shimogaki, *Microelectron. Eng.*, 2014, **120**, 230–234.

45 Y. Zhang, L. Du, X. Liu and Y. Ding, *Nanoscale*, 2019, **11**, 3401–3758.

46 M. Sarr, N. Bahlawane, D. Arl, M. Dossot, E. McRae and D. Lenoble, *J. Phys. Chem. C*, 2014, **118**, 23385–23392.

47 L. C. Kalutarage, P. D. Martin, M. J. Heeg and C. H. Winter, *J. Am. Chem. Soc.*, 2013, **135**, 12588–12591.

48 B. S. Lim, A. Rahtu and R. G. Gordon, *Nat. Mater.*, 2003, **2**, 749–754.

49 M. Kim, S. Nabeya, D. K. Nandi, K. Suzuki, H.-M. Kim, S.-Y. Cho, K.-B. Kim and S.-H. Kim, *ACS Omega*, 2019, **4**, 11126–11134.

50 L. X. Song, Z. K. Yang, Y. Teng, J. Xia and P. Du, *J. Mater. Chem. A*, 2013, **1**, 8731–8736.

51 S. W. Ryu, J. Yoon, H.-S. Moon, B. Shong, H. Kim and H.-B.-R. Lee, *Nanotechnology*, 2017, **28**, 115301 (8pp).

52 A. L. Smeigh, L. Le Pleux, J. Fortage, Y. Pellegrin, E. Blart, F. Odobel and L. Hammarstrom, *Chem. Commun.*, 2012, **48**, 678–680.

53 B. Perez-Fernandez, D. Martin-Yerga and A. Costa-Garcia, *RSC Adv.*, 2016, **6**, 83748–83757.

54 G. H. Yue, Y. C. Zhao, C. G. Wang, X. X. Zhang, X. Q. Zhang and Q. S. Xie, *Electrochim. Acta*, 2015, **152**, 315–322.

55 Y. Zhang, Y. Liu, Y. Guo, Y. X. Yeow, H. Duan, H. Li and H. Liu, *Mater. Chem. Phys.*, 2015, **151**, 160–166.

56 R. Hones and J. Ruhe, *Langmuir*, 2018, **34**, 5342–5351.

57 Z. H. Ibupoto, K. Khun, V. Beni and M. Willander, *Soft Nanosci. Lett.*, 2013, **3**, 46–50.

58 H. Yang, G. Gao, F. Teng, W. Liu, S. Chen and Z. Ge, *J. Electrochem. Soc.*, 2014, **161**, B216–B219.

59 X. Niu, M. Lan, H. Zhao and C. Chen, *Anal. Chem.*, 2013, **85**, 3561–3569.

60 S. B. Erenburg, N. V Bausk, L. N. Mazalov, R. S. Shulman, T. V Us, V. A. Emelianov and V. G. Torgov, *J. Mol. Liq.*, 2005, **118**, 71–76.

61 A. I. Frenkel, *Chem. Soc. Rev.*, 2012, **41**, 8163–8178.

62 D. C. Koninsberger and R. Prins, *X-ray Absorption: Principles, Applications, Techniques of XAFS, SEXAFS and XANES*, Wiley, New York, 1998.

63 L. Zhu, Y. Jiang, J. Zheng, N. Zhang, C. Yu, Y. Li, C.-W. Pao, J.-L. Chen, C. Jin, J.-F. Lee, C.-J. Zhong and B. H. Chen, *Small*, 2015, **34**, 4385–4393.

64 K. Mori, K. Miyawaki and H. Yamashita, *ACS Catal.*, 2016, **6**, 3128–3135.

65 J. Zhang, J. Teo, X. Chen, H. Asakura, T. Tanaka, K. Teramura and N. Yan, *ACS Catal.*, 2014, **4**, 1574–1583.

66 S. Storck, H. Bretinger and W. F. Maier, *Appl. Catal. A Gen.*, 1998, **174**, 137–146.

Chapter 3: Evaluation of the Catalytic Activity and the Confinement Effects of MNPs@GNFs using Batch Hydrogenation Reactions

3.1 Introduction

CNTs have been demonstrated to be effective supports for immobilising MNPs and have been employed for a variety of reactions including; Fischer-Tropsch synthesis,[1–6] NH_3 decomposition,[7] hydrogenation/ dehydrogenation,[8–12] selective oxidation[13] and photocatalysis.[14]

Compared to other nano-containers they are significantly more thermally stable, have a higher tensile strength (higher than steel) and have chemically unreactive internal channels, making them ideal reaction vessels for performing a vast range of chemical reactions.[15,16] Very narrow containers such as single-walled carbon nanotubes (SWNTs), with an internal diameter of 1-2 nm, impose extreme confinement on encapsulated molecules making them ideal for the exploration of the fundamental effects of confinement.[16] However, the narrow channels of SWNTs lead to mass transfer limitations necessitating the use of high pressures to aid diffusion into and out of the internal channels of the SWNTs.[16,17]

GNFs have a significantly wider internal channel than CNTs, with internal diameters typically between 50-70 nm, greatly reducing transport resistance, allowing effective transport of molecules through the internal channels and ensuring that the internal cavity is continuously accessible.[16,18] Although significantly wider, GNFs still have the ability to create localised nanoscale environments, where the concentrations of certain reactants are different when compared to the bulk solution. The degree of this local concertation effect is dependent upon the affinity of the reactants to the GNF support, which is linked to both the aromaticity and steric bulk of reactants. Reactants with an increased affinity for the GNFs (i.e. aromatic reagents) can enter the GNF inner cavities at a more efficient rate, therefore leading to an increase in the local concentration of the reactant in the vicinity of the catalytic NPs.[15,17]

Encapsulating MNPs inside these support structures can drastically alter the properties of the MNPs as the internal channels of the GNFs act as both a template and stabilising layer, preventing sintering and leaching of the metal during catalysis.[18–20]

3.1.1 Activity

The effect of the location of the NPs in/on nanoreactors on the resultant activity, has been investigated for a number of catalytic systems. In general, though NPs located on the exterior of the nanoreactors are more accessible to reagents, than those located on the interior of the nanoreactor, they have been found to be less active.

Chen *et al*.[21] investigated the difference in activity for chirally modified PtNPs immobilised on the interior (denoted Pt/CNTs(in), 5% Pt by wt.) and on the exterior of CNTs (denoted Pt/CNTs(out), 5% Pt by wt.), using asymmetric hydrogenation reactions (Scheme 3.1).

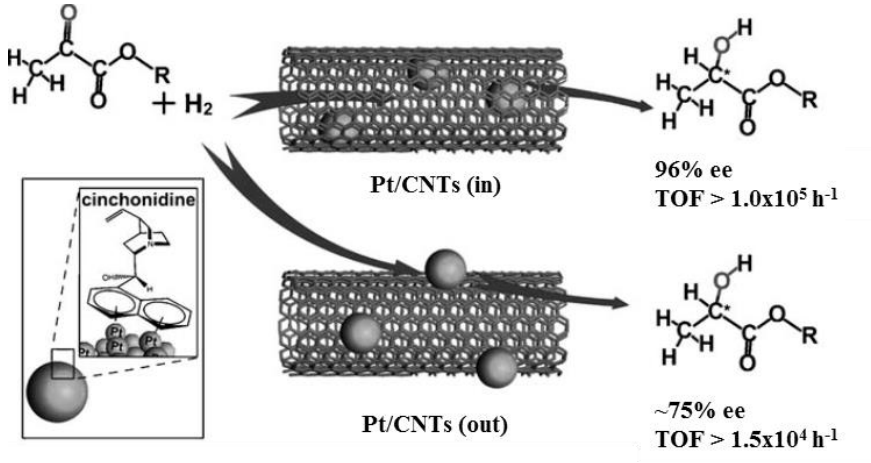

Scheme 3.1: Symmetric hydrogenation of α-ketoesters used to access chirally modified Pt/CNTs (in) and Pt/CNTs (out), where cinchonidine was used as the chiral modifier. Showing a greater activity for the NPs immobilised inside the CNTs.[21]

The activity of the PtNPs confined within the CNTs was greatly enhanced (~80% conversion) compared to Pt/CNTs(out) (<30% conversion). It is also worth noting that not only did they exhibit a higher activity, but also gave greater enantioselectivity; Pt/CNTs(in) gives the product with 96% *ee,* compared to 75% *ee* obtained for Pt/CNTs(out). The enhancement in activity and enantioselectivity for the confined PtNPs was attributed to an enrichment of the chiral modifier, as well as the reactants, inside the channels of the CNTs.[21]

Ran *et al*.[22] investigated the difference in activity for Ru-based catalysts supported on/in CNTs, using the hydrogenation of cellobiose to sugar alcohols. They found an enhancement in activity for RuNPs@CNT (57% conversion) compared to that of RuNPs/CNT (~40% conversion). The effect of varying the CNT channel size was also investigated via fabrication and utilisation of three RuNPs@CNT catalysts where the size in the CNT channel

varied from 6 to 12 nm. TEM confirmed that the RuNPs were approximately 2-4 nm in each case (Figure 3.1), indicating that the CNT channel diameter was not a critical factor in determining the RuNP size. This also meant that any changes in activity observed were due to the change in the diameter of the CNTs only. It was found that the catalytic activity of the RuNPs@CNT catalyst was enhanced with decreasing CNT channel size. This is important as it suggests that the confinement effect decreases with increasing CNT diameter, lowering the catalytic performance of the material.[22]

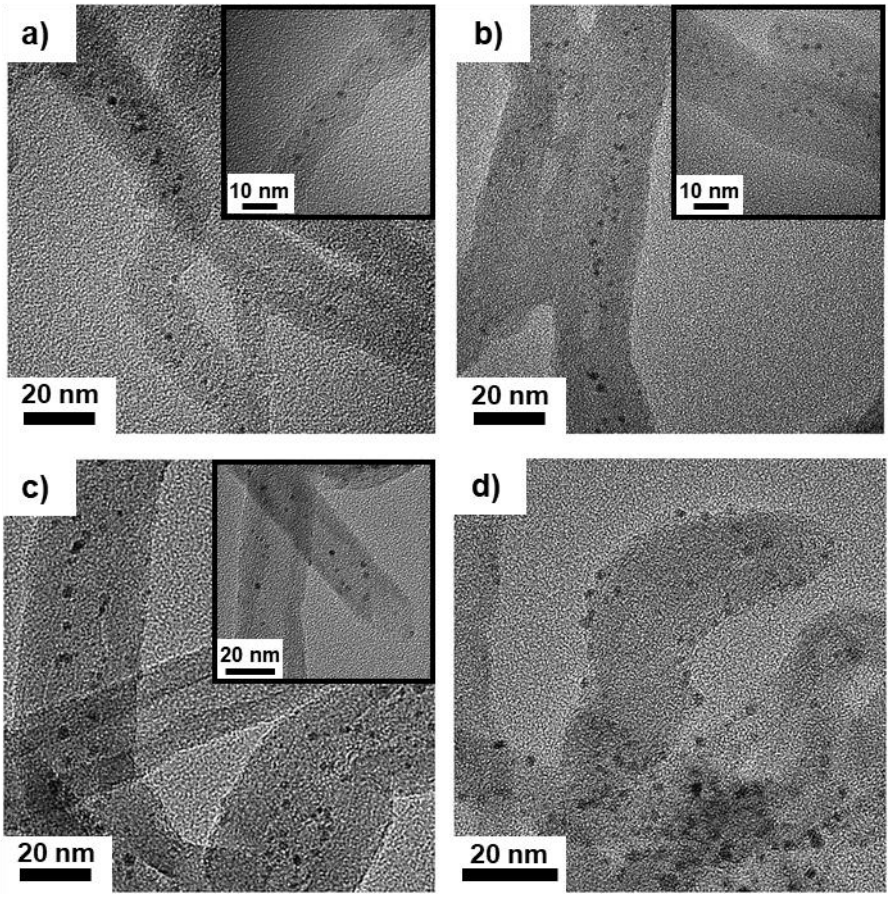

Figure 3.1: TEM images of RuNP based catalysts with different CNT internal diameters a) RuNPs@CNT-6, b) RuNPs@CNT-8, c) RuNPs@CNT-12 and RuNPs/CNT-6.[22]

Rance *et al.*[19] also investigated the use of CuNPs immobilised on/in GNFs as nanoreactors in click chemistry (~4% Cu by wt. for both the confined and unconfined catalyst). The CuNPs anchored to the graphitic step edges within GNFs exhibited higher catalytic activity, with an increase in reaction rate and an improved conversion to the desired product, compared to catalytic centres on the exterior of the nanoreactors. This was attributed to an increased local concentration of reactants, due to favourable van der Waals interactions between the aromatic starting materials and the graphitic step edges.[19]

In summary, confining MNPs inside of these carbon supports has been shown to greatly alter the catalytic activity of the materials.

3.1.2 Recyclability

Recyclability is an important feature for effective catalysts and is key for their use in industrial applications. Rance *et al.*[19] demonstrated that confinement in carbon nanoreactors has a significant effect on the stability of the active sites (MNPs) by looking at the recyclability of CuNPs@GNFs compared to CuNPs/GNF and CuNPs dispersed in solution (Figure 3.2). In the case of the CuNPs/GNF, analysis of consecutive click reactions using the same catalyst material showed reduced conversion of reactants over time with almost total loss of catalytic activity after 5 cycles. In contrast to this, no drop in reactant conversion was seen for CuNPs@GNFs (Figure 3.2b).

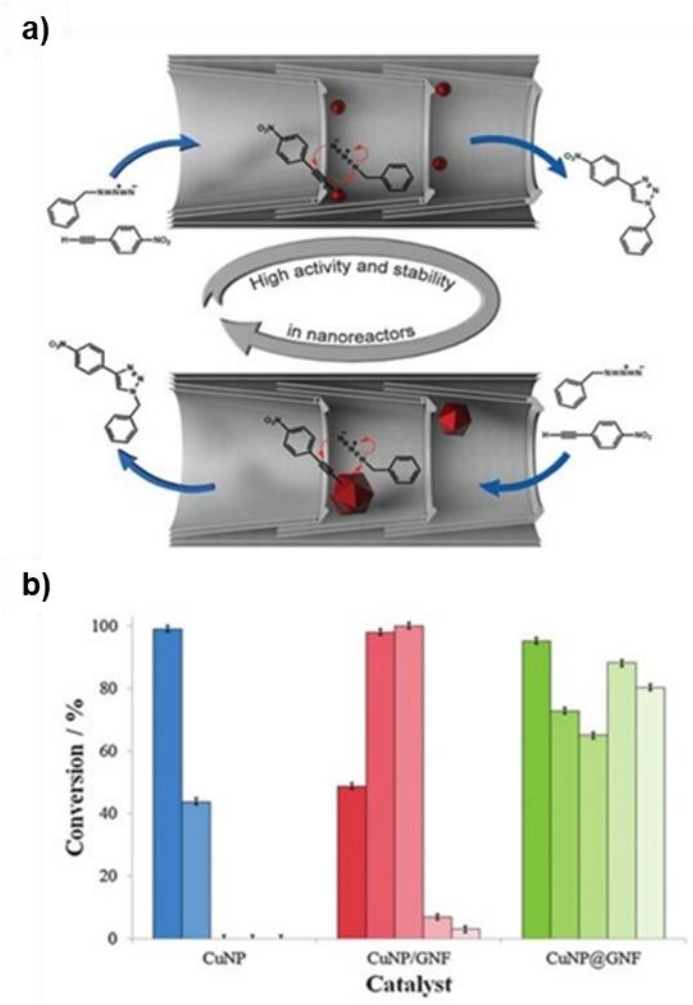

Figure 3.2: a) Schematic illustration of the retention of high activity of CuNPs@GNF showing the increase in the size of the CuNPs due to coalescence. b) Recyclability of CuNPs (blue), CuNPs/GNF (red) and CuNPs@GNF (green) measured over 5 cycles (each cycle lasting 72 h), showing an enhancement in recyclability for the confined CuNPs@GNF catalyst.[19]

TEM revealed that whilst the CuNPs in the CuNPs@GNFs material remained “anchored” to the graphitic step edges of the GNF, undergoing slight dynamic coalescence resulting in an increase in particle size to approximately 30 nm, the CuNPs in the CuNPs/GNF were gradually desorbed with no Cu material remaining after 5 cycles.[19]

Though the general observations made in this study are reinforced by the experimental data, it is apparent from Figure 3.2b that the conversion obtained for the recyclability investigation of the Cu/GNF and CuNPs@GNF catalysts contains some inconsistencies. For example, there is a drastic increase in conversion for the Cu/GNF catalyst after the first cycle with no explanation given as to why this may be the case. In the case of the CuNPs@GNF catalyst the fluctuation in results for each cycle was attributed solely to the change in size of the CuNPs, which does not completely explain the variation in reactivity of the CuNP catalyst over time.

However, the results of this investigation still indicate that the GNF step-edges interact with the immobilised MNPs, increasing their stability, which in turn, reduces leaching of the MPs into solution, ultimately keeping the nanoreactor catalytically active for subsequent reaction cycles.

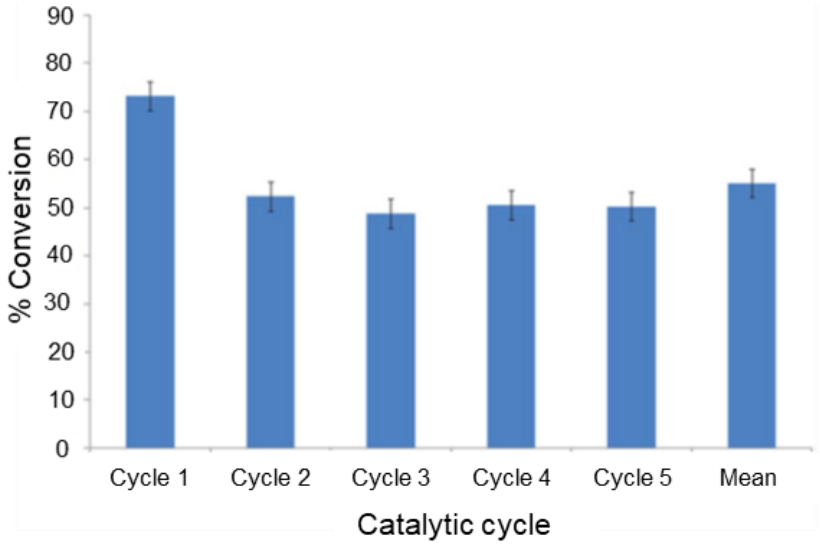

Figure 3.3: Recyclability of PdNPs@GNF (~8 wt.%) over 5 catalytic cycles (each cycle was 16 h) showing that, despite an initial decrease after the first cycle, conversion remained consistent for at least 5 cycles.[23]

The coalescence of NPs to form larger particles, in the supported catalyst, was also observed by Cornelio and co-workers[23] who looked at the effect of confinement on Suzuki-Miyaura reaction using GNF supported Pd nanoparticle catalysts. Their results showed an initial decrease in activity after the first cycle which was attributed to an increase in NP size from 7.0 ± 2.2 to

21.8 ± 14.8 nm. Subsequent cycles however, remained consistent for a least 5 cycles (Figure 3.3).[23]

3.1.3 Selectivity and Confinement Effects in CNRs

GNF nanoreactors have the ability to create localised nanoscale reaction environments, were the concentrations of certain reactants are different when compared to the bulk solution. The degree of this local concentration effect is dependent upon the affinity of the reactants to the GNF support, which is linked to both the aromaticity and steric bulk of reactants. Reactants with increased affinity for the GNFs (e.g. aromatic reagents) can enter the GNF inner cavities at a more efficient rate, therefore leading to an increase in local concentration of the reactant. [15,17]

The effect of confinement upon selectivity has been investigated by Solomonsz and co-workers,[16] using RhNPs@GNF (~4 wt.%) catalysts for the hydrosilylation of terminal alkynes. They reported that the regioselectivity of the reactions were significantly affected by the spatial confinement in the carbon nanoreactors, with a 3-fold increase in products of dehydrogenative silylation, for the confined catalyst.

As supramolecular interactions of reactant molecules with nanoreactors are often responsible for the altered reactivity observed in confined reactions, they investigated if the balance of aliphatic and aromatic moieties in the local concentration (inside the inner channel of the GNFs) was an important parameter in the regioselectivity of the reaction. They found that when both of the reactants were aliphatic no confinement effect was observed due to the absence of favourable interactions between the reactants and the internal channels of the GNFs. When the alkyne was aromatic but the silane derivative was aliphatic an increase in dehydrogenative silylation products (**4** and **5**) but a decrease in the isomeric ratio, β-(Z):β-(E), was observed. This was attributed to the increased local concentration of the aromatic alkyne. When both of the reactants were aromatic, the favoured product was the β-(Z)isomer, due to the maximised interactions between the starting materials and the inner channel of the GNFs, resulting in the favoured product being the less thermodynamically stable (Z)-isomer.[16] Results are summarised in Figure 3.4 and Table 3.1.

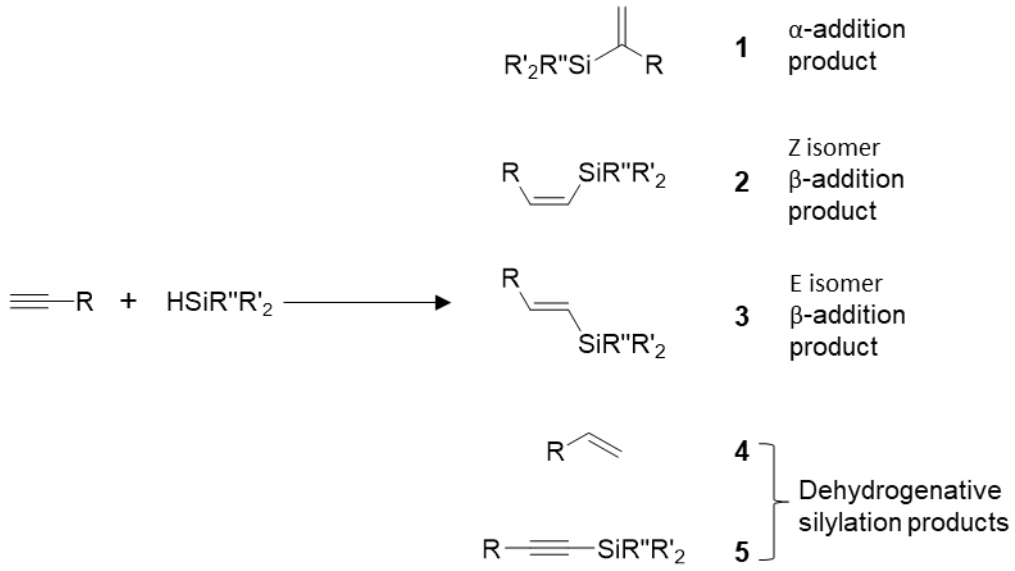

Figure 3.4: Generalised reaction scheme for the hydrosilylation of a terminal alkyne.[16]

Table 3.1: Summary of results obtained for the investigation into the effect of confinement for the RhNPs@GNFs catalysts.[16]

R	R'	R''	Regioselectivity	
			Change in Z/E isomeric ratio	Change in amount of **4** and **5**
Ph	Et	Et	5.8-fold decrease	3.0-fold increase
Ph	Me	Ph	2.6-fold increase	No change
Cy	Et	Et	No change	No change
***n*-Oct**	Et	Et	No change	No change

Solomonsz *et al.*[17] then investigated the effects of confinement for a Pt-based catalyst (PtNPs@GNF, ~6% by wt.), looking specifically at the formation of styrene. When both of the starting materials were aromatic (Figure 3.5, Reaction I), the relative concentrations within the nanoreactor are analogous to that of the bulk solution, and so no change in the yield of styrene produced was reported. However, for a reaction involving to an aliphatic silane (Figure 3.5, Reaction II) an increase in styrene formation was observed indicating that the local concentration of aromatic reactants, within the

nanoreactor, is increased due to favourable π-π interactions, ultimately leading to an altered reaction pathway.

To quantify the local concentration effects observed for these hydrosilylation reactions, competitive reactions were employed where two silane starting materials (one aromatic and the other aliphatic) competed to react with the same alkyne (Figure 3.5, Reaction III). They reported that the aromatic starting material reacted preferentially, favouring the formation of aromatic products, due to the increased local concentration of aromatic reactants within the GNF compared to the bulk solution.[17]

This research clearly demonstrates the ability of GNF nanoreactors to increase the local concentration of aromatic reactants over aliphatic reactants, and therefore govern the selectivity of a given reaction. It would have been interesting, however, to see competitive reactions done with two aromatic silanes, where one contained a bulky R group, to see whether or not transport limitations through the internal channel of the GNFs arise.

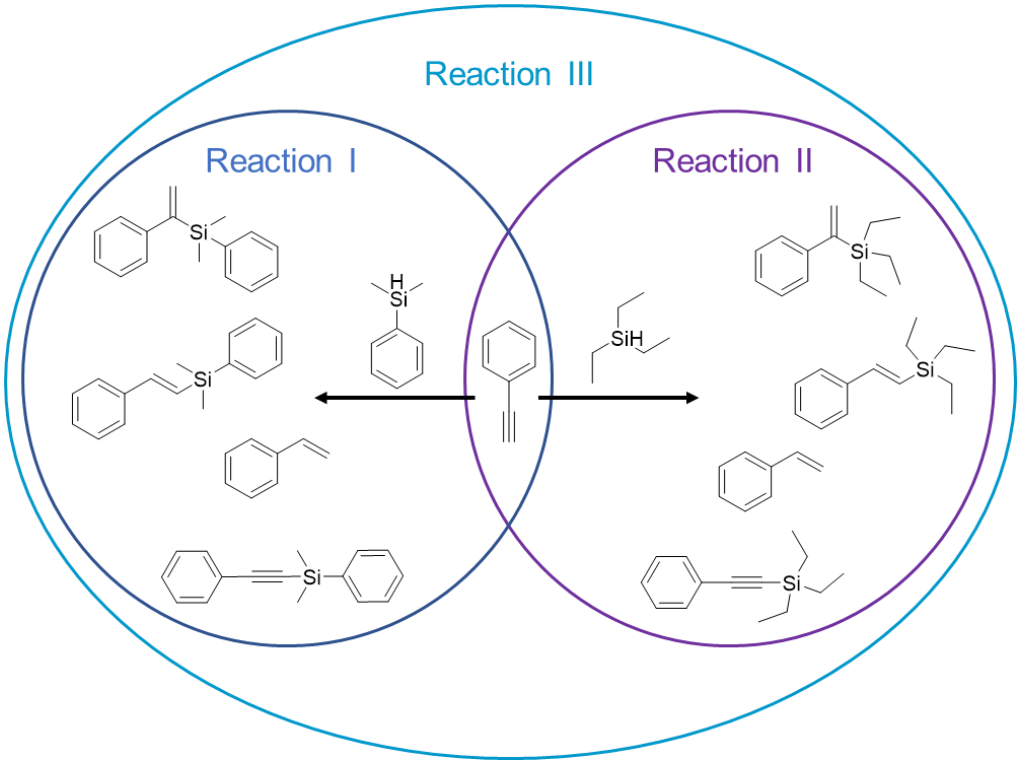

Figure 3.5: The range of products formed in non-competitive and competitive PtNP-catalysed hydrosilylation reactions, used to assess the effect of confinement.[17]

Chamberlain *et al.*[24] encapsulated ruthenium nanoparticles inside single walled carbon nanotubes (SWNTs) and tested their activity for a series of hydrogenation reactions in continuous flow using a milliscale reactor (see Figure 3.6). The internal channel of the SWNTs allowed them to precisely

control the size and thus the catalytic properties of the RuNPs. Negligible conversion was obtained when the reactions were performed using a gaseous mixture of cyclohexane and H_2. However, it was found that adding supercritical CO_2 ($scCO_2$) as the reaction solvent drastically increased the conversions for all hydrogenation reactions tested. This was attributed to the low viscosity of $scCO_2$ enabling it to deliver molecules into the very narrow nanotubes. The catalyst showed excellent stability over extended reaction times when tested for a range of hydrogenation reactions (hydrogenation of cyclooctene, butyraldehyde and cinnamaldehyde).[24]

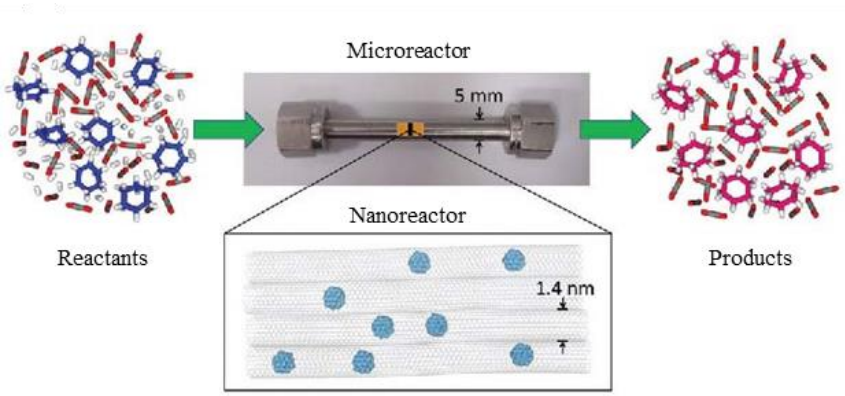

Figure 3.6: Selective hydrogenation of cyclohexene (blue) to cyclohexane (pink) using RuNPs@SWNT catalytic nanoreactors (shown in the expanded box) in a continuous flow $scCO_2$ milliscale reactor.[24]

3.1.3.1 Competitive Reactions

The use of competitive reactions to explore confinement effects has been previously reported. Aygun *et al.*,[25] investigated the catalytic properties of RuNPs supported in different nanoreactors, with differing diameters (SWNTs, width: 1.5 nm and GNFs, width: 50-70 nm), using exploratory alkene hydrogenation reactions. Norbornene and benzonorbornadiene were chosen as the reactant molecules to investigate due to their van der Waals size (less than 1.5 nm) and their similarity in shape (non-planar) with benzonorbornadiene having an additional aromatic ring which increases it's steric bulk[25] and should allow for favourable π-π stacking interactions with the support structure.[16,19,26]

Initially, individual reactions for the reduction of norbornene and benzonorbornadiene were performed. It was found that RuNPs@CNRs preferentially reduced benzonorbornadiene over norbornane (evident from increase in conversions observed). This was attributed to the aromatic character of the support material facilitating favourable π-π stacking

interactions with the aromatic reagent and thus increasing its local concentration within the support structure.

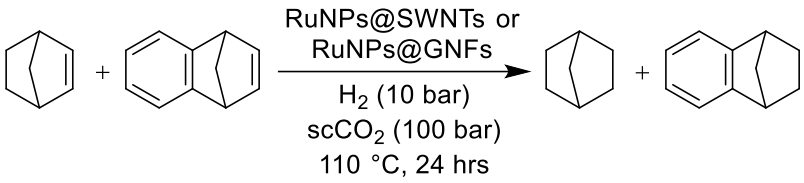

Scheme 3.2: Reaction scheme highlighting the conditions used for competitive reactions of norbornene and benzonorbornadiene. Catalyst metal loading approximately 1 wt.%.[25]

Competitive reactions were carried out in a high-pressure batch reactor in which equimolar amounts of the two starting materials where simultaneously reduced. Full reaction conditions are highlighted in Scheme 3.2. Greater TONs for competitive reactions compared to individual reactions for RuNPs@GNFs and Ru/C were observed, with RuNPs@GNFs displaying greater activity and selectivity compared to RuNPs@SWNTs (enhanced selectivity towards benzonorbornadiene observed). This was attributed to the GNF support structure having a significantly wider internal cavity meaning that the RuNP active sites were continuously accessible, and an increase in local concentration of reactants.[25]

3.1.4 Summary and Conclusion

GNFs are an exciting material to be used as a solid support for immobilising MNPs to form nanoreactors. They have numerous advantages over other support structures such as; (1) a wider and continuous internal channel allowing for effect transport of reagents through their internal channels; and (2) their graphitic step-edges at which MNPs are preferentially anchored due to an increase in favourable van der Waals interactions. This creates localised nanoscale reaction environments, with greatly altered concentrations of reactants as compared to the bulk phase, which can lead to changes in activity and product selectivity.

3.1.4.1 Hydrogenation Reaction

The use of ruthenium in catalysis is highly attractive due to its low cost and versatility, which is demonstrated by its ability to catalyse a number of reactions including; Fischer-Tropsch synthesis,[27,28] metathesis,[29,30] and simple hydrogenation reactions.[10,24,31,32]

This Chapter looks at using immobilised ruthenium metal nanoparticles (RuNPs) and bimetallic ruthenium and nickel nanoparticles (RuNiNPs) in the inner cavities of GNFs as heterogeneous catalysts.

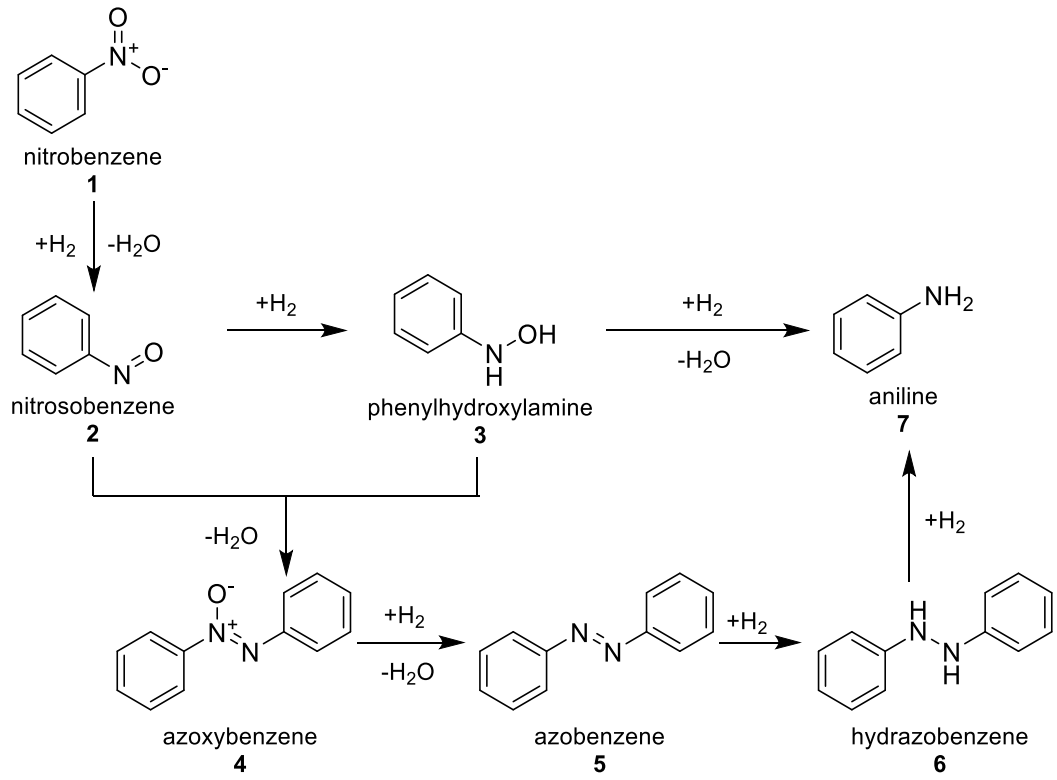

Scheme 3.3: Possible reaction pathways for the reduction of nitrobenzene.[33,34]

Reduction of nitrobenzene was selected as a model reaction to access the use of RuNPs@GNFs and RuNiNPs@GNFs as nanoreactors, in terms of activity, selectivity and recyclability, for the following reasons; (1) Aniline, one of the major products from the reduction of nitrobenzene, can be used in the production of pharmaceuticals, polymers, pigments and dyes;[35–37] (2) there are two reaction pathways leading to the formation of aniline (see Scheme 3.3) allowing for the effects of confinement on reaction selectivity to be explored, by comparison to a commercially available unconfined Ru/C catalyst;[33,34] and (3) RuNPs have already been shown to catalyse the reduction of nitrobenzene.[31]

3.2 Results and Discussion

3.2.1 Catalytic Activity Screening using Hydrogenation of Nitrobenzene

The hydrogenation of nitrobenzene was employed to probe the catalytic performance of the mono- and bimetallic materials fabricated. By investigating

the activity of these materials' fundamental insight into how the conditions used during the fabrication process not only influence the structural features of the resultant material, but also the catalytic performance.

3.2.1.1 Catalytic Transfer Hydrogenation

3.2.1.1.1 Investigating the Catalytic Activity of RuNPs@GNFs

The catalytic activity of RuNPs@GNFs (5 wt.%) was investigated using the transfer hydrogenation of nitrobenzene. To ensure that a reasonable amount of conversion, in a reasonable amount of time was obtained, initial optimisation reactions were carried out using commercially available Ru/C (5% by wt. Ru) as the catalyst. This will also act as a non-porous control to allow for the investigation into the confinement effect imposed by the GNFs for the fabrication MNPs@GNFs and has been previously reported to catalyse this reaction.[31] As a starting point, experimental conditions adapted from a study conducted by Sarmah and Dutta,[38] who investigated the catalytic transfer hydrogenation of nitro groups in the presence of Ru^0NPs supported on montmorillonite clay, were used (Table 3.2).

For reactions 1 and 2, a mixture of products was obtained; azobenzene (**5**) and azoxybenzene (**4**), with the major product being **5**. Although no aniline was obtained the aim was to monitor the reaction over a reasonable amount of time with a reasonable amount of conversion obtained, in order to assess the use of RuNPs@GNFs as nanoreactors, and so reaction was deemed suitable for this purpose. The formation of the different products was monitored by GC.

Although good conversion was obtained for reaction 3, a large amount of catalyst was required. Therefore, the reaction was scaled down from 50 mg to 2 mg (all other reagents where scaled approximately by a factor of 10). However, after 20 h it was evident that the reaction had not gone to completion, possibly due to the lower concentration of NaOH used. The concentration of NaOH was therefore increased (reaction 5) to match that reported by Sarmah and Dutta.[38] With an increase in the concentration of NaOH no conversion of nitrobenzene was observed, suggesting it was not the concentration of NaOH affecting the reaction. Reaction 6 was completed, ensuring that the concentration of NaOH solution was equal to that of reactions 2 and 3. This was successful and after 3.5 hours no starting material was observed by TLC. This was then confirmed by GC analysis.

Table 3.2: Summary of the reaction conditions used for the optimisation of the reduction of nitrobenzene catalysed by Ru/C (5 wt.%). The black box indicates the conditions used by Sarmah and Dutta.[38]

Reaction no.	Mass of catalyst / mg	Nitrobenzene / mmol	Conc. of NaOH in IPA / mol dm^{-3}	Volume of NaOH in IPA / mL	NaOH equiv.	Time / h
Sarmah[38]	50	0.2	0.025	0.5	2.5	12
1	50	2.0	0.025	0.5	0.25	16
2	50	2.0	0.1	2	1	17
3	50	2.0	0.1	2	1	4
4	2	0.16	0.01	0.05	0.3	20
5	2	0.16	0.04	0.4	2.5	6
6	2	0.16	0.1	0.5	3	3.5
7	2	0.16	0.2	1	6	6
8	2	0.16	0.4	2	12	6

Reactions 7 and 8 were carried out at an increased concentration of NaOH in IPA solution to try and push the reaction to form aniline. However, no conversion to aniline was observed.

Reactions 6-8 were repeated but in the absence of a catalyst to ensure that the NaOH solution was not acting as a co-catalyst in the reaction. The results showed that within the times tested, no reaction occurred for 0.1 and 0.2 M NaOH. In the case of 0.4 M NaOH, a small amount of the starting material reacted; however, was not enough to yield complete conversion. Control reactions where then carried out in the absence of biphenyl to ensure that it was not blocking the active sites of the nanoreactors. No significant difference in activity was observed suggesting that the use of biphenyl as an internal standard did not hinder the reaction.

The optimum conditions for the reduction of nitrobenzene catalysed by commercially available Ru/C (5 wt.%) are outlined in Scheme 3.4 (these conditions correspond to those outlined in Table 3.2, line 6). These optimum conditions were used in order to test the activity of RuNPs@GNFs (5 wt.%).

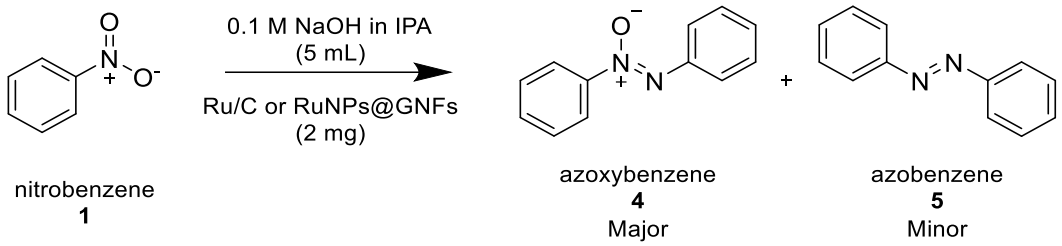

Scheme 3.4: Reaction conditions used (Table 3.2, line 6) to compare the activity of RuNPs@GNFs to Ru/C, showing that the major product obtained is azoxybenzene (4).

It was evident through GC analysis that the reaction did not go to completion, as a small amount of nitrobenzene (3%) remained after 3.5 h (full conversion had occurred for Ru/C (example GC shown in Figure 3.7) after this reaction time, see Figure 3.8). However, a much larger amount of azobenzene (**5**) was produced than when Ru/C was used. This could be due to an increased local concentration of reactants.[17] In order to form azoxybenzene (**4**) both nitrosobenzene (**2**) and phenylhydroxylamine (**3**) need to react, both of which are aromatic and will, therefore have favourable interactions with the internal channel of the GNF, resulting in an increase in concentration of **2** and **3** within the channel of the GNF as compared to the bulk solution. As a result of this **4** will be formed faster than in an unconfined environment (such as Ru/C). This will then in turn form azobenzene (**5**) more quickly (see Section 3.1.4.1, Scheme 3.3 for the full reaction pathway).

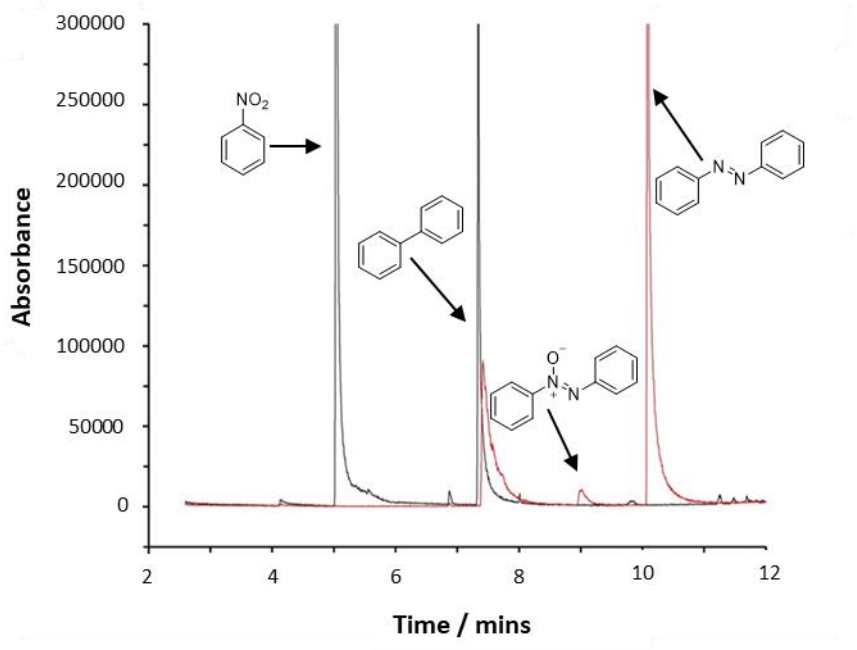

Figure 3.7: Example GC spectrum for nitrobenzene hydrogenation where the black and red line represent GC traces for 0 and 3.5 hours, respectively.

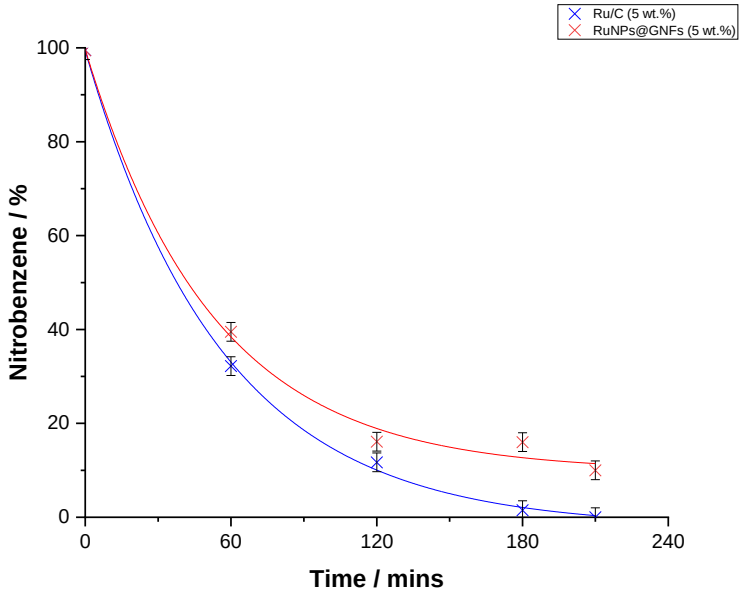

Figure 3.8: The % decrease of nitrobenzene over time for the Ru/C (blue line) and RuNPs@GNFs (red line) catalysts (both 5 wt. %). TON = 111 and 150, respectively. % Decrease of nitrobenzene given as an average of 3 runs.

The turnover numbers (TON), calculated as number of moles of converted starting material per number of moles of Ru metal in the catalyst, were 111 and 150 for the Ru/C and RuNPs@GNFs catalysts, respectively.

3.2.1.1.2 Recyclability

To test the stability of the catalytic system the recyclability of Ru/C and RuNPs@GNFs (both 5 wt.%) over a number of repeat catalytic cycles was studied. The performance of the catalysts was tested in five consecutive nitrobenzene reduction reactions (Figure 3.9), under the reaction conditions highlighted in Scheme 3.5, with each cycle lasting 6 h. The catalyst was removed from the reaction mixture by filtration, washed thoroughly with isopropanol to remove any trace amounts of starting material/products, and then dried overnight before being used in the next reaction cycle. This process was repeated in triplicate to ensure reproducibility of results.

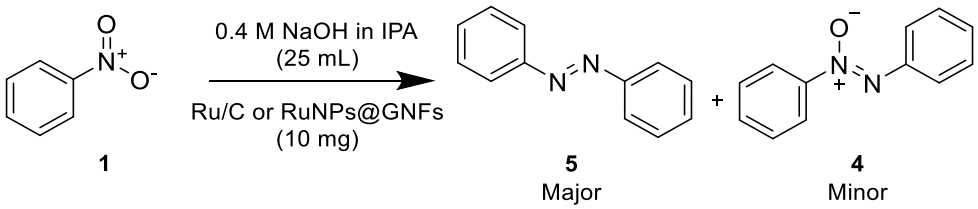

Scheme 3.5: Reaction conditions used for the recyclability testing. The yield of azobenzene (5) was monitored by GC analysis after each successive cycle.

Similar yields of azobenzene were achieved for the first cycle of catalysis, 79% and 77% for Ru/C and RuNPs@GNFs respectively. However, whilst the catalytic activity of Ru/C stayed almost constant during the 5 consecutive runs, with only a slight decrease in activity which was probably due to a small loss of catalyst mass during the recovery operations (Figure 3.9), the catalytic activity of RuNPs@GNFs (Figure 3.9) shows a significant decrease in the second cycle, forming only a 60% yield of azobenzene. From Figure 3.9, after the initial lose in catalytic activity after the second cycle subsequent runs yield similar yields of azobenzene.

There are three possibilities that could explain the observed decrease in catalytic activity: (1) the MNPs could have undergone dynamic coalescence, where the size of the NPs increases but they remain anchored to the step-edges of the GNF; (2) detachment of the MNPs from the support surface; and (3) leaching of the catalyst into solution.

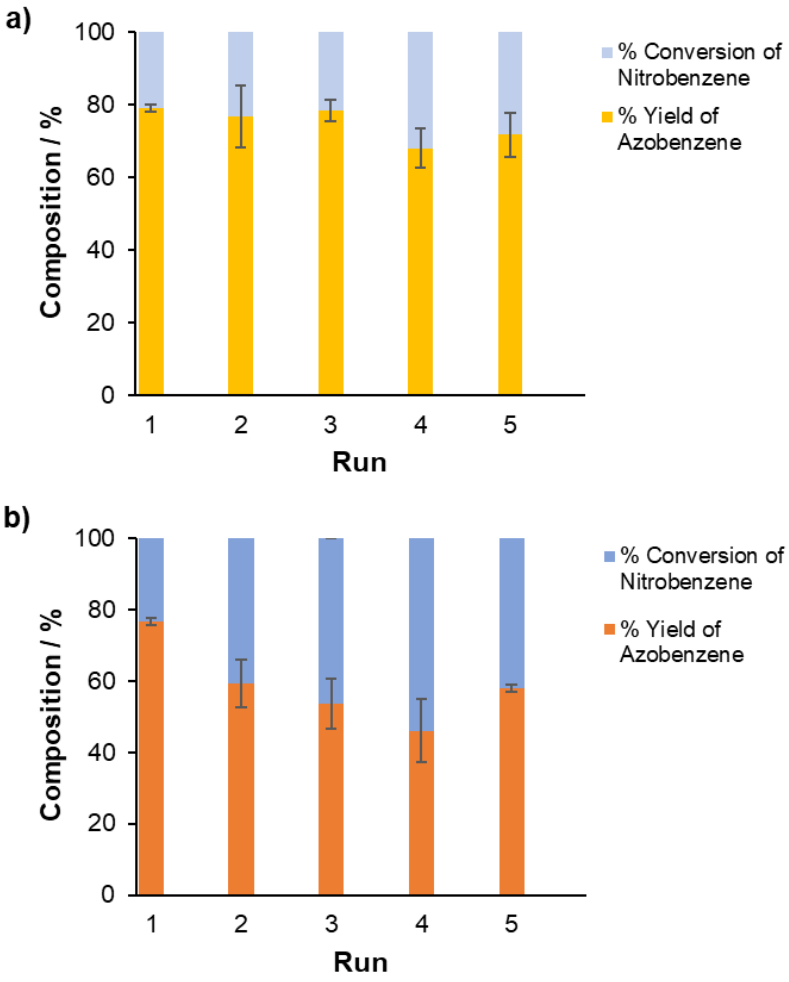

Figure 3.9: Comparison of the stability and recyclability of a) Ru/C and b) RuNPs@GNFs in 5 consecutive nitrobenzene reduction reaction cycles, each lasting 6 hours. % Composition given as an average of 3 runs.

From TEM analysis of the recycled catalyst (Figure 3.10), it is evident that the majority of the RuNPs have become detached from the graphitic step edges and have started to form clusters (the RuNPs are no longer uniformly dispersed within the inner cavity of the GNF). As well as this, there is a significant change in the shape of the RuNPs where they have become less spherical, with a change in aspect ratio of 1:1.2 to 1:1.8. This change in shape could potentially be caused by the basic conditions of the reaction. In order to test this theory, the reaction would need to be carried out using a lower concentration of NaOH, to determine if the same change in shape is observed. These changes in RuNP distribution and shape are probably the cause of the observed decrease in activity for the RuNPs@GNFs (5 wt.%) catalyst.

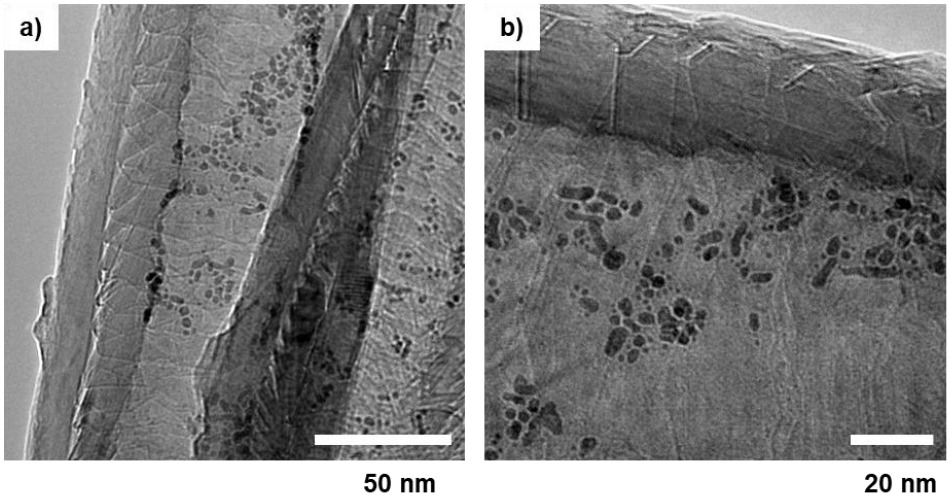

Figure 3.10: TEM micrographs of recycled RuNPs@GNFs (5 wt.%) showing a change in nanoparticle shape and the detachment of the RuNPs from the step edges of the interior of the GNF. Average aspect ratio 1:1.8.

3.2.1.1.3 Investigation into The Effect that the Ratio of Carbon Support to Metal has on the Rate of Reaction

The effect of altering the ratio of carbon support to Ru metal was investigated using the reduction of nitrobenzene catalysed by RuNPs@GNFs with different metal loadings (1, 2, 5 and 10 wt.%). In each case the total amount of ruthenium present was kept the same to ensure any observed changes in reaction were caused by the differing ratios of carbon support to metal, rather than more/less metal catalyst being present. The reaction conditions used are detailed in Table 3.3.

From Figure 3.11 it is evident that there is no profound effect on rate of reaction by altering the ratio of active sites, RuNPs, to carbon support, GNFs. However, interestingly, the ratio of RuNPs to GNF does seem to affect the selectivity of the reaction, with greater yields of azobenzene obtained the

smaller the ratio. This is potentially due to an increase in the surface area of the carbon support in which the reactants can absorb onto the interior of the GNF.

Table 3.3: Reaction conditions used for the investigation into the effect of altering the ratio of carbon support to metal has on the rate of reaction for the reduction of nitrobenzene. Due to the quantity of catalyst required for 1 wt.% the reaction was scaled down, all other conditions were kept constant. [a]

	1 wt.%	**1 wt.% (scaled)**	**2 wt.%**	**5 wt.%**	**10 wt.%**
Mass of catalyst / mg	10	5	5	2	1
Mass of biphenyl / mg	2	1	2	2	2
Mass of nitrobenzene / mg	20	10	20	20	20
Volume of NaOH in IPA / mL	5	2.5	5	5	5
Conc. of NaOH / mol dm^{-3}	0.2	0.2	0.2	0.2	0.2

[a]Refluxed for 5 hours.

It can be seen that, for the confined RuNPs@GNFs (5 wt.%) catalyst, between 3-5 h there is a dramatic increase in the production of azobenzene (Figure 3.11b). In comparison to this, the unconfined Ru/C (5 wt.%) catalyst shows no obvious increase in the production of azobenzene despite having the same ratio of metal to carbon support. This is most likely due to the local concentration effect seen upon confinement due to favourable interactions between nitrobenzene and the GNF support allowing for an increase in the local concentration of reactants, ultimately leading to the quicker formation of azobenzene. This increase in local concentration of aromatic molecules within GNFs has been previously reported by Solomonsz *et al.*.[17]

Contrary to the literature, in this case, the size of the RuNPs doesn't greatly affect the catalytic activity.

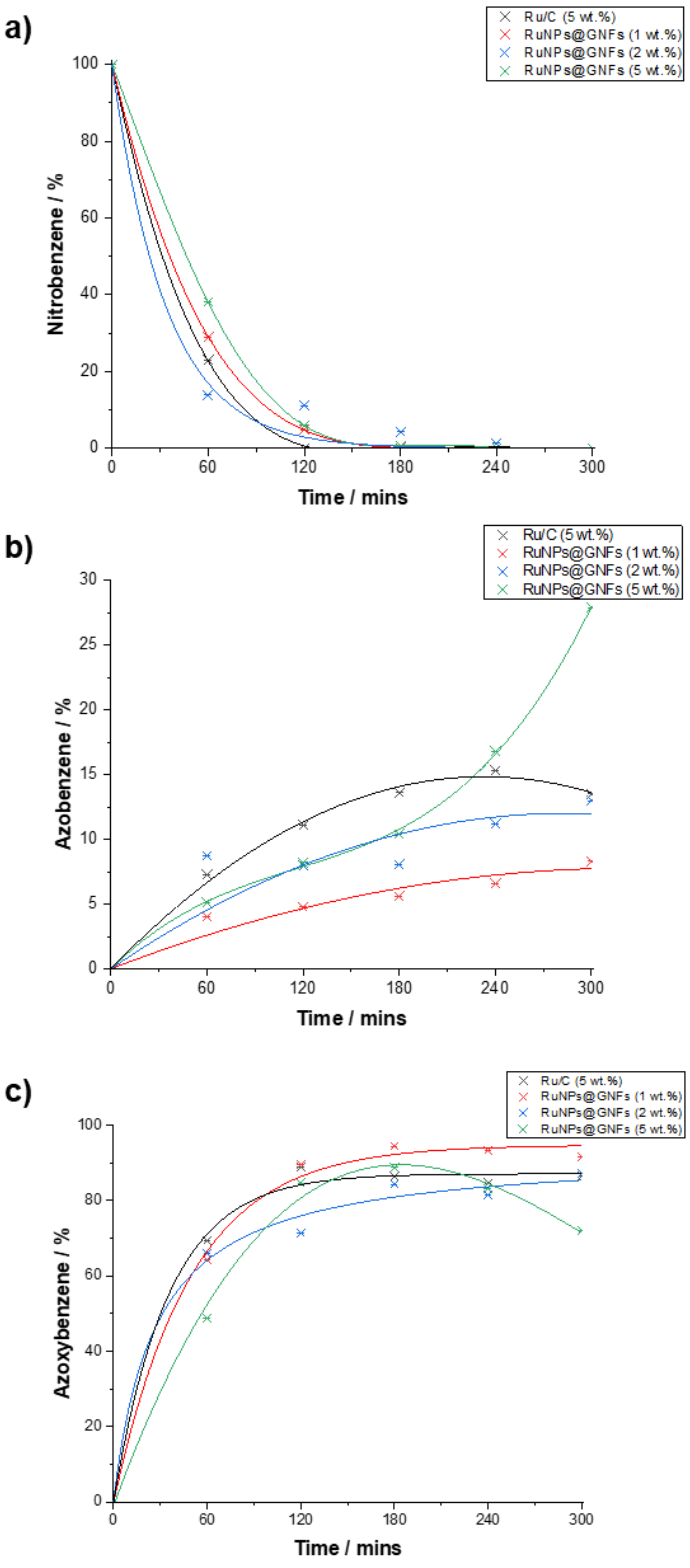

Figure 3.11: a) Plot of % starting material as a function of time for each catalyst with differing Ru metal wt.%; showing no profound effect on the rate of reaction by altering the ratio of active sites to carbon support; b) Plot of azobenzene % against time, showing that decreasing the ratio of RuNPs to carbon support increases the yield of azobenzene; c) Plot of azoxybenzene % against time; b) and c) also show the effect of confinement by comparison between Ru/C and RuNPs@GNFs (both 5wt.%).

3.2.1.2 Batch H_2 Reactions

Hydrogenation reactions were performed using a stainless-steel batch reactor (see Figure 3.19 in Section 3.4.3). Initially, optimisation reactions for the hydrogenation of nitrobenzene catalysed by commercially available Ru/C (5 wt.%) were carried out. As a starting point, experimental conditions were adapted from a study conducted by Aygun *et al*.,[39] who investigated the reduction of nitrobenzene catalysed by PtNPs@GNFs and PdNPs@GNFs. Initial reaction conditions: Ru/C (10 mg, 5 wt.% Ru), ethanol (0.2 mL), nitrobenzene (1.0 mmol) and 1,3,5-trimethoxybenzene (16 mg). Reagents were sealed in the high-pressure reactor before being flushed with nitrogen to exclude air. H_2 (10 bar) was then introduced into the system 5 times before the reactor was charged to the desired pressure for reactions (10 bar). The reactor was stirred at room temperature for 1 – 24 hours and reactions were monitored by ^{1}H NMR. From Figure 3.12 it is evident that conversion of nitrobenzene to aniline increases with increased reaction times.

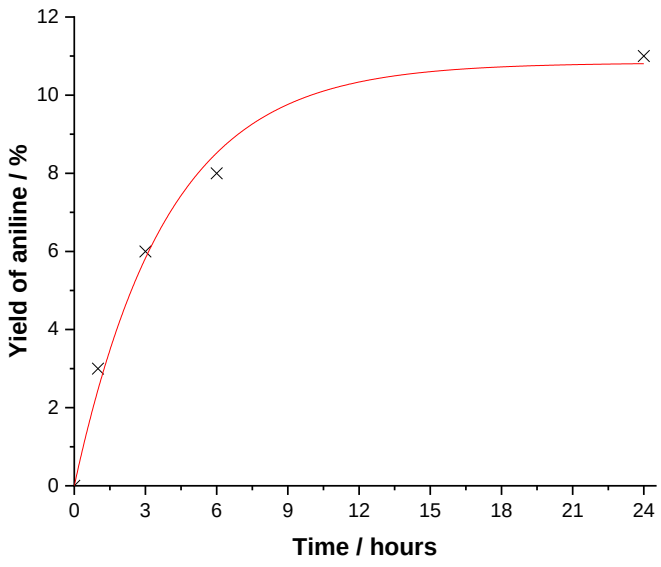

Figure 3.12: Plot of % yield of aniline obtained with increasing reaction time showing an increase in conversion with increasing reaction times. All other reaction conditions were kept constant: ethanol (0.2 mL), Ru/C (10 mg, 5 wt.% Ru), internal standard (16 mg), room temperature.

A control reaction with no catalyst was carried out to ensure that the Ru/C (5 wt.%) was required for the hydrogenation reaction to proceed. No conversion of nitrobenzene was observed after 3 hours suggesting that Ru/C is catalysing the reaction.

Although Ru/C (5 wt.%) was proven to catalyse the reaction at room temperature, after 24 hours the achieved yield of aniline was low. This could be due to the small amount of solvent used not completely wetting the catalyst meaning that all active sites within the carbon support were not accessible. To test this theory the amount of ethanol was increased from 0.2 to 0.5 mL to ensure complete wetting of the material (all other reaction conditions remained the same). No increase in conversion was obtained after 24 hours with an increase in ethanol. To improve the conversion of nitrobenzene to aniline the reactions were repeated at 50 °C between 6-24 hours. Heating the reaction to 50 °C increased the amount of aniline produced for each reaction time (see Figure 3.13). It is also evident that with an increase in reaction time the yield of aniline obtained also increases.

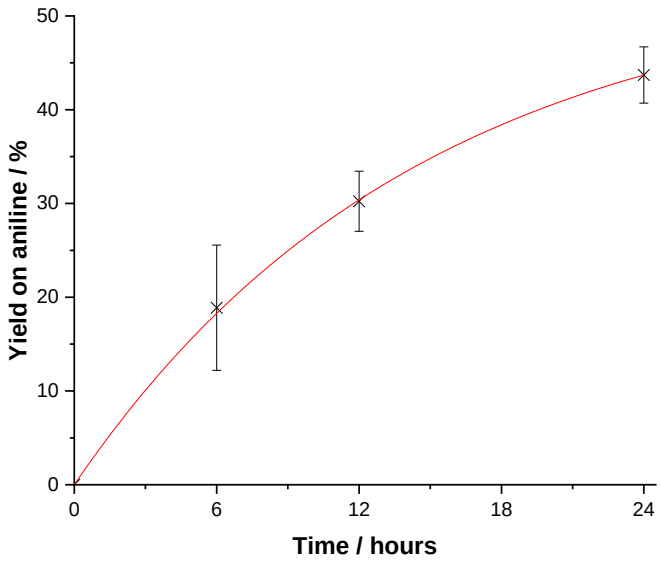

Figure 3.13: Plot of % yield of aniline obtained against reaction time showing an increase in conversion with an increase in reaction time. All other reaction conditions were kept constant: ethanol (0.5 mL), Ru/C (10 mg, 5 wt.% Ru), internal standard (16 mg), 50 °C. Yield of aniline given as an average of 3 runs.

The hydrogenation of nitrobenzene was preformed using the fabricated RuNPs@GNFs catalyst to ensure that the reaction conditions obtained for Ru/C were transferable. Due to the low density of the GNF catalyst the solvent volume was increased for 0.5 mL to 2 mL to ensure complete wetting of the catalyst so that all active sites where accessible to the reactants (the Ru/C catalysed reaction was repeated with this increased volume of ethanol). As 100% conversion of nitrobenzene to aniline was obtained for RuNPs@GNFs (5 wt.%) after 6 hours the reaction time was shortened to 4 hours (i.e. insufficient time for the reaction to reach 100% conversion) to ensure the

catalyst was working at full capacity during the whole experiment and thus enable changes in activity to be observed during recyclability testing.

Table 3.4: Summary of aniline yield obtained for the reduction of nitrobenzene after 4 or 6 hours catalysed by Ru/C or RuNPs@GNFs (both 5% by wt. Ru). All other reaction conditions were kept constant: ethanol (2 mL), catalyst (10 mg, 5 wt.% Ru), internal standard (16 mg), 50 °C.

Catalyst[a]	Reaction time / hours	Yield of aniline / %
Ru/C	6	56
	4	5
RuNPs@GNFs	6	100
	4	34

[a]Both 5% by weight Ru.

The activity of all other materials, mono- and bimetallic MNPs@GNFs, were investigated under the optimised reaction conditions highlighted in Scheme 3.6.

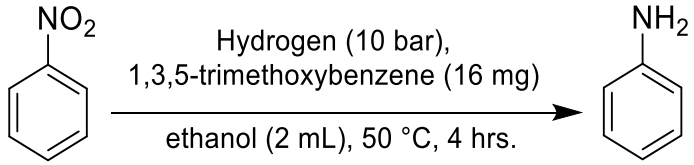

Scheme 3.6: Hydrogenation of nitrobenzene showing the reaction conditions used to probe the activity of the MNPs@GNFs materials.

3.2.1.2.1 RuNPs@GNFs (1, 2, 5 and 10 wt.%)

Previous studies have shown that the size and crystal structure of RuNPs have important effects on the catalytic activity of RuNPs in hydrogenation reactions.[40–44] The activity of RuNPs@GNFs with different metal loadings (1, 2, 5 and 10 wt.%) were investigated using the hydrogenation of nitrobenzene. An increase in conversion was observed with an increase in metal loading 5 wt.% > 2 wt.% > 1 wt.% (see Table 3.5).

The TOF defined as molecules of aniline produced per mole of Ru per second was determined for each material and follows the trend: 1 wt.% > 2 wt.% ≈ 5 wt.% > 10 wt.%. It is observed that the activity in terms of TOF decreases from 1 wt.% to 2 / 5 wt.% (Figure 3.14) and a further decrease is seen from 5 wt.% to 10 wt.%. This is due to an increase in particle size resulting in a smaller amount of Ru atoms exposed at the surface of the MNPs leading to less Ru atoms available to catalyse the reaction.

Table 3.5: Summary of yields, TONs of TOFs obtained for the conversion of nitrobenzene to aniline, with respect to number of moles of Ru for RuNPs@GNFs (1, 2, 5 and 10 wt.%).[a]

RuNPs@GNFs / wt.%	Yield / %	TON / $mol_{AN}mol_{Ru}^{-1}$	TOF / $(mol_{AN}mol_{Ru}^{-1})\ h^{-1}$
1	9.2 ± 0.7	90.8 ± 6.2	22.7 ± 1.5
2	13.3 ± 1.8	65.1 ± 9.0	16.2 ± 2.2
5	31.0 ± 0.4	62.0 ± 0.1	15.5 ± 0.1
10	9.9 ± 1.0	10.2 ± 5.1	2.6 ± 1.4

[a] Yields, TONs and TOFs given as an average of 3 runs.

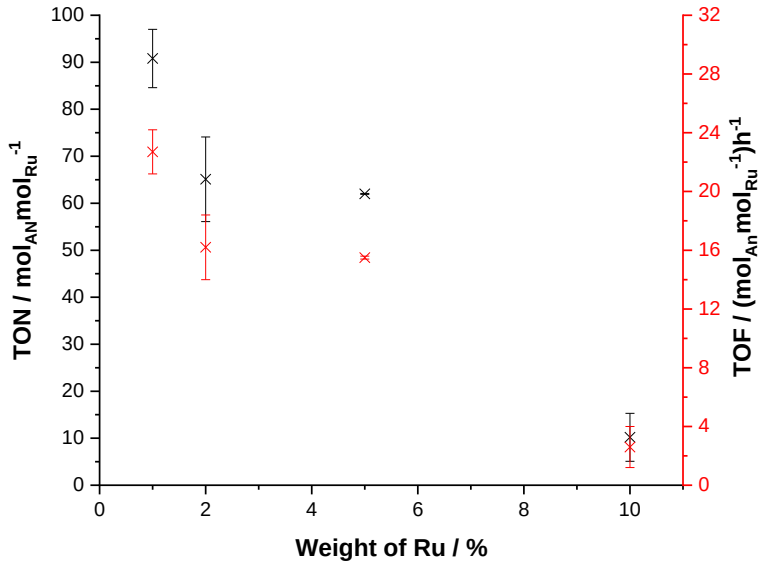

Figure 3.14: Plot of TONs and TOFs against the different metal loadings of RuNPs in RuNPs@GNFs showing an initial decrease in TON and TOF with increase wt.%.

3.2.1.2.2 Materials Fabricated using Different Addition Sequences

The activity of the materials prepared via the different addition sequences were investigated and results are summarised in Table 3.6. The material fabricated during the concerted addition approach was the only $Ru_{0.5}Ni_{0.5}$NPs@GNFs catalyst found to be active for the conversion of nitrobenzene giving a turn over number (TON) and turn over frequency (TOF) of 96.3 ± 6.9 $mol_{An}mol_{M}^{-1}$ and 24.1 ± 1.7 $mol_{An}mol_{M}^{-1}$/h, respectively, (where M is total amount of metal in the system).

Table 3.6: Summary of TONs and TOFs obtained for the materials made via different addition sequences with respect to total metal present, showing that the concerted addition approach afforded the only active catalyst towards the hydrogenation of nitrobenzene.[a]

Material	TON / $mol_{An}mol_{M}^{-1}$	TOF / $(mol_{An}mol_{M}^{-1})\ h^{-1}$
Sequential addition (Ru 1st)	0	0
Concerted addition	96.3 ± 6.9	24.1 ± 1.7
Sequential addition (Ni 1st)	0	0
Ru/C	4.9 ± 0.1	1.2 ± 0.04

[a] TONs and TOFs given as an average of 3 runs.

From TEM analysis, both the concerted addition and the sequential addition (Ru 1st) materials had metal alloyed RuNiNPs present within the GNF support structure and monometallic NiNPs with a similar ratio of bimetallic MNPs to monometallic MNPs of 1:1 (for MNPs of similar sizes, approximately 5 nm). These metal alloyed MNPs were absent in the concerted addition (Ni 1st) material. Figure 3.15 shows a schematic representation of each material fabricated using the different addition approaches. If the bimetallic RuNiNPs alone were responsible for the observed activity for the concerted addition material, then it would be expected that the sequential addition (Ru 1st) material would also show some activity towards the reduction of nitrobenzene. However, this is not the case. Unlike the sequential addition (Ru 1st) material the concerted addition material had MNPs of two distinctively different sizes present within the GNF support structure which were determined to be monometallic RuNPs of approximately 2 nm. These small RuNPs were also present in the sequential addition (Ni 1st) material. If these small RuNPs alone were responsible for the observed activity for the concerted addition material, then it would be expected that the sequential addition (Ni 1st) material would also show some activity towards the reduction of nitrobenzene. Again, this is not the case.

The observed activity for the concerted addition material could, therefore, be the result of a synergistic interaction between Ru/Ni in the bimetallic RuNiNP and surrounding smaller RuNPs. To investigate this near edge features for each material were analysed by XANES along with control measurements for RuNPs@GNFs and NiNPs@GNFs (see Chapter 2, Section 2.2.3.3). The Ni K-edge showed no significant change in edge energy across the series of materials, whereas an increase in the Ru K-edge energy was observed for the

concerted addition material. This implies a change in the electronic state of the small RuNPs due to the electron-donating ability of Ni (because of their differences in electronegativity)[45] and/or the carbon support, and it is proposed that this will result in a stronger binding of the reagents (nitrobenzene and H_2) and thus explain the observed increase in the activity of the catalyst system.

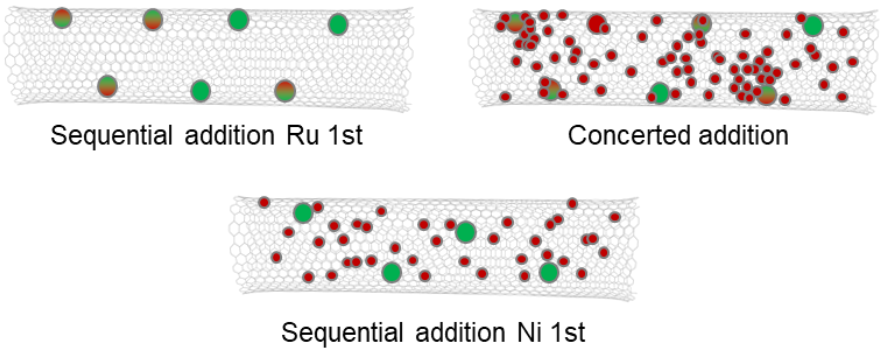

Figure 3.15: Schematic representation of the structures obtained for the fabrication of $Ru_{0.5}Ni_{0.5}$NPs@GNFs using the different addition approaches where red indicates Ru and green indicates Ni.

3.2.1.2.3 Materials Fabricated with Different Ratios of Ru:Ni

The activity of the materials with differing ratios of Ru:Ni, but the same addition sequence, were also investigated using the same probe reaction. For each material the average sizes of the MNPs were similar (within error (see Chapter 2, Section 2.2.3.1)) therefore any changes in activity can be attributed to composition of MNPs rather than particle size which has been shown previously to affect reactivity of a material.[28,46,47] The TONs and TOFs for each material with respect to total metal present are summarised in Table 3.7. The TOF obtained for RuNPs@GNFs was 12.7 ± 3.2 $mol_{An}mol_{M}^{-1}/h$ showing a 10-fold activity enhancement compared to commercially available Ru/C (TOF = 1.2 ± 0.04 $mol_{An}mol_{M}^{-1}/h$). Monometallic NiNPs@GNFs gave no conversion of nitrobenzene suggesting that the active metal in the bimetallic systems is Ru. Bimetallic $Ru_{0.5}Ni_{0.5}$NPs@GNFs (Ru:Ni 1:1) gave the greatest TOF of 24.1 ± 1.7 $mol_{An}mol_{M}^{-1}/h$, almost double the TOF obtained for monometallic RuNPs@GNFs (highlighted in Figure 3.16).

As Ru appears to be the active metal, and the most expensive component within the catalyst system, we can look at the TOFs with respect to Ru only (rather than total metal present). Interesting the $Ru_{0.25}Ni_{0.75}$NPs@GNFs material has a TOF of 27.6 ± 3.0 $mol_{An}mol_{Ru}^{-1}/h$, double that for RuNPs@GNFs and over 20 times that of commercially available Ru/C

Table 3.7: Summary of TONs and TOFs obtained, with respect to total metal and Ru, across the series for bimetallic RuNiNPs@GNFs (with differing ratios of Ru:Ni) showing that the Ru:Ni 1:1 ratio material gave the greatest TOF of 24.1 ± 1.7 ($mol_{An}mol_{M}^{-1}$) h^{-1} (highlighted by red box).[a]

	Per mole metal		Per mole Ru	
Catalyst	**TON / $mol_{AN}mol_{M}^{-1}$**	**TOF / ($mol_{AN}mol_{M}^{-1}$) h^{-1}**	**TON / $mol_{AN}mol_{Ru}^{-1}$**	**TOF / ($mol_{AN}mol_{Ru}^{-1}$) h^{-1}**
Ru/C	4.9 ± 0.1	1.2 ± 0.04	4.9 ± 0.1	1.2 ± 0.04
RuNPs@GNFs	50.9 ± 13.0	12.7 ± 3.2	50.9 ± 13.0	12.7 ± 3.2
$Ru_{0.75}Ni_{0.25}$NPs@GNFs	9.9 ± 1.7	2.5 ± 0.4	15.6 ± 2.7	3.9 ± 0.7
$Ru_{0.5}Ni_{0.5}$NPs@GNFs	96.3 ± 6.9	24.1 ± 1.7	258.1 ± 13.1	64.5 ± 3.3
$Ru_{0.25}Ni_{0.75}$NPs@GNFs	17.1 ± 0.8	4.3 ± 0.2	110.3 ± 11.8	27.6 ± 3.0
NiNPs@GNFs	0	0	0	0

[a] TONs and TOFs given as an average of 3 runs.

In order to ensure that the enhanced activity observed for $Ru_{0.5}Ni_{0.5}$NPs@GNFs was due to an electronic effect between the Ru and Ni a RuNPs@GNFs catalyst with a 2.5 wt.% metal loading was fabricated. Powder XRD revealed that the average size of the RuNPs present were 4.8 nm (comparable to the average particle size of RuNPs@GNFs (5 wt.%) which were determined to be 4.5 ± 0.3 nm from powder XRD (see Figure 3.17)). The TOF obtained was analogous to that observed for RuNPs@GNFs (5 wt.%) (TOF = 12.4 ± 0.3 ($mol_{AN}mol_{M}^{-1}$) h^{-1}) suggesting that the increase in activity observed for $Ru_{0.5}Ni_{0.5}$NPs@GNFs is due to an electronic effect between the Ru and Ni.

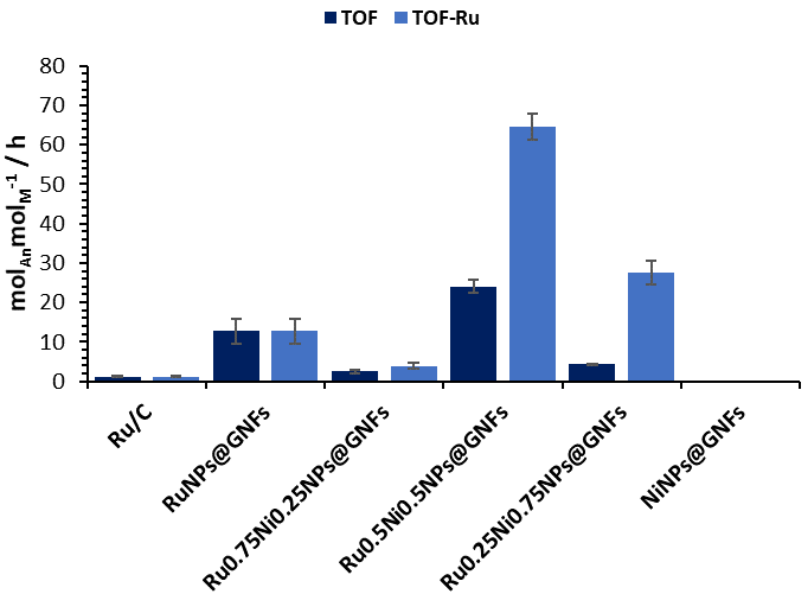

Figure 3.16: Summary of TOFs obtained, with respect to total metal and Ru, across the series for bimetallic RuNiNPs@GNFs (with differing ratios of Ru:Ni) showing that the Ru:Ni 1:1 ratio material gave the greatest TOF of 24.1 ± 1.7 ($mol_{An}mol_{M}^{-1}$) h^{-1}. TOFs given as an average of 3 runs.

To investigate this near edge features for each material were analysed by XANES along with control measurements for RuNPs@GNFs and NiNPs@GNFs (see Chapter 2, Section 2.2.3.4). Both the Ru K-edge and Ni K-edge showed no significant change in edge energy across the series of materials (different ratios of Ru:Ni).

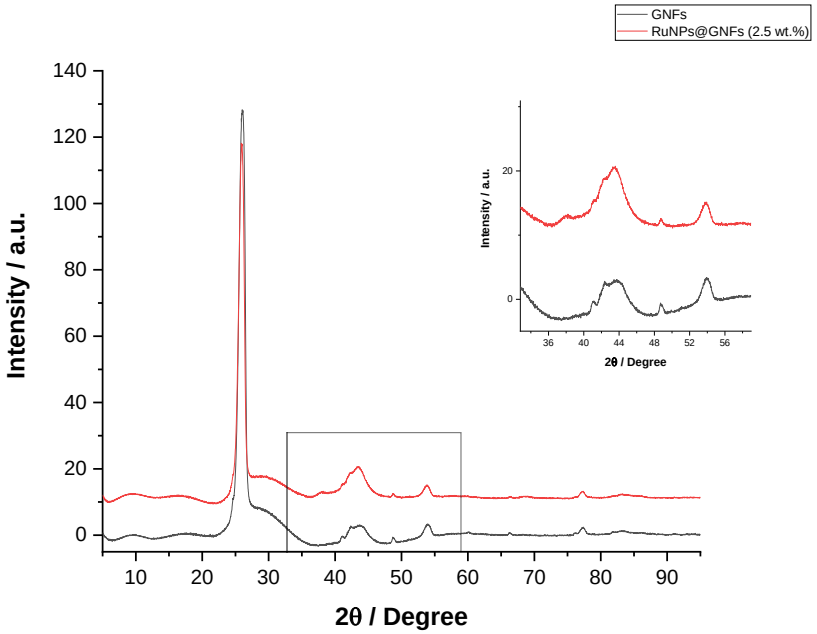

Figure 3.17: Powder XRD pattern for RuNPs@GNFs (2.5% by wt. Ru) compared to that obtained for GNFs. Peak at 2θ = 38° was used to determine the Ru particle size which was found to be 4.8 nm.

Similar observations in activity for supported bimetallic RuNiNPs have been previously reported. Dhanda *et al.*,[48] studied the H_2 generation rate and TOF value for ammonia borane (AB) hydrolysis over various Ru_xNi_{1-x}/RGO (where RGO = reduced graphene oxide) materials. They found that the RGO supported metal alloy showed a greater/faster activity compared to its monometallic counterparts. This was attributed to synergistic effects between the two electronegativity different individual metals (Ru and Ni) by changing electronic levels (leading to faster catalysis). They also observed that the $Ru_{0.5}Ni_{0.5}$/RGO material was the optimal ratio (Ru:Ni ratio of 1:1) for the greatest activity towards AB hydrolysis.[48]

3.2.2 Competitive Reactions

To further explore the effects of confinement on selectivity, competitive reactions were employed where the starting materials contained the same nitro functional group, but differing sizes, shapes and degrees of aromaticity (see Figure 3.18). When selecting appropriate reactant molecules to investigate the effects of confinement it is important to consider their possible interactions with the GNF support structure. The sp^2 hybridised step-edges within GNFs exhibit favourable π-π stacking interactions with reactant molecules containing aromatic or largely conjugated systems, compared to the rest of the support surface.[16,19,26] This has been explored previously by comparing the reactivity of aromatic and non-aromatic molecules. Previous

work conducted has investigated molecules with similar shapes but with an extended aromatic system.[25] Nitrocyclohexane and nitrobenzene are similar in size and shape with nitrobenzene also exhibiting aromaticity. The ability of reactants and products to diffuse through the nanoreactor, and therefore size of the reactant molecules, is also a crucial factor to consider crucial when investigating the effects of confinement.[15] 1-Nitroadamantane was chosen as it has a non-planar, 3-dimensional shape making it much larger/bulkier than nitrocyclohexane or nitrobenzene.

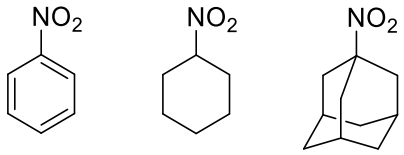

1 **8** **9**

Figure 3.18: Structures of substrates used in competitive reduction reactions with differing shapes and degrees of aromaticity.

Initially, reduction reactions were carried out for each substrate separately to ensure that, under the same conditions, each substrate could be reduced. It was also important to ensure that a suitable reaction time was determined, in which both the product and starting material was still present to allow for determination of which one preferentially reacted over the others.

3.2.2.1 Catalytic Transfer Hydrogenation

For catalytic transfer hydrogenations it was found that, for nitrobenzene and nitrocyclohexane, the reaction requirements were met under the following reaction conditions; starting material (0.3 mmol), 0.4 M NaOH in IPA (5 mL), IPA (5 mL), catalyst (10 mg), 1,3,5-trimethoxybenzene (16 mg), reflux for 22 hours. Unfortunately, under these conditions the reduction of 1-nitroadamantane showed no conversion. The reaction mixture was left to stir at reflux for 1 week and samples collected every 24 hr for TLC and ^{1}H NMR analysis. However, no conversion was observed after 1 week and so 1-nitroadamantane was removed from the competitive catalytic transfer hydrogenation study.

Single component reactions where performed on each substrate individually to act as comparisons to the competitive reactions (see Figure 3.19 for example ^{1}H NMR spectra). From Table 3.8 it is apparent that higher conversions are obtained for the reduction of nitrocyclohexene (**8**) than nitrobenzene (**1**) for both Ru/C and RuNPs@GNFs. The azo compounds for **8** and **1** and are preferentially formed for these catalysts. It is important to note that no amine is observed for the **8** reactions as the azo compound is

favoured. The same activity is not obtained for bimetallic RuNiNPs@GNFs where higher a conversion of **1** is observed (compared to **8**) with the amine product being favoured.

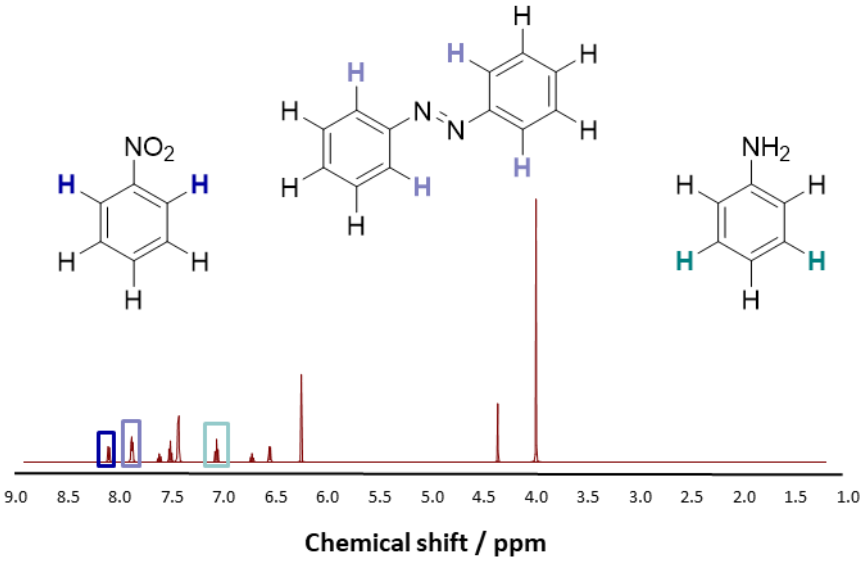

Figure 3.19: Example ^{1}H NMR spectrum for the hydrogenation of nitrobenzene, highlighting the peaks used to calculate conversion/TONs.

For competitive reactions (see Scheme 3.7) there is no observed selectivity between **1** and **8** for Ru/C.

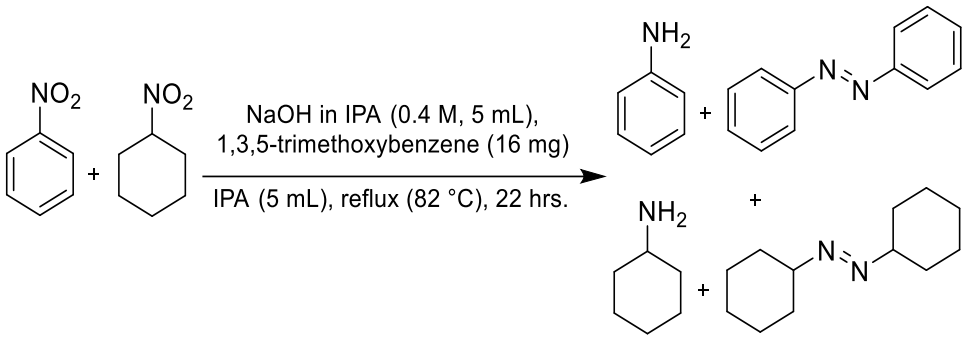

Scheme 3.7: Competitive transfer hydrogenation of nitrobenzene (**1**) and nitrocyclohexane (**8**) showing the reaction conditions used and products obtained.

However, as **8** is more reactive in the single substrate reactions it can be hypothesised that there is a slight enhancement in the reactivity of **1**.For both GNF supported catalysts, there is a substantial enhancement in the reactivity/selectivity for **1**. This preferential reduction of **1** is evidence of enhanced concentrations of aromatic reagents within GNFs which has been previously reported by Solomanz and co-workers.[17] No dramatic change in selectivity was observed for **8** (azo compound preferred over amine) or **1** (amine preferred over azo product) for Ru/C compared to single substrate

reactions. Bimetallic RuNiNPs@GNFs was found to be the most reactive and selective catalyst for the reduction of **1** to aniline which correlates to the enhancement in activity observed in Section 3.2.1.2.3, which can be attributed to an electronic effect between the Ru and Ni present in the MNPs. Interestingly, the amount of **8** or **1** converted to their corresponding amine, in the competitive reactions, shows no real trend, especially considering that there is a lack of aniline present for RuNPs@GNFs.

In summary this competitive reaction study has shown that aromatic reagents are preferentially reduced over non-aromatic reagents for both GNF supported MNP systems and higher conversions of **1** to aniline is obtained for bimetallic RuNiNPs compared to RuNPs which correlates with previous reported observations from other research groups (see Section 3.2.1.2.3).

Table 3.8: Summary of conversion/TON and yields of corresponding amine obtained for the catalytic transfer competitive reaction study (where TON is given in units of moles of starting material converted per mole of metal ($mol_C mol_M^{-1}$).[a]

Catalyst / Reaction	Ru/C (5 wt.%)			RuNPs@GNFs (5 wt.%)			RuNiNPs@GNFs (5 wt.%)		
	Conversion (%) / TON	Yield of amine (%)	Yield of azo compound (%)	Conversion (%) / TON	Yield of amine (%)	Yield of azo compound (%)	Conversion (%) / TON	Yield of amine (%)	Yield of azo compound (%)
1	78 / 47	12	18	68 / 40	16	25	97 / 44	18	7
8	97 / 59	0	91	79 / 48	0	65	17 / 8	0	10
1+8	**1**: 88 / 53 **8**: 81 / 48	**1**: 36 **8**: 5	**1**: 4 **8**: 70	**1**: 97 / 59 **8**: 66 / 40	**1**: 2 **8**: 0	**1**: 8 **8**: 54	**1**: 100 / 45 **8**: 22 / 10	**1**: 28 **8**: 0	**1**: 4 **8**: 16

[a] Conversions and yields given as an average of 3 runs.

Table 3.9: Summary of conversion/TON and yields of corresponding amine obtained for the H_2 hydrogenation study (where TON is given in units of moles of starting material converted per mole of metal ($mol_C mol_M^{-1}$).[a]

Catalyst / Reaction	Ru/C (5 wt.%)		RuNPs@GNFs (5 wt.%)		RuNiNPs@GNFs (5 wt.%)	
	Conversion (%) / TON	Yield of amine (%)	Conversion (%) / TON	Yield of amine (%)	Conversion (%) / TON	Yield of amine (%)
1	53 / 53	47	62 / 62	62	86 / 63	69
8	62 / 63	59	32 / 32	31	68 / 50	51
9	48 / 49	44	39 / 40	18	42 / 31	29
1+8	**1**: 18 / 18 **8**: 68 / 69	**1**: 13 **8**: 32	**1**: 48 / 48 **8**: 67 / 67	**1**: 10 **8**: 33	**1**: 56 / 40 **8**: 22 / 16	**1**: 14 **8**: 5
1+9	**1**: 74 / 76 **9**: 37 / 38	**1**: 31 **9**: 35	**1**: 100 / 102 **9**: 56 / 57	**1**: 99 **9**: 20	**1**: 100 / 73 **9**: 29 / 21	**1**: 99 **9**: 23
8+9	**8**: 59 / 57 **9**: 54 / 52	**8**: 18 **9**: 33	**8**: 75 / 76 **9:** 60 / 61	**8**: 39 **9**: 25	**8**: 86 / 63 **9**: 48 / 35	**8**: 20 **9**: 26
1+8+9	**1**: 78 / 77 **8**: 53 / 52 **9**: 43 / 42	**1**: 22 **8**: 16 **9**: 38	**1**: 90 / 90 **8**: 46 / 46 **9**: 43 / 43	**1**: 33 **8**: 16 **9**: 27	**1**: 58 / 42 **8**: 19 / 14 **9**: 41 / 30	**1**: 23 **8**: 12 **9**: 39

[a] Conversions and yields given as an average of 3 runs.

3.2.2.2 H_2 Batch Reactions

The reaction requirements (stated in Section 3.2.2) were met under the following reaction conditions; starting material (0.5 mmol), ethanol (2 mL), H_2 (10 bar), 1, 3, 5-trimethoxybenezene (16 mg), catalyst (10 mg), 50 °C, 4 hours. Single component reactions where performed on each substrate individually to act as comparisons to the competitive reactions. From Table 3.9 it is evident that, compared to the catalytic transfer hydrogenation study, conversions to amine are greater in all cases. Higher conversions of **1** to aniline are obtained for both GNF supported MNP catalysts compared to Ru/C. No significant difference in conversion is observed for the reduction of **8** to cyclohexylamine which could be due to the fact that **8** is not aromatic and so is not affected by confinement.

This is also the case for 1-nitroadamantane (**9**) i.e. no significant difference in conversion to 1-adamantylamine as the substrate is not aromatic and so is not affected by confinement. It is also important to note that the reactivity in confined systems is comparable to Ru/C and so reactions are not hindered by confinement.

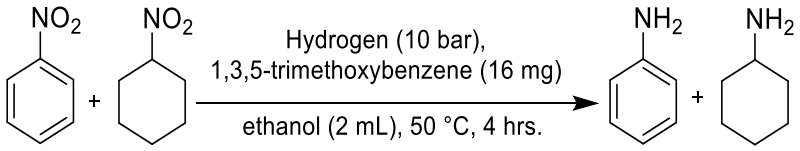

Scheme 3.8: Reaction conditions used for the competitive hydrogenation of nitrobenzene (**1**) and nitrocyclohexane (**8**).

For competitive reactions **1** + **8** (see Scheme 3.8) there is a high selectivity for the reduction of **8** over **1** observed for Ru/C. This selectivity is less pronounced for the reaction catalysed by RuNPs@GNFs and for the bimetallic RuNiNPs@GNFs catalyst the conversion of **1** is actually favoured. This emphasises the affinity of the GNF supported systems for **1**.

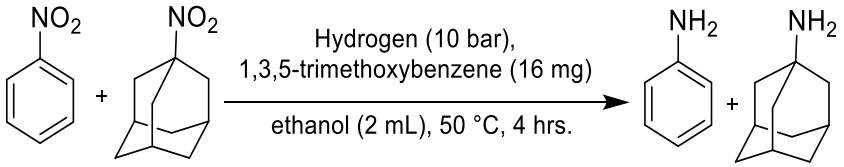

Scheme 3.9: Reaction conditions used for the competitive hydrogenation of nitrobenzene (**1**) and 1-nitroadamantane (**9**).

For competitive reactions **1** + **9** (see Scheme 3.9) the Ru/C catalysed reaction favours the reduction of **1**, as higher conversions are obtained compared to the single substrate reactions, this is also observed for the RuNPs@GNFs

catalysed reaction but to a far greater extent due to the increased affinity of aromatic **1** for the sp^2 hybridised carbon walls.

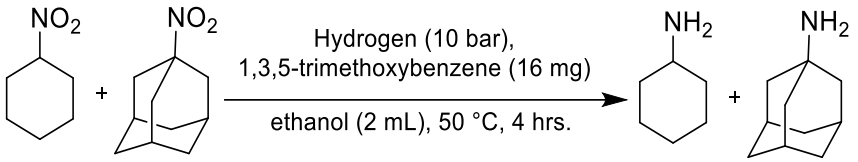

Scheme 3.10: Reaction conditions used for the competitive hydrogenation of nitrocyclohexane (**8**) and 1-nitroadamantane (**9**).

For competitive reactions **8** + **9** (see Scheme 3.10) there is no considerable difference in the activity of **8** or **9** compared to the single substrate reaction, therefore, the aromaticity of the substrate in far more important for selectivity than size/shape. This is unsurprising as the internal channels of GNFs are significantly larger than more conventional CNT supports i.e. SWNTs. Although Aygun *et al.*,[25] previously studied confinement affects in RuNPs@CNRs with odd shaped bicyclic derivatives selectivity between different sized/shaped reagents hasn't been explored and as such this is a key finding.

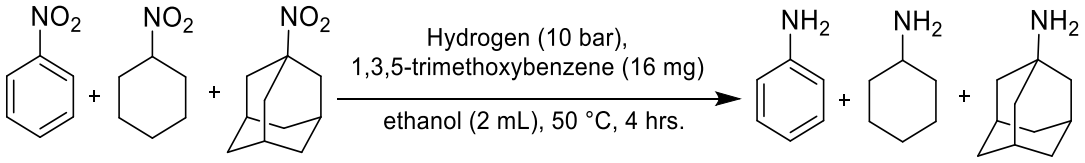

Scheme 3.11: Reaction conditions used for the competitive hydrogenation of nitrobenzene (**1**), nitrocyclohexane (**8**) and 1-nitroadamantane (**9**).

For competitive reaction **1** + **8** + **9** (see Scheme 3.11 and Figure 3.20 for example ^{1}H NMR spectra) there is a preference for **1** (aromatic substrate) over **8** or **9** (non-aromatic substrates) with similar activities towards **8** and **9** observed for reactions catalysed by Ru/C and RuNPs@GNFs. This again suggests that the size/shape of the substrate does not affect selectivity. However, it is important to note that for RuNiNPs@GNFs there is a significant decrease in the activity towards **8** observed which is also evident for the **8** + **9** competitive reaction.

In summary, this competitive reaction study has shown that the aromaticity of a reagent is far more important for the selectivity of a reaction catalysed by GNF supported MNPs, compared to the size and/or shape of a reagent and higher conversions of **1** to aniline were obtained for MNPs@GNFs.

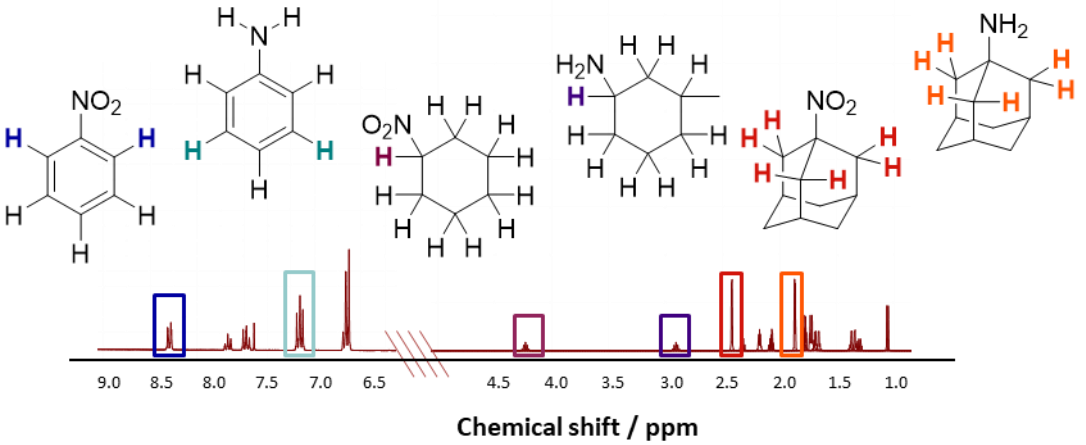

Figure 3.20: Example ^{1}H NMR spectrum of the reaction mixture for the competitive hydrogenation of nitrobenzene, nitrocyclohexane and 1-nitroadamanyane; highlighting the peaks used for each starting material and product to calculate conversion/TONs (N.B. not all hydrogens shown in the structures of 1-nitroadamantane and 1-adamantylamine).

3.3 Conclusions

The use of monometallic RuNPs@GNFs and bimetallic RuNiNPs@GNFs as nanoreactors was investigated in batch reactions, using the reduction of nitro group containing molecules, and quantified in terms of activity, selectivity and recyclability.

Recyclability tests of the commercially available Ru/C and the fabricated RuNPs@GNFs (both 5 wt.%) catalysts have been conducted. Whilst the activity of Ru/C remained mostly unchanged, with a slight decrease in activation probably due to a small loss of catalyst mass during the recovery operations, there was a significant decrease in activity for RuNPs@GNFs after the 2nd cycle. TEM analysis showed that the deactivation was caused by a significant change in the shape of the NPs (increased aspect ratio of 1:1.8) and the detachment of the RuNPs from the graphitic edges of the GNF leading to an non-uniform distribution of NPs within the inner cavities of the GNF.

For bimetallic RuNiNPs@GNFs it was found that the concerted addition fabrication method afforded the only active material towards the reduction of nitrobenzene to aniline with the optimum ratio of Ru:Ni being 1:1 ($Ru_{0.5}Ni_{0.5}$NPs@GNFs (concerted addition) had the highest TOF of 24.1 ± 1.7 $mol_{An}mol_{M}^{-1}/h$).

Competitive reaction studies have been performed for both catalytic transfer hydrogenation and H_2 batch reactions. For the catalytic transfer

hydrogenations it was found that aromatic reagents are preferentially reduced over non-aromatic reagents for both GNF supported MNP systems (i.e. RuNPs@GNFs and RuNiNPs@GNFs). This preferential reduction of aromatic reagents is evidence of an enhancement in the concentration of the aromatic reagent within GNFs due to favourable interactions between the π-system of aromatic molecule and the sp^2 hybridised carbon walls. It was also found that higher conversions of **1** to aniline were obtained for bimetallic RuNiNPs compared to RuNPs which compares to previous results. For the H_2 batch reactions is was found that the aromaticity of a reagent is far more important for the selectivity of a reaction, catalysed by MNPs@GNFs, compared to the size and/or shape of a reagent, which has not been previously reported.

3.4 Experimental

3.4.1 General Considerations

Ru/C (5 wt.%) was purchased from Sigma Aldrich and used as supplied. All other reagents were of analytical grade quality and used as supplied from Sigma Aldrich and Fischer Scientific, unless otherwise stated.

GC analysis was performed using an Agilent HP5 column fitted with a flame ionisation detector. ^{1}H NMR was performed on a Brucker Advance III HD-400 spectrometer. TEM analysis was performed on a FEI Tecnai F20 field emission gun with an information limit of 0.25 nm at 200 KeV. Samples were prepared by dispersing the material in 2-propanol using an ultrasonic bath and deposited onto a lacey carbon film coated copper grid.

3.4.2 Transfer Hydrogenations

3.4.2.1 Investigation into the Catalytic Activity of RuNPs@GNFs (5 wt.%)

General procedure: All reactions were carried out under a nitrogen atmosphere, in a 3-neck round bottom flask fitted with a reflux condenser. The catalyst, starting material, and biphenyl were added to the reaction flask under a flow of nitrogen. The NaOH solution was added via injection. The reaction mixture was heated at reflux for the desired time. Detailed reaction conditions are highlighted in Table 3.10.

Table 3.10: Summary of the reaction conditions used for the optimisation of the reduction of nitrobenzene catalysed by Ru/C (5 wt.%).

Reaction no.	Mass of catalyst / mg	Nitrobenzene / mmol	Conc. of NaOH in IPA / mol dm^{-3}	Volume of NaOH in IPA / mL	NaOH Equiv.	Time / h
1	50	2.0	0.025	0.5	0.25	16
2	50	2.0	0.1	2	1	17
3	50	2.0	0.1	2	1	4
4	2	0.16	0.01	0.05	0.3	20
5	2	0.16	0.04	0.4	2.5	6
6[a]	2	0.16	0.1	0.5	3	3.5
7	2	0.16	0.2	1	6	6
8	2	0.16	0.4	2	12	6

[a] The reaction conditions used for the investigation into the activity of RuNPs@GNFs vs. Ru/C (both 5% by wt. Ru).

3.4.2.2 Recyclability

3.4.2.2.1 Ru/C (5 wt.%)

General procedure: Run 1: All reactions were performed under a nitrogen atmosphere. Nitrobenzene (100 mg, 0.8 mmol), Ru/C (10 mg), biphenyl (10 mg), and NaOH in isopropanol (0.400 mol dm^{-3}, 25 mL) were refluxed, under nitrogen, for 6 hours. After this time an aliquot was collected and analysed by GC. After the reaction the catalyst was washed filtered through a PTFE membrane filter (pore size: 0.2 μm) using a cannular filter, washed with isopropanol (2 x 20 mL) and dried under vacuum overnight. To ensure no catalyst was lost the PTFE membrane was added to the reaction vessel of the subsequent reaction.

Run 2: To the PTFE membrane, nitrobenzene (100 mg, 0.8 mmol), biphenyl (10 mg), and NaOH in isopropanol (0.400 mol dm^{-3}, 25 mL) were added. The reaction mixture was then refluxed for 6 hours before an aliquot was collected and analysed by GC. After the reaction the catalyst was filtered and washed, as above, and left in the reaction flask ready for run 3. This procedure was repeated for the subsequent reaction cycles (runs 3-5). This was repeated in triplicate.

3.4.2.2.2 RuNPs@GNFs (5 wt.%)

The procedure followed is the same as that highlighted in Section 2.4.1.2.1. All reactions were carried out in triplicate. Once the reactions were completed, the flask and membrane were washed with IPA and placed in an ultrasonic bath for 30 minutes, to ensure that all the catalyst was removed from the membrane. This was then filtered with a fresh PTFE membrane, washed with IPA, dried overnight in a desiccator, and kept for TEM analysis.

A TEM sample was prepared by dispersing the material in IPA (HPLC grade) using an ultrasonic bath and deposited onto a lacey carbon film coated copper grid.

3.4.2.3 Investigation into the Effect that the Ratio of Carbon Support to Metal has on the Rate of Reaction

General procedure: All reactions were performed under a nitrogen atmosphere. Nitrobenzene (10 mg, 0.09 mmol), Ru/C or RuNPs@GNFs (2 mg), NaOH in isopropanol (0.200 mol dm^{-3}, 5 mL) and isopropanol (5 mL) were refluxed for 1 hour. Samples were collected at 30 mins and 1 h for GC analysis.

3.4.3 H_2 Batch Reactions

General procedure: These reactions were performed in a high-pressure single-well reactor (see Figure 3.21). In a typical experiment, the reactor was charged with nitrobenzene (100 µL, 1 mmol), ethanol (2 mL), 1,3,5-trimethoxybenezene (16 mg, 0.10 mmol, as an internal standard) and catalyst (total mass of material equivalent to 0.5 mg by wt. of metal nanoparticles), before being flushed with nitrogen to exclude air. H_2 (10 bar) was then introduced into the system 5 times before the reactor was charged to the desired pressure for reactions (10 bar). The reaction mixture was heated at 50 °C for 4 hours. The reactions were monitored by GC and ^{1}H NMR.

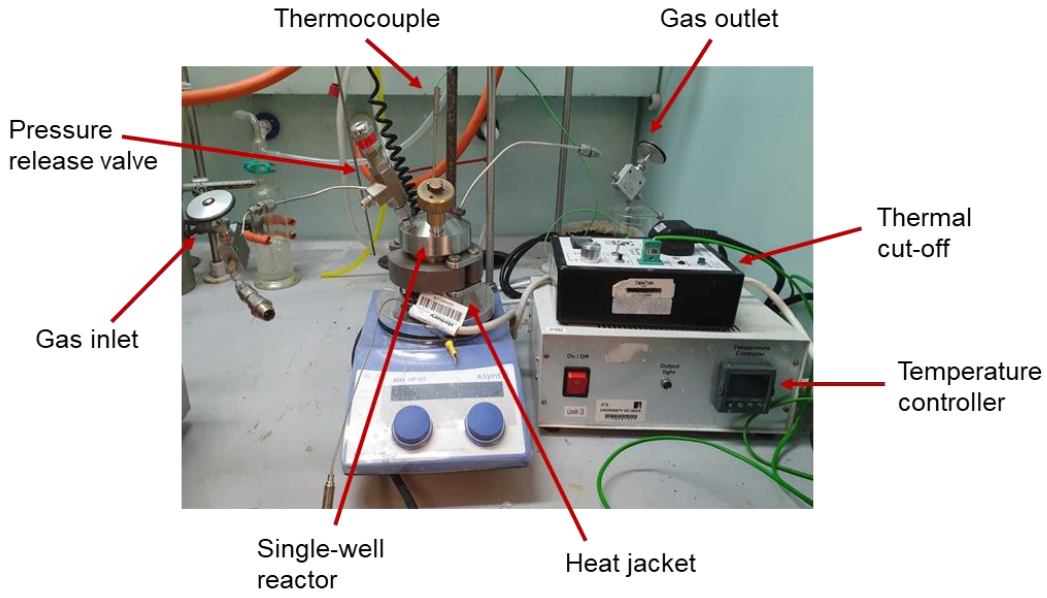

Figure 3.21: A photograph of the H_2 batch reactor used for the hydrogenation of nitro group containing molecules.

3.4.4 Competitive Reactions

3.4.4.1 Transfer hydrogenation

General procedure: All reactions were carried out under a nitrogen atmosphere, in a 3-neck round bottom flask fitted with a reflux condenser. In a typical experiment the catalyst (10 mg) was added to the reaction flask under a flow of nitrogen. A solution of isopropanol (5 mL), starting material/s (0.3 mmol) and 1,3,5-trimethoxybenzene (16 mg) were added via injection, followed by NaOH in IPA (5 mL, 0.4 M). The reaction mixture was heated at reflux for 22 hours. The reactions were monitored by ^{1}H NMR.

3.4.4.2 H_2 batch reaction

General procedure: In a typical experiment the starting material/s (0.5 mmol), ethanol (2 mL), 1,3,5-trimethoxybenzene (16 mg, 0.10 mmol) and catalyst (10 mg) were added to the reactor and flushed with nitrogen to remove air. These reactions were performed in a high-pressure single-well reactor. H_2 (10 bar) was then introduced into the system 5 times before the reactor was charged to the desired pressure for reactions (10 bar). The reaction mixture was heated at 50 °C for 4 hours. The reactions were monitored by ^{1}H NMR.

3.5 References

1 M. C. Bahome, L. L. Jewell, D. Hildebrandt, D. Glasser and N. J. Coville, *Appl. Catal. A Gen.*, 2005, **287**, 60–67.

2 X. Chen, D. Deng, X. Pan and X. Bao, *Chinese J. Catal.*, 2015, **36**,

1631–1637.

3 W. Chen, Z. Fan, X. Pan and X. Bao, *J. Am. Chem. Soc.*, 2008, **130**, 9414–9419.

4 H. J. Schulte, B. Graf, W. Xia and M. Muhler, *ChemCatChem*, 2012, **4**, 350–355.

5 M. C. Bahome, L. L. Jewell, K. Padayachy, D. Hildebrandt, D. Glasser, A. K. Datye and N. J. Coville, *Appl. Catal. A Gen.*, 2007, **328**, 243–251.

6 A. Tavasoli, M. Trepanier, R. M. Malek Abbaslou, A. K. Dalai and N. Abatzoglou, *Fuel Process. Technol.*, 2009, **90**, 1486–1494.

7 J. Zhang, J.-O. Müller, W. Zheng, D. Wang, D. Su and R. Schlögl, *Nano Lett.*, 2008, **8**, 2738–2743.

8 P. Tomkins, E. Gebauer-Henke, W. Leitner and T. E. Müller, *ACS Catal.*, 2015, **5**, 203–209.

9 A. M. Zhang, J. L. Dong, Q. H. Xu, H. K. Rhee and X. L. Li, *Catal. Today*, 2004, **95**, 347–352.

10 H. Vu, F. Gonçalves, R. Philippe, E. Lamouroux, M. Corrias, Y. Kihn, D. Plee, P. Kalck and P. Serp, *J. Catal.*, 2006, **240**, 18–22.

11 J. Tessonnier, L. Pesant, G. Ehret, M. J. Ledoux and C. Pham-huu, *Appl. Catal. A Gen.*, 2005, **288**, 203–210.

12 X. Ni, B. Zhang, C. Li, M. Pang, D. Su, C. T. Williams and C. Liang, *Catal. Commun.*, 2012, **24**, 65–69.

13 J. Nhut, R. Vieira, L. Pesant, J. Tessonnier, N. Keller, G. Ehret, C. Pham-huu and M. J. Ledoux, *Catal. Today*, 2002, **76**, 11–32.

14 W. Wang, P. Serp and P. Kalck, *Mater. Res. Bull.*, 2008, **43**, 958–967.

15 A. N. Khlobystov, *ACS Nano*, 2011, **5**, 9306–9312.

16 W. A. Solomonsz, G. A. Rance, M. Suyetin, A. La Torre, E. Bichoutskaia and A. N. Khlobystov, *Chem. Eur. J.*, 2012, **18**, 13180–13187.

17 W. a Solomonsz, G. a Rance, B. J. Harris and A. N. Khlobystov, *Nanoscale*, 2013, **5**, 12200–12205.

18 A. La Torre, M. del C. Gimenez-Lopez, M. W. Fay, G. A. Rance, W. A. Solomonsz, T. W. Chamberlain, P. D. Brown and A. N. Khlobystov, *ACS Nano*, 2012, **6**, 2000–2007.

19 G. a Rance, W. a Solomonsz and A. N. Khlobystov, *Chem. Commun.*, 2013, **49**, 1067–1069.

20 B. R. Cuenya, *Thin Solid Films*, 2010, **518**, 3127–3150.

21 Z. Chen, Z. Guan, M. Li, Q. Yang and C. Li, *Angew. Chemie - Int. Ed.*, 2011, **50**, 4913–4917.

22 M. Ran, W. Chu, Y. Liu and A. Borgna, *RSC Adv.*, 2015, **5**, 103669–103673.

23 B. Cornelio, A. R. Saunders, W. A. Solomonsz, M. Laronze-Cochard, A. Fontana, J. Sapi, A. N. Khlobystov and G. A. Rance, *J. Mater. Chem. A*, 2015, **3**, 3918–3927.

24 T. W. Chamberlain, J. H. Earley, D. P. Anderson, A. N. Khlobystov and R. a Bourne, *Chem. Commun.*, 2014, **50**, 5200–5202.

25 M. Aygün, C. T. Stoppiello, M. A. Lebedeva, E. F. Smith, M. C. Gimenez-lopez, N. Khlobystov and T. W. Chamberlain, *J. Mater. Chem. A*, 2017, **5**, 21467–21477.

26 W. A. Solomonsz, G. A. Rance and A. N. Khlobystov, *Small*, 2014, **10**, 1866–1872.

27 J. Xiao, X. Pan, S. Guo, P. Ren and X. Bao, *J. Am. Chem. Soc.*, 2014, **137**, 477–482.

28 J. Kang, W. Deng, Q. Zhang and Y. Wang, *J. Energy Chem.*, 2013, **22**, 321–328.

29 J. P. Martínez, V. Chaitanya, L. Falivene, S. P. Nolan, L. Cavallo, M. Solà and A. Poater, *Chem. a Eur. J.*, 2016, **22**, 6617–6623.

30 S. Bouzbouz, L. Boulard and J. Cossy, *Org. Lett.*, 2007, **9**, 3765–3768.

31 J. H. Kim, J. H. Park, Y. K. Chung and K. H. Park, *Adv. Synth. Catal.*, 2012, **354**, 2412–2418.

32 P. Panagiotopoulou and D. G. Vlachos, *Appl. Catal. A Gen.*, 2014, **480**, 17–24.

33 A. Corma, P. Concepción and P. Serna, *Angew. Chemie - Int. Ed.*, 2007, **46**, 7266–7269.

34 P. Zhang, C. Yu, X. Fan, X. Wang, Z. Ling, Z. Wang and J. Qiu, *Phys. Chem. Chem. Phys.*, 2015, **17**, 145–150.

35 R. S. Downing and P. J. Kunkeler, *Catal. Today*, 1997, **37**, 121–136.

36 A. M. Tafesh and J. Weiguny, *Chem. Rev.*, 1996, **96**, 2035–2052.

37 T. J. Blacklock, Y. Liu, Y. Lu, M. Prashad and O. Repic, *Adv. Synth. Catal.*, 2005, **347**, 217–219.

38 D. A. Links, P. P. Sarmah and D. K. Dutta, *Green Chem.*, 2012, **14**, 1086–1093.

39 M. Aygün, T. W. Chamberlain, M. C. Gimenez-lopez and A. N. Khlobystov, *Adv. Funct. Mater.*, 2018, **28**, 1–15.

40 S. Guo, K. Y. Liew and J. Li, *J. Am. Oil Chem. Soc.*, 2009, **86**, 1141–1147.

41 B. Xu, K. Y. Liew and J. Li, *J. Am. Oil Chem. Soc.*, 2007, **84**, 117–122.

42 E. T. Silveira, A. P. Umpierre, L. M. Rossi, G. Machado, J. Morais, G. V Soares, I. J. R. Baumvol, S. R. Teixeira, P. F. P. Fichtner and J. Dupont, *Chem. Eur. J.*, 2004, **10**, 3734–3740.

43 J. Mao, W. Chen, W. Sun, Z. Chen, J. Pei, D. He, C. Lv, D. Wang and Y. Li, *Angew. Chemie*, 2017, **56**, 11971–11975.

44 K. Kusada, H. Kobayashi, T. Yamamoto, S. Matsumura, N. Sumi, K. Sato, K. Nagaoka, Y. Kubota and H. Kitagawa, *J. Am. Chem. Soc.*, 2013, **135**, 5493–5496.

45 K. Mori, K. Miyawaki and H. Yamashita, *ACS Catal.*, 2016, **6**, 3128–

3135.

46 S. Siankevich, G. Savoglidis, Z. Fei, G. Laurenczy, D. T. L. Alexander, N. Yan and P. J. Dyson, *J. Catal.*, 2014, **315**, 67–74.

47 M. Haruta, *Catal. Today*, 1997, **36**, 153–166.

48 R. Dhanda and M. Kidwai, *ChemistrySelect*, 2017, **2**, 335–341.

Chapter 4: Characterisation of MNPs Immobilised in Multifunctional Polymer Supports for Heterogeneous Catalysis

4.1 Introduction

Ionic liquids (ILs) are an interesting class of solvents that have been widely used in a variety of catalytic reactions.[1–5] ILs have been generating increased interest over the last decade due to their unique properties such as: low vapour pressure, wide electrochemical window, chemical and thermal stability, excellent solvation properties and their potential use as greener alternatives to volatile organic solvents.[6–9] They have been shown to act as both solvent and stabiliser for a host of transition metal nanoparticles and have the ability to modify and tailor their physicochemical properties and functionality which offers enormous potential for developing new catalyst technologies.[6–8]

However, there are several practical limitations in the use of ILs which inhibit their wide spread application, including; high costs in comparison with traditional solvents, high viscosity and leaching of the ionic liquid during work-up and recovery.[10–12] Moreover, whilst the stabilisation of NPs by ILs has been thoroughly explored and is believed to result from weak electrostatic interactions that are easily displaced to allow access to the active sites, they are often not sufficient stabilisers to prevent nanoparticle agglomeration under working reaction conditions.[13–15] Incorporating a metal-binding donor group such as an amine,[16,17] phosphine,[18–20] nitrile,[21–24] bipyridine,[25–28] thiol[29] or hydroxyl[30,31] onto the ionic liquid is a potential solution to this problem. The heteroatom donors provide an additional covalent interaction between the IL ions and the nanoparticles improving the long-term stability of the NPs as well as controlling the kinetics of formation.[32] For example, the improved recyclability of NiNPs stabilised by an amino-modified imidazolium-based ionic liquid was reported by Hu and co-workers.[33] RhNPs stabilised by a phosphine-functionalised ionic liquid have also been reported to allow switchable chemoselectivity for the hydrogenation of aryl ketones and aldehydes as well as improving the lifetime of the RhNP-based catalyst.[34]

Even though, this strategy has been successfully applied in numerous cases, large volumes are often required for catalysis and recovery of the ionic liquid

during work-up after catalysis can be difficult (due to leaching) which limits their implementation.[35]

4.1.1 Polymer Immobilised Ionic Liquids

Polymer immobilised ionic liquids (PILP) are a class of functional material that combine the well-documented advantages of an ionic liquid environment with the advantageous properties of a polymer support such as: catalyst stabilisation, ease of recycling and enhancements in the activity and selectivity.[36–39] Additionally, covalent attachment of an ionic liquid to a polymer support has various added benefits as it improves the durability of the catalyst, prevents leaching of the ionic liquid, reduces the quantity of ionic liquid required and facilitates easy separation and recovery of the catalyst, ultimately these benefits could result in a significant cost saving.[35] For example, PdNPs stabilised by an imidazolium-based ionic polymer were fabricated by Wang and co-workers.[39] They investigated the activity and recyclability of the material for the hydrogenation of nitroarenes and found that an excellent yield of amine (≥ 90%) was retained after 7 cycles. TEM analysis of the recycled material showed no clear agglomeration of the NPs which was attributed to the support providing effective stability.[39]

In addition to improving the long term stability and recyclability of MNPs incorporating heteroatom donors into polymer immobilised ionic liquids could also result in additional benefits including modification of the electronic surface structure of the metal surface, control over the formation of the NPs, specifically their size and morphology, and the capability to tune the hydrophilicity and/or steric properties of the ligand as well as the ionic micro-environment.[35,40–42] For example, Yuan *et al.*,[43] reported a method for precise control of the growth of a range of MNPs (where M = Au, Pt, Ru, Rh, Ni, Cu and Co) to 1 nm on average by utilising a combination of a polymer immobilised ionic liquid and polytriazolium derived poly(N-heterocyclic carbene) as a support structure. A high catalytic performance of Rh catalysed methanolysis of ammonia borane was also reported and attributed to a strong stabilising interaction between the carbene and MNPs.[43] Additionally, Chen *et al.*,[44] demonstrated that the chemisorption of an appropriate capping ligand on supported MNPs can lead to an enhancement in their activity and selectivity. They reported a substantial enhancement in selectivity from 43% to ~100% for the liquid phase aerobic oxidation of benzyl alcohol catalysed by silica supported AuNPs, capped with chemisorbed polyvinylpyrrolidone.[44]

This Chapter looks at the development of heteroatom donor-decorated polymer immobilised ionic liquids for MNP supports, with the aim of combining the stabilisation provided by a heteroatom donor and an ionic liquid with a polymer support to explore if the nature of the heteroatom donor and its loading influences nanoparticle formation, specifically size, morphology and in turn the efficiency of the catalyst system.

4.2 Synthesis and Characterisation of Materials

This section highlights the fabrication and characterisation of numerous heteroatom donor-decorated polymer immobilised ionic liquid supported MNPs (Pd or Au), with differing functionalities. All materials were fabricated via a previously reported method[35,45–47] at The University of Newcastle by Dr Tom Backhouse under the supervision of Dr Simon Doherty and Dr Julian Knight. A general method for the fabrication of a heteroatom donor-decorated polymer immobilised ionic liquid MNP is highlighted in Scheme 4.1 and described below, see Experimental section 4.5.1 for full details.

Phosphino-decorated PILP was prepared by azobisisobutyronitrile (AIBN) initiated radical polymerisation of the corresponding imidazolium-modified monomer, 4-diphenylphosphino styrene and di-cationic cross-linker in the desired ratio (x = 1.84, y = 1, z = 0.16).

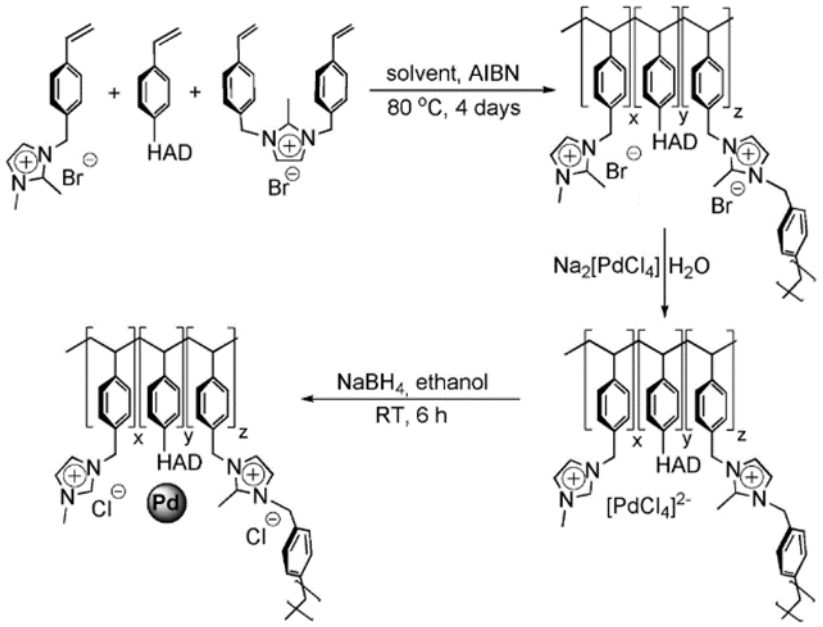

Scheme 4.1: General synthetic procedure for PdNP supported polymer immobilised ionic liquid systems (where the heteroatom donor (HAD) in this case is PPh_2).[35]

Its pegylated counterpart was prepared in a similar manner with the aim of introducing additional weak stabilising NP interactions and improving water solubility for aqueous phase catalysis.[48] Both polymers were impregnated with $[PdCl_4]^{2-}$ to afford $PdCl_4$@PPh_2-PILP and $PdCl_4$@PPh_2-PEGPILP as red-brown solids in near quantitative yield. The corresponding PILP-stabilised NPs, PdNP@PPh_2-PILP and PdNP@PPh_2-PEGPILP, were prepared by the sodium borohydride reduction of $PdCl_4$@PPh_2-PILP and $PdCl_4$@PPh_2-PEGPILP respectively, in ethanol and isolated as black powders in good yields (see Section 4.5.1 for full experimental details).

The nomenclature chosen to describe these polymers and corresponding NP-loaded systems outlines the composition and/or modification according to Figure 4.1. Polymer immobilised ionic liquids (PILP) combine the benefits of an ionic liquid (been shown to act as a stabiliser for a host of transition metal nanoparticles) and polymer (easier to recycle, polymer support prevents leaching of the ionic liquid during catalysis). The heteroatom donor (HAD) is incorporated in the support system to stabilise the MNPs and may also influence their formation i.e. particle size. Additionally, the polyethylene glycol unit (PEG) is incorporated to improve the dispersibility of material in aqueous solution.

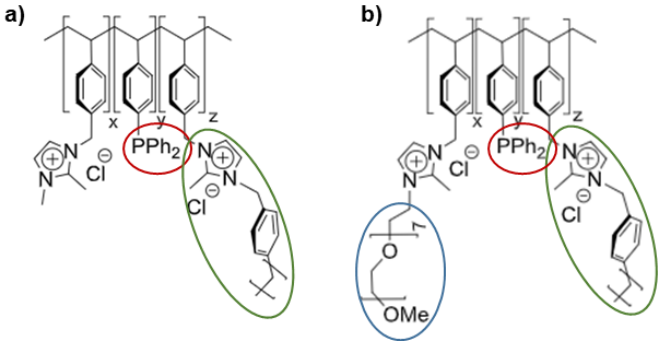

Figure 4.1: Structures of a) PPh_2-PILP where PPh_2 = heteroatom donor used to modify styrene and PILP = polymer immobilised ionic liquid; and b) PPh_2-PEGPILP where PEG = polyethylene glycol unit.

4.2.1 Incorporating a Phosphino Heteroatom Donor into Ionic Liquid Polymer Supported Palladium Nanoparticles

The stabilisation of PdNPs in aqueous media remains an area of interest as it offers enormous potential to develop greener and more sustainable processes.[49,50] Heteroatom donors incorporated into polymer supported ionic liquids allow for additional covalent interactions between the IL ions and the NPs improving the stability of the NPs. P-containing ionophilic ligands have been previously shown to generate smaller PdNPs when the ligand is present

compared to when it is not, resulting in a more active and selective catalyst material.[18] To further investigate the effects of incorporating a phosphino HAD on PdNP formation i.e. particle size, the preparation of phosphino-decorated PILP-stabilised PdNPs (PdNP@PPh_2-PILP) and their pegylated counterpart (PdNP@PPh_2-PEGPILP) was undertaken (see below for structural characterisation). The aqueous phase chemoselective reduction of cinnamaldehyde was chosen as a platform reaction to evaluate the effects of particle size as well as the effect of incorporating a polyethylene glycol unit (increase dispersibility in aqueous media) had on the reactivity/ selectivity of the catalyst materials (see Section 4.3.1 for catalyst results/discussion).

4.2.1.1 PdNP@PPh_2-PILP

The structure of PdNP@PPh_2-PILP is highlighted in Figure 4.2.

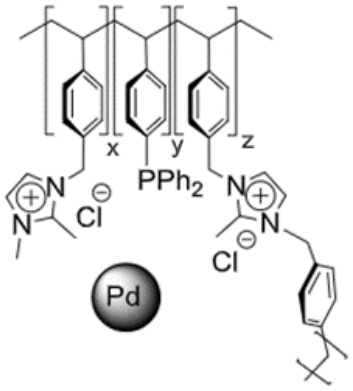

Figure 4.2: Structure of PdNP@PPh_2-PILP where x = imidazolium-modified monomer, y = HAD-modified styrene and z = dicationic cross-linker, in the following ratio: x = 1.84, y = 1, z = 0.16.

TEM was employed to quantify the size, shape and distribution of the NPs on the support structure for PdNP@PPh_2-PILP (see Figure 4.3). Quantitative size analysis was performed by measuring the diameter of a statistically relevant number of different nanoparticles (>100 samples) from different regions of the TEM sample grid and revealed the average size of the MNPs to be 2.29 ± 0.96 nm.

EDX spectroscopy showed characteristic peaks of Pd at 2.8 KeV confirming the composition of the NPs formed on the polymer support (Figure 4.4).

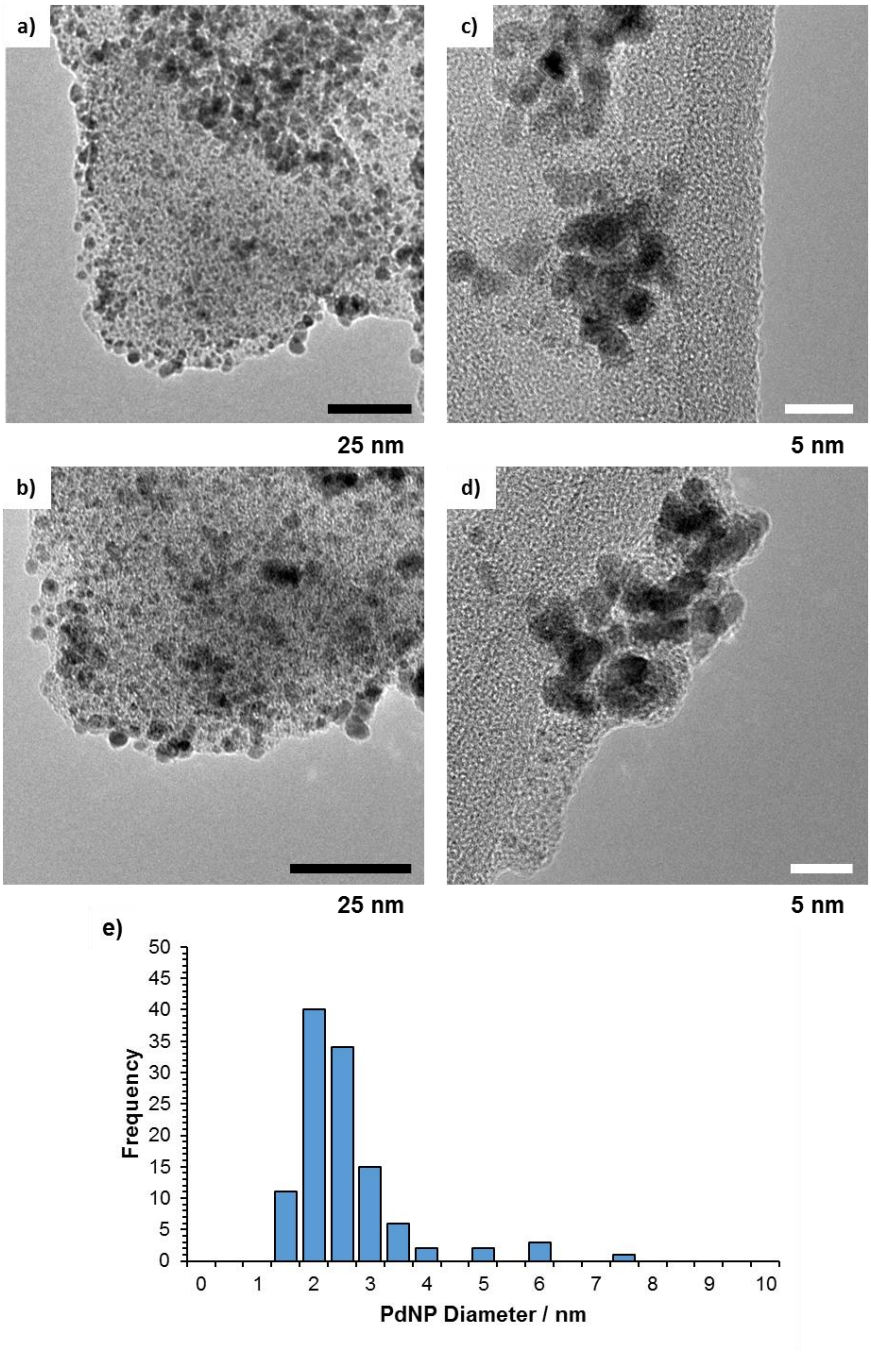

Figure 4.3: a-d) TEM micrographs of PdNP@PPh_2-PILP showing the general structure, size, and distribution of the MNPs; and e) size distribution d_{NP} = 2.29 ± 0.96 nm.

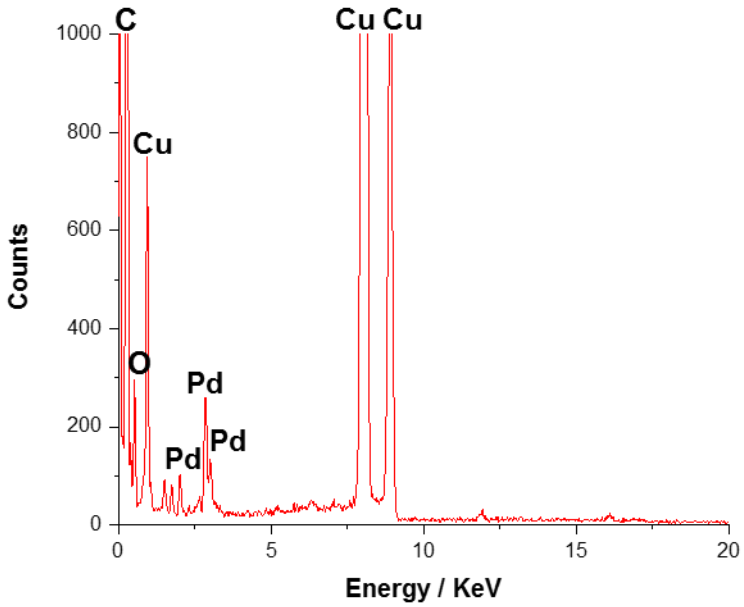

Figure 4.4: EDX spectrum of PdNP@PPh_2-PILP. Characteristic peaks were identified at 2.8 KeV. Cu peaks are due to the TEM grid used.

Surface characterization of PdNP@PPh_2-PILP was undertaken with X-ray photoelectron spectroscopy (XPS) by analysis of the Pd $3d_{3/2}$ and Pd $3d_{5/2}$ doublets (Figure 4.5). Binding energies at 335.3 and 340.6 eV were observed which can attributed to the Pd(0) species as well as binding energies at 337.3 and 342.7 eV which can attributed to the Pd(II) species.[20,51]

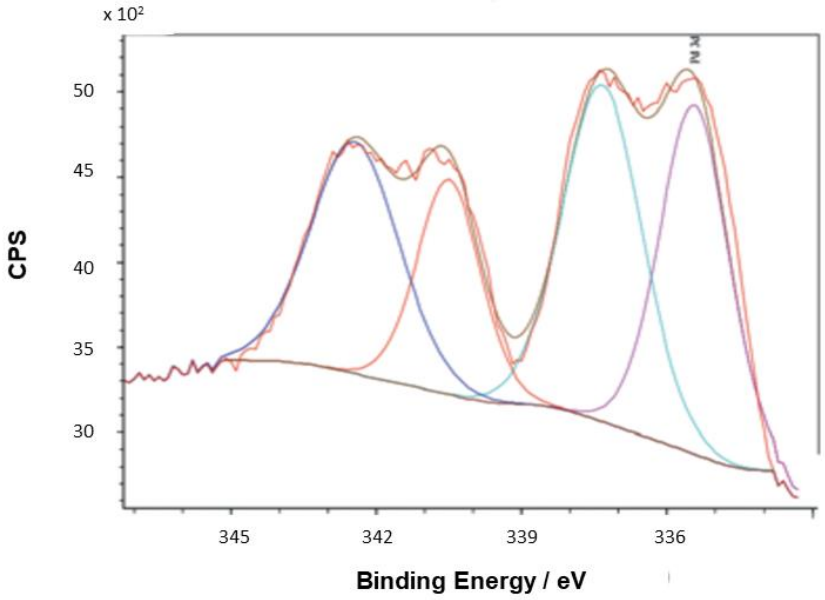

Figure 4.5: Pd 3d core level XPS of PdNP@PPh_2-PILP, referenced to the hydrocarbon C 1s, showing the Pd $3d_{3/2}$ and Pd $3d_{5/2}$ doublets.

4.2.1.2 PdNP@PPh_2-PEGPILP

The structure of PdNP@PPh_2-PEGPILP is highlighted in Figure 4.6.

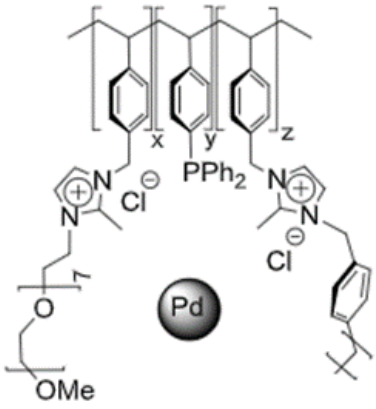

Figure 4.6: Structure of PdNP@PPh_2-PEGPILP where x = imidazolium-modified pegylated monomer, y = HAD-modified styrene and z = dicationic cross-linker, in the following ratio: x = 1.84, y = 1, z = 0.16.

Surface characterization of PdNP@PPh_2-PEGPILP was undertaken with XPS by analysis of the Pd $3d_{3/2}$ and Pd $3d_{5/2}$ doublets (Figure 4.7). Binding energies at 335.3 and 340.5 eV were observed which can attributed to the Pd(0) species as well as binding energies at 337.4 and 342.6 eV which can attributed to the Pd(II) species.[20,51]

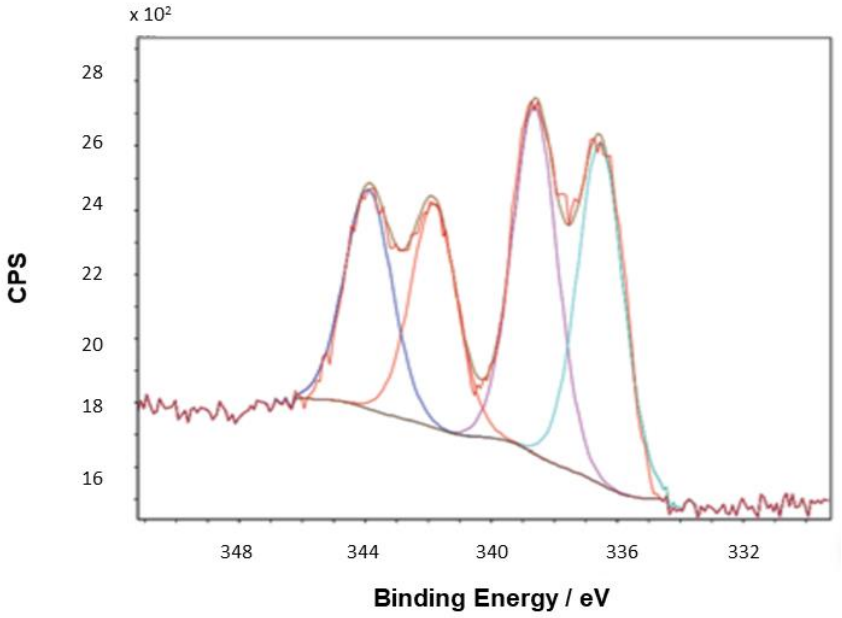

Figure 4.7: Pd 3d core level XPS of PdNP@PPh_2-PEGPILP, referenced to the hydrocarbon C 1s, showing the Pd $3d_{3/2}$ and Pd $3d_{5/2}$ doublets.

TEM was employed to quantify the size, shape and distribution of the NPs on the support structure for PdNP@PPh_2-PEGPILP (see Figure 4.8).

Quantitative size analysis was performed by measuring the diameter of a statistically relevant number of different nanoparticles (>100 samples) from different regions of the TEM sample grid and revealed the average size of the MNPs to be 1.93 ± 0.67 nm.

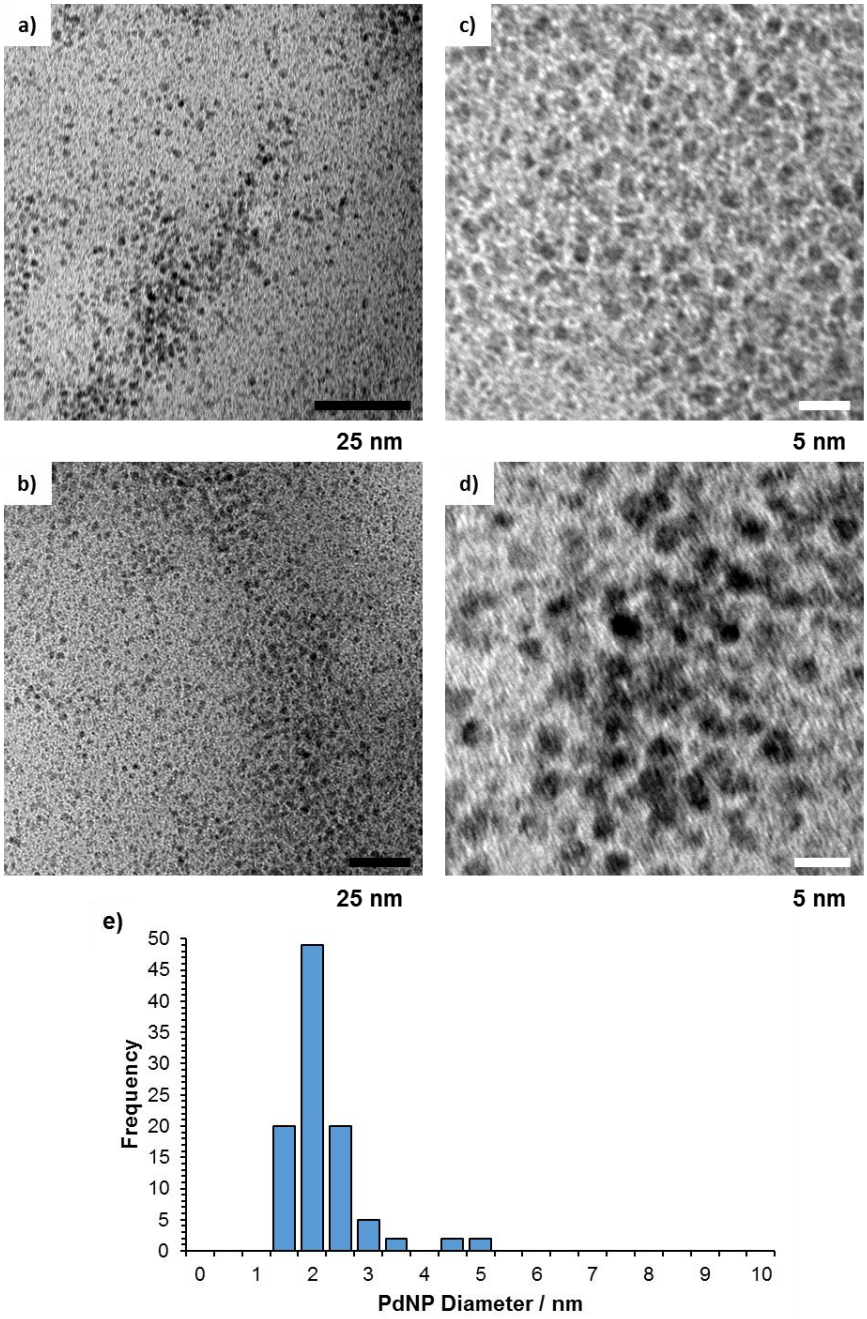

Figure 4.8: a-d) TEM micrographs of PdNP@PPh_2-PEGPILP showing the general structure, size and distribution of the MNPs; and e) size distribution d_{NP} = 1.93 ± 0.67 nm.

4.2.1.3 Summary

TEM analysis of PdNPs@PPh_2-PILP and PdNP@PPh_2-PEGPILP shows that the PdNPs are monodispersed within the support structure with average

diameters of 2.29 ± 0.96 and 1.93 ± 0.67 nm, respectively. As the PdNPs are similar in each material this indicates that incorporation of PEG into the support system has little effect on NP size. XPS shows no change in palladium binding energies between the two materials.

4.2.2 Effect of Changing the Heteroatom Donor and Other Components of the Support System

As mentioned previously, the heteroatom donor has the potential to influence not only the stability of the PdNPs but also their formation and can therefore influence the particle size. The preparation of various PdNPs stabilised by different heteroatom donor-modified immobilised ionic liquid systems (PdNP@HAD-PILP) were prepared to investigate the effect of the heteroatom donor on PdNP formation.

As well as investigating the effects of the heteroatom donor chosen, the influence of the surface ionic liquid (IL) and polyethylene glycol (PEG) unit on PdNP size and catalyst performance was also investigated by evaluating the activity of a series of catalysts containing differing combinations of each component (see below for structural characterisation). PdNP@PPh_2-PILP and PdNP@PPh_2-PEGPILP were also included in this study; their structural characterisation can be found in Section 4.2.1.

The Suzuki-Miyaura cross-coupling reaction was chosen to evaluate the structure/performance relationship in terms of catalytic performance for these materials (see Section 4.3.2 for catalyst results/discussion).

4.2.2.1 PdNP@CN-PILP

The structure of PdNP@CN-PILP is highlighted in Figure 4.9.

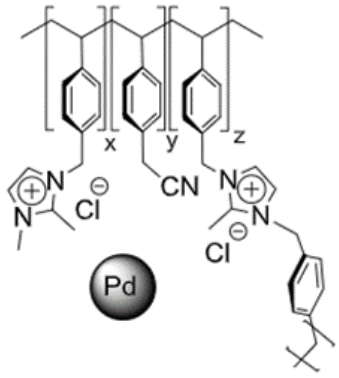

Figure 4.9: Structure of PdNP@CN-PILP where x = imidazolium-modified monomer, y = HAD-modified styrene and z = dicationic cross-linker, in the following ratio: x = 1.84, y = 1, z = 0.16.

TEM was employed to quantify the size, shape and distribution of the NPs on the support structure for PdNP@CN-PILP (see Figure 4.10). Quantitative size analysis was performed by measuring the diameter of a statistically relevant number of different nanoparticles (>100 samples) from different regions of the TEM sample grid and revealed the average size of the MNPs to be 3.20 ± 0.62 nm.

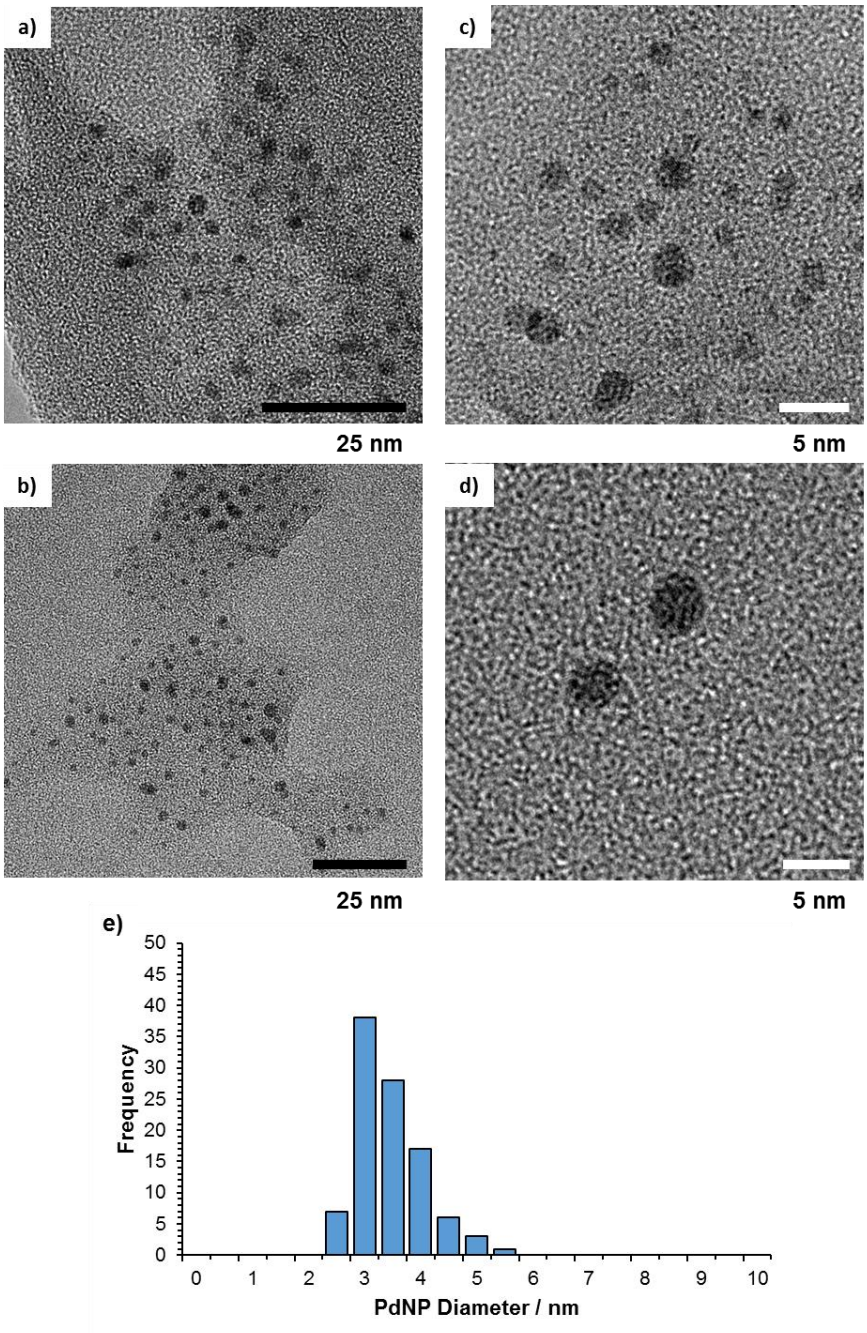

Figure 4.10: a-d) TEM micrographs of PdNP@CN-PILP showing the general structure, size and distribution of the MNPs; and e) size distribution d_{NP} = 3.20 ± 0.62 nm.

Surface characterization of PdNP@PEGPILP was undertaken with XPS by analysis of the Pd $3d_{3/2}$ and Pd $3d_{5/2}$ doublets (Figure 4.11). Binding energies at 335.0 and 340.5 eV were observed which can be attributed to the Pd(0) species as well as binding energies of 337.3 and 342.6 eV which can be attributed to the Pd(II)species.[20,51]

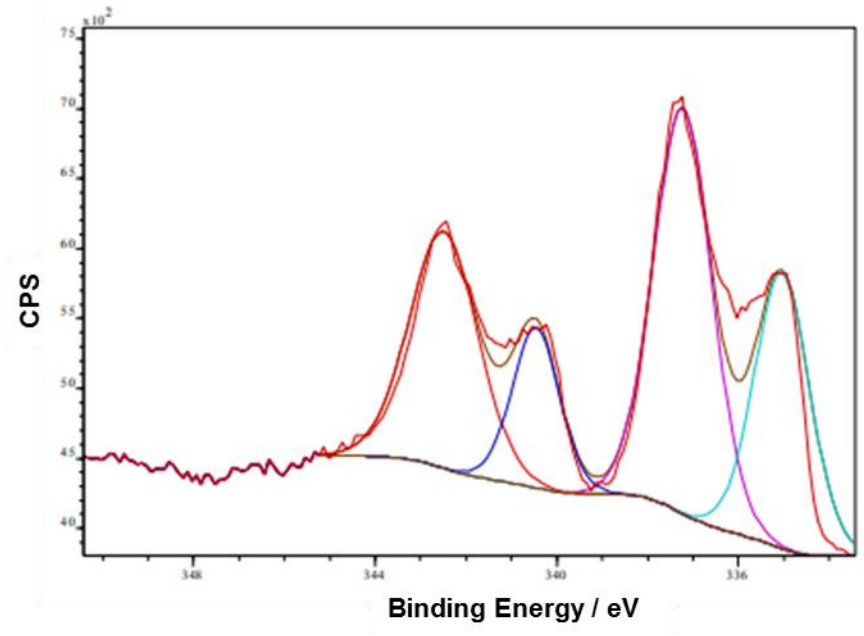

Figure 4.11: Pd 3d core level XPS of PdNP@CN-PILP, referenced to the hydrocarbon C 1s, showing the Pd $3d_{3/2}$ and Pd $3d_{5/2}$ doublets.

4.2.2.2 PdNP@Pyrr-PILP

The structure of PdNP@Pyrr-PILP is highlighted in Figure 4.12.

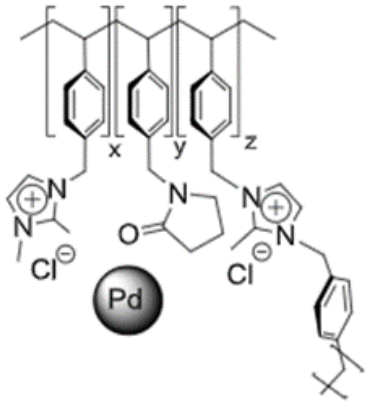

Figure 4.12: Structure of PdNP@Pyrr-PILP (Pyrr = pyrrolidin-2-one) where x = imidazolium-modified monomer, y = HAD-modified styrene and z = dicationic cross-linker, in the following ratio: x = 1.84, y = 1, z = 0.16.

TEM was employed to quantify the size, shape and distribution of the NPs on the support structure for PdNP@Pyrr-PILP (see Figure 4.13). Quantitative size analysis was performed by measuring the diameter of a statistically

relevant number of different nanoparticles (>100 samples) from different regions of the TEM sample grid and revealed the average size of the MNPs to be 2.38 ± 0.50 nm.

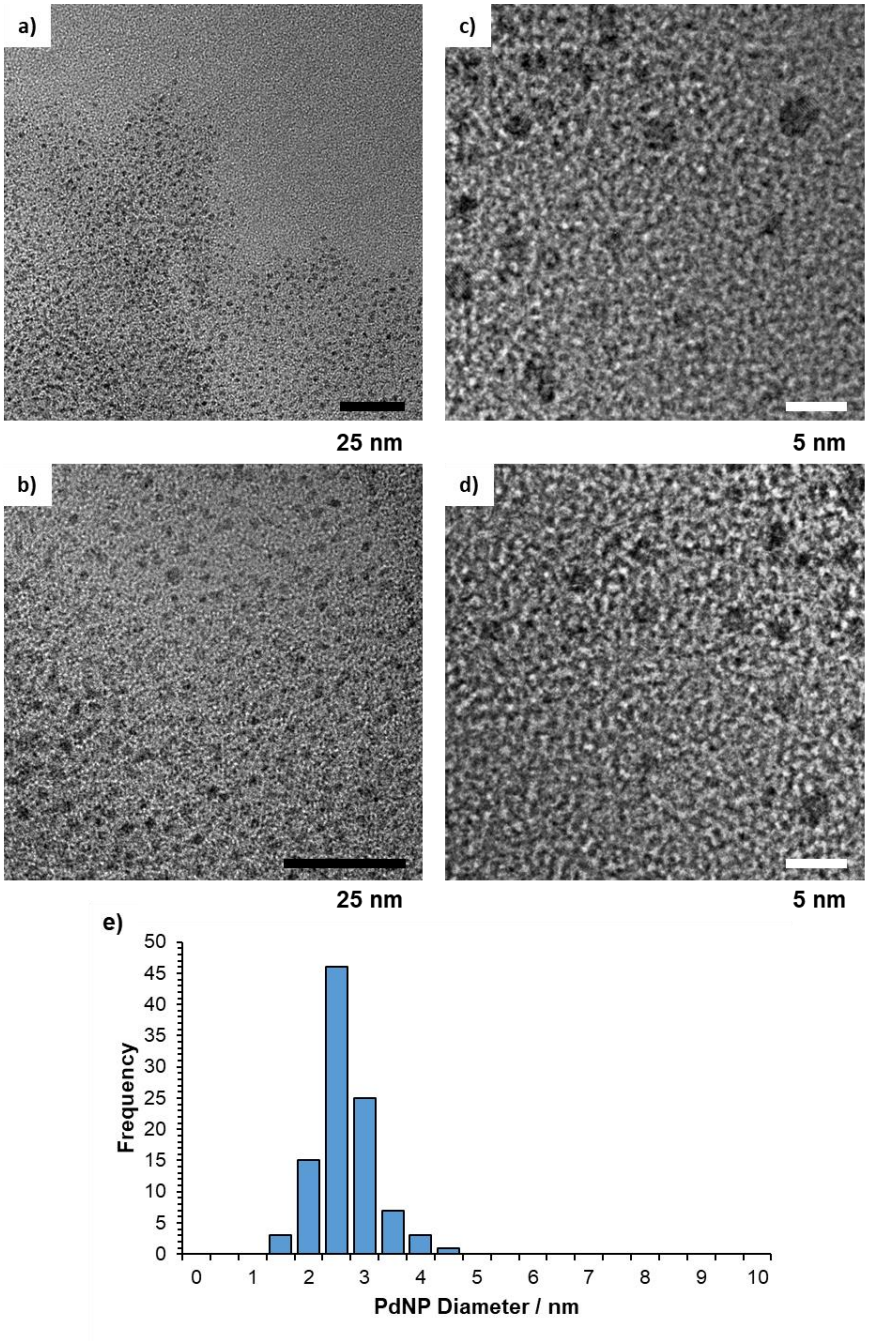

Figure 4.13: a-d) TEM micrographs of PdNP@Pyrr-PILP showing the general structure, size and distribution of the MNPs; and e) size distribution d_{NP} = 2.38 ± 0.50 nm

Surface characterization of PdNP@PSty$_3$-PILP was undertaken with XPS by analysis of the Pd 3d$_{3/2}$ and Pd 3d$_{5/2}$ doublets (Figure 4.14). Binding energies where observed at 335.16 and 340.5 eV which can be attributed to the Pd(0)

species as well as binding energies at 337.52 and 342.91 eV which can be attributed to the Pd(II) species.[20,51]

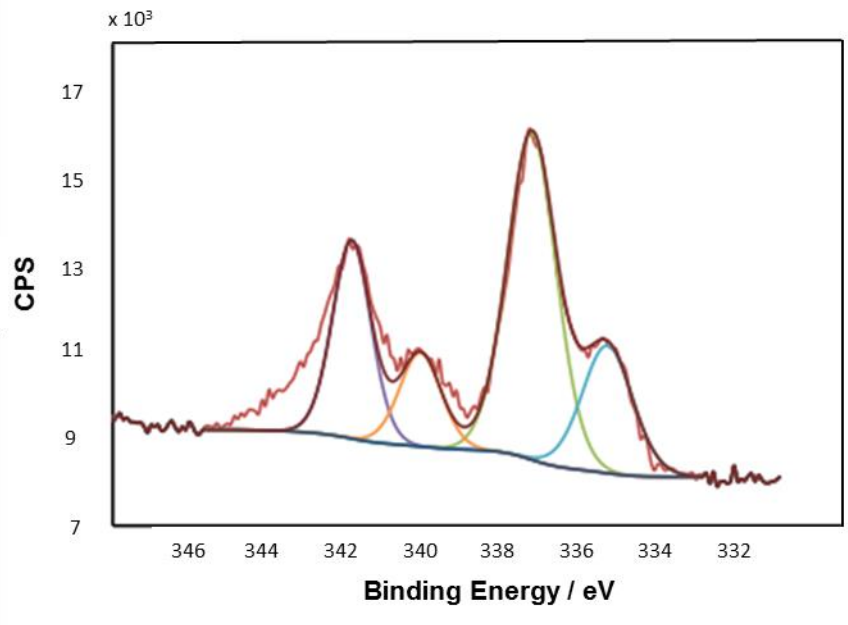

Figure 4.14: Pd 3d core level XPS of PdNP@Pyrr-PILP, referenced to the hydrocarbon C 1s, showing the Pd $3d_{3/2}$ and Pd $3d_{5/2}$ doublets.

4.2.2.3 PdNP@PILP

The structure of PdNP@PILP is highlighted in Figure 4.15.

Figure 4.15: Structure of PdNP@PILP.

TEM was employed to quantify the size, shape and distribution of the NPs on the support structure for PdNP@PILP (see Figure 4.16). Quantitative size analysis was performed by measuring the diameter of a statistically relevant number of different nanoparticles (>100 samples) from different regions of the TEM sample grid and revealed the average size of the MNPs to be 3.01 ± 0.63 nm.

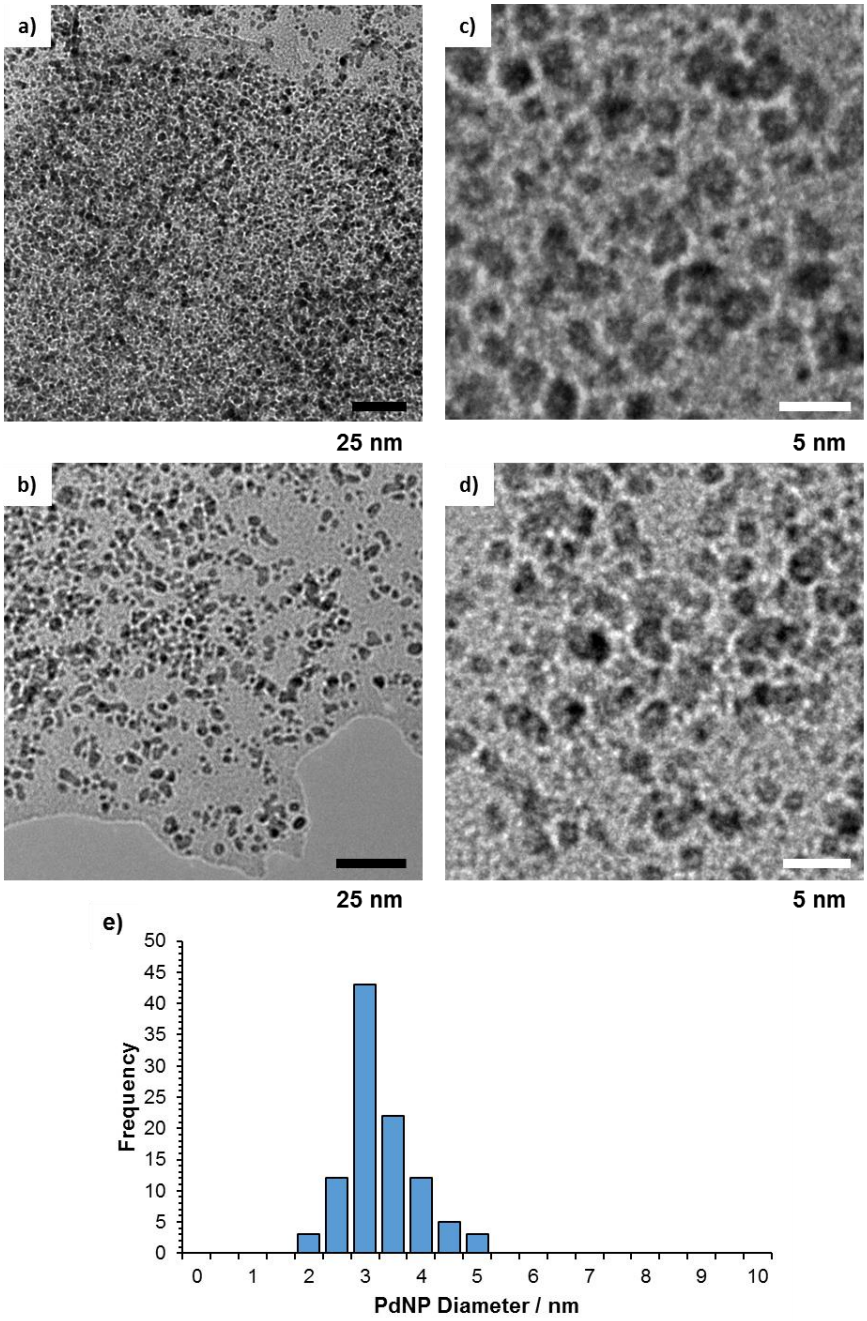

Figure 4.16: a-d) TEM micrographs of PdNP@PILP showing the general structure, size and distribution of the MNPs; and e) size distribution d_{NP} = 3.01 ± 0.63 nm.

Surface characterization of PdNP@PILP was undertaken with XPS by analysis of the Pd $3d_{3/2}$ and Pd $3d_{5/2}$ doublets (Figure 4.17). Binding energies were observed at 335.0 and 340.1 eV which can be attributed to the Pd(0) species as well as 336.1 and 341.2 eV which can be attributed to the Pd(II) species.[20,51]

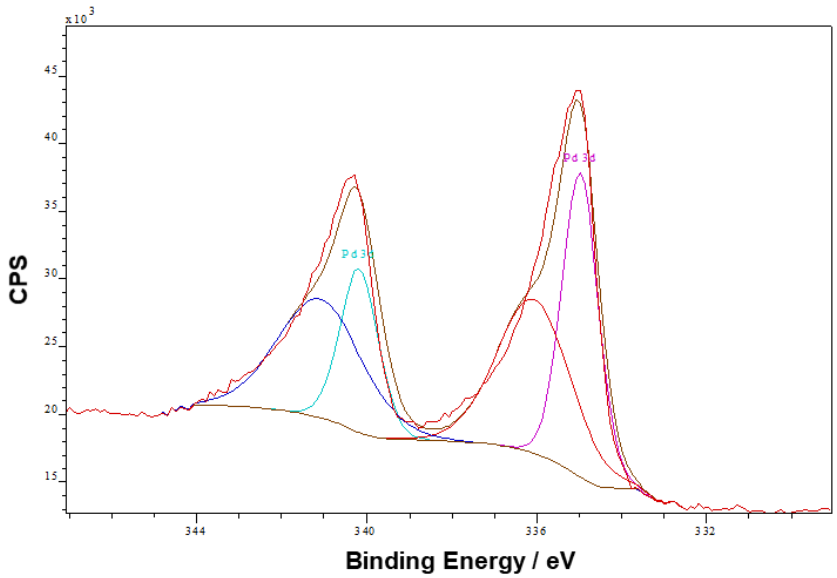

Figure 4.17: Pd 3d core level XPS spectrum of PdNP@PILP, referenced to the hydrocarbon C 1s, showing the Pd $3d_{3/2}$ and Pd $3d_{5/2}$ doublets.

4.2.2.4 PdNP@PPh_2-styrene

The structure of PdNP@PPh_2-styrene is highlighted in Figure 4.18.

Figure 4.18: Structure of PdNP@PPh_2-styrene.

TEM was employed to quantify the size, shape and distribution of the NPs on the support structure for PdNP@PPh_2-styrene (see Figure 4.19). Quantitative size analysis was performed by measuring the diameter of a statistically relevant number of different nanoparticles (>100 samples) from different regions of the TEM sample grid and revealed the average size of the MNPs to be 1.39 ± 0.19 nm.

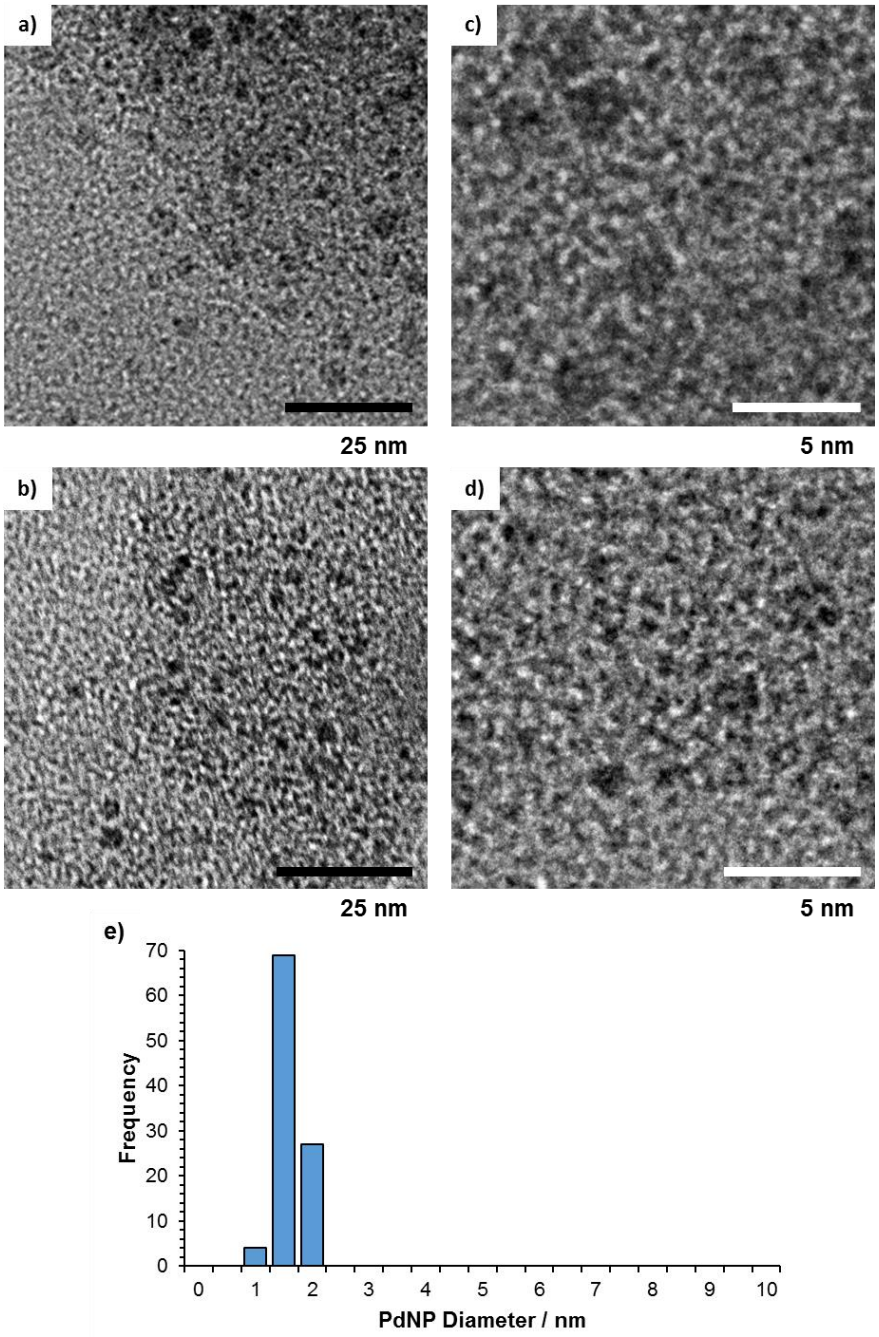

Figure 4.19: a-d) TEM micrographs of PdNP@PPh_2-styrene showing the general structure, size and distribution of the MNPs; and e) size distribution d_{NP} = 1.39 ± 0.19 nm.

Surface characterization of PdNP@PPh_2-styrene was undertaken with XPS by analysis of the Pd $3d_{3/2}$ and Pd $3d_{5/2}$ doublets (Figure 4.20). Binding energies were observed at 335.6 and 340.7 eV which can be attributed to the Pd(0) species. In addition, binding energies were also observed at 337.5 and 342.8 eV which can be attributed to the Pd(II) species.[20,51]

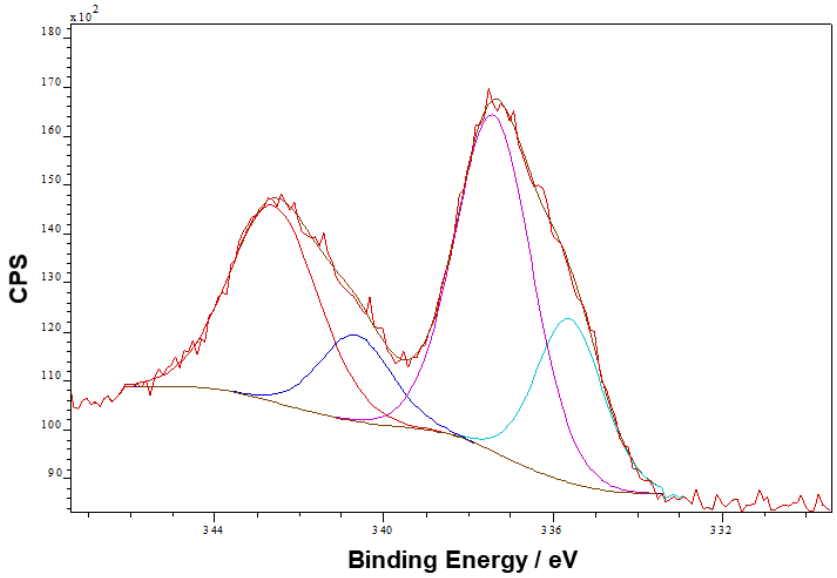

Figure 4.20: Pd 3d core level XPS of PdNP@PPh_2-polystrene, referenced to the hydrocarbon C 1s, showing the Pd $3d_{3/2}$ and Pd $3d_{5/2}$ doublets.

4.2.2.5 PdNP@PEGPILP

The structure of PdNP@PEGPILP is highlighted in Figure 4.21.

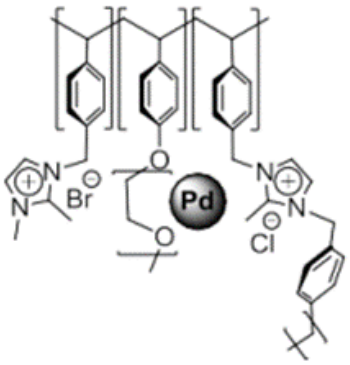

Figure 4.21: Structure of PdNP@PEGPILP.

TEM was employed to quantify the size, shape and distribution of the NPs on the support structure for PdNP@PEGPILP formed in situ (see Figure 4.22). Quantitative size analysis was performed by measuring the diameter of a statistically relevant number of different nanoparticles (>100 samples) from different regions of the TEM sample grid and revealed the average size of the MNPs to be 3.23 ± 0.61 nm.

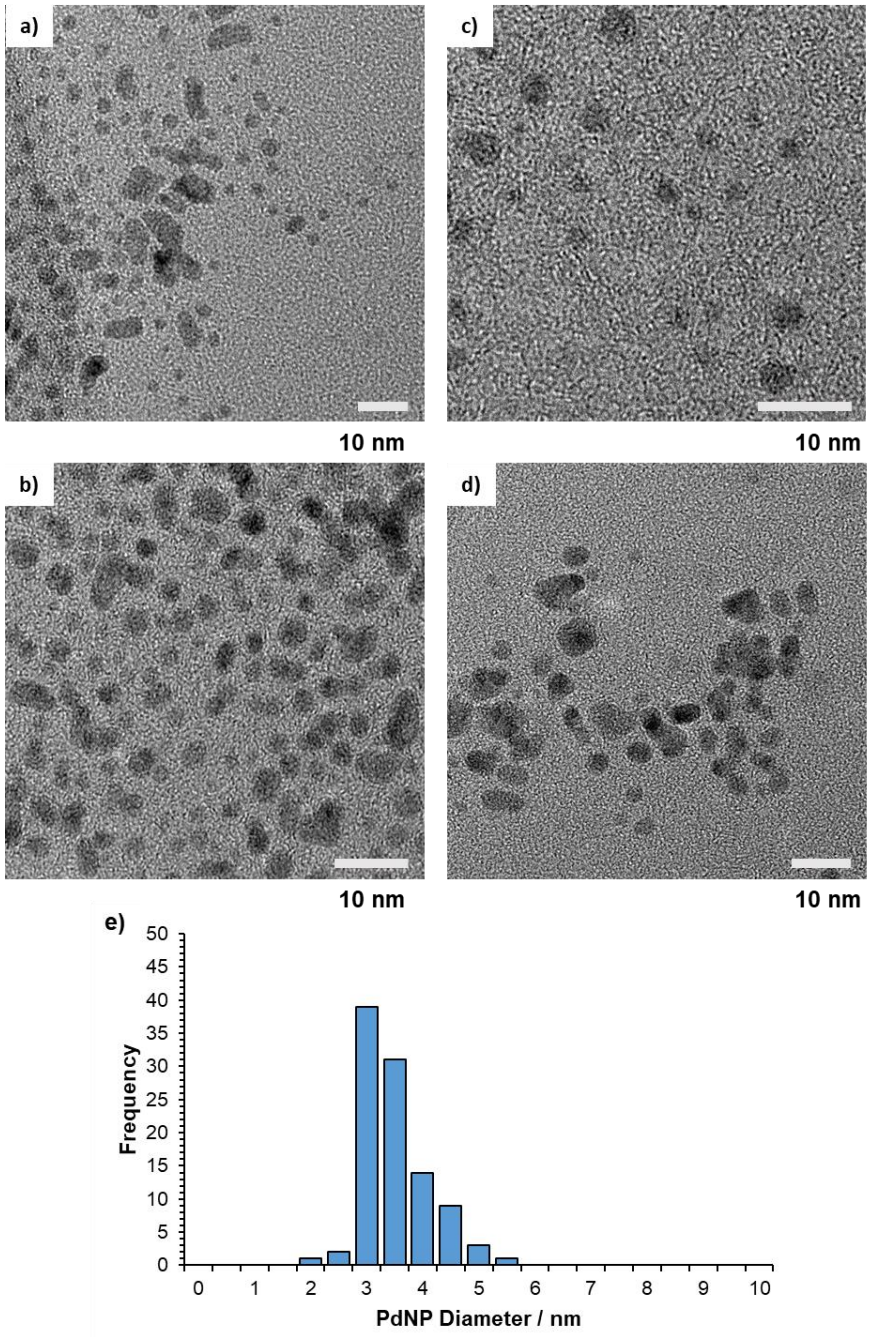

Figure 4.22: a-d) TEM micrographs of PdNP@PEGPILP showing the general structure, size and distribution of the MNPs; and e) size distribution d_{NP} = 3.23 ± 0.61 nm.

Surface characterization of PdNP@PEGPILP was undertaken with XPS by analysis of the Pd $3d_{3/2}$ and Pd $3d_{5/2}$ doublets (Figure 4.23). Binding energies at 335.3 and 340.7 eV were observed which can be attributed to the Pd(0) species as well as binding energies of 337.4 and 342.7 eV which can be attributed to the Pd (II) species.[20,51]

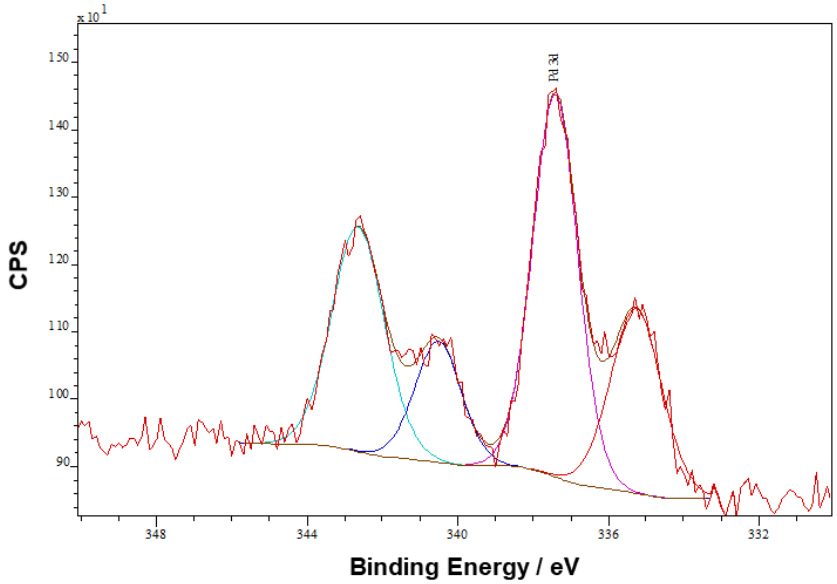

Figure 4.23: Pd 3d core level XPS of PdNP@PEGPILP, referenced to the hydrocarbon C 1s, showing the Pd $3d_{3/2}$ and Pd $3d_{5/2}$ doublets.

4.2.2.6 PdNP@PPh_2-PEGstyrene

The structure of PdNP@PPh_2-PEGstyrene is highlighted in Figure 4.24.

Figure 4.24: Structure of PdNP@PPh_2-PEGstyrene.

TEM was employed to quantify the size, shape and distribution of the NPs on the support structure for PdNP@PPh_2-PEGstyrene (see Figure 4.25). Quantitative size analysis was performed by measuring the diameter of a statistically relevant number of different nanoparticles (>100 samples) from different regions of the TEM sample grid and revealed the average size of the MNPs to be 1.83 ± 0.44 nm.

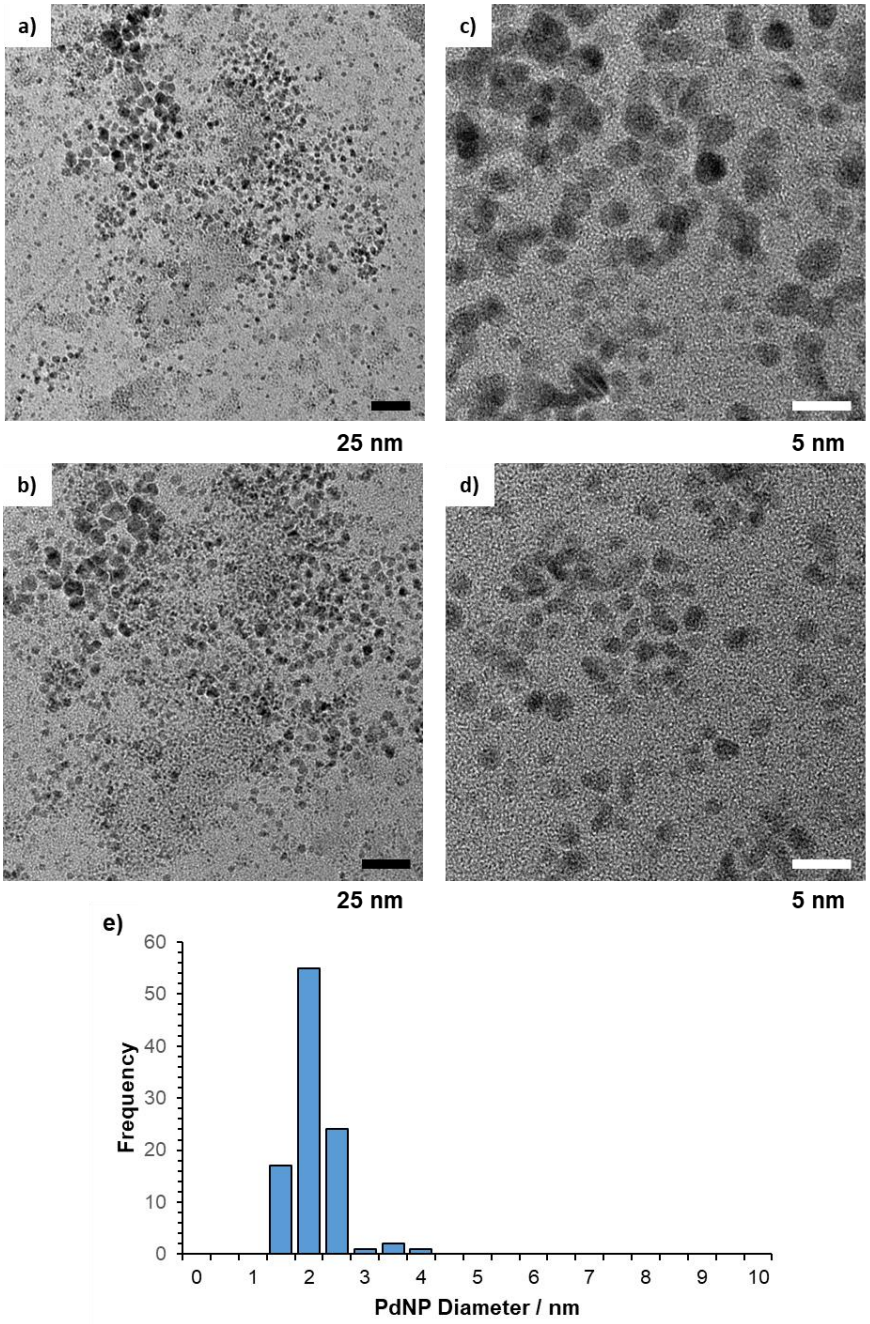

Figure 4.25: a-d) TEM micrographs of PdNP@PPh_2-PEGstyrene showing the general structure, size and distribution of the MNPs; and e) size distribution d_{NP} = 1.83 ± 0.44 nm.

Surface characterization of PdNP@PPh_2-PEGstyrene was undertaken with XPS by analysis of the Pd $3d_{3/2}$ and Pd $3d_{5/2}$ doublets (Figure 4.26). Binding energies were observed at 335.2 and 341.0 eV which can be attributed to the Pd(0) species as well as binding energies at 337.1 and 342.5 eV which can be attributed to the Pd(II) species.[20,51]

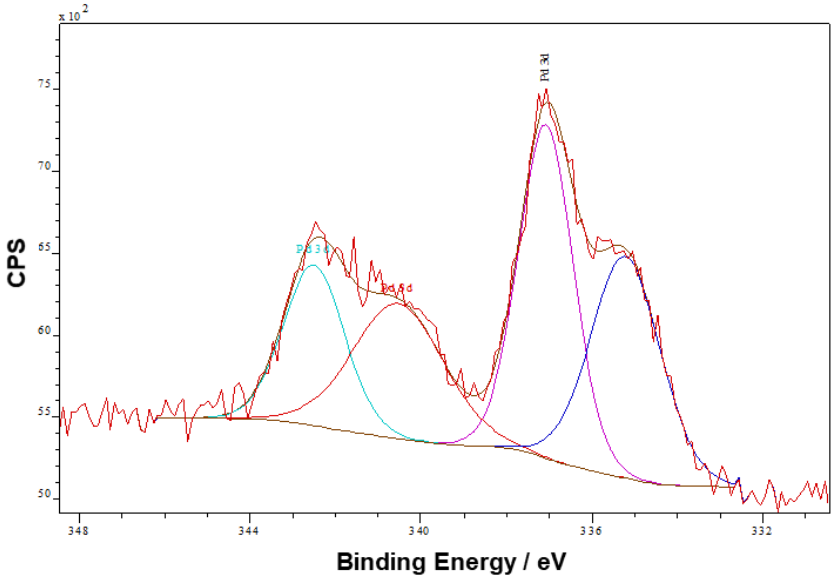

Figure 4.26: Pd 3d core level XPS of PdNP@PPh_2-PEGstyrene, referenced to the hydrocarbon C 1s, showing the Pd $3d_{3/2}$ and Pd $3d_{5/2}$ doublets.

4.2.2.7 PdNP@PPh_2-PILP in situ

As the polymer immobilised ionic liquid stabilised PdNPs are fabricated from the reduction of their tetrachloropalladate-based precursors, using sodium borohydride as the reducing agent, preparation of PdNP@PPh_2-PILP formed in-situ during a reduction reaction was investigated. By preparing the catalyst system in-situ the need to prepare, separate and store the catalysts before their use in reactions is eliminated ultimately streamlining the process for rapid reaction screening of catalysts.

TEM was employed to quantify the size, shape and distribution of the NPs on the support structure for PdNP@PPh_2-PILP formed in situ (see Figure 4.27). Quantitative size analysis was performed by measuring the diameter of a statistically relevant number of different nanoparticles (>100 samples) from different regions of the TEM sample grid and revealed the average size of the MNPs to be 2.61 ± 0.38 nm.

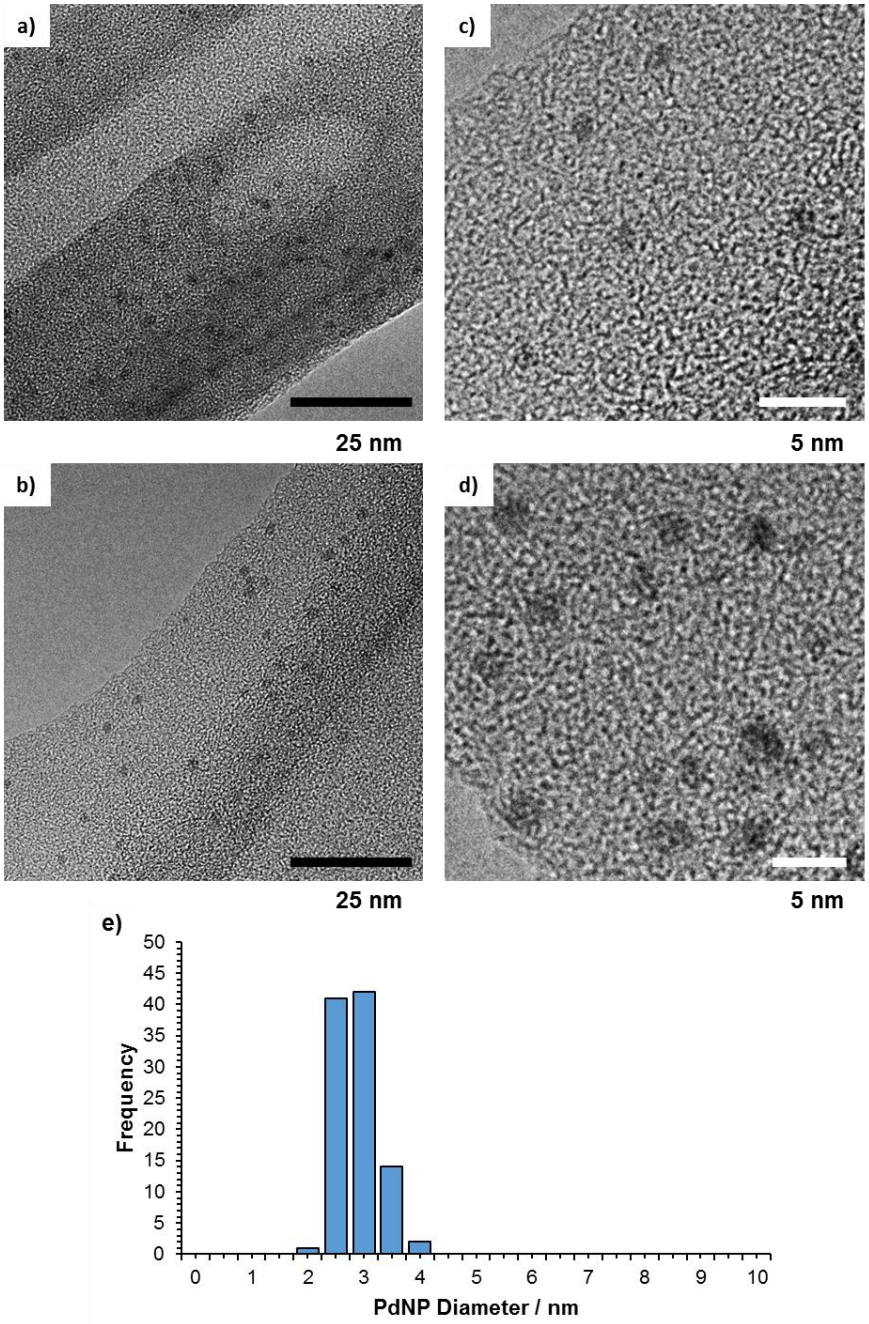

Figure 4.27: a-d) TEM micrographs of PdNP@PPh_2-PILP (formed in situ) showing the general structure, size and distribution of the MNPs; and e) size distribution d_{NP} = 2.61 ± 0.38 nm.

4.2.2.8 PdNP@PPh_2-PEGPILP in situ

Preparation of PdNP@PPh_2-PEGPILP in-situ during a reduction reaction was also investigated. TEM was employed to quantify the size, shape and distribution of the NPs on the support structure for PdNP@PPh_2-PEGPILP formed in situ (see Figure 4.28). Quantitative size analysis was performed by measuring the diameter of a statistically relevant number of different

nanoparticles (>100 samples) from different regions of the TEM sample grid and revealed the average size of the MNPs to be 3.36 ± 0.61 nm.

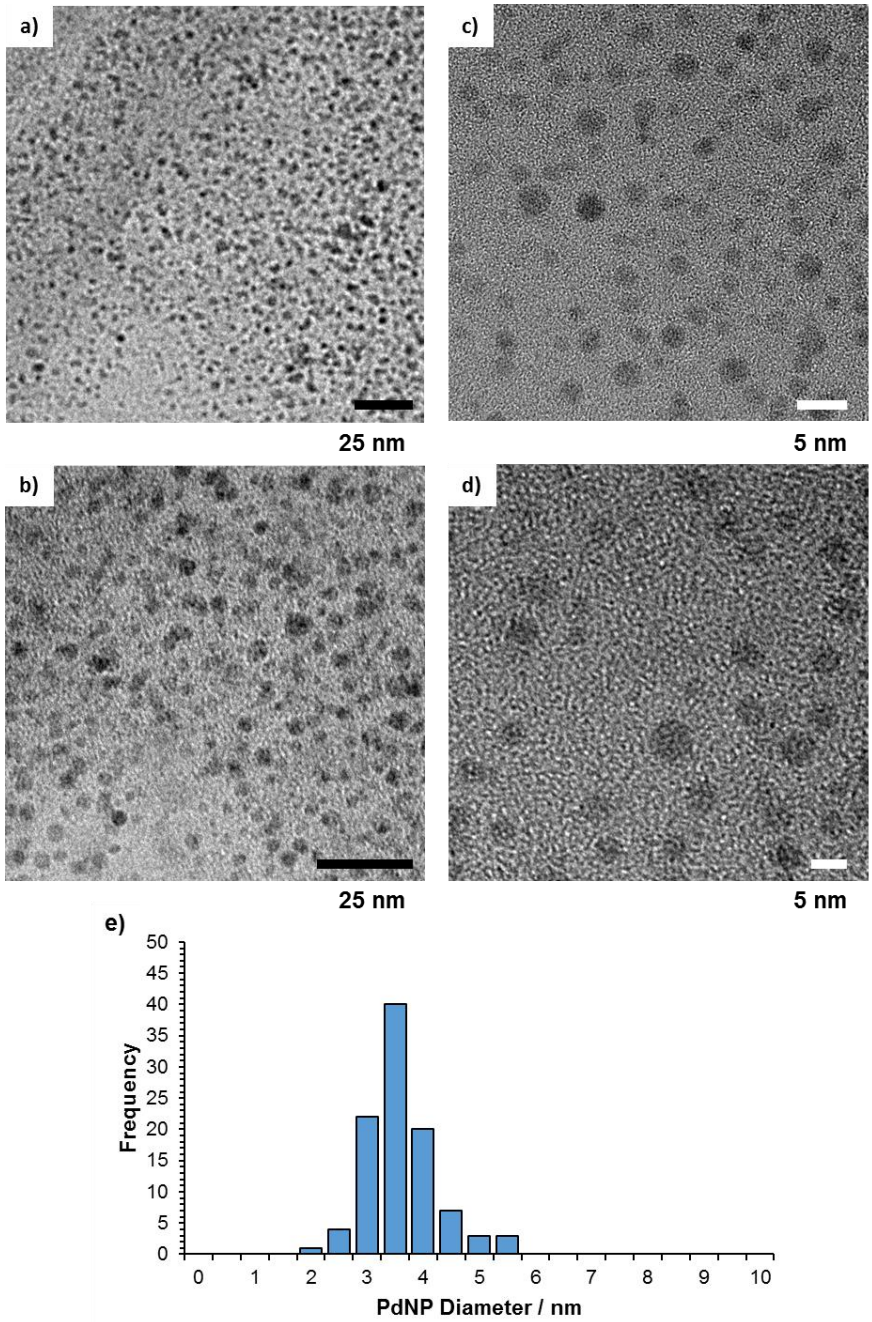

Figure 4.28: a-d) TEM micrographs of PdNP@PPh_2-PEGPILP (formed in situ) showing the general structure, size and distribution of the MNPs; and e) size distribution d_{NP} = 3.36 ± 0.61 nm.

4.2.2.9 Summary

TEM analysis of the materials with differing heteroatom donors showed that that in all cases the PdNPs were monodispersed within the support system and that the size of the PdNPs were dependent upon the heteroatom donor present with average diameter ranging from 1.75 ± 0.78 to 3.20 ± 0.62 nm.

Changing the components of the support structure e.g. selective removal of the IL, was also shown to have little effect on the dispersion of the MNPs within the support system. No significant change in the XPS binding energies was observed for these materials.

4.2.3 Effect on Catalytic Performance by Isolating the Heteroatom Donor

The effect on the catalyst properties and performance by introducing three-fold cross-linking, in the form of tris(*p*-vinylphenyl)phospine, was investigated in the hope of obtaining a more robust catalyst system. Two materials PdNP@PSty$_3$-PILP and PdNP@PSty$_3$-PEGPILP were successfully prepared (see below for structural characterisation) to ascertain if the three-fold cross-linking isolated the heteroatom donor and therefore influenced the number/type of metal-donor interactions.

Additionally, in order to further explore the efficiency of the PdNP@PILP-based systems and investigate whether the same features determine catalyst performance in other reactions the study was extend study to include the aqueous phase hydrogenation and transfer hydrogenation of nitroarenes. PdNP@PPh$_2$-PILP and PdNP@PPh$_2$-PEGPILP were also included in this study; their structural characterisation can be found in Section 4.2.1.

4.2.3.1 PdNP@PSty$_3$-PILP

The structure of PdNP@PSty$_3$-PILP is highlighted in Figure 4.29.

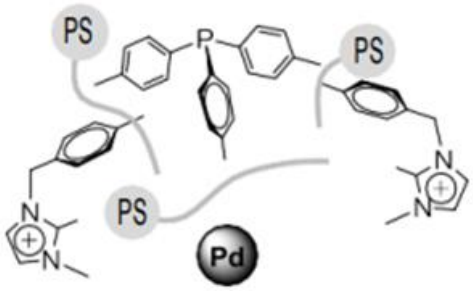

Figure 4.29: Structure of PdNP@PSty$_3$-PILP.

TEM was employed to quantify the size, shape and distribution of the NPs on the support structure for PdNP@PSty$_3$-PILP (see Figure 4.30). Quantitative size analysis was performed by measuring the diameter of a statistically relevant number of different nanoparticles (>100 samples) from different regions of the TEM sample grid and revealed the average size of the MNPs to be 3.67 ± 0.67 nm.

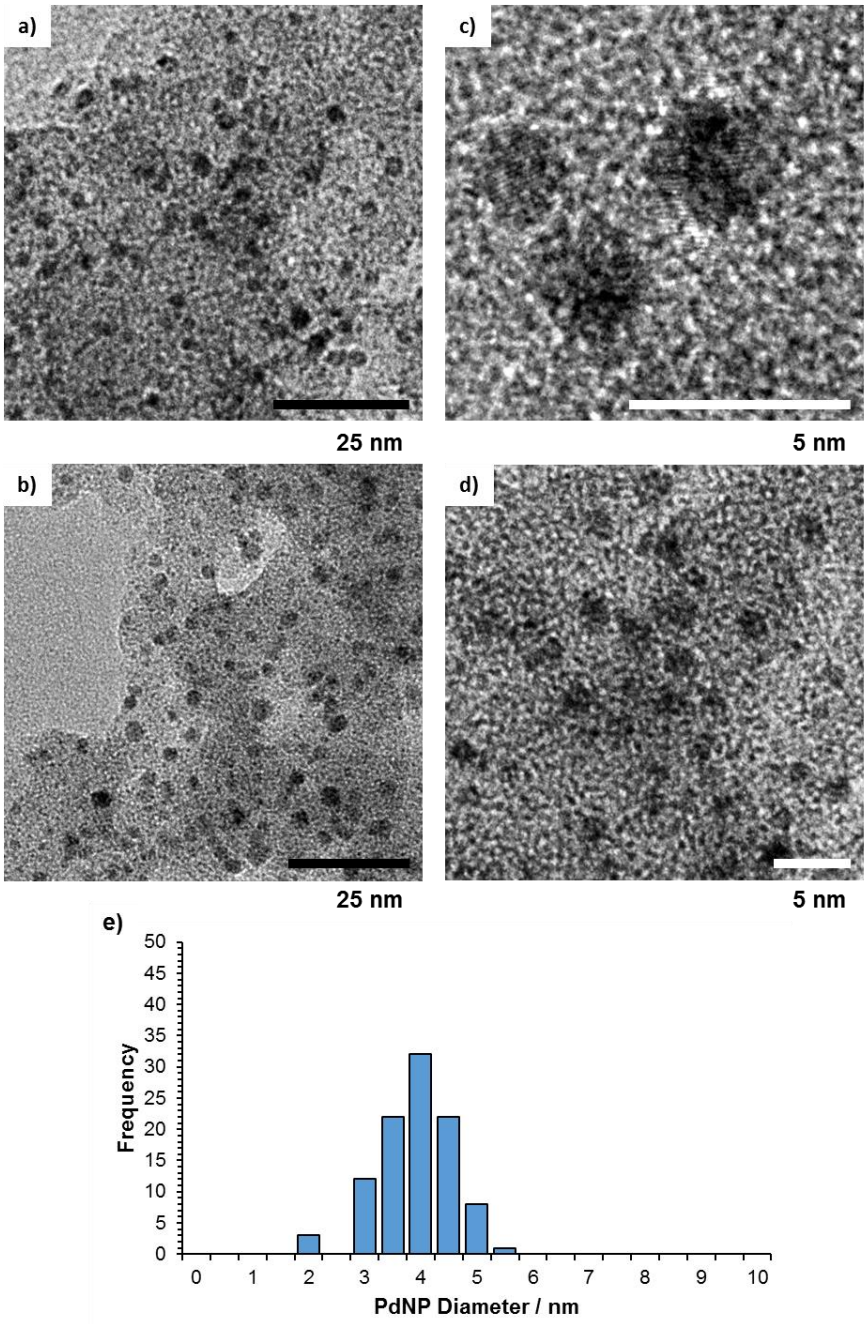

Figure 4.30: a-d) TEM micrographs of PdNP@PSty$_3$-PILP showing the general structure, size and distribution of the MNPs; and e) size distribution d_{NP} = 3.67 ± 0.67 nm.

Surface characterization of PdNP@PSty$_3$-PILP was undertaken with XPS by analysis of the Pd 3d$_{3/2}$ and Pd 3d$_{5/2}$ doublets (Figure 4.31). Binding energies were observed at 335.5 and 340.6 eV which can be attributed to the Pd(0) species as well as binding energies at 337.3 and 342.7 eV which can be attributed to the Pd(II) species.[20,51]

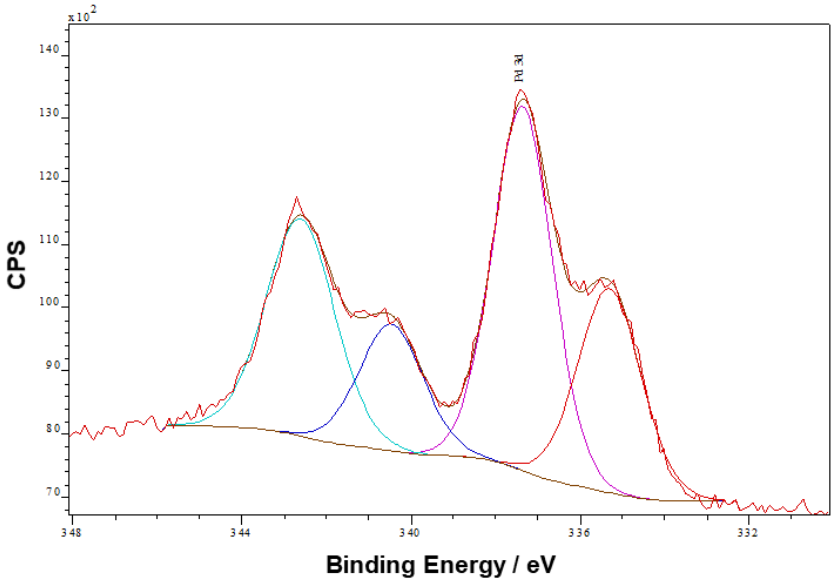

Figure 4.31: Pd 3d core level XPS of PdNP@PSty$_3$-PILP, referenced to the hydrocarbon C 1s, showing the Pd 3d$_{3/2}$ and Pd 3d$_{5/2}$ doublets.

4.2.3.2 PdNP@PSty$_3$-PEGPILP

The structure of PdNP@PSty$_3$-PEGPILP is highlighted in Figure 4.32.

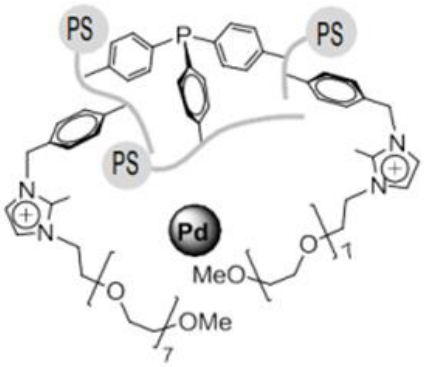

Figure 4.32: Structure of PdNP@PSty$_3$-PEGPILP.

TEM was employed to quantify the size, shape and distribution of the NPs on the support structure for PdNP@PSty$_3$-PEGPILP (see Figure 4.33). Quantitative size analysis was performed by measuring the diameter of a statistically relevant number of different nanoparticles (>100 samples) from different regions of the TEM sample grid and revealed the average size of the MNPs to be 4.02 ± 1.11 nm.

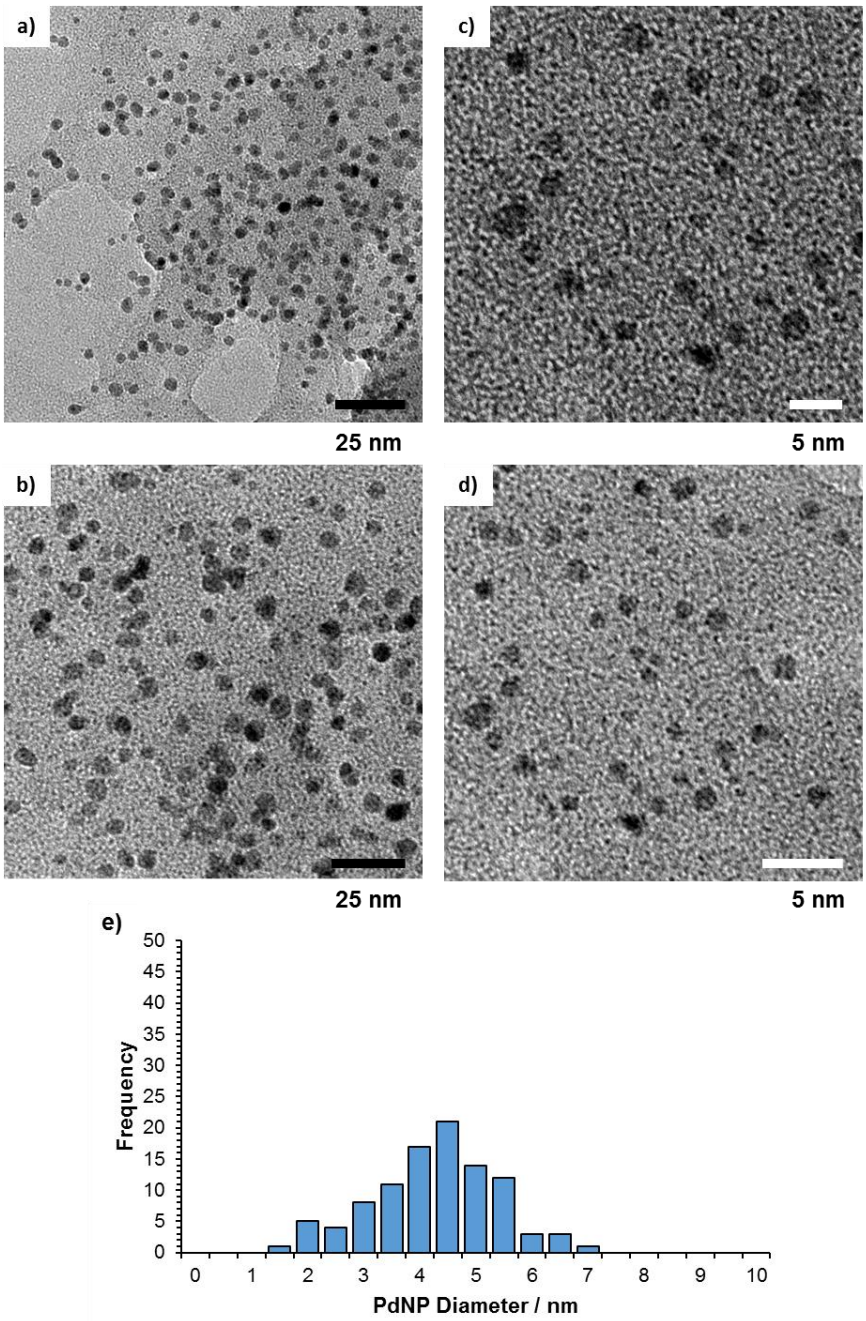

Figure 4.33: a-d) TEM micrographs of PdNP@PStyr$_3$-PEGPILP showing the general structure, size and distribution of the MNPs; and e) size distribution d_{NP} = 4.02 ± 1.11 nm.

Surface characterization of PdNP@PSty$_3$-PEGPILP was undertaken with XPS by analysis of the Pd 3d$_{3/2}$ and Pd 3d$_{5/2}$ doublets (Figure 4.34). Binding energies where observed at 333.8 and 339.0 eV which can be attributed to the Pd(0) species as well as binding energies at 335.9 and 341.1 eV which can be attributed to the Pd(II) species.[20,51]

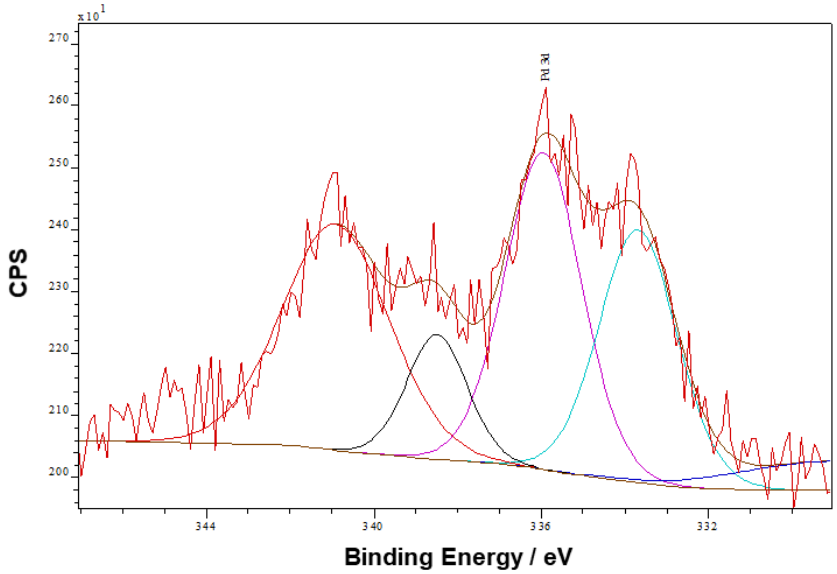

Figure 4.34: Pd 3d core level XPS of PdNP@PSty$_3$-PEGPILP, referenced to the hydrocarbon C 1s, showing the Pd 3d$_{3/2}$ and Pd 3d$_{5/2}$ doublets.

4.2.3.3 PdNP@PSty$_3$-PEGPILP in situ

As the polymer immobilised ionic liquid stabilised PdNPs are fabricated from the reduction of their tetrachloropalladate-based precursors, using sodium borohydride as the reducing agent, preparation of PdNP@PSty$_3$-PILP formed in-situ during a reduction reaction was also investigated.

TEM was employed to quantify the size, shape and distribution of the NPs on the support structure for PdNP@PSty$_3$-PEGPILP formed in situ (see Figure 4.35). Quantitative size analysis was performed by measuring the diameter of a statistically relevant number of different nanoparticles (>100 samples) from different regions of the TEM sample grid and revealed the average size of the MNPs to be 2.55 ± 0.97 nm.

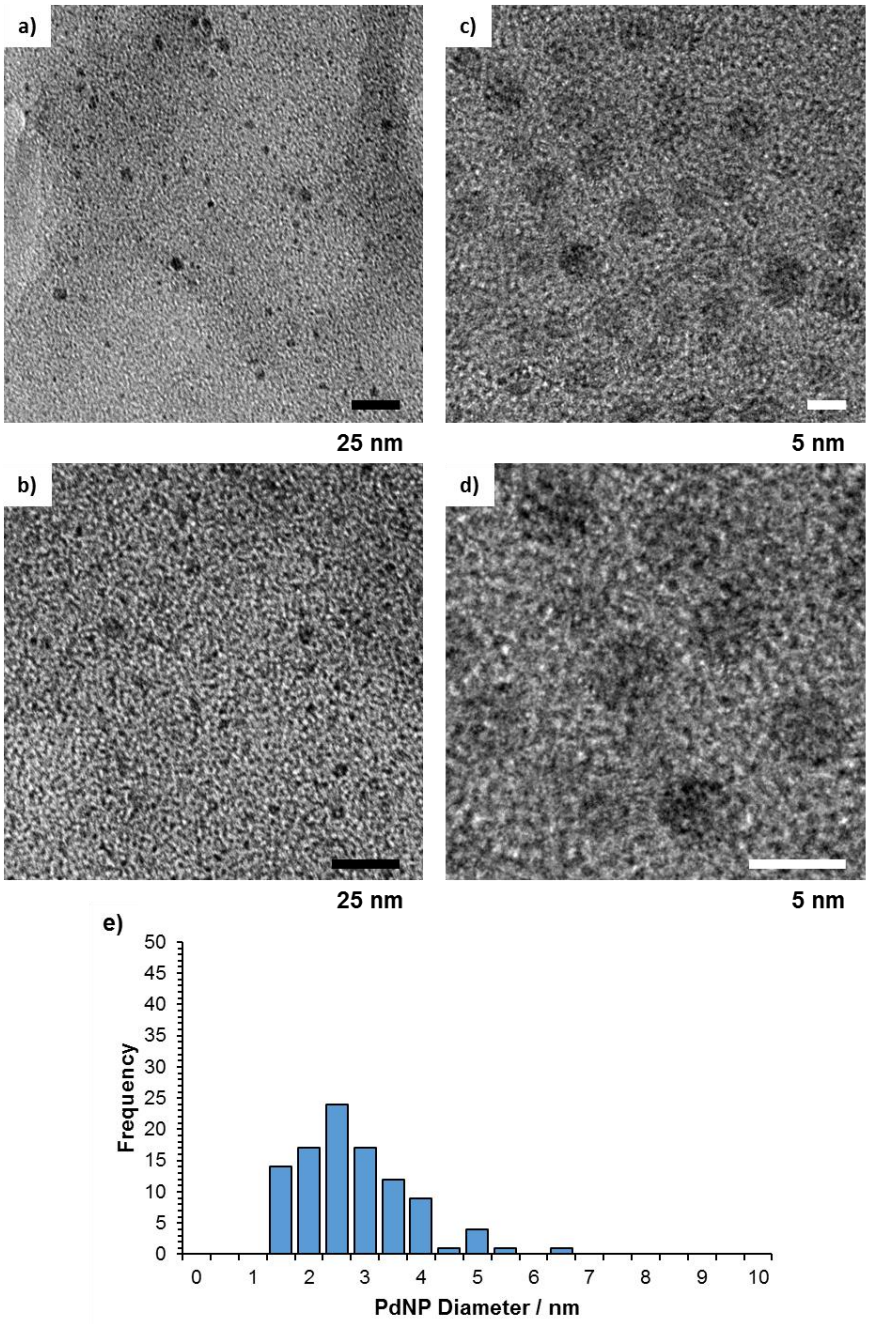

Figure 4.35: a-d) TEM micrographs of PdNP@PSty$_3$-PEGPILP (formed in situ) showing the general structure, size and distribution of the MNPs; and e) size distribution d_{NP} = 2.55 ± 0.97 nm.

4.2.3.4 Summary

TEM micrographs show that PdNP@PPh$_2$-PILP and PdNP@PPh$_2$-PEGPILP consist of small, near monodispersed PdNPs with average diameters of 2.29 ± 0.96 and 1.93 ± 0.67 nm, respectively, while the NPs in the highly cross-linked systems PdNP@PSty$_3$-PILP and PdNP@PSty$_3$-PEGPILP are larger with average diameters of 3.67 ± 0.67 and 4.01 ± 0.11 nm, respectively. Incorporation of PEG in both heteroatom-donor systems has little effect on the

average diameter of the PdNPs. The increase in average PdNP diameter with highly cross-linked systems indicates that isolating the heteroatom site has a marked effect on particle size and distribution of the PdNPs as the ratio of Pd to phosphine is the same in each system (2:1 ratio of phosphine to imidazolium-based monomer).

TEM micrographs of in-situ generated PdNP@PPh_2-PEGPILP and PdNP@$PSty_3$-PEGPILP show that the PdNPs are monodispersed within the support system and average diameter were found to be 3.36 ± 0.61 and 2.55 ± 0.97 nm, respectively, compared to their ex-situ prepared counterparts with average diameters of 1.93 ± 0.96 and 4.02 ± 1.11 nm for PdNP@PPh_2-PEGPILP and PdNP@$PSty_3$-PEGPILP, respectively. No significant change in the XPS binding energies was observed for these materials.

4.2.4 X-ray Photoelectron Spectroscopy of Pd-based Materials

Surface characterisation of the palladium in the support systems was undertaken with XPS by analysis of the Pd $3d_{3/2}$ and Pd $3d_{5/2}$ doublets. Representative XPS spectra for PdNP@PPh_2-PILP, PdNP@PPh_2-PEGPILP, PdNP@$PSty_3$-PILP and PdNP@$PSty_3$-PEGPILP are shown in Figure 4.36. The peaks corresponding to binding energies between 339.1 – 340.7 eV (Pd $3d_{3/2}$) and 333.8 – 355.5 eV Pd ($3d_{5/2}$) are attributed to Pd(0) species. Binding energies between 341.1 – 342.7 eV (Pd $3d_{3/2}$) and 335.9 – 337.4 eV ($3d_{5/2}$) are attributed to Pd(II) species, most likely resulting from the re-oxidation of Pd(0). The XPS spectra of the tetrachloropalladate-based precursors contain doublets characteristic of Pd 3d with binding energies of 336.6 – 337.5 eV (Pd $3d_{3/2}$) and 341.8 – 342.8 eV ($3d_{5/2}$), which is consistent with the presence of Pd(II) associated with phosphine co-ordinated chloropalladate. The palladium binding energies ($3d_{5/2}$ and $3d_{3/2}$) are consistent with the phosphine donor providing the primary stabilization of the PdNPs, which agrees with data previously reported for other phosphine-stabilized palladium nanoparticles.[20,51]

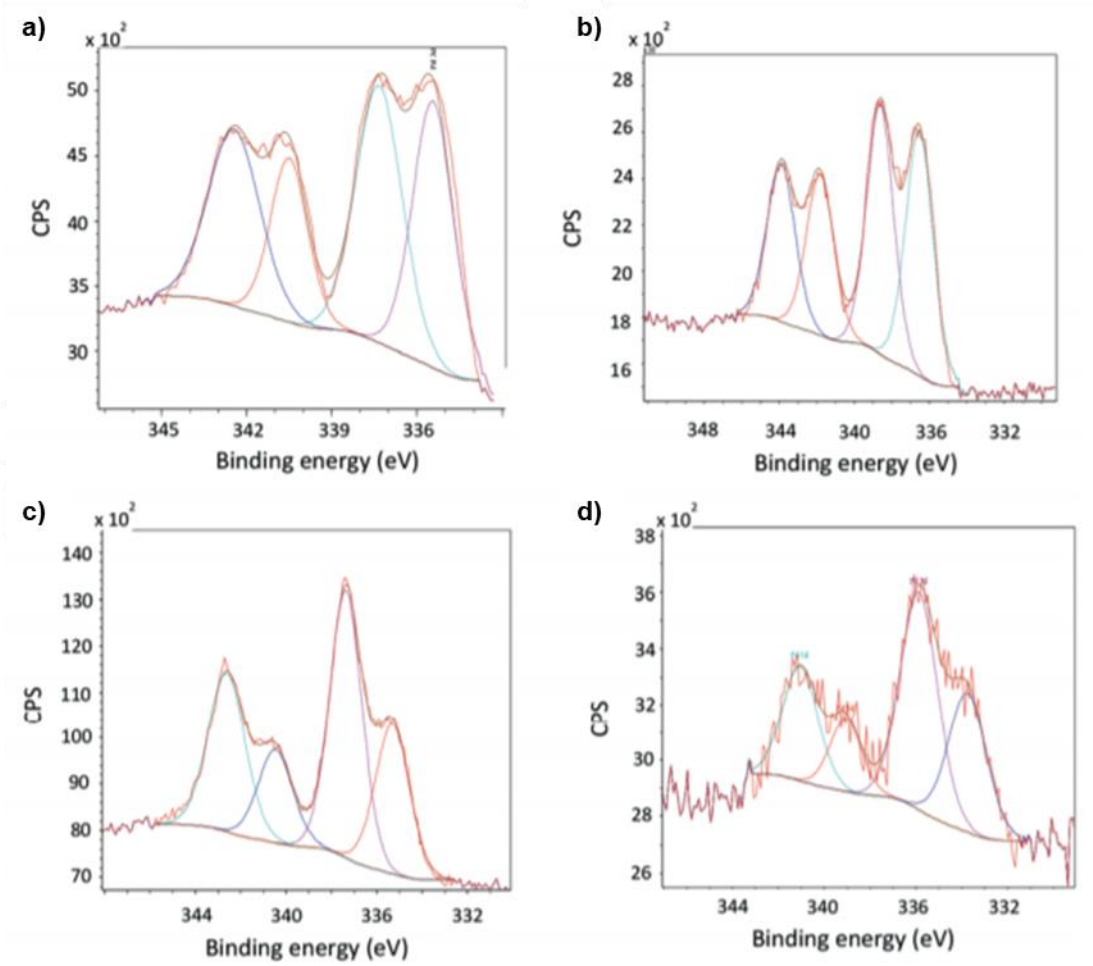

Figure 4.36: Pd 3d core level XPS of a) PdNP@PPh_2-PILP, b) PdNP@PPh_2-PEGPILP, c) PdNP@$PSty_3$-PILP; and d) PdNP@$PSty_3$-PEGPILP. All reference to the hydrocarbon C 1s.

4.2.4 Summary of all Pd-based Materials

In summary the preparation of multiple PdNP-based polymer supported systems has be achieved. These supports have been successfully modified to incorporate different heteroatom donors, ionic liquids and PEG units. The effect on particle size imposed by each component of the support systems was investigated through TEM. It was found that whilst the incorporation of PEG (into PdNP@PPh_2-PILP and PdNP@$PSty_3$-PILP) had no effect on particle size changes to the heteroatom donor lead to changes in average PdNP diameter (diameter ranging from 1.75 ± 0.78 to 3.20 ± 0.62 nm). Additionally, incorporation of a highly cross-linked system resulted in larger PdNPs formed which indicates that isolating the heteroatom site has a marked effect on particle size and distribution. Changing the components of the support structure e.g. selective removal of the IL, has been shown to have little effect on the dispersion of the MNPs within the support system. No

significant change in the XPS binding energies was observed for these materials.

4.2.5 Stabilisation of Other Metal Nanoparticles using Polymer Immobilised Ionic Liquid Systems

To further explore the stabilisation effects of PILP-based MNP systems the study was extended to include gold nanoparticle-based systems. This allows for a comparative investigation of the efficiency of the materials as catalysts for the reduction of nitrobenzene.

AuNP-based polymer immobilised ionic liquid systems were prepared in-situ by the sodium borohydride reduction of potassium tetrachloroaurate (see Scheme 4.2), and are denoted AuNP@PPh_2-PILP, AuNP@PPh_2-PEGPILP, AuNP@PILP and AuNP@PEGPILP. For full experimental details see Section 4.5.1.

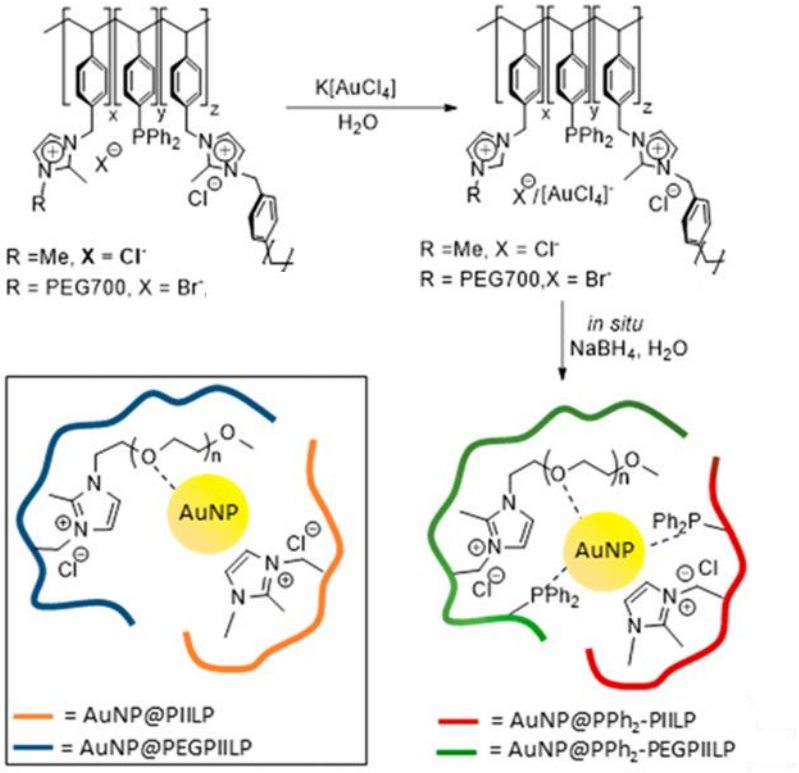

Scheme 4.2: Schematic representation of the preparation of AuNPs supported on polymer immobilised ionic liquid systems; AuNP@PPh_2-PILP (red), AuNP@PPh_2-PEGPILP (green), AuNP@PILP (orange) and AuNP@PEGPILP (blue).[47]

TEM reveals that in-situ generated catalytic systems contained near monodispersed AuNPs with average diameters of 3.36 ± 0.88, 2.52 ± 0.60, 3.41 ± 1.08 and 3.26 ± 0.88 nm, respectively (representative TEM micrographs and size distributions for each material are shown below).

4.2.5.1 AuNP@PPh_2-PILP

The structure of AuNP@PPh_2-PILP is highlighted in Figure 4.37.

Figure 4.37: Structure of AuNP@PPh_2-PILP where x = imidazolium-modified monomer, y = HAD-modified styrene and z = dicationic cross-linker, in the following ratio: x = 1.84, y = 1, z = 0.16.

TEM was employed to quantify the size, shape and distribution of the NPs on the support structure for AuNP@PPh_2-PILP (see Figure 4.38). Quantitative size analysis was performed by measuring the diameter of a statistically relevant number of different nanoparticles (>100 samples) from different regions of the TEM sample grid and revealed the average size of the MNPs to be 3.36 ± 0.88 nm.

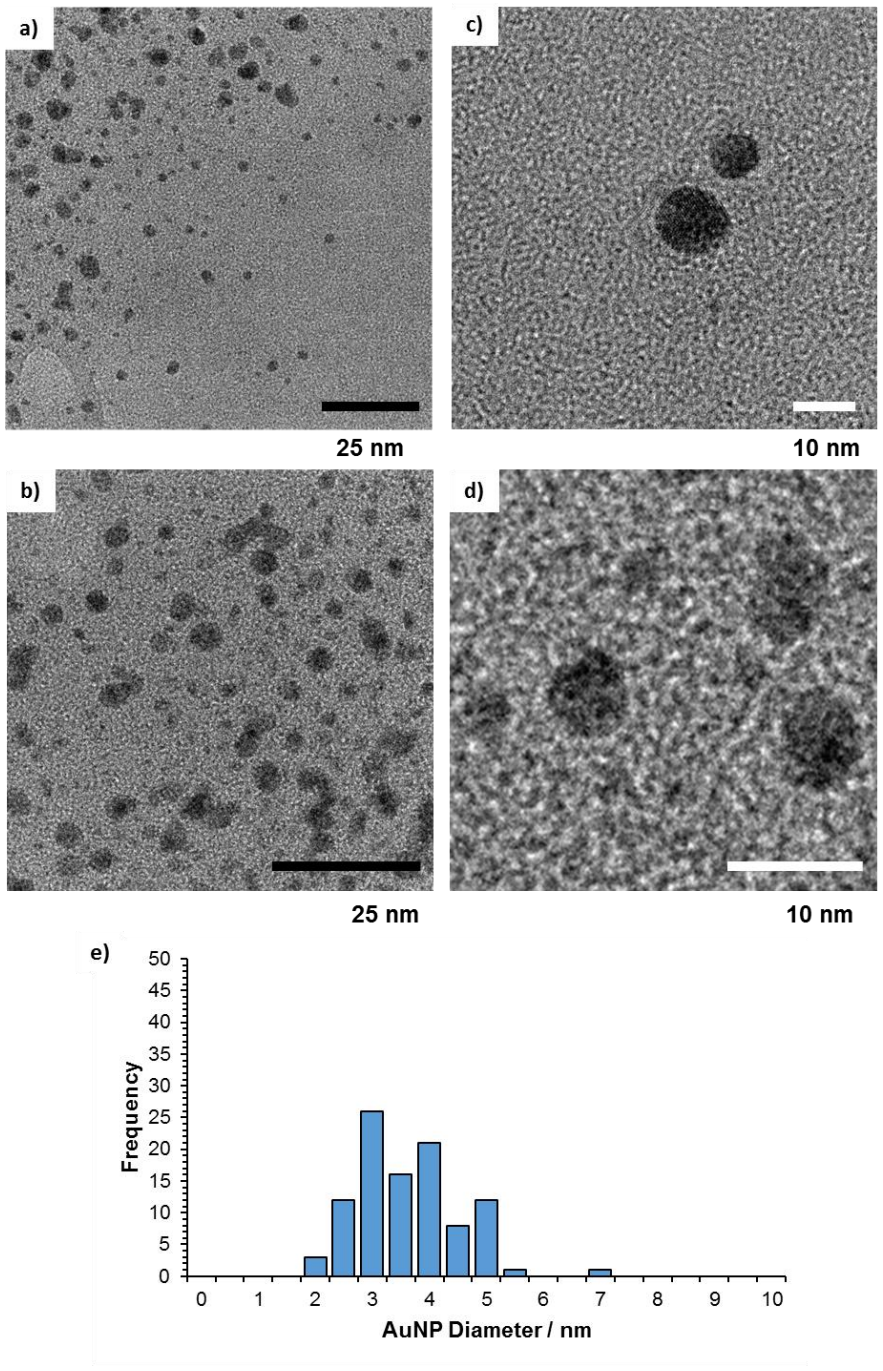

Figure 4.38: a-d) TEM micrographs of AuNP@PPh_2-PILP (formed in situ) showing the general structure, size and distribution of the MNPs; and e) size distribution d_{NP} = 3.36 ± 0.88 nm.

EDX spectroscopy showed characteristic peaks of Au at 2.1, 9.7 and 11.5 KeV confirming the composition of the NPs formed on the polymer support (Figure 4.39).

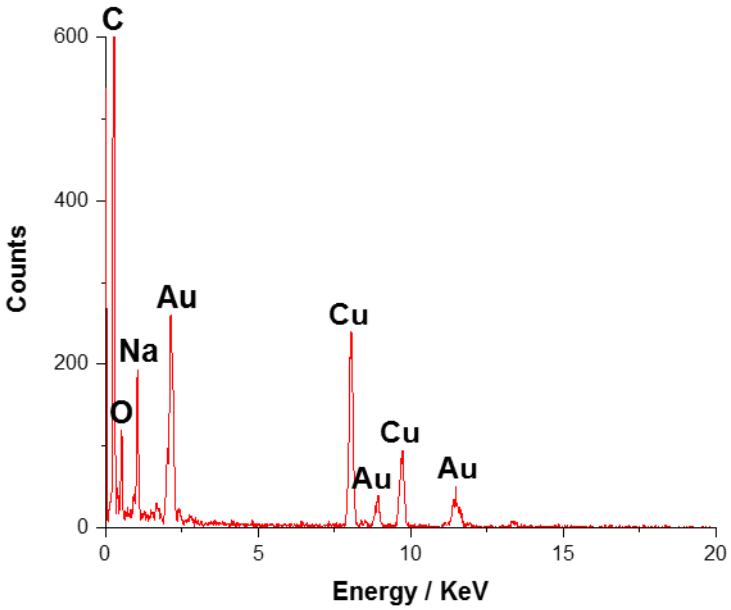

Figure 4.39: EDX spectrum of AuNP@PPh_2-PILP (AuNPs formed in situ). Characteristic peaks of Au were identified at 2.1, 9.7 and 11.5 KeV. Cu peaks are due to the TEM grid used.

4.2.5.2 AuNP@PPh_2-PEGPILP

The structure of AuNP@PPh_2-PEGPILP is highlighted in Figure 4.40.

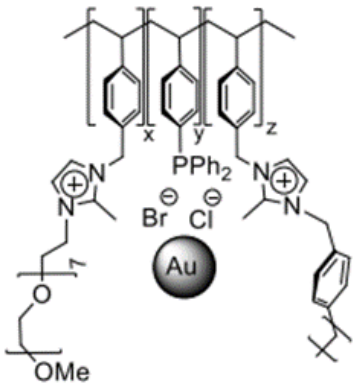

Figure 4.40: Structure of AuNP@PPh_2-PEGPILP where x = imidazolium-modified pegylated monomer, y = HAD-modified styrene and z = dicationic cross-linker, in the following ratio: x = 1.84, y = 1, z = 0.16.

TEM was employed to quantify the size, shape and distribution of the NPs on the support structure for AuNP@PPh_2-PEGPILP (see Figure 4.41). Quantitative size analysis was performed by measuring the diameter of a statistically relevant number of different nanoparticles (>100 samples) from different regions of the TEM sample grid and revealed the average size of the MNPs to be 2.52 ± 0.60 nm.

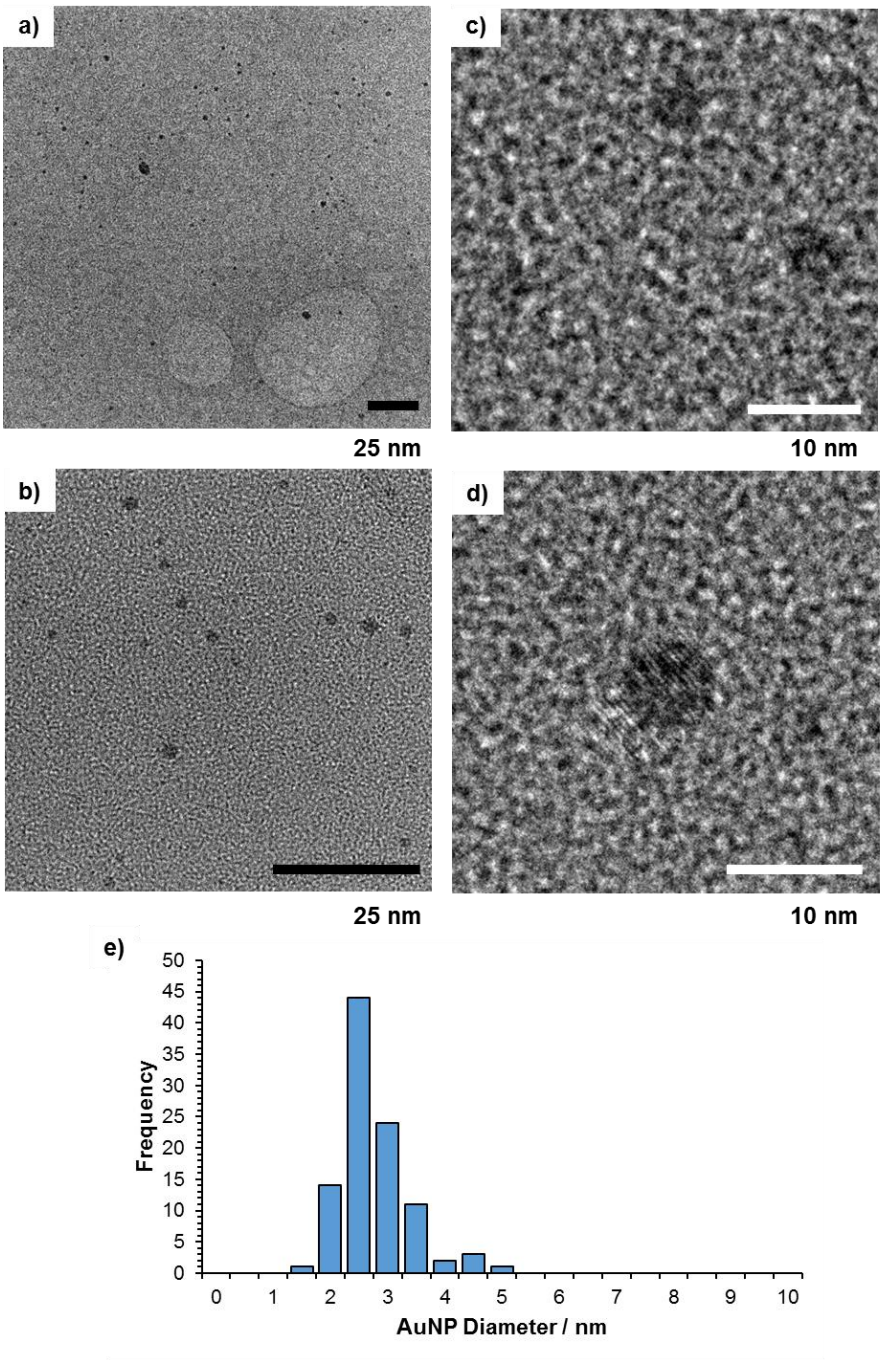

Figure 4.41: a-d) TEM micrographs of AuNP@PPh_2-PEGPILP (formed in situ) showing the general structure, size and distribution of the MNPs; and e) size distribution d_{NP} = 2.52 ± 0.60 nm.

EDX spectroscopy showed characteristic peaks of Au at 9.7 and 11.5 KeV confirming the composition of the NPs formed on the polymer support (Figure 4.42).

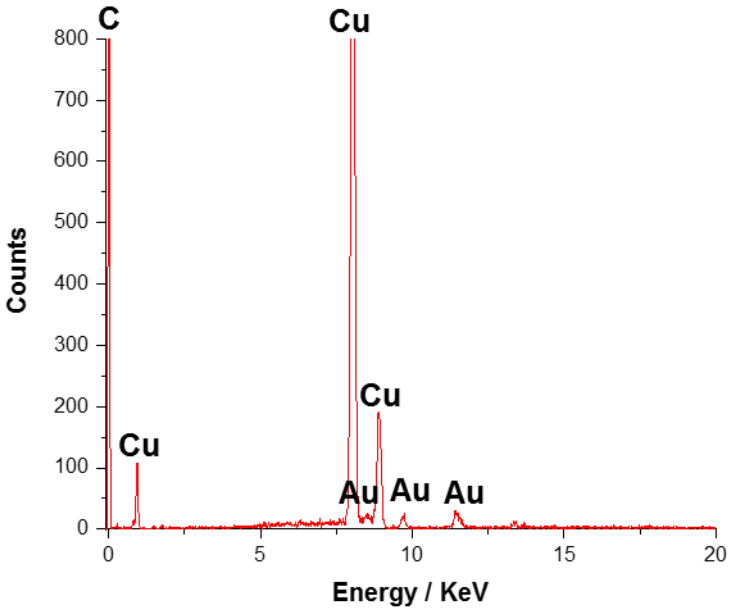

Figure 4.42: EDX spectrum of AuNP@PPh_2-PEGPILP (AuNPs formed in situ). Characteristic peaks of Au were identified at 9.7 and 11.5 KeV. Cu peaks are due to the TEM grid used.

4.2.5.3 AuNP@PILP

The structure of AuNP@PILP is highlighted in Figure 4.43.

Figure 4.43: Structure of AuNP@PILP where x = imidazolium-modified monomer, y = styrene and z = dicationic cross-linker, in the following ratio: x = 1.84, y = 1, z = 0.16.

TEM was employed to quantify the size, shape and distribution of the NPs on the support structure for AuNP@ (see Figure 4.44). Quantitative size analysis was performed by measuring the diameter of a statistically relevant number of different nanoparticles (>100 samples) from different regions of the TEM sample grid and revealed the average size of the MNPs to be 3.41 ± 1.08 nm.

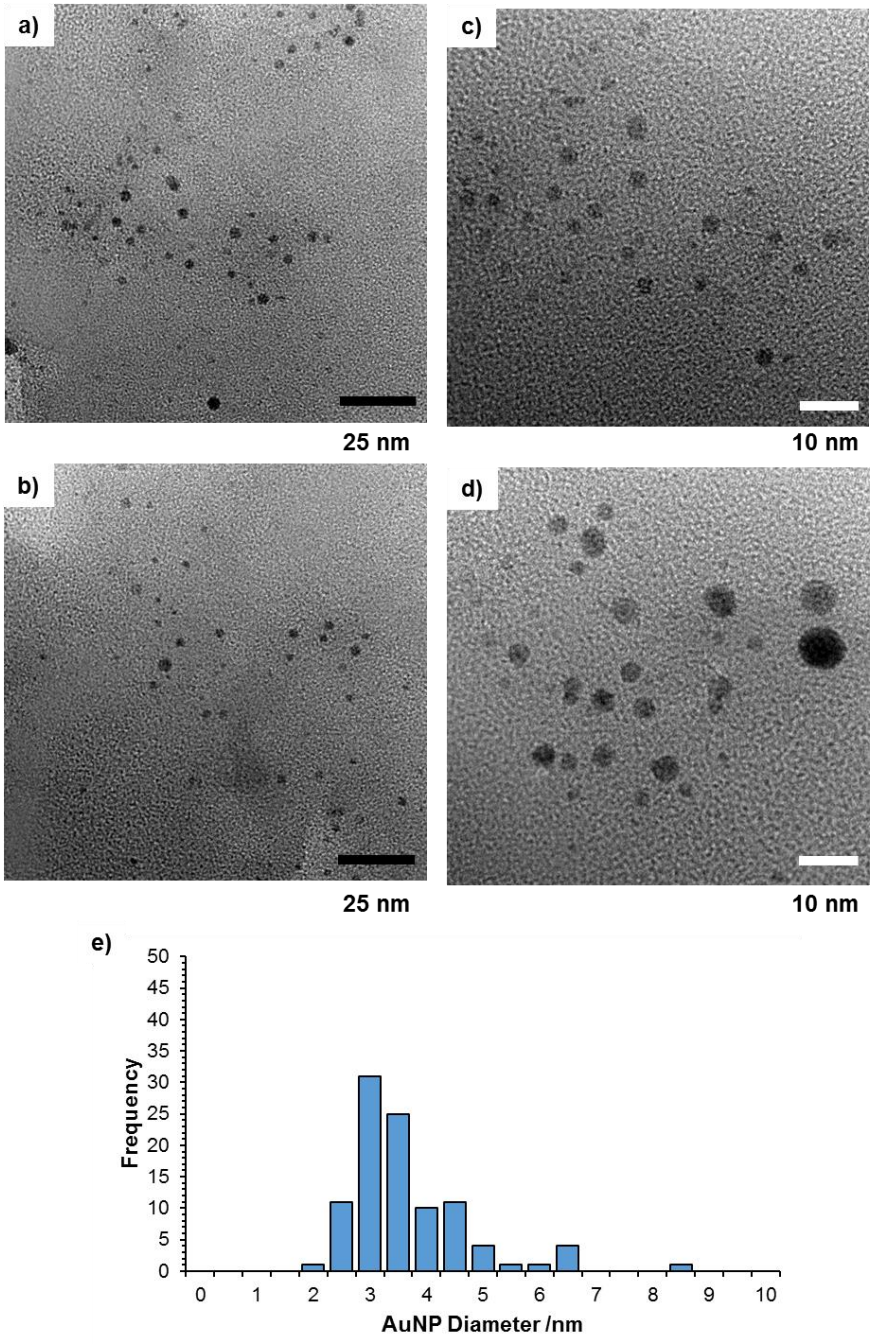

Figure 4.44: a-d) TEM micrographs of AuNP@PILP (formed in situ) showing the general structure, size and distribution of the MNPs; and e) size distribution d_{NP} = 3.41 ± 1.08 nm.

EDX spectroscopy showed characteristic peaks of Au at 2.1, 9.7 and 11.5 KeV confirming the composition of the NPs formed on the polymer support (Figure 4.45).

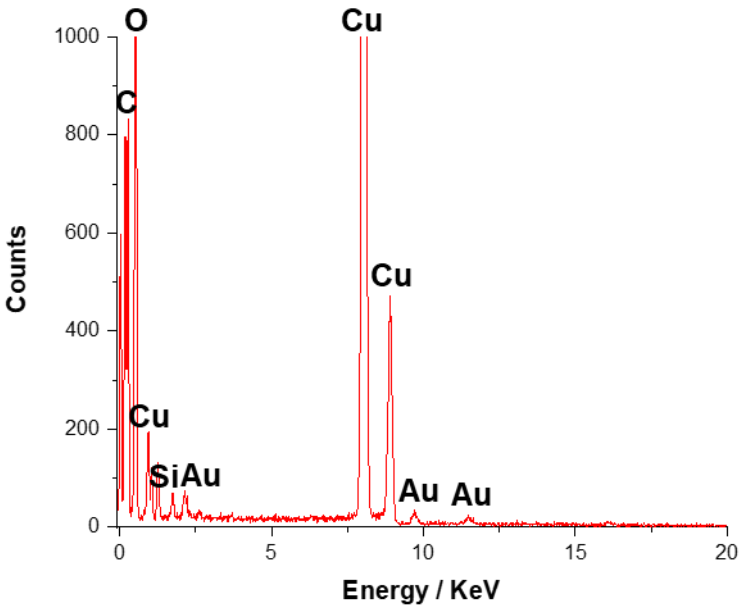

Figure 4.45: EDX spectrum of AuNP@PILP (AuNPs formed in situ). Characteristic peaks of Au were identified at 2.1, 9.7 and 11.5 KeV. Cu peaks are due to the TEM grid used.

4.2.5.4 AuNP@PEGPILP

The structure of AuNP@PEGPILP is highlighted in Figure 4.46.

Figure 4.46: Structure of AuNP@PEGPILP where x = imidazolium-modified pegylated monomer, y = styrene and z = dicationic cross-linker, in the following ratio: x = 1.84, y = 1, z = 0.16.

TEM was employed to quantify the size, shape and distribution of the NPs on the support structure for AuNP@PEGPILP (see Figure 4.47). Quantitative size analysis was performed by measuring the diameter of a statistically relevant number of different nanoparticles (>100 samples) from different regions of the TEM sample grid and revealed the average size of the MNPs to be 3.26 ± 0.88 nm.

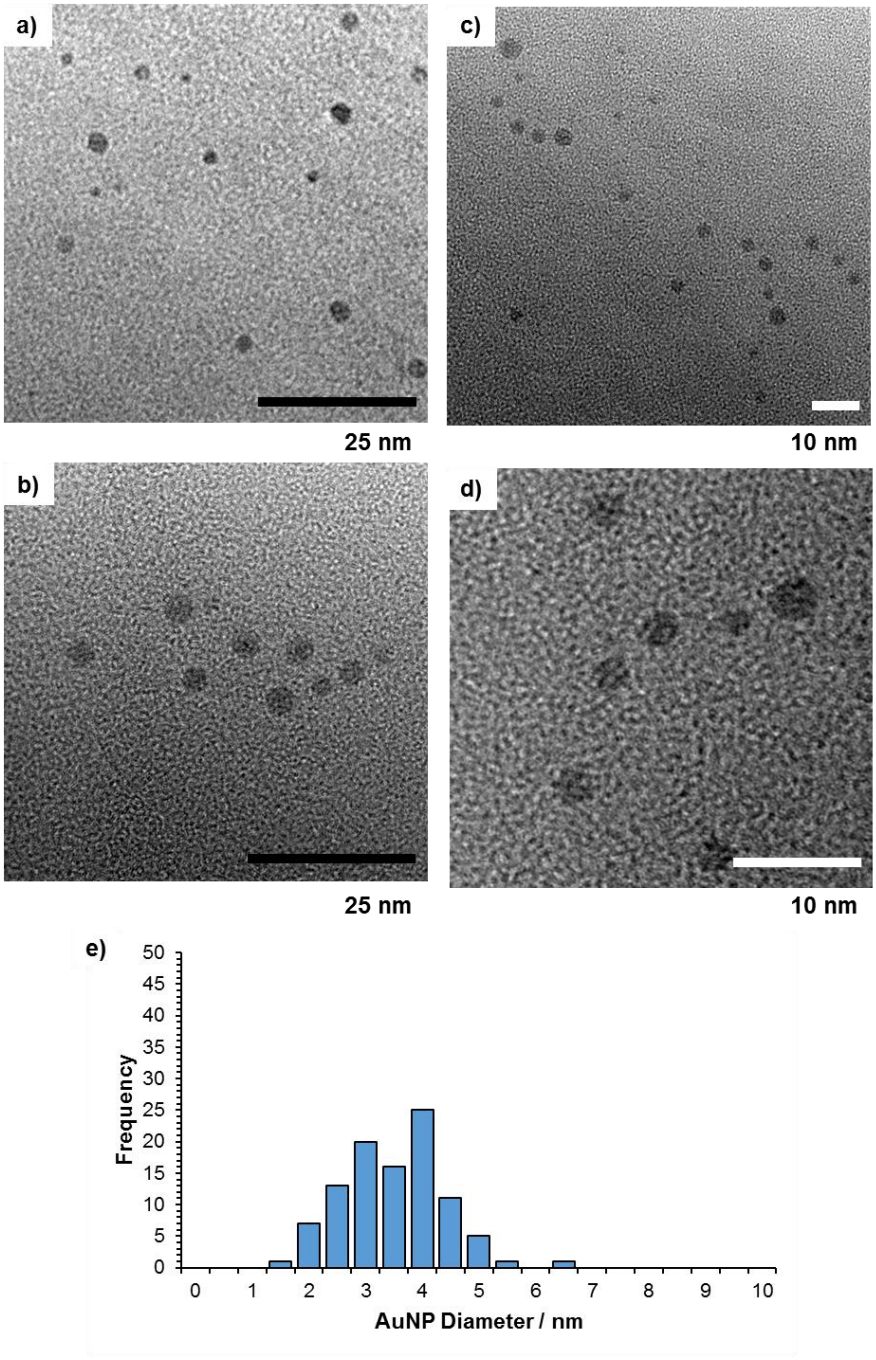

Figure 4.47: a-d) TEM micrographs of AuNP@PEGPILP (formed in situ) showing the general structure, size and distribution of the MNPs; and e) size distribution d_{NP} = 3.26 ± 0.88 nm.

EDX spectroscopy showed characteristic peaks of Au at 2.1 and 9.7 KeV confirming the composition of the NPs formed on the polymer support (Figure 4.48).

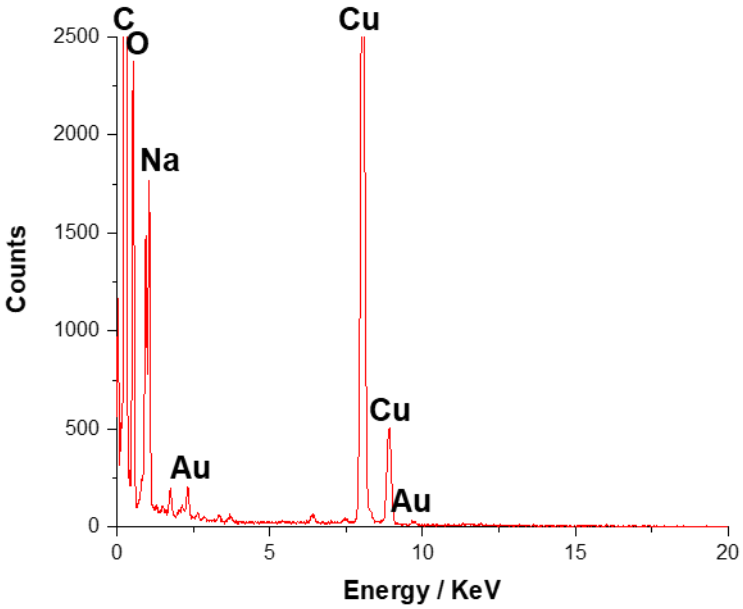

Figure 4.48: EDX spectrum of AuNP@PEGPILP (AuNPs formed in situ). Characteristic peaks of Au were identified at 2.1 and 9.7 KeV. Cu peaks are due to the TEM grid used.

4.2.6 X-ray Photoelectron Spectroscopy of Au-based Materials

Surface characterisation of the tetrachloroaurate-based precursors and equivalent reduced catalysts was undertaken with XPS by analysis of the Au $4f_{5/2}$ and Au $4f_{7/2}$ peaks. Upon reduction a shift in the Au $4f_{5/2}$ and Au $4f_{7/2}$ doublets to lower binding energies was observed. For example, Au $4f_{7/2}$ binding energies of 87.4 eV for $AuCl_4$@PILP and 87.6 eV for $AuCl_4$@PEGPILP are consistent with Au(III)[52–54] whilst lower binding energies of 83.8 eV for AuNP@PILP and 83.8 eV for AuNP@PEGPILP are assigned to a Au(0) species (see Figure 4.49a).[54,55] Additional Au 4f doublets can be seen in the precursor spectra at higher binding energies than the Au(0) doublets observed for the chemically reduced catalysts, which can be assigned as Au(I) species most likely resulting from decomposition caused by exposure to the X-ray source during acquisition.[56] This is corroborated by considering the N 1s region which shows additional signals in each sample (along with those expected for the imidazolium environment) at lower binding energies which correspond to uncharged, and/or anionic, nitrogen species which are assigned to damage.[57] There is no evidence from XPS of any Au···P interactions, caused by electron donation from the phosphino group, as the binding energies for the Au $4f_{5/2}$ and Au $4f_{7/2}$ doublets for both $AuCl_4$@PPh_2-PILP and $AuCl_4$@PPh_2-PEGPILP are very similar to those of $AuCl_4$@PILP and $AuCl_4$@PEGPILP (Figure a). Additionally, no shift in the

binding energies of the P $2p_{3/2}$ and P $2p_{1/2}$ doublets was observed upon the reduction of the gold salt (Figure 4.49b).

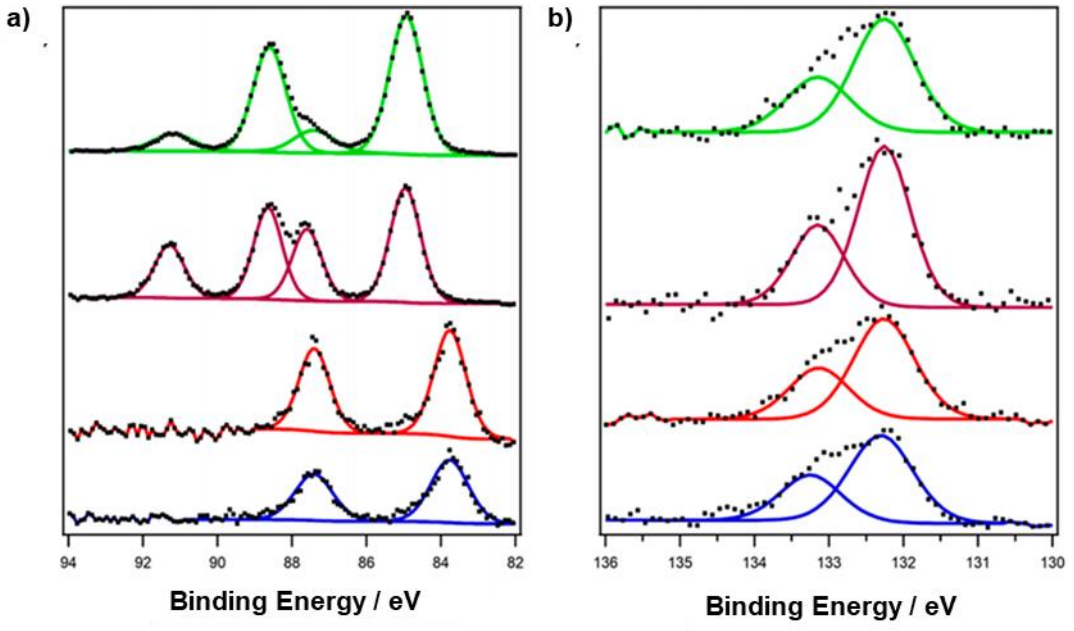

Figure 4.49: a); XPS spectra showing Au 4f core level of $AuCl_4$@PILP (green), $AuCl_4$@PEGPILP (pink), AuNP@PILP (orange) and AuNP@PEGPILP (blue); and b) P 2p core level of $AuCl_4$@PPh_2-PILP (green), $AuCl_4$@PPh_2-PEGPILP (pink), AuNP@PPh_2-PILP (orange) and AuNP@PPh_2-PEGPILP (blue). All spectra are referenced to the C 1s alkyl peak at 284.8 eV.

4.3 Discussion on Reactivity

4.3.1 Pd Catalysed Hydrogenation of α, β - Unsaturated Aldehydes

The stabilisation of PdNPs for use in aqueous phase catalysis offers the potential for developing greener sustainable processes.[49,50,58,59] The selective hydrogenation of the α, β - unsaturated aldehyde, cinnamaldehyde, is an important process as its two partial hydrogenation products, hydrocinnamaldehyde and cinnamyl alcohol, are important intermediates for the synthesis of fine chemicals, perfumes and pharmaceuticals;[58,60–62] however, it is often difficult to prevent the formation of the fully unsaturated alcohol (see Scheme 4.3). The use of promoters, different supports and modifying catalyst preparation allows for a range of selectivities to be possible.[63] Additionally, numerous PdNP based systems have been previously reported to afford high selectivity towards hydrocinnamaldehyde. For example, Nagpure and co-workers, reported that PdNPs deposited on nitrogen-doped mesoporous carbon gave 100% conversion of cinnamaldehyde and a 93% selectivity toward hydrocinnamaldehyde;[64] and PdNPs supported on MWNT/AC composites have been reported to afford a

96% selectivity towards hydrocinnamaldehyde.[65] Additionally, the incorporation of phosphorus groups into ionophilic ligands has been reported to generate smaller PdNPs (3-4 nm) than when a ligand was not present, and the resulting catalysts gave higher selectivities for the hydrogenation of cyclohexadiene (94% selectivity to cyclohexene) and 2-pentyne (87% selectivity to *cis*-2-pentene).[18]

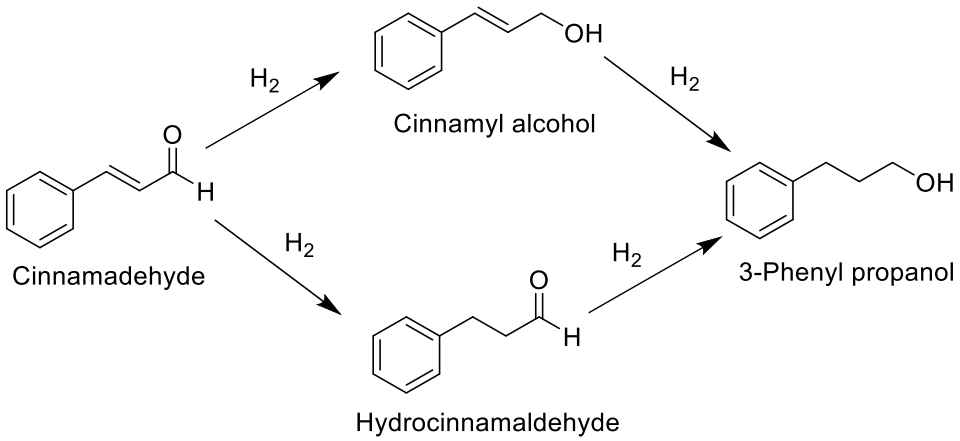

Scheme 4.3: Possible reaction pathways for the reduction of *trans*-cinnamaldehyde.

PdNP@PPh2-PILP and PdNP@PPh2-PEGPILP were prepared as highlighted in Section 4.2. TEM analysis of each material showed that the PdNPs were monodispersed within the support structure with average diameters of 2.29 ± 0.96 and 1.93 ± 0.67 nm, respectively (see Figure 4.50).

The selective hydrogenation of cinnamaldehyde to hydrocinnamaldehyde was investigated under the optimised reaction conditions highlighted in Scheme 4.4.

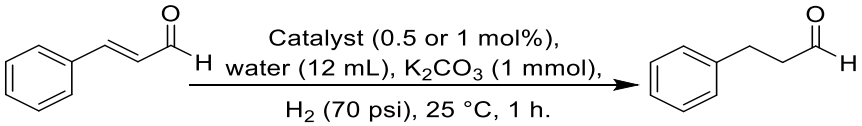

Scheme 4.4: Reaction conditions used for the reduction of cinnamaldehyde to hydrocinnamaldehyde (1 mmol of cinnamaldehyde used).

For each material the average sizes of the MNPs were similar (within error, see Figure 4.50) therefore any changes in activity can be attributed the modification of electronic surface structure of the PdNP or a change in the dispersibility of the catalyst system caused by the differences in the support structures. The conversions, TOFs (given as mole of product per mole of Pd per hour) and selectivities for each material are summarised in Table 4.1.

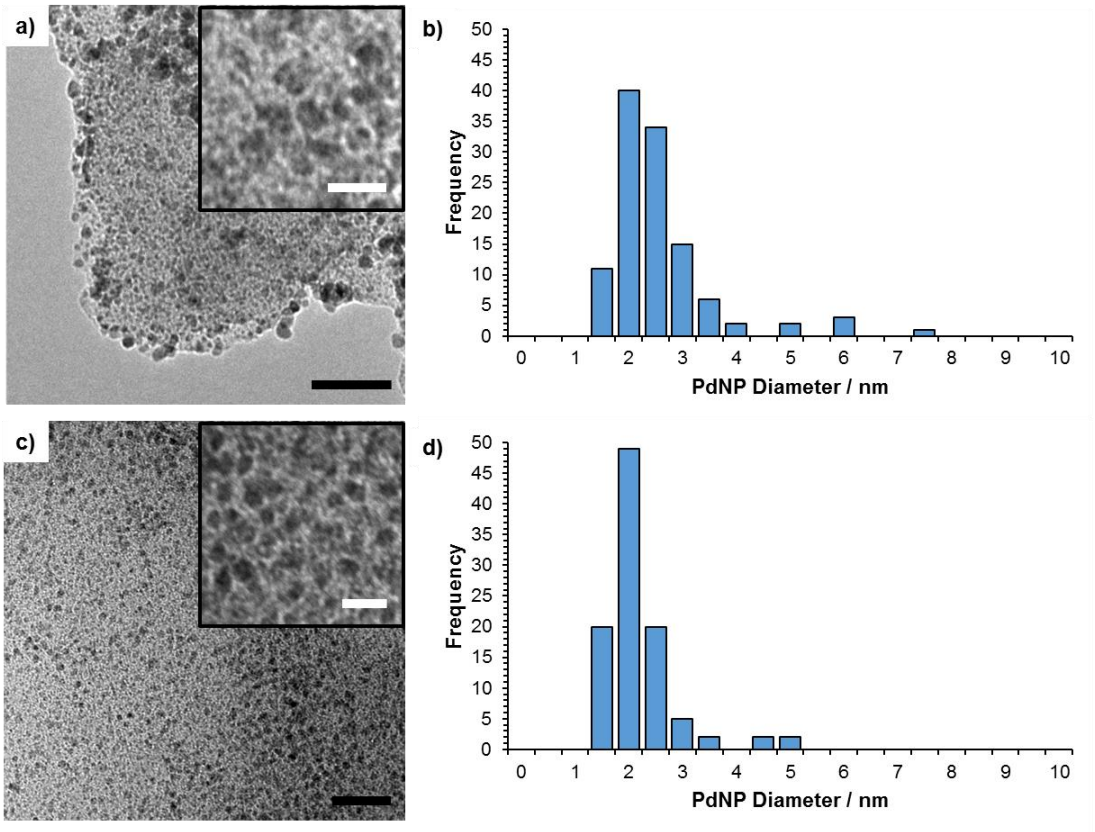

Figure 4.50: TEM micrographs showing the size and distribution of PdNPs for a) PdNP@PPh_2-PILP and c) PdNP@PPh_2-PEGPILP; and the corresponding size distributions for b) PdNP@PPh_2-PILP and d) PdNP@PPh_2-PEGPILP showing the average sizes for and to be 2.29 ± 0.96 nm and 1.93 ± 0.67 nm, respectively. Black and white scale bars are 25 nm and 5 nm, respectively.

While the activity of PdNP@PPh_2-PILP is similar to commercially available Pd/C, TOFs of 43 and 44 ($mol_p\ mol_M^{-1}$) h^{-1}, respectively, there is a marked improvement for its pegylated counterpart which had a TOF of 200 ($mol_p\ mol_M^{-1}$) h^{-1} and 100% selectivity towards hydrocinnamaldehyde.

Table 4.1: Summary of conversions, TOFs (given as mol of product per mol of Pd per hour) and selectivities obtained for the selective hydrogenation of cinnamaldehyde to hydrocinnamaldehyde.[a]

Catalyst	Conversion / %	TOF / ($mol_p\ mol_M^{-1}$)h^{-1}	Selectivity / %
PdNP@PPh_2-PILP	43	43	95
PdNP@PPh_2-PEGPILP	>99	200	>99
Pd/C	42	44	93

[a] Conversion and selectivity given as an average of 3 runs.

This selectivity is the highest to be reported for the aqueous phase hydrogenation of cinnamaldehyde and whilst an almost 100% selectivity has

been obtained for Pd/C in ionic liquids, these reactions were much slower than those performed in traditional organic solvents and the cost of the ionic liquid extremely high.[63]

To test the stability of the catalytic system the recyclability of PdNP@PPh_2-PEGPILP over several repeat catalytic cycles was studied. The performance of the catalyst was tested in 6 consecutive cinnamaldehyde reduction reactions (Figure 4.51) under the conditions highlight in Scheme 4.4 (0.5 mol% catalyst was used), each cycle lasting 1 hour.

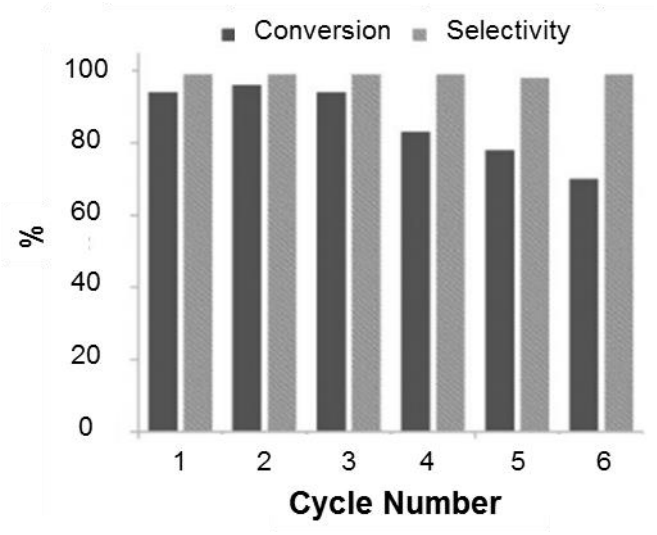

Figure 4.51: Recyclability study for the reduction of cinnamaldehyde catalysed by PdNP@PPh_2-PEGPILP.

The product and unreacted substrate were extracted, and the catalyst solution was recharged with cinnamaldehyde. Similar conversions were achieved for the first 3 cycles, with only a small drop in conversion observed for the subsequent cycles, whilst the selectivity of the catalyst remained unchanged across all 6 cycles.

From TEM analysis of the recycled catalyst (Figure 4.52), it is evident that the PdNPs remained monodispersed within the support structure with a mean diameter of 1.97 ± 0.38 nm.

As no change in the average diameter of the PdNPs was observed after the recycling experiments the drop in conversion seen could be due to small amounts of catalyst being lost which was confirmed by ICP analysis of the aqueous phase after the 5^{th} cycle, Pd content decreased from 44 ppm (0.5 mol%) to 28 ppm. This corresponds to a 38% decrease in catalyst across the 5 cycles.

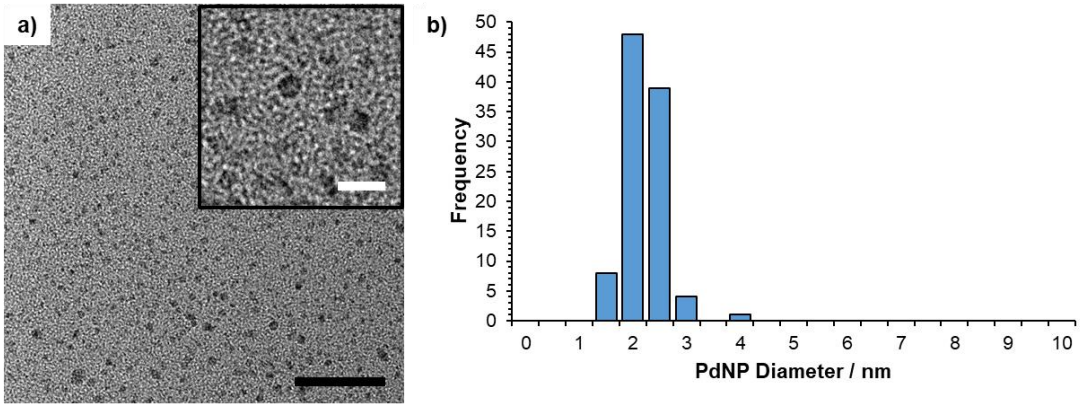

Figure 4.52: a) TEM micrographs of PdNP@PPh_2-PEGPILP after 6 catalytic cycles for the reduction of cinnamaldehyde, showing the general size and distribution of the PdNPs; and b) size distribution showing the average size of the PdNPs to be 1.97 ± 0.38 nm. Black and white scale bars are 25 nm and 5 nm, respectively.

4.3.2 Pd Catalysed Suzuki-Miyaura Cross-Coupling Reactions

Transition metal catalysed cross-coupling reactions to form aryl-aryl bonds are important reactions as the biaryl products are key motifs in a host of important bioactive natural products, functional materials, fine chemicals and pharmaceutical intermediates.[66–70] Whilst coupling of aryl chlorides to aryl boronic acids has been achieved in high yield through the use of homogeneous Pd-based catalysts, based on sterically electron rich phosphines,[71–78] these system have many disadvantages including the use of organic solvents (rather than environmentally greener solvents e.g. water), expensive oxygen sensitive phosphines, contamination of the product with palladium and recovery the catalyst for purification and recycling reaction can be difficult. MNPs are emerging as highly versatile catalysts not only for the Suzuki-Miyaura cross-coupling reaction,[79–81] but for a host of other useful organic transformations also.[82–84] The high activity of MNPs has been attributed to their high surface to volume ratio.[85,86] However, the high surface area of small MNPs drives their agglomeration to larger particles which are often less active and/or selective.[87] Using support structures such as heteroatom donor functionalised polymer immobilised ionic liquids can enhance the stability of the MNPs by preventing agglomeration.

As the size of PdNPs can greatly affect their activity, further insight into how the heteroatom donor affects the formation of PdNPs was investigated by fabricating a series of PdNPs supported on functionalised polymer immobilised ionic liquid with different heteroatom donors. These materials were fabricated via the same method highlighted in Section 4.2 Scheme 4.1. For full experimental details see Section 4.5.1. TEM analysis of the materials

revealed that in all cases the PdNPs were monodispersed and the size of the PdNPs were dependent upon the heteroatom donor present with average diameter ranging from 1.75 ± 0.78 to 3.20 ± 0.62 nm (see Table 4.2 for further details). As the ratio of heteroatom donor is the same in each material the differences in average diameter obtained suggest that the heteroatom donor influences the nucleation and growth of the PdNPs. Previously, numerous reports have provided evidence that the heteroatom influences nanoparticle size.[88–92] For example, Yang *et al.*,[88] reported the preparation of PtNPs stabilised on triphenylphosphine-modified silica afforded smaller PtNPs than those on unmodified silica supports.[88]

TEM micrographs and the size distribution of each material can be found in Section 4.2.2

Table 4.2: Summary of the polymer immobilised ionic liquid supports with varying heteroatom donors and the average diameter of the resultant PdNPs.

Catalyst	dNP / nm
PdNP@PPh_2-PILP	2.29 ± 0.96
PdNP@CN-PILP	3.20 ± 0.62
PdNP@Pyrr-PILP	2.38 ± 0.50
PdNP@NH_2-PILP	1.80 ± 0.53
PdNP@OMe-PILP	1.75 ± 0.78

The activity of the polymer immobilised ionic liquid system with varying heteroatom donors were investigated for the Suzuki-Miyaura cross-coupling reaction between 4-bromoacetophenone and phenyl boronic acid using the optimised reaction conditions highlighted in Scheme 4.5 (see Scheme 4.6 catalytic cycle).

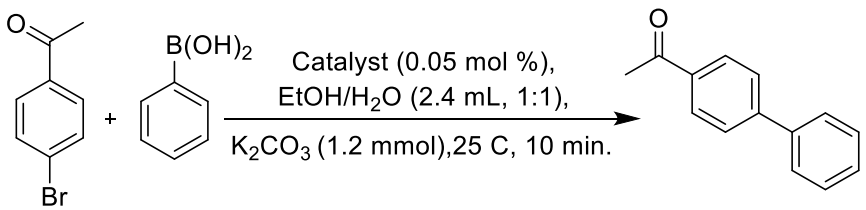

Scheme 4.5: Reaction conditions used for the Suzuki-Miyaura cross-coupling between 4-bromoacetophenone and phenyl boronic acid. (1 mmol of 4-bromoacetophenone and 1.13 mmol of phenyl boronic acid used).

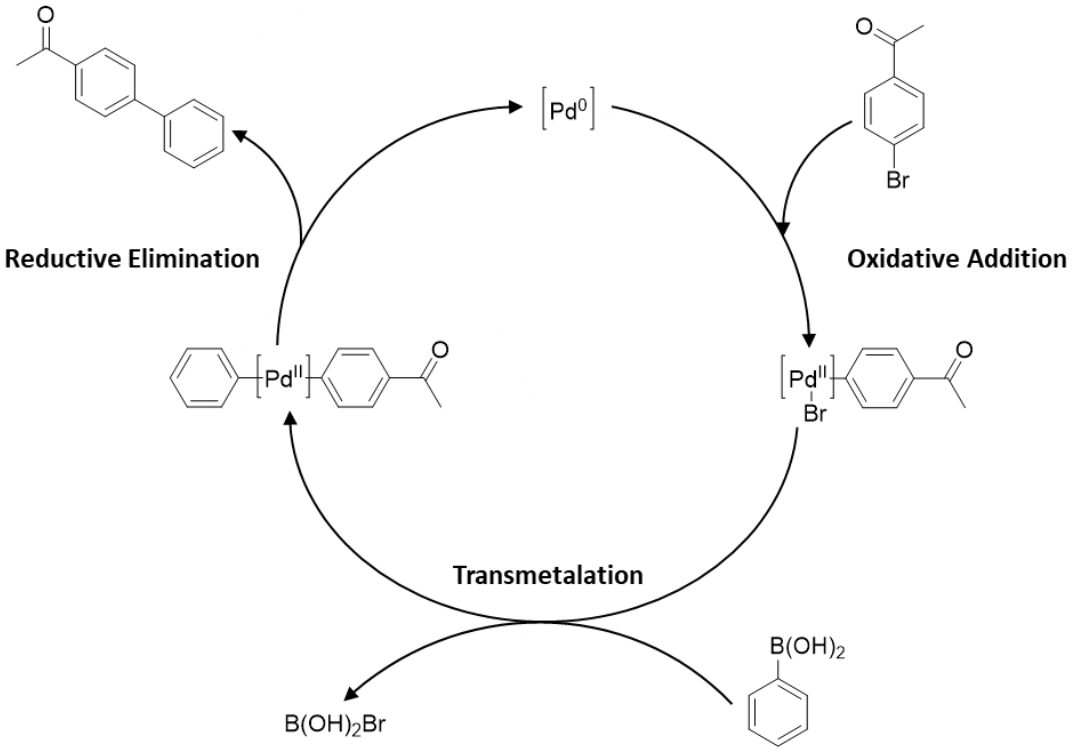

Scheme 4.6: Catalytic cycle for the Suzuki-Miyaura cross-coupling reaction between 4-bromoacetophenone and phenyl boronic acid.

The conversion and TOFs (given as mole of product per mole of Pd per hour) obtained for each catalyst, compared to the heteroatom present within the material, are summarised in Table 4.3. It is evident that high activities are obtained across the series of materials with differing heteroatom donors (78-98%), whereas a decrease in conversion to 58% was observed when the catalyst system did not contain a stabilising heteroatom donor i.e. PdNP@PILP.

The influence of the surface ionic liquid (IL), diphenyl phosphine donor (PPh_2) and PEG on catalyst performance was investigated by evaluating the activity of a series of catalysts containing differing combinations of each component. The materials investigated, the average diameters for the PdNPs in each material (determined by TEM), and the TOFs (given as mol of product per mol of Pd per hour) obtained for the Suzuki-Miyaura cross-coupling reaction are summarised in Table 4.4. Selective removal of the PEG results in a substantial decrease in TOF from 9840 to 8760 ($mol_p\ mol_M^{-1}$) h^{-1} for PdNP@PPh_2-PEGPILP and PdNP@PPh_2-PILP, respectively. The same trend was observed for PdNP@PEG-PILP and PdNP@PILP where a more drastic decrease in TOF was observed (1560 to 360 ($mol_p\ mol_M^{-1}$) h^{-1}). Selective removal of the ionic liquid component also resulted in a decrease in

TOF from 9840 ($mol_p\ mol_M^{-1}$) h^{-1} (obtained for PdNP@PPh_2-PEGPILP) to 6600 ($mol_p\ mol_M^{-1}$) h^{-1} (obtained for PdNP@PPh2-PEGstyrene).

Table 4.3: Summary of conversions and TOFs (given as mol of product per mol of Pd per hour) obtained for the Suzuki-Miyaura cross coupling reaction between 4-bromoacetophenone and phenyl boronic acid,a compared to the heteroatom donor present within the system.

Catalyst	Heteroatom Donor	Conversion of 4-bromoacetophenone / %	TOF / ($mol_p\ mol_M^{-1}$)h^{-1}
PdNP@PPh_2-PILP	PPh_2	98	3920
PdNP@NH_2-PILP	CH_2NH_2	78	3120
PdNP@CN-PILP	CH_2CN	90	3600
PdNP@OMe-PILP	CH_2OMe	94	3760
PdNP@Pyrr-PILP	Pyrrolidone	94	3760
PdNP@PILP	H	58	3220

[a] Conversion and TOF given as an average of at least 3 runs.

These results clearly indicate that the different components each have a direct effect on the resultant activity of the material. However, further studies are required to determine the how these effects come about and whether or not the heteroatom donor influences NP formation and size and/or surface electronic structure.

Table 4.4: Summary of TOFs (given as mol of product per mol of Pd per hour) obtained for the Suzuki-Miyaura cross-coupling reaction between 4-bromoacetophenone and phenyl boronic acid as a function of catalyst composition.

Catalyst	Components present	TOF / ($mol_p\ mol_M^{-1}$)h^{-1}	d_{NP} / nm
PdNP@PPh_2-PEGPILP	PPh_2, IL, PEG	9840	1.93 ± 0.67
PdNP@PPh_2-PILP	PPh_2, IL	8760	2.29 ± 0.96
PdNP@PILP	IL	360	3.01 ± 0.63
PdNP@PPh_2-styrene	PPh_2	4800	1.39 ± 0.19
PdNP@PEGPILP	IL, PEG	1560	3.23 ± 0.61
PdNP@PPh_2-PEGstryene	PPh_2, PEG	6600	1.39 ± 0.19

Additionally, as a drop in activity is observed by removal of the PEG or IL component the hydrophilicity/hydrophobicity presumably effects the dispersibility of the material and therefore access of reagents to the active site.

As the polymer immobilised ionic liquid stabilised PdNPs are fabricated from the reduction of their tetrachloropalladate-based precursors, using sodium borohydride as the reducing agent, preparation of the catalyst in-situ was investigated using phenyl boronic acid as the reducing agent (in which the catalyst is generated immediately prior to addition of the substrate). By preparing the catalyst system in-situ the need to prepare, separate and store the catalysts before their use in reactions is eliminated streamlining the process for rapid reaction screening of catalysts. Representative TEM micrographs and the corresponding size distributions for in-situ generated PdNP@PPh_2-PILP and PdNP@PPh_2-PEGPILP are shown in Figure 4.53.

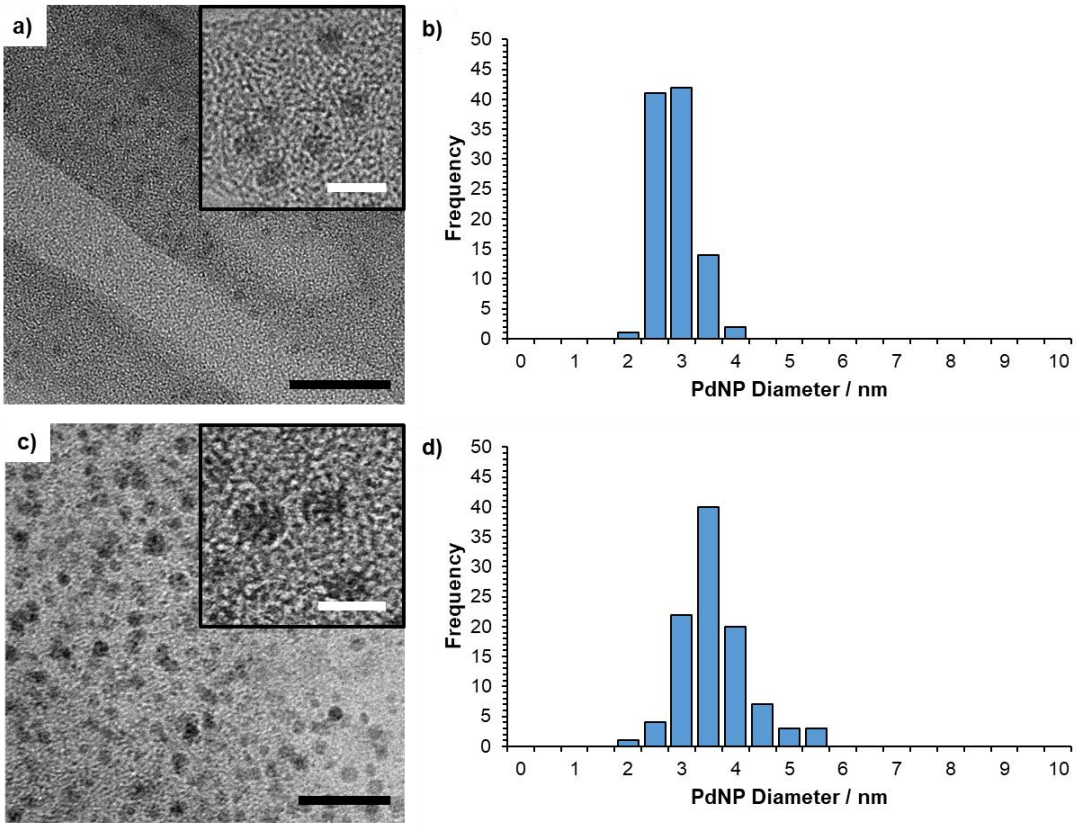

Figure 4.53: TEM micrographs showing the size and distribution of PdNPs for in-situ prepared a) PdNP@PPh_2-PILP and c) PdNP@PPh_2-PEGPILP; and the corresponding size distributions for b) PdNP@PPh_2-PILP and d) PdNP@PPh_2-PEGPILP showing the average sizes for and to be 2.61 ± 0.38 nm and 3.36 ± 0.61 nm, respectively. Black and white scale bars are 25 nm and 5 nm, respectively.

The average diameters of the PdNPs where determined to be 2.61 ± 0.38 and 3.36 ± 0.61 nm, respectively (for comparison the average diameters of the ex-situ prepared materials where 2.29 ± 0.96 and 1.93 ± 0.67 nm for

PdNP@PPh_2-PILP and PdNP@PPh_2-PEGPILP, respectively). Despite the smaller average diameters of the PdNPs obtained in the in-situ prepared materials comparable or higher activities of 96% and 100% were obtained for the cross-coupling reaction between 4-bromoacetophenone and phenyl boronic acid.

To test the stability of the catalytic system the recyclability of PdNP@PPh_2-PEGPILP over several repeat catalytic cycles was studied. The performance of the catalyst was tested in 5 consecutive reaction cycles each lasting 30 or 60 minutes (Figure 4.54) under the conditions highlight in Scheme 4.5. The product and unreacted substrates where extracted into ethyl acetate before the aqueous phase was recharged with ethanol, 4-bromoacetophenone and phenyl boronic acid. A decrease in conversion of 18% is seen, for reactions of 30 minutes per cycle, across the 5 catalytic cycles. However, when reactions are increased to 60 minutes per cycle the conversations obtained remain mostly constant across the 5 cycles.

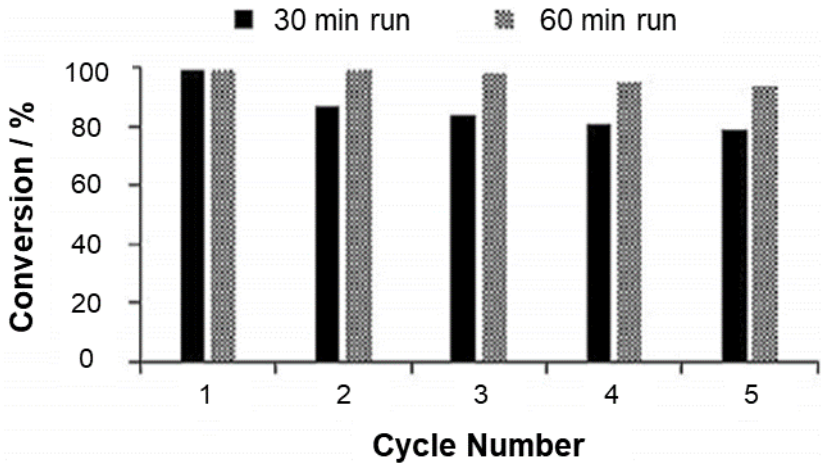

Figure 4.54: Recyclability study for the cross-coupling reaction between 4-bromoactephone and phenyl boronic acid catalysed by the ex-situ prepared PdNP@PPh_2-PEGPILP for reaction times of 30 and 60 minutes and 5 consecutive runs.

TEM analysis of PdNPs@PPh_2-PEGPILP after the 5^{th} 60 min catalytic cycle was employed to determine if any structural changes had occurred during catalysis. From Figure 4.55, it is evident that the PdNPs have a much larger average diameter of 4.86 ± 0.99 nm (compared to 1.93 ± 0.67 nm for the freshly prepared catalyst). This increase in particle size could be the cause of the slight drop in conversion observed.

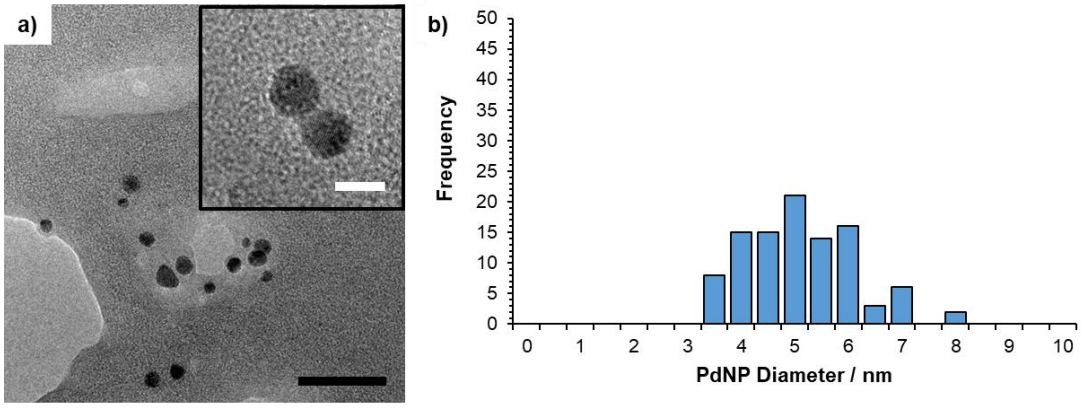

Figure 4.55: a) TEM micrograph of ex-situ prepared PdNP@PPh_2-PEGPILP after 5 catalytic cycles for the cross-coupling reaction between 4-bromoacetophenone and phenyl boronic acid, showing the general size and distribution of the PdNPs; and b) size distribution showing the average size of the PdNPs to be 4.86 ± 0.99 nm. Black and white scale bars are 25 nm and 5 nm, respectively.

4.3.3 Pd Catalysed Hydrogenation of Nitroarenes

Aromatic amine are key motifs in a wide range of bioactive molecules, their corresponding amines and reaction intermediates can be used in the production of pharmaceuticals, agro-chemicals, polymers, pigments and dyes.[93–96] Although there are numerous synthetic pathways to this class of compounds, such as, catalytic reduction of nitriles or imines[97–99] N-arylation,[100–102] the most widely adopted is the reduction of nitro containing compounds e.g. reduction of nitrobenzene to aniline.[103–107] Although the most common, there are several disadvantages to this approach including the need for either high catalyst loadings,[108–110] or stoichiometric amounts of earth abundant metal regents, often in combination with acid,[111-113] and/or the use of toxic reducing agents.[114] Moreover, harmful organic solvents, harsh reaction conditions and partial reduction to hydroxylamines, hydrazones, azoxyarenes and azoarenes limit the potential application of this synthetic pathway. Consequently, there is a growing interest in developing catalyst materials that are not only selective but operate under milder conditions at low catalyst loadings and in environmentally green solvents i.e. water.[46]

Whilst the stabilisation of PdNP by ionic liquids immobilised on a porous polymer[39] or other supports such as silica,[115] graphene oxide-based nanocomposites,[116] and magnetic core shell nanoparticles[117] have been previously reported to catalyse the reduction of nitroarenes, the systems suffer from limitations such as the need for high catalyst loadings, long reaction times, a large excess of reducing agent required, elevated reaction temperatures and/or the use of organic solvents.

PdNP@PPh_2-PILP, PdNP@PPh_2-PEGPILP, PdNP@Sty_3-PILP and PdNP@$PSty_3$-PEGPILP were prepared via the same method highlighted in Scheme 4.1. For full experimental details see Section 4.5.1.

TEM micrographs show that PdNP@PPh_2-PILP and PdNP@PPh_2-PEGPILP consist of small, near monodispersed PdNPs with average diameters of 2.29 ± 0.96 and 1.93 ± 0.67 nm, respectively, while the NPs in in the highly cross-linked systems PdNP@$PSty_3$-PILP and PdNP@$PSty_3$-PEGPILP are larger with average diameters of 3.67 ± 0.67 and 4.01 ± 0.11 nm, respectively (representative TEM micrographs and corresponding size distributions are shown in Figure 4.56).

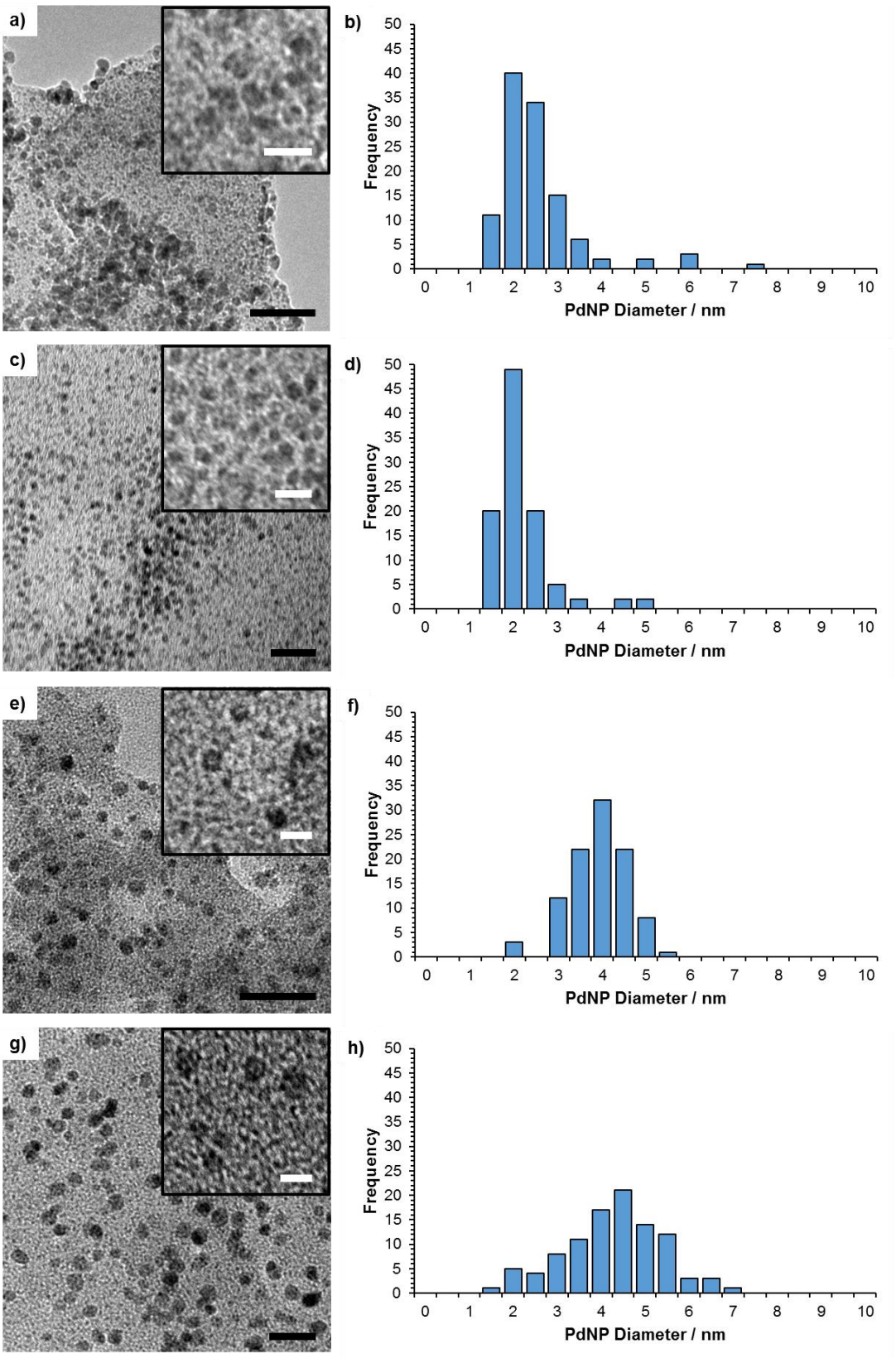

Figure 4.56: TEM micrographs showing the size and distribution of PdNPs for a) PdNP@PPh_2-PILP, c) PdNP@PPh_2-PEGPILP, e)PdNP@$PSty_3$-PILP and g) PdNP@$PSty_3$-PEGPILP; and the corresponding size distributions for showing the average sizes for and to be 2.29 ± 0.96 nm, 1.93 ± 0.67 nm, 3.67 ± 0.67 nm and 4.02 ± 1.11 nm, respectively. Black and white scale bars are 25 nm and 5 nm, respectively.

4.3.3.1 Hydrogenation of Nitrobenzene

The influence of the phosphine, surface ionic liquid and PEG component on catalyst performance has been examined by comparing the performance of PdNP@PPh_2-PILP, PdNP@PPh_2-PEGPILP, PdNP@PPh_2-PEGstyrene and PdNP@PEGPILP under the optimised reaction conditions highlighted in Scheme 4.7.

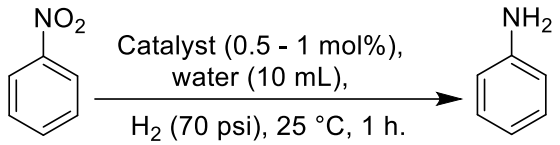

Scheme 4.7: Reaction conditions used for the reduction of nitrobenzene to aniline (1 mmol of nitrobenzene used).

The yield and TOFs (given as mole of product per mole of Pd per hour) obtained for each material compared to the average PdNP diameter are summarised in Table 4.5. A decrease in TOF from 140 to 43 ($mol_p\ mol_M{}^{-1}$) h^{-1} is observed with selective removal of the PEG component (Table 4.5 line 1 and 2). As the average PdNP diameters in both systems are of a similar size, this decrease in activity is probably due to the PEG-based system having an improved dispensability in water.

Table 4.5: Hydrogenation of nitrobenzene as a function of catalyst composition. Summary of conversions and TOFs (given as mol of product per mol of Pd per hour) obtained for the reduction of nitrobenzene to aniline[a] compared to the average diameter of the PdNPs in each system.

No.	Catalyst	Yield / %	TOF / ($mol_p\ mol_M{}^{-1}$)h^{-1}	d_{NP} / nm
1	PdNP@PPh_2-PILP	38	43	2.29 ± 0.96
2	PdNP@PPh_2-PEGPILP	66	140	1.93 ± 0.67
3	PdNP@$PSty_3$-PILP	55	122	3.68 ± 0.67
4	PdNP@$PSty_3$-PEGPILP	45	56	4.02 ± 1.11
5	PdNP@PPh_2-PEGstyrene	34	69	1.39 ± 0.19
6	PdNP@PEGPILP	38	44	3.23 ± 0.61
7	PdNP@PPh_2-styrene	21	62	1.39 ± 0.19
8	PdNP@PILP	44	23	3.01 ± 0.63

[a] Conversion and TOF given as an average of at least 3 runs.

A significant decrease in TOF to 44 ($mol_p\ mol_M^{-1}$) h^{-1} is also observed for the selective removal of PPh_2 (Table 4.5 line 2 and 6) which could be associated with a significant increase in PdNP diameter as the PEG-ionic liquid based system is predicted to have a high dispensability in water. The selective removal of the ionic liquid component also results in an observed decrease in TOF to 69 ($mol_p\ mol_M^{-1}$) h^{-1} (Table 4.5 line 2 and 5). As the average diameter of the PdNPs in PdNP@PPh_2-PEGstyrnene and PdNP@PPh_2-PEGPILP are similar, 1.39 ± 0.19 and 1.93 ± 0.67 nm, respectively, this observed change in activity could result from the water stabilising effect of the ionic liquid component. The efficiency of catalytic systems with two components removed was also investigated i.e. PdNP@PPh_2-styrene and PdNP@PILP, both of which are shown to have substantial decrease in activity (Table 4.5 line 7 and 8).

To test the stability of the catalytic system the recyclability of PdNP@PPh_2-PEGPILP over several repeat catalytic cycles was studied. The performance of the catalyst was tested in 6 consecutive reduction reactions under the same conditions highlighted in Scheme 4.6 (0.5 mol% catalyst used). The product and unreacted substrate where extracted into ethyl acetate before recharging the aqueous solution of catalyst with nitrobenzene and re-pressurising the reactor with H_2. From Figure 4.57, it is evident that there is a significant decrease in conversion over the first 3 catalytic cycles (67% - 42%). After the initial lose in catalytic activity after the fourth cycle subsequent runs yield similar yields of aniline.

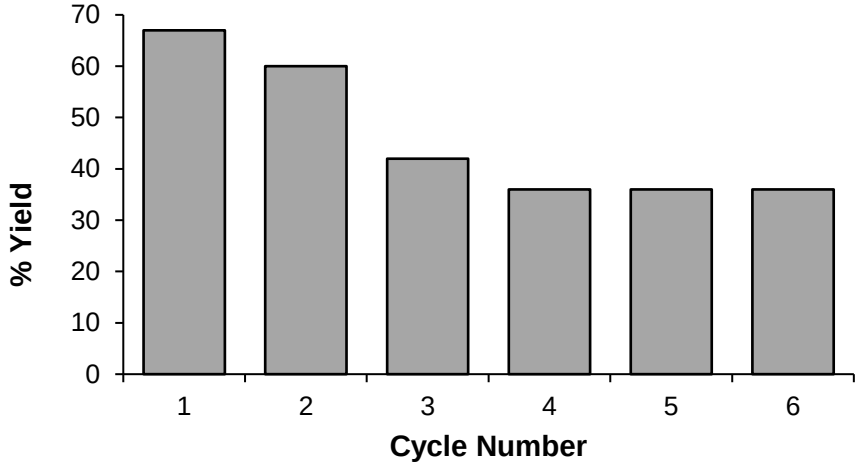

Figure 4.57: Recyclability study for the reduction of nitrobenzene catalysed by the ex-situ prepared PdNP@PPh_2-PEGPILP for 6 consecutive runs.

From TEM analysis of the recycled catalyst (Figure 4.58), it is evident that the average PdNPs diameter has increased in size from 1.93 ± 0.67 nm to

3.05 ± 0.86 nm possibly due to migration of the PdNPs from the polymer support system followed by coalescence. This increase in particle size leads to a decrease surface area by approximately 35% which seems to correlate with the overall drop in conversion.

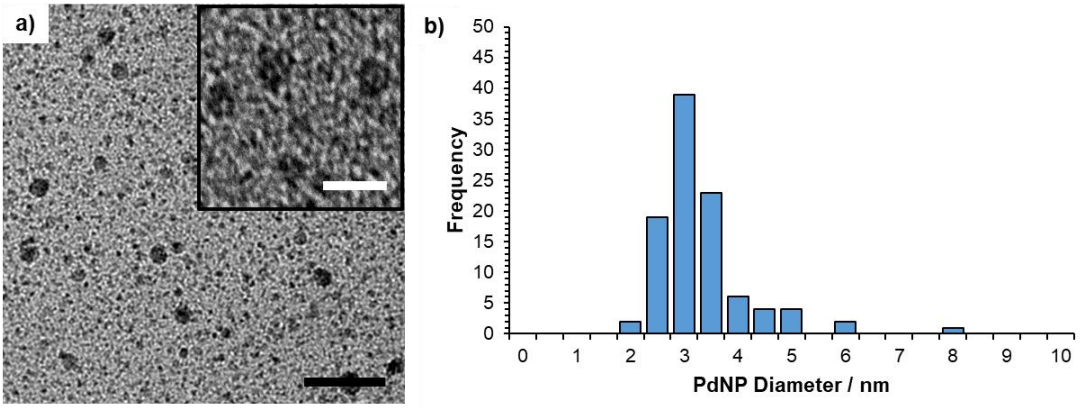

Figure 4.58: a) TEM micrograph of ex-situ prepared PdNP@PPh_2-PEGPILP after 5 catalytic cycles for the reduction of nitrobenzene showing the general size and distribution of the PdNPs; and b) size distribution showing the average size of the PdNPs to be 3.05 ± 0.86 nm. Black and white scale bars are 10 nm and 5 nm, respectively.

4.3.3.2 Transfer Hydrogenation of Nitrobenzene

As the catalytic systems are fabricated from the reduction of their corresponding salt using sodium borohydride as the reducing agent, preparation of the catalyst in-situ was investigated for the transfer hydrogenation of nitrobenzene (in which the catalyst is generated immediately prior to addition of nitrobenzene). By preparing the catalyst system in-situ the need to prepare, separate and store the catalysts before their use in reactions is eliminated. A series of reactions were performed for 0.05 mol% loading of $PdCl_4$ precursors on a range of functionalised ionic liquid polymer support systems.

TEM micrographs of in-situ generated PdNP@PPh_2-PEGPILP and PdNP@$PSty_3$-PEGPILP and their corresponding size distributions are shown in Figure 4.59. It is evident that the PdNPs are monodispersed within the support system and average diameter were found to be 3.36 ± 0.61 and 2.55 ± 0.97 nm, respectively, compared to their ex-situ prepared counterparts with average diameters of 1.93 ± 0.96 and 4.02 ± 1.11 nm for PdNP@PPh_2-PEGPILP and PdNP@$PSty_3$-PEGPILP, respectively. Interestingly, a change in particle size of approximately 40% is seen for both systems which does not appear to influence the conversions obtained for the reduction of nitrobenzene as both systems afford a yields similar to the ex-situ

prepared counter parts; PdNP@PPh_2-PEGPILP ex-situ and in-situ gave conversion of 99% while PdNP@$PSty_3$-PEGPILP prepare in-situ and ex-situ gave yield of 93% and 92%, respectively.

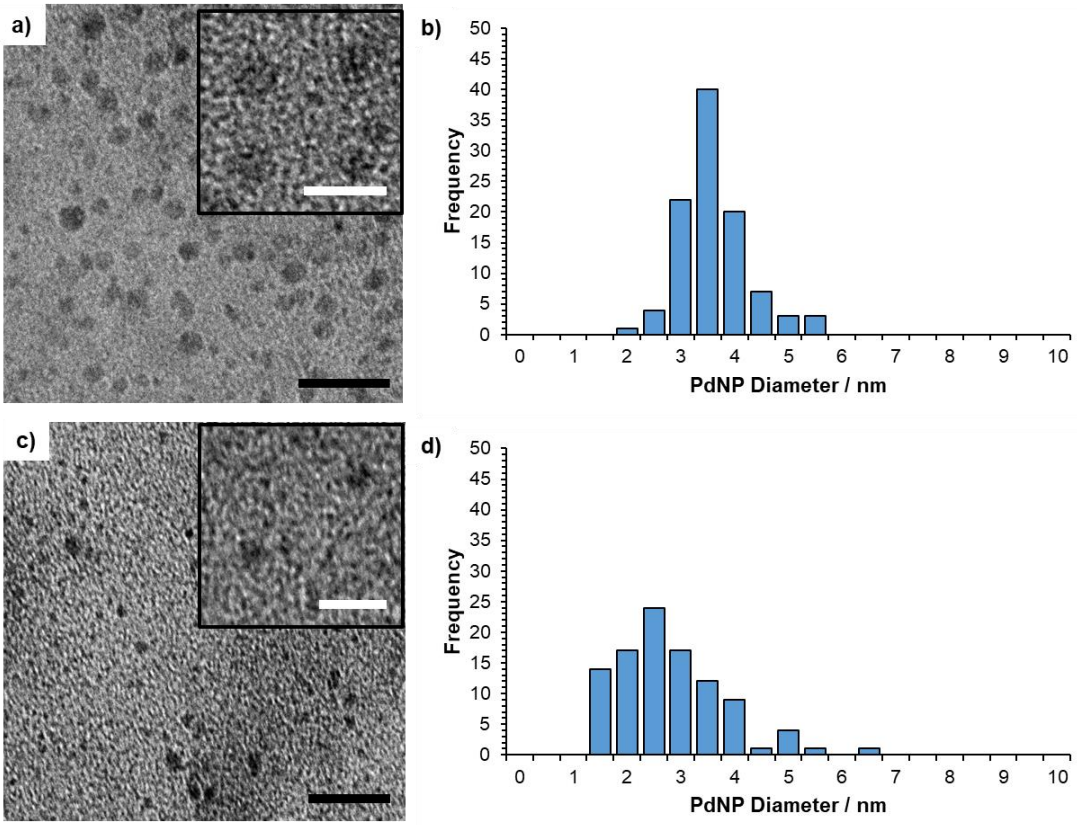

Figure 4.59: TEM micrographs showing the size and distribution of PdNPs for in-situ prepared a) PdNP@PPh_2-PEGPILP and c) PdNP@$PSty_3$-PEGPILP; and the corresponding size distributions for b) PdNP@PPh_2-PEGPILP and d) PdNP@$PSty_3$-PEGPILP showing the average sizes for and to be 3.36 ± 0.61 nm and 2.55 ± 0.97 nm, respectively. Black and white scale bars are 25 nm and 5 nm, respectively.

4.3.4 Au Catalysed Hydrogenation of Nitroarenes

Catalyst selectivity is important for the industrial scale synthesis of many commodity chemicals in addition to fine chemicals and pharmaceuticals.[118–120] Whilst the selectivity in homogeneous catalysts is well understood,[121,122] tuning selective reactions catalysed by NPs or heterogeneous materials remains less established.[123,124] A common theme in previous studies in this area is employing the use of organic modifiers to improve/enhance selectivity through steric effects resulting from specific non-covalent molecular interactions.[44,125–127] However, more recent reports show that the activity and selectivity of NP-based catalysts can be tuned by modulating their surface electronic structure.[88,128–131] For example, Snelders *et al.*,[132] investigated how the use of phosphine ligands with different steric and electronic properties can

modify the properties of RhNPs and in turn influence their catalytic activity. They found that for the reduction of phenylacetone to cyclohexylacetone, via the selective reduction of the aromatic ring, catalysed by phosphine modified polyvinylpyrrolidone-stabilised RhNPs, an increase from 70 to 92% could be achieved (compared to the unmodified catalyst). This increase in selectivity was attributed to the modification of the NP surface due to the coordination of the phosphine ligands.[132]

The selective partial reduction of nitroarenes to N-arylhydroxylamines is particularly important as N-arylhydroxylamines are intermediates to high value products including polymerisation inhibitors,[133] biologically active motifs[134,135] and reagents for use inorganic synthesis as they undergo a range of transformations including cyclisation's[136] and the Bamberger rearrangement.[137] Although numerous methods for the synthesis of N-arylhydroxylamines have been reported including catalytic reductions using Pt/SiO_2,[138] RuNPs/polyester,[139] Rh/C[140,141] and stoichiometric reductions with zinc or tin[142–144] there are several disadvantages to these approaches. In most cases low activities and selectivities are obtained as well as poor stability/recyclability of the catalysts. Development of a catalyst that is not only selective towards N-arylhydroxylamines but is also easily recyclable and able to operate under mild reaction conditions is needed.

Four AuNP polymer immobilised ionic liquid systems were prepared in-situ by the sodium borohydride reduction of potassium tetrachloroaurate (see Scheme 4.2), and are denoted AuNP@PPh_2-PILP, AuNP@PPh_2-PEGPILP, AuNP@PILP and AuNP@PEGPILP. For full experimental details see Section 4.5.1. TEM reveals that in-situ generated catalytic systems contained near monodispersed AuNPs with average diameters of 3.36 ± 0.88, 2.52 ± 0.60, 3.41 ± 1.08 and 3.26 ± 0.88 nm, respectively (see Section 4.2.5 for TEM micrographs and corresponding size distributions).

The activity of the four catalytic systems was investigated for the selective reduction nitrobenzene to N-phenyl hydroxylamine using the optimised reaction conditions highlighted in Scheme 4.8 to ascertain the influence of the phosphine, and PEG component on catalyst performance.

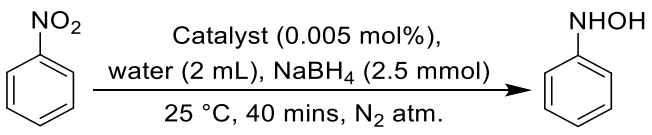

Scheme 4.8: Reaction conditions used for the selective reduction of nitrobenzene to N-phenyl hydroxylamine.

The conversions and selectivities for each material are summarised in Table 4.6. AuNP@PPh_2-PEGPILP afford complete conversion of nitrobenzene with a high selectivity toward N-phenyl hydroxylamine (99%). Upon the removal of the PEG component the activity of the catalytic system decreases substantially to afford a conversion of 45% under the same reaction conditions.

Table 4.6: Summary of conversions and selectivities obtained for the selective hydrogenation of nitrobenzene to N-phenyl hydroxylamine,[a] compared to the average diameter of the AuNPs in each system.

Catalyst	Conversion / %	Selectivity / %	d_{NP} / nm
AuNP@PPh_2-PILP	45	97	3.36 ± 0.88
AuNP@PPh_2-PEGPILP	100	99	2.52 ± 0.60
AuNP@PILP	27	97	3.41 ± 1.08
AuNP@PEGPILP	55	96	3.26 ± 0.88

[a] Conversion and selectivity given as an average of at least 3 runs.

Although the overall conversion of nitrobenzene catalysed by AuNP@PPh_2-PILP is much lower than its pegylated counterpart selectivity towards N-phenyl hydroxylamine remains high (97%). Selective removal of the diphenyl phosphine from both the pegylated and un-pegylated systems results in a further decrease in activity with a 55% conversion obtained for AuNP@PEGPILP and a 27% conversion obtained for AuNP@PILP whilst selectivity towards N-phenyl hydroxylamine remained high at 96%, and 97%, respectively.

Whilst the difference in average diameters for AuNP@PPh_2-PEGPILP (2.52 ± 0.60 nm) and AuNP@PPh_2-PILP (3.36 ± 0.88 nm) could be the reason for the difference in activity observed, AuNP@PEGPILP and AuNP@PILP have similar average diameters with the pegylated system being the most active of the two. This indicates that AuNP size alone isn't the cause of the differences observed in activity and that the pegylated support contributes to the improvement in activity.

TEM analysis of AuNP@PPh_2-PEGPILP after catalysis (Figure 4.60) reveals that although the AuNPs remain monodispersed throughout the system there is a slight increase in diameter from 2.52 ± 0.60 to 3.28 ± 0.88 nm.

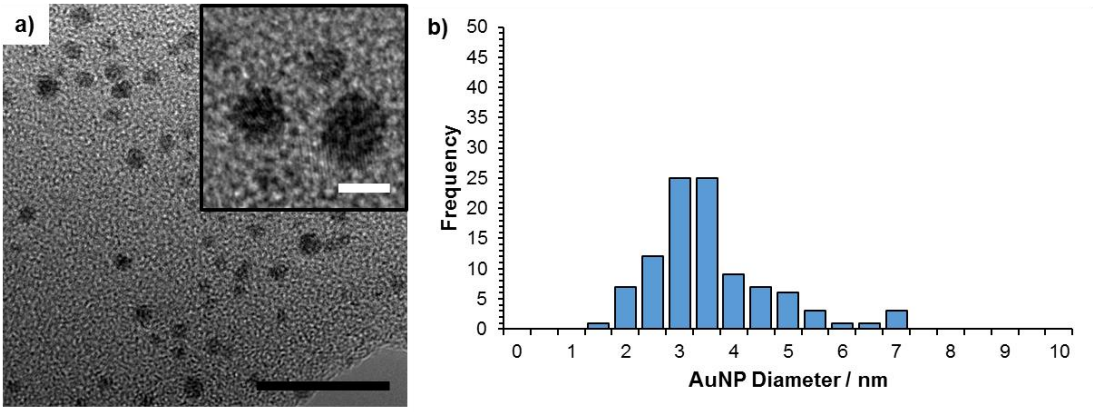

Figure 4.60: a) TEM micrograph of AuNP@PPh_2-PEGPILP after catalysis showing the general size and distribution of the AuNPs; and b) size distribution showing the average size of the AuNPs to be 3.28 ± 1.10 nm. Black and white scale bars are 25 nm and 2 nm, respectively.

4.4 Conclusions

It has been demonstrated that polymer supports can be modified in various ways (selective inclusion of various heteroatom donors, inclusion of an ionic liquid and inclusion of a polyethylene glycol unit) to enable MNP stabilisation. These materials have been shown to be highly active/selective heterogeneous catalysts in which each component of the system plays a vital role; ionic liquid provides stabilisation of MNPs, polymer support prevents leaching of the ionic liquid during catalysis and affords easier recyclability, the heteroatom donor provides further stabilisation of the MNPs, and the polyethylene glycol unit improves the dispersibility of material in aqueous media.

For the aqueous phase hydrogenation of cinnamaldehyde PdNP@PPh_2-PILP was found to be highly efficient catalysts (43% conversion, 95% selectivity) under mild reaction conditions and in short reaction times. Modification with PEG improved the catalyst performance to near quantitative conversions and afforded 100% selectivity towards hydrocinnamaldehyde. This is the highest reported selectivity for the aqueous phase hydrogenation of this class of substrates to date.

PdNPs stabilised by phosphine-decorated polymer immobilised ionic liquid (PdNP@PPh_2-PILP) and its pegylated counterpart (PdNP@PPh_2-PEGPILP) were found to be the most active catalysts for the Suzuki-Miyaura cross-coupling reaction between 4-bromoacetophenone and phenyl boronic acid, when compared with all of the other heteroatom donor-decorated system tested. The improvement in catalyst performance associated with the

inclusion of PEG is thought to be due to an increase in dispersibility and/or solubility allowing for greater access of reagents to the active site.

PdNP@PPh_2-PILP was found to also be the most efficient Pd-based system for the aqueous hydrogenation of nitrobenzene under mild reaction conditions. As the catalytic system is fabricated from the reduction of the corresponding salt using sodium borohydride as the reducing agent, preparation of the catalyst in-situ, for the transfer hydrogenation of nitrobenzene, was successfully achieved.

The stabilisation by phosphine-decorated polymer immobilised ionic liquids was successfully extended to AuNPs. High activities and selectivities towards N-phenylhydroxylamine was achieved under mild reaction conditions. AuNPs@PPh_2-PEGPILP was found be to be the most efficient system giving quantitative conversion of nitrobenzene and 99% selectivity towards N-phenylhydroxylamine.

MNP stabilised phosphine-decorated polymer immobilised ionic liquids have been shown to be active catalysts for a number of reactions under mild reaction conditions. Changing the components of the supported structure e.g. selective removal of the IL, has little effect on average MNP size but greatly effects the efficiency of the catalyst material. Both the phosphine-donor and the IL competent have both be found to be required in order to reach optimum reaction efficacy.

4.5 Experimental

4.5.1 Catalyst Preparation

Catalysts were prepared as outlined by Doherty, *et al*.[35,45–47] The general procedure is outlined below.

4.5.1.1 General procedure for the preparation of heteroatom-donor decorated PILP

A Schlenk flask was charged with 1,2-dimethyl-3-(4-vinylbenzyl)-1H-imidazol-3-ium chloride (5.00 g, 20.1 mmol), 2-methyl-1,3-bis(4-vinylbenzyl)-1H-imidazol-3-ium chloride (0.53 g, 1.52 mmol), 2-(4-vinylphenyl)acetonitrile (1.56 g, 10.9 mmol), azobisisobutyronitrile (to make CN heteroatom donor material, 0.25 g, 1.52 mmol) and dry ethanol. The resulting mixture was degassed via the freeze-thaw method (6 times) before being heated at 85 °C for 96 hours. After this time an additional equivalent of AIBN was added to the flask and the mixture degassed again (5 times) and

heated at 85 °C for a further 20 hours. After cooling to room temperature, the solvent was removed under reduced pressure and the residue triturated with a spatula to afford a solid which was washed with diethyl ether, filtered and then dried under reduced pressure to afford the desired material.

4.5.1.2 General procedure for the preparation of pegylated heteroatom-donor decorated PILP

A Schlenk flask was charged with 2-methyl-1- (2,5,8,11,14,17,20,23-octaoxapentacosan-25-yl)-3-(4-vinylbenzyl)-1H-3λ4-imidazolium chloride (3.61 g, 6.38 mmol), diphenyl(4-vinylphenyl)phosphine (1.00 g, 3.47 mmol), 2-methyl-1,3-bis(4-vinylbenzyl)-1H-imidazol-3-ium chloride (0.17 g, 0.49 mmol), AIBN (0.09 g, 0.49 mmol), ethanol (30 mL) and THF (45 mL). The resulting mixture was degassed using the freeze thaw method (6 times) before being heated at 80 °C for 4 days. After this time, an additional equivalent of AIBN (0.09 g, 0.49 mmol) was added to the flask and the degassing procedure repeated before being heated at 80 °C for a further 24 hours. The solvent was removed under reduced pressure and the resultant residue was dissolved in dichloromethane (35 mL) and added dropwise to a beaker of diethyl ether (350 mL) with vigorous stirring. The solution was left to stir for 45 minutes before being left to settle. The mixture was filtered and the solid washed with ether to yield the desired material.

4.5.1.3 General procedure for the impregnation of the metal salt precursor

A round bottom flask was charged with the appropriate support system e.g. PPh_2-PILP and a solution of pallidum dichloride (1.7–3.1 mmol) and NaCl (38-60 mmol) in water (45 mL) or potassium tetrachloroaurate (2.0 mmol) in water (4-5 mL) was added. The resulting reaction mixture was stirred vigorously at room temperature for 5-6 hours. The precipitate was collected by filtration through a frit and the resulting solid washed with ethanol and diethyl ether.

4.5.1.4 General procedure for the reduction of the metal salt precursor to the MNPs

A Schlenk flask was charged with the appropriate pre-catalyst material e.g. $PdCl_4PPh_2$-PILP and ethanol (20 mL). The resulting mixture was cooled in an ice bath, before the dropwise addition of $NaBH_4$ (0.16 g, 4.4 mmol) in water (4 mL) with stirring. After the addition was complete the flask was stirred at room temperature for 5 hours. After this time, the solid was filtered and washed with water (20 mL), ethanol (20 mL) and diethyl ether (20 mL) to yield

the PdNP based catalyst. AuNP-based catalyst were made in-situ from the relevant pre-catalyst, see Section 4.5.3.4.1 for further details.

4.5.2 Characterisation

Transmission electron microscopy was performed on a FEI Tecnai field emission gun with an accelerating voltage of 200 kV. Samples for TEM were prepared by dispersing the material in 2-propanol using an ultrasonic bath and deposited onto a lacey carbon film coated copper grid. Energy dispersive X-ray spectroscopy was carried out using an Oxford Instruments INCA 350 EDX system/80 mm X-Max SDD detector fitted to the Tecnai.

Samples for X-ray photoelectron spectroscopy were prepared by either loading the solid powder directly onto double-sided carbon tape, mounted atop a glass microscope slide or by being initially suspended in IPA and then dropped directly onto the surface of the glass microscope slide and left to dry for 1 hour prior to insertion into the flexi-lock chamber. XPS measurements of PdNP based materials were carried out using a Theta Probe system (Thermo Scientific, UK) equipped with a micro-focused monochromatic Al Kα source. The X-ray source was operated at 100 W and 15 kV. CasaXPS peak fitting software was employed to analyse the obtained spectra. The Pd 3d region was fitted using Gaussian/Lorentzian peak shapes with a mixing ratio of 30:70, respectively, without imposing parameter constraints on the fwhm. The Shirley background subtraction algorithm was used to subtract the background. For XPS of Pd 3d, each electronic environment of Pd gives two components due to spin-orbit coupling: Pd $3d_{3/2}$ and Pd $3d_{5/2}$.

X-ray photoelectron spectroscopy measurements of AuNP based materials were carried using a Kratos Axis Ultra DLD equipped with a monochromatic Al Kα source. The X-ray source was operated at 100 W and 15 kV. CasaXPS peak fitting software was employed to analyse the obtained spectra. All regions were fitted using Gaussian/Lorentzian peak shapes with a mixing ratio of 30:70, respectively, without imposing parameter constraints on the fwhm. The Shirley background subtraction algorithm was used to subtract the background. For XPS of Au 4f, each electronic S9 environment of Au yields two components due to spin-orbit coupling: Au $4f_{5/2}$ and Au $4f_{7/2}$ which were constrained by area in a ratio of 3:4, respectively. P 2p electronic environments also give rise to two components due to spin-orbit coupling: P $2p_{1/2}$ and P $2p_{3/2}$ which were constrained by area in a ratio of 1:2 respectively. N 1s environments were constrained by area in accordance with their known stoichiometry.

^{1}H NMR spectra were recorded on JEOL LAMBDA-500 or ECS-400 instruments. GC was performed on a Shimadzu2010 series gas chromatograph equipped with a split-mode capillary injection system and flame ionization detection using a Supelco Beta DEX column.

4.5.3 Reaction Conditions

4.5.3.1 Reduction of Cinnamaldehyde

All catalytic hydrogenation reactions were carried out in a 50 mL temperature-controlled Parr reactor equipped with a magnetically coupled stirrer and gas ballast. Reactions were conducted in a glass insert which was charged with substrate (1 mmol), catalyst (0.5-1 mol% loading), water (12 mL), K_2CO_3 (1.0 mmol) and H_2 (70 psi) and heated with stirring at 25 °C for 1 hr. The product was extracted into ethyl acetate (3 x 25 mL) the organic fractions combined, dried over $MgSO_4$, filtered and the solvent removed. ^{1}H NMR (1,3-dinitrobenzene added as the internal standard) and GC (decane used as the internal standard) were employed to determine the conversion and selectivity of the reactions in both cases.

4.5.3.2 Suzuki-Miyaura Cross-Coupling

4.5.3.2.1 General procedure for the palladium catalysed cross-coupling reactions using ex-situ prepared materials

A Schleck flask was degassed, filled with N_2 and charged with aryl bromide (1.0 mmol), phenyl boronic acid (0.14 g, 1.13 mmol), potassium carbonate (0.17 g, 1.2 mmol) and the PdNP catalyst material (0.001 mmol, 0.1 mol%). A 1:1 mixture of EtOH/H_2O (2.4 mL) were added to initiate the reaction and the mixture was stirred at room temperature for 10 minutes. Decane (0.19 mL, 1.0 mmol) was then added to act as an internal standard and the reaction mixture was dilute with water (5 mL) and diethyl ether before being shaken vigorously. The organic layer was passed through a short silica plug which was eluted with diethyl ether (3 mL). An aliquot was taken for GC analysis and the solvent was removed from the remaining solution which was then analysed by ^{1}H NMR.

4.5.3.2.2 General procedure for the palladium catalysed cross-coupling reactions using in-situ prepared materials

A Schleck flask was degassed, filled with N_2 and charged with aryl bromide (1.0 mmol), phenyl boronic acid (0.14 g, 1.13 mmol), potassium carbonate (0.17 g, 1.2 mmol) and the $PdCl_4$ precursor (0.001 mmol, 0.1 mol%). A 1:1 mixture of EtOH/H_2O (2.4 mL) were added to initiate the reaction and the

mixture was stirred at room temperature for 30 minutes. Decane (0.19 mL, 1.0 mmol) was then added to act as an internal standard and the reaction mixture was dilute with water (5 mL) and diethyl ether before being shaken vigorously. The organic layer was passed through a short silica plug which was eluted with diethyl ether (3 mL). An aliquot was taken for GC analysis and the solvent was removed from the remaining solution which was then analysed by ^{1}H NMR.

4.5.3.2.3 General procedure for the recycling experiments for the ex-situ prepared PdNP@PPh$_2$-PILP catalyst

A Schleck flask was degassed, filled with N_2 and charged with 4-bromoacetophenone (1.0 mmol), phenyl boronic acid (0.14 g, 1.13 mmol), potassium carbonate (0.17 g, 1.2 mmol) and PdNP@PPh$_2$-PEG (0.001 mmol, 0.1 mol%). A 1:1 mixture of EtOH/H_2O (2.4 mL) were added to initiate the reaction and the mixture was stirred at room temperature for 30 or 60 minutes. The reaction mixture was extracted with diethyl ether (3 x 10 mL) and decane (0.19 mL, 1.0 mmol) was added to act as the internal standard. An aliquot was taken for GC analysis and the solvent was removed from the remaining solution which was then analysed by ^{1}H NMR. The remaining aqueous phase was recharged with 4-bromoacetophenone (1.0 mmol), phenyl boronic acid (0.14 g, 1.13 mmol), potassium carbonate (0.17 g, 1.2 mmol) and ethanol (1.2 mL) and the reaction mixture was stirred at room temperature for 30 or 60 minutes. This procedure was repeated for subsequent runs.

4.5.3.3 PdNP Catalysed Reduction of Nitroarenes

4.5.3.3.1 General procedure for the hydrogenation of nitrobenzene

All catalytic hydrogenation reactions were carried out in a 50 mL temperature-controlled Parr reactor equipped with a magnetically coupled stirrer and gas ballast. Reactions were conducted in a glass insert which was charged with catalyst (0.5-1 mol% loading), nitrobenzene (1 mmol), solvent (13 mL) and H_2 (70 psi) and heated with stirring at 20 °C for 1 hour. For reactions conducted in organic solvent, the pressure was released, the reaction mixture diluted with ethyl acetate (5 mL) and passed through a short silica plug and the solvent removed. For reactions conducted in water, the product was extracted into ethyl acetate (3 x 25 mL) the organic fractions combined, dried over $MgSO_4$, filtered and the solvent removed. ^{1}H NMR (1,4-dioxane added as the internal standard) and GC (decane used as the internal standard) were employed to determine the conversion and selectivity of the reactions in both cases.

4.5.3.3.2 General procedure for the recycling experiments for the PdNP@PPh_2-PEGPILP catalysed sodium borohydride reductions

A Schleck flask was charged with the catalyst (0.5 μmol, 0.05 mol%) and distilled water (2 mL). $NaBH_4$ (95 mg, 2.5 mmol) was added and the mixture stirred vigorously for 2 min during which time rapid evolution of gas was observed. Nitrobenzene (1.0 mmol) was slowly added to the flask in order to initiate the reaction. The resultant yellow solution was stirred at room temperature for 2 hours. The products were extracted using ethyl acetate (3 x 10 mL), dried over $MgSO_4$ and filtered before the solvent was removed under reduced pressure. The residue was analysed by ^1H NMR (1,4-dioxane added as the internal standard), and GC (decane used as the internal standard). The remaining aqueous layer was added back into the Schlenk flask, recharged with nitrobenzene (1.0 mmol) and stirred at room temperature for 2 hours. This procedure was repeated for subsequent runs.

4.5.3.3.3 General procedure for the palladium catalysed reduction of nitrobenzene using in-situ prepared materials

A Schlenk flask was charged with pre-catalyst (0.5 μmol, 0.05 mol%) and water (2 mL). $NaBH_4$ (95 mg, 2.5 mmol) was added and reaction mixture was stirred vigorously at room temperature for 2 min. Nitrobenzene (1 mmol) was added slowly to initiate the reaction addition the resulting solution was stirred at room temperature for 2 hours. The products were extracted using ethyl acetate (3 x 10 mL), dried over $MgSO_4$, filtered and the solvent removed under reduced pressure. The residue was analysed by ^1H NMR (1,4-dioxane added as the internal standard), and GC (decane used as the internal standard).

4.5.3.4 AuNP Catalysed Reduction of Nitroarenes

4.5.3.4.1 General procedure for the selective reduction of nitrobenzene to N-phenyl hydroxylamine

A Schleck flash was degassed, filled with N_2 and charged with pre-catalyst (0.5 μmol, 0.05 mol %) and $NaBH_4$ (95 mg, 2.5 mmol) was added followed immediately by water (2.5 mL) and the resulting mixture stirred vigorously at room temperature for 5 minutes. Nitrobenzene (1 mmol) was added to the reaction mixture and the resultant solution was stirred for 40 minutes. The reaction was quenched by addition of water (5 mL), the product extracted with ethyl acetate (2 x 10 mL) and the solvent removed under reduced pressure. The residue was analysed by ^1H NMR (1,4-dioxane added as the internal standard), and GC (decane used as the internal standard).

4.6 References

1 T. Welton, *Coord. Chem. Rev.*, 2004, **248**, 2459–2477.

2 D. Zhao, M. Wu, Y. Kou and E. Min, *Catal. Today*, 2002, **74**, 157–189.

3 R. D. Rogers and K. R. Seddon, *Inoic liquids: industrial applications for green chemistry*, American Chemical Society, 2002.

4 P. J. Dyson and T. J. Geldbach, *Metal catalysed reactions in ionic liquids*, Springer Science & Business, 2005.

5 R. L. Vekariya, *J. Mol. Liq.*, 2017, **227**, 44–60.

6 S. Doherty, in *Catalysis in Ionic Liquids: From Catalyst Synthesis to Applications*, eds. C. Hardacre and V. Parvulescu, The Royal Society of Chemistry, 2014, pp. 44–308.

7 J. Dupont, *Acc. Chem. Res.*, 2011, **44**, 1223–1231.

8 P. Wasserchеid and T. Welton, *Ionic liquids in synthesis*, Wiley-VCH, Weinheim, 2007.

9 Q. Zhang, S. Zhang and Y. Deng, *Green Chem.*, 2011, **13**, 2619–2637.

10 A. Papp, K. Miklos, P. Forgo and A. Molnar, *J. Mol. Catal. A Chem.*, 2005, **229**, 107–116.

11 X. Mu, D. G. Evans and Y. Kou, *Catal. Letters*, 2004, **97**, 151–154.

12 M. Besson and P. Gallezot, *Catal. Today*, 2003, **81**, 547–559.

13 G. S. Fonseca, A. P. Umpierre, P. F. P. Fichtner, S. R. Teixeira and J. Dupont, *Chem. Eur. J.*, 2003, **9**, 3263–3269.

14 F. Bellina and C. Chiappe, *Molecules*, 2010, **15**, 2211–2245.

15 Y. Liu, S. Wang, W. Liu, Q. Wan, H. Wu and G. Gao, *Curr. Org. Chem.*, 2009, **13**, 1322–1346.

16 Z. Wang, Q. Zhang, D. Kuehner, A. Ivaska and L. Niu, *Green Chem.*, 2008, **10**, 907–909.

17 H. Zhang and H. Cui, *Langmuir*, 2009, **25**, 2604–2612.

18 B. C. Leal, C. S. Consorti, G. Machado and J. Dupont, *Catal. Sci. Technol.*, 2015, **5**, 903–909.

19 S. A. Stratton, K. L. Luska and A. Moores, *Catal. Today*, 2012, **183**, 96–100.

20 K. L. Luska and A. Moores, *Adv. Synth. Catal.*, 2011, **353**, 3167–3177.

21 D. Zhao, Z. Fei, T. J. Geldbach, R. Scopelliti and P. J. Dyson, *J. Am. Chem. Soc.*, 2004, **126**, 15876–15882.

22 C. Chiappe, D. Pieraccini, D. Zhao, Z. Fei and P. J. Dyson, *Adv. Synth. Catal.*, 2006, **348**, 68–74.

23 Z. Fei, D. Zhao, D. Pieraccini, W. H. Ang, T. J. Geldbach, R. Scopelliti, C. Chiappe and P. J. Dyson, *Organometallics*, 2007, **26**, 1588–1598.

24 M. H. G. Prechtl, J. D. Scholten and J. Dupont, *J. Mol. Catal. A Chem.*, 2009, **313**, 74–78.

25 B. Leger, A. Denicourt-Nowicki, H. Olivier-Bourbigou and A. Roucoux, *Inorg. Chem.*, 2008, **47**, 9090–9096.

26 B. Leger, A. Denicourt-Nowicki, A. Roucoux and H. Olivier-Bourbigou, *Adv. Synth. Catal.*, 2008, **350**, 153–159.

27 A. Denicourt-Nowicki, B. Leger and A. Roucoux, *Phys. Chem. Chem. Phys.*, 2011, **13**, 13510–13517.

28 R. R. Dykeman, N. Yan, R. Scopelliti and P. J. Dyson, *Inorg. Chem.*, 2011, **50**, 717–719.

29 H. Itoh, K. Naka and Y. Chujo, *J. Am. Chem. Soc.*, 2004, **126**, 3026–3027.

30 N. Yan, X. Yang, Z. Fei, Y. Li, Y. Kou and P. J. Dyson, *Organometallics*, 2009, **28**, 2008–2010.

31 X. Yuan, N. Yan, S. A. Katsyuba, E. E. Zvereva, Y. Kou and P. J. Dyson, *Phys. Chem. Chem. Phys.*, 2012, **14**, 6026–6033.

32 K. L. Luska and A. Moores, *ChemCatChem*, 2012, **4**, 1534–1546.

33 Y. Hu, Y. Y. Yu, Z. S. Hou, H. M. Yang, B. Feng, H. Li, Y. X. Qiao, X. R. Wang, L. Hua, Z. Y. Pan and X. Zhao, *Chem. Asian J.*, 2010, **5**, 1178–1184.

34 H. Jiang and X. Zheng, *Appl. Catal. A Gen.*, 2015, **499**, 118–123.

35 S. Doherty, J. G. Knight, T. Backhouse, E. Abood, H. Al-shaikh, A. R. Clemmet, J. R. Ellison, R. A. Bourne, T. W. Chamberlain, R. Stones, N. J. Warren, I. J. S. Fairlamb and K. R. J. Lovelock, *Adv. Synth. Catal.*, 2018, **360**, 3716–3731.

36 M. I. Burguete, E. García-verdugo, I. Garcia-villar, F. Gelat, P. Licence, S. V Luis and V. Sans, *J. Catal.*, 2010, **269**, 150–160.

37 B. Van Vaerenbergh, J. Lauwaert, W. Bert, J. W. Thybaut, J. De Clercq and P. Vermeir, *ChemCatChem*, 2017, **9**, 451–457.

38 Y. Su, X. Li, Y. Wang, H. Zhong and R. Wang, *Dalt. Trans.*, 2016, **45**, 16896–16903.

39 Y. Wang, H. Zhong, L. Li and R. Wang, *ChemCatChem*, 2016, **8**, 2234–2240.

40 K. R. Kahsar, D. K. Schwartz and J. W. Medlin, *J. Am. Chem. Soc.*, 2014, **136**, 520–526.

41 S. G. Kwon, G. Krylova, A. Sumer, M. M. Schwartz, E. E. Bunel, C. L. Marshall, S. Chattopadhyay, B. Lee, J. Jellinek and E. V Shevchenko, *Nano Lett.*, 2012, **12**, 5382–5388.

42 Z. Guo, C. Xiao, R. V Maligal-Ganesh, L. Zhou, T. W. Goh, X. Li, D. Tesfagaber, A. Thiel and W. Huang, *ACS Catal.*, 2014, **4**, 1340–1348.

43 J. Sun, Z. Kochovski, W. Zhang, H. Kirmse, Y. Lu, M. Antonietti and J. Yuan, *J. Am. Chem. Soc.*, 2017, **139**, 8971–8976.

44 K. Chen, H. Wu, Q. Hua, S. Chang and W. Huang, *Phys. Chem. Chem. Phys.*, 2013, **15**, 2273–2277.

45 S. Doherty, J. G. Knight, T. Backhouse, E. Abood, H. Alshaikh, I. J. S. Fairlamb, R. A. Bourne, T. W. Chamberlain and R. Stones, *Green Chem.*, 2017, **19**, 1635–1641.

46 S. Doherty, J. G. Knight, T. Backhouse, A. Bradford, F. Saunders, R. A. Bourne, T. W. Chamberlain, R. Stones, A. Clayton and K. Lovelock, *Catal. Sci. Technol.*, 2018, **8**, 1454–1467.

47 S. Doherty, J. G. Knight, T. Backhouse, R. J. Summers, E. Abood, W. Simpson, W. Paget, R. A. Bourne, T. W. Chamberlain, R. Stones, K. R. J. Lovelock, J. M. Seymour, M. A. Isaacs, C. Hardacre, H. Daly and N. H. Rees, *ACS Catal.*, 2019, **9**, 4777–4791.

48 C. Wang, R. Ciganda, L. Salmon, D. Gregurec, J. Irigoyen, S. Moya, J. Ruiz and D. Astruc, *Angew. Chem. Int. Ed.*, 2016, **55**, 3091–3095.

49 J. Feng, S. Handa, F. Gallou and B. H. Lipshutz, *Angew. Chemie - Int. Ed.*, 2016, **55**, 8979–8983.

50 Y. Lee, S. Shabbir, S. Lee, H. Ahn and H. Rhee, *Green Chem.*, 2015, **17**, 3579–3583.

51 K. Sawai, R. Tatumi, T. Nakahodo and H. Fujihara, *Angew. Chem. Int. Ed.*, 2008, **47**, 6917–6919.

52 H. Kitagawa, N. Kojima and T. Nakajimab, *J. Chem. Soc. Dalton. Trans.*, 1991, **11**, 3121–3125.

53 A. McNeillie, D. H. Brown, W. E. Smith, M. Gibson and L. Watson, *J. Chem. Soc. Dalton. Trans.*, 1980, **5**, 767–770.

54 M. Conte, C. J. Davies, D. J. Morgan, T. E. Davies, D. J. Elias, A. F. Carley, P. Johnston and G. J. Hutchings, *J. Catal.*, 2013, **297**, 128–136.

55 J. Zhao, S. Gu, X. Xu, T. Zhang, Y. Yu, X. Di, J. Nl, Z. Pan and X. Li, *Catal. Sci. Technol.*, 2016, **6**, 3263–3270.

56 Y. Fong, B. R. Visser, J. R. Gascooke, B. C. C. Cowie, L. Thomsen, G. F. Metha, M. A. Buntine and H. H. Harris, *Langmuir*, 2011, **27**, 8099–8104.

57 K. R. J. Lovelock, E. F. Smith, A. Deyko, I. J. Villar-garcia, P. Licence and R. G. Jones, *Chem. Commun.*, 2007, 4866–4868.

58 X. Chen, H. Li, W. Dai, J. Wang, Y. Ran and M. Qiao, *Appl. Catal. A Gen.*, 2003, **253**, 359–369.

59 W. Zhu, H. Yang, Y. Yu, L. Hua, H. Li, B. Feng and Z. Hou, *Phys. Chem. Chem. Phys.*, 2011, **13**, 13492–13500.

60 P. Gallezot and D. Richard, *Catal. Rev.*, 1998, **40**, 81–126.

61 E. Bus, R. Prins and J. A. van Bokhoven, *Catal. Commun.*, 2007, **8**, 1397–1402.

62 P. Virtanen, T. Salmi and J. Mikkola, *Ind. Eng. Chem. Res.*, 2009, **48**, 10335–10342.

63 K. Anderson, P. Goodrich, C. Hardacre and D. W. Rooney, *Green Chem.*, 2003, **5**, 448–453.

64 A. S. Nagpure, L. Gurrala, P. Gogoi and S. V Chilukuri, *RSC Adv.*, 2016, **6**, 44333–44340.

65 P. H. Z. Ribeiro, E. Y. Matsubara, J. M. Rosolen, P. M. Donate and R. Gunnella, *J. Mol. Catal. A Chem.*, 2015, **410**, 34–40.

66 C. Torborg and M. Beller, *Adv. Synth. Catal.*, 2009, **351**, 3027–3043.

67 C. C. C. J. Seechurn, M. O. Kitching, T. J. Colacot and V. Snieckus, *Angew. Chem. Int. Ed.*, 2012, **51**, 5062–5085.

68 B. A. Khakiani, K. Pourshamsian and H. Veisi, *Appl. Organomet. Chem.*, 2015, **29**, 259–265.

69 N. Miyaura and A. Suzuki, *Chem. Rev.*, 1995, **95**, 2457–2483.

70 J. Magano and J. R. Dunetz, *Chem. Rev.*, 2011, **111**, 2177–2250.

71 S. Doherty, J. G. Knight, C. H. Smyth and G. A. Jorgenson, *Adv. Synth. Catal.*, 2008, **350**, 1801–1806.

72 S. Doherty, J. G. Knight, N. A. B. Ward, D. O. Perry, D. M. Bittner, M. R. Probert and S. A. Westcott, *Organometallics*, 2014, **33**, 5209–5219.

73 R. Martin and S. L. Buchwald, *Acc. Chem. Res.*, 2008, **41**, 1461–1473.

74 N. C. Bruno, M. T. Tudge and S. L. Buchwald, *Chem. Sci.*, 2013, 916–920.

75 A. Bruneau, M. Roche, M. Alami and S. Messaoudi, *ACS Catal.*, 2015, **5**, 1386–1396.

76 S. Harkal, F. Rataboul, A. Zapf, C. Fuhrmann, T. Riermeier, A. Monsees and M. Beller, *Adv. Synth. Catal.*, 2004, **346**, 1742–1748.

77 K. D. Hesp, R. J. Lundgren and M. Stradiotto, *J. Am. Chem. Soc.*, 2011, **133**, 5194–5197.

78 R. J. Lundgren, A. Sappong-kumankumah and M. Stradiotto, *Chem. Eur. J.*, 2010, **16**, 1983–1991.

79 M. Perez-Lorenzo, *J. Phys. Chem. Lett.*, 2012, **3**, 167–174.

80 A. Bej, K. Ghosh, A. Sarkar and D. W. Knight, *RSC Adv.*, 2016, **6**, 11446–11453.

81 M. Beller, A. Balanta, C. Godard and C. Claver, *Chem. Soc. Rev.*, 2011, **40**, 4973–4985.

82 M. Turner, V. B. Golovko, O. P. H. Vaughan, P. Abdulkin, A. Berenguer-murcia, M. S. Tikhov, B. F. G. Johnson and R. M. Lambert, *Nature*, 2008, **454**, 981–984.

83 M. Stratakis and H. Garcia, *Chem. Rev.*, 2012, **112**, 4469–4506.

84 R. J. White, R. Luque, V. L. Budarin, J. H. Clark and D. J. Macquarrie, *Chem. Soc. Rev.*, 2009, **38**, 481–494.

85 H. Goesmann and C. Feldmann, *Angew. Chem. Int. Ed.*, 2010, **49**, 1362–1395.

86 A. Roucoux, J. Schulz and H. Patin, *Chem. Rev.*, 2002, **102**, 3757–3778.

87 X. Yang, A. Wang, B. Qiao, J. Li, J. Liu and T. Zhang, *Acc. Chem. Res.*, 2013, **46**, 1740–1748.

88 S. Jayakumar, A. Modak, M. Guo, H. Li, X. Hu and Q. Yang, *Chem. Eur. J.*, 2017, **23**, 7791–7797.

89 N. J. S. Costa, P. K. Kiyohara, A. L. Monteiro, Y. Coppel, K. Philippot and L. M. Rossi, *J. Appl. Electrochem.*, 2010, **276**, 382–389.

90 L. M. Rossi, I. M. Nangoi and N. J. S. Costa, *Ind. Eng. Chem. Res.*, 2009, **48**, 4640–4642.

91 D. Zhang, Y. Guan, E. J. M. Hensen, T. Xue and Y. Wang, *Catal. Sci. Technol.*, 2014, **4**, 795–802.

92 E. Rafter, T. Gutmann, F. Low, G. Buntkowsky, K. Philippot, B. Chaudret and P. W. N. M. van Leeuwen, *Catal. Sci. Technol.*, 2013, **3**, 595–599.

93 R. S. Downing and P. J. Kunkeler, *Catal. Today*, 1997, **37**, 121–136.

94 A. M. Tafesh and J. Weiguny, *Chem. Rev.*, 1996, **96**, 2035–2052.

95 T. J. Blacklock, Y. Liu, Y. Lu, M. Prashad and O. Repic, *Adv. Synth. Catal.*, 2005, **347**, 217–219.

96 H. K. Kadam and S. G. Tilve, *RSC Adv.*, 2015, **5**, 83391–83407.

97 S. Semwal and J. Choudhury, *ACS Catal.*, 2016, **6**, 2424–2428.

98 T. C. Nugent and M. El-Shazly, *Adv. Funct. Mater.*, 2010, **352**, 753–819.

99 S. Elangovan, C. Topf, S. Fischer, H. Jiao, A. Spannenberg, W. Baumann, R. Ludwig, K. Junge and M. Beller, *J. Am. Chem. Soc.*, 2016, **138**, 8809–8814.

100 C. Thomas, M. Wu and K. L. Billingsley, *J. Org. Chem.*, 2016, **81**, 330–335.

101 Y. Aubin, C. Fischmeister, C. M. Thomas and J.-L. Renaud, *Chem. Soc. Rev.*, 2010, **39**, 4130–4145.

102 D. S. Surry and S. L. Buchwald, *Angew. Chemie - Int. Ed.*, 2008, **47**, 6338–6361.

103 S. M. Kelly and B. H. Lipshutz, *Org. Lett.*, 2014, **16**, 98–101.

104 F. Zamani and S. Kianpour, *Catal. Commun.*, 2014, **45**, 1–6.

105 R. J. Kalbasi and F. Zamani, *RSC Adv.*, 2014, **4**, 7444–7453.

106 M. M. Moghaddam, B. Pieber, T. Glasnov and C. O. Kappe, *ChemSusChem*, 2014, **7**, 3122–3131.

107 Z. Zhao, H. Yang, Y. Li and X. Guo, *Green Chem.*, 2014, **16**, 1274–1281.

108 L. Huang, P. Luo, W. Pei, X. Liu, Y. Wang, J. Wang, W. Xing and J. Huang, *Adv. Synth. Catal.*, 2012, **354**, 2689–2694.

109 D. Cantillo, M. M. Moghaddam and C. O. Kappe, *J. Org. Chem.*, 2013, **78**, 4530–4542.

110 U. Sharma, P. Kumar, N. Kumat, V. Kumar and B. Singh, *Adv. Synth. Catal.*, 2010, **352**, 1834–1840.

111 X. Liu, H. Li, S. Ye, Y. Liu, H. He and Y. Cao, *Angew. Chem. Int. Ed.*, 2014, **53**, 7624–7628.

112 P. Wang, H. Liu, J. Niu, R. Li and J. Ma, *Catal. Sci. Technol.*, 2014, **4**, 1333–1339.

113 S. G. Oh, V. Mishra, J. K. Cho, B. Kim, H. S. Kim, Y. Suh, H. Lee, H. S. Kim and Y. J. Kim, *Catal. Commun.*, 2014, **43**, 79–83.

114 G. Rothenberg, *Catalysis, Concepts and Green Applications*, Wiley-VCH, Weinheim, 2008.

115 J. Li, X. Shi, Y. Bi, J. Wei and Z. Chen, *ACS Catal.*, 2011, **1**, 657–664.

116 A. Pourjavadi, N. Safaie, S. H. Hosseini and C. Bennett, *J. Ind. Eng. Chem.*, 2016, **38**, 82–92.

117 S. Bahadorikhalili, L. Ma'mani, H. Mahdavi and A. Shafiee, *RSC Adv.*, 2015, **5**, 71297–71305.

118 G. A. Somorjai and R. M. Rioux, *Catal. Today*, 2005, **100**, 201–215.

119 R. A. Sheldon and H. Van Bekkum, *Fine Chemicals through Heterogeneous Catalysis*, Wiley-VCH, Weinheim, 2008.

120 R. Noyori, *Nat. Chem.*, 2009, **1**, 5–6.

121 D.-H. Wang, K. M. Engle, B.-F. Shi and J.-Q. Yu, *Science (80-.).*, 2010, **327**, 315–320.

122 P. W. N. M. van Leeuwen, *Homogeneous Catalysis: Understanding the Art*, Kluwer, Dordrecht, The Netherlands, 2004.

123 D. Astruc, F. Lu and J. R. Aranzaes, *Angew. Chem. Int. Ed.*, 2005, **44**, 7852–7872.

124 S. Kunz, P. Schreiber, M. Ludwig, M. M. Maturi, O. Ackermann, M. Tschurl and U. Heiz, *Phys. Chem. Chem. Phys.*, 2013, **15**, 19253–19261.

125 C. A. Schoenbaum, D. K. Schwartz and J. W. Medlin, *Acc. Chem. Res.*, 2014, **47**, 1438–1445.

126 S. T. Marshall, M. O'Brien, B. Oetter, A. Corpuz, R. M. Richards, D. K. Schwartz and J. W. Medlin, *Nat. Mater.*, 2010, **9**, 853–858.

127 S. Albani, G. Vile, S. Mitchell, P. T. Witte, N. Almora-Barrios, R. Verel, N. López and J. Pérez-ramírez, *Catal. Sci. Technol.*, 2016, **6**, 1557–1968.

128 A. Fedorov, H. Liu, H. Lo and C. Coperet, *J. Am. Chem. Soc.*, 2016, **138**, 16502–16507.

129 M. Guo, C. Li and Q. Yang, *Catal. Sci. Technol.*, 2017, **7**, 2221–2227.

130 G. Chen, C. Xu, X. Huang, J. Ye, L. Gu, G. Li, Z. Tang, B. Wu, H. Yang, Z. Zhao, Z. Zhou, G. Fu and N. Zheng, *Nat. Mater.*, 2016, **15**, 564–569.

131 E. H. Boymans, P. T. Witte and D. Vogt, *Catal. Sci. Technol.*, 2015, **5**, 176–183.

132 D. J. M. Snelders, N. Yan, W. Gan, G. Laurenczy and P. J. Dyson, *ACS Catal.*, 2012, **2**, 201–207.

133 Patent EP0240297, 1987.

134 P. M. Vyas, S. Roychowdhury, P. M. Woster and C. K. Svensson, *Biochem. Pharmacol.*, 2005, **70**, 275–286.

135 J. S. Yadav, B. V. S. Reddy and P. Sreedhar, *Adv. Synth. Catal.*, 2003, **345**, 564–567.

136 R. N. Ram and V. K. Soni, *J. Org. Chem.*, 2013, **78**, 11935–11947.

137 S. Liu, Y. Hao and J. Jiang, *Ind. Eng. Chem. Res.*, 2014, **53**, 8372–8375.

138 L. Pernoud, J. P. Candy, R. Jacquot and J. M. Basset, *Stud. Surf. Sci. Catal.*, 2000, **130**, 2057–2062.

139 J. H. Tyler, S. H. Nazari, R. H. Patterson, V. Udumula, S. J. Smith and D. J. Michaelis, *Tetrahedron Lett.*, 2017, **58**, 82–86.

140 P. W. Oxley, B. M. Adger, M. J. Sasse and M. A. Forth, *Org. Synth.*, 1989, **67**, 187–192.

141 I. D. Entwistle, T. Gilkerson, R. A. W. Johnstone and R. P. Telwrd, *Tetrahedron*, 1978, **34**, 213–215.

142 Q. X. Shi, R. W. Lu, K. Jin, Z. X. Zhang and D. F. Zhao, *Chem. Lett.*, 2006, **35**, 226–227.

143 S. Ung, A. Falguieres, A. Guy and C. Ferroud, *Tetrahedron Lett.*, 2005, **46**, 5913–5917.

144 M. Bartra, P. Romea, F. Urpf and J. Vilarrasa, *Tetrahedron*, 1990, **46**, 587–594.

Chapter 5: Summary and Concluding Remarks

Heterogeneous catalysis is of critical importance in a variety of chemical, environmental, and energy-conversion processes. Transition metal nanoparticles have been found to be excellent candidates for catalysis due to their remarkable chemical and physical properties. However, they are intrinsically thermodynamically metastable making their application difficult, therefore, the stabilisation of MNPs is important in order to prevent aggregation, sintering and leaching of the metal during catalysis. An effective method to combat this problem is to immobilise the MNPs on porous solid supports. Two system for the support/stabilisation of catalytically active transition metals have been explored in this work: carbon nanoreactors (Chapters 2 and 3) and polymer immobilised ionic liquids (Chapter 4).

Chapter 2 investigates how simple changes in a sublimation deposition fabrication method lead to structural changes in the resultant MNP@GNF materials. A series of monometallic RuNPs encapsulated within GNFs (RuNP@GNFs) were fabricated with different metal loadings (1-10% by wt. Ru) and it was found that the diameter of the RuNPs increased with increasing wt.% of Ru metal present. Additionally, a lower metal loading also resulted in a more well defined structures with the nanoparticles aligned along the step-edges of the GNFs and uniformly distributed throughout the material.

To gain further insight into how the size of RuNPs formed could potentially be controlled the effect of changing to the decomposition temperature, between 200-700 °C, was also investigated for RuNPs@GNFs (2 wt.%). No change in the average diameters of the RuNPs was observed suggesting that the step-edges of the GNFs template the size of the RuNPs formed and that the material is stable up to 700 °C which is exciting as it provides the opportunity for catalytic reactions to be carried out at high temperatures with no loss in catalytic activity due to migration or coalescence of the MNPs, ultimately increasing the rate of reaction.

For bimetallic RuNi-based systems (Ru:Ni 1:1) there are three options by which the metals can be added during the fabrication process. It was found that simply changing the addition sequence of the metal precursor resulted in substantial changes in the structure of the RuNiNPs@GNFs. The sequential addition of both Ru first and Ni first resulted in the formation of interesting nickel sheets and flower-like structure adhered to the exterior surface of the

GNFs support structure. These structures have the potential for use as novel electrode materials in electrochemical devices due to their high surface areas.

Using the concerted addition approach the effect of varying the ratio of Ru:Ni was also investigated through the fabrication of three bimetallic RuNiNPs@GNFs, with differing ratios of Ru:Ni (3:1, 1:1 and 1:3) but the same total metal (5 wt.%). No significant change to the average diameter of the MNPs was observed and as such, any changes in the activity of the MNPs can be attributed to other factors such as MNP composition rather than particle size. This facile fabrication methodology could be extended to allow for the fabrication of more sustainable bimetallic MNPs supported in GNFs (e.g. NiFeNPs@GNFs). However, the development of a successful digestion method of RuNPs and RuNiNPs is needed to obtain accurate determination of the metal content in the MNP@GNFs materials by ICP-MS.

In Chapter 3 the catalytic performance of the MNP@GNF systems, in terms of activity, selectivity and recyclability, was probed using exploratory hydrogenation reactions. By investigating the activity of the mono- and bimetallic materials fundamental insight was revealed into how the conditions used during the fabrication process not only influences the structural features of the resultant material, but also the catalytic performance.

For bimetallic RuNiNPs@GNFs it was found that the concerted addition fabrication method afforded the only active material towards the reduction of nitrobenzene to aniline with the optimum ratio of Ru:Ni being 1:1 ($Ru_{0.5}Ni_{0.5}$NPs@GNFs (concerted addition) had the highest TOF of 24.1 ± 1.7 $mol_{An}mol_{M}^{-1}$/h).

Competitive reaction studies (using molecules with the same functional group but with different shapes or degrees of aromaticity) were performed for both catalytic transfer hydrogenation and H_2 batch reactions. For the catalytic transfer hydrogenations, it was found that aromatic reagents are preferentially reduced over non-aromatic reagents for both GNF supported MNP systems (i.e. RuNPs@GNFs and RuNiNPs@GNFs). Additionally, for the H_2 batch reactions is was found that the aromaticity of a reagent was far more important for the selectivity of a reaction, catalysed by MNPs@GNFs, compared to the size and/or shape of a reagent, which has not been previously reported. This is evidence of an enhancement in the local concertation effect of aromatic molecules within the inner cavities of GNFs due to favourable interactions between the π-system of aromatic molecule and the sp^2 hybridised carbon walls.

These catalyst systems could be transferred into a fixed bed continuous flow reactor to exploit self-optimisation algorithms to allow for rapid optimisation of reaction conditions and screening of the catalytic performance of the materials. Time on stream experiments would allow for the stability of the MNPs@GNFs materials to be further examined.

Chapter 4 investigates how polymer supports can be modified, to enhance the stabilisation of Pd and Au NPs, by the incorporation of different functionalities such as; ionic liquids, heteroatom donors and polyethylene glycol units. These materials were investigated, in terms of activity, selectivity and recyclability, in a number of relevant reactions (using environmentally friendly reaction conditions). It was found that changing the components of the supported structure e.g. selective removal of the ionic liquid, has little effect on average MNP size but greatly effects the efficiency of the catalyst material. Both the phosphine-donor and the ionic liquid competent have both be found to be required in order to reach optimum reaction efficacy.

For the aqueous phase hydrogenation of cinnamaldehyde PdNP-based materials were found to be efficient catalysts under mild reaction conditions and short reaction times. Additionally, PdNPs stabilised by phosphine-decorated polymer immobilised ionic liquid (PdNP@PPh_2-PILP) and its pegylated counterpart (PdNP@PPh_2-PEGPILP) were found to be the most active catalysts for the Suzuki-Miyaura cross-coupling reaction between 4-bromoacetophenone and phenyl boronic acid, when compared with all of the other heteroatom donor-decorated systems tested. Moreover, PdNP@PPh_2-PILP was found to also be the most efficient Pd-based system for the aqueous hydrogenation of nitrobenzene under mild reaction conditions.

The stabilisation by phosphine-decorated polymer immobilised ionic liquids was successfully extended to AuNPs. High activities and selectivities towards the formation of N-phenylhydroxylamine from nitrobenzene were achieved under mild reaction conditions.

The ability to perform industrially relevant reactions under mild reaction conditions will lead to a reduction in their environmental impact.

This study could be extended to investigate other industrially relevant reactions to explore the potentially to be carried out in greener reaction conditions (e.g. in water at lower temperatures). Further investigation is needed to explore the influence of the heteroatom donor on the nucleation and growth of the MNPs and their efficiency as catalysts. These catalyst

systems could also be transferred into a fixed bed continuous flow reactor to allow for the rapid screening of their catalytic performance.

In summary, catalysis is a critical enabler required to improve the productivity of chemical processes. The resulting chemicals and materials are sold into all other sectors of the UK economy and the impact of this improved productivity will have significant benefit for downstream sectors, for example the production of pharmaceuticals, food additives and conversion of biomass derived products to value added chemicals. Therefore, there is a real need to develop and understand novel catalyst systems. The materials explored in this thesis, i.e. carbon nanoreactors and polymer immobilised ionic liquid supports for MNPs represent exciting candidates for the preparation of catalyst materials with increased activity and stability and it is expected that they will become utilised in commercial processes in the near future.